Ph.D. DISSERTATION

Modelling and Experimental Analysis of Frequency Dependent MIMO Channels

Polytechnical University of Valencia

Communications Department

Valencia, Spain, July 2009

Presented by:

Alexis Paolo García Ariza

Supervisor:

Dr. Lorenzo Rubio Arjona

Tesis Doctoral

Modelado y Análisis Experimental del Canal MIMO en Función de la Frecuencia

Universidad Politécnica de Valencia

Departamento de Comunicaciones

Valencia, España, Julio 2009

Realizada por:

Alexis Paolo García Ariza

Dirigida por:

Dr. Lorenzo Rubio Arjona

To my family

“La inspiración existe, pero tiene que encontrarte trabajando”

Pablo Ruiz Picasso.

Official Acknowledgments

This work was supported by the Programme AlBan, the European Union Programme of High Level Scholarships for Latin America, scholarship No. E04D044088CO, and the Research Support Programme of the Generalitat Valenciana (Spain) No. GV06/076.

Part of this work was done within the Network of Excellence in Wireless COMmunications - NEWCOM, Work Package 2 (WPR2): Research Integration for Department 2 "Radio channel modelling for design optimisation and performance assessment of next generation communication systems".

As well, part of this work was developed in a research stay (between 11/04/07-11/07/07) at the Mobile Communications Group, University of Agder, Grimstad-Norway, under the supervision of Dr. Prof. Matthias Pätzold. The topic addressed was "Perfect modelling and simulation of MIMO channels using real-world measurement data".

Personal Acknowledgments

Special thanks to my supervisor, Professor Dr. Lorenzo Rubio, for his technical and personal support and all his advises given during the last years.

I thank the iTEAM Research Institute staff for the administrative and facilities support, to its sub-director Professor Dr. Narcís Cardona, and all my colleagues at the Mobile Communications Group –MCG, for their friendship and support.

I would like to thank Dr. Prof. Matthias Pätzold and MSc. Dmitry Umansky from University of Agder, Norway, for their very useful discussions about channel modelling. I also thank MSc. Antonio Garcia for his support during one of the measurement campaigns performed for this Dissertation.

I thank Dr. Saúl A. Torrico, at The George Washington University, Washington, D.C, and Comsearch and Andrew Corporation Company, for his support during COST and URSI meetings, and his useful suggestions to improve this work.

Thanks a lot to the Professors Dr. Alirio Cala, Dr. Gabriel Ordonez, Dr. Gilberto Carrillo, Dr. Gerardo Latorre, and Dr. Homero Ortega from the Industrial University of Santander (*Universidad Industrial de Santander - UIS*), Bucaramanga-Colombia, and Dr. Andres Navarro from the ICESI University, Cali-Colombia, whom encouraged me to develop this stay at the European Union.

I thank so much to my colleagues and friends in Europe and Colombia, whose friendship, advices and support helped me during this challenge.

Thanks a lot to my family, my parents Pablo and Isabel, my sister Diana, my brother Erick and my niece Angie. Their love and support were with me all the last years. Thanks to Yeny, your care and love make me always happy. Finally, I thank to *Lady*, my dear sister, anywhere you are.

All of you are a part of this work.

Abstract

The integration of ultra-wideband, cognitive radio, and multiple-input multiple-output (MIMO) radio technologies represents a powerful tool to improve the spectral efficiency of different wireless communication systems. In that way, new strategies for MIMO channel modelling and characterisation are necessary in order to investigate how the central frequency and the bandwidth affect the system performance. Previous investigations have focused less attention how these parameters affect the MIMO channel characteristics. In this PhD Dissertation, a frequency dependent MIMO channel characterisation is presented from both experimental and theoretical view points. The problems addressed in this Dissertation treat five main areas: measurements, data post-processing, channel synthetic generation, multivariate statistics of MIMO data, and MIMO channel modelling.

A measurement setup based on a vector network analyzer (VNA) has been designed and validated, and wideband measurements between 2 and 12 GHz in static indoor scenarios in both line-of-sight (LOS) and non-line-of-sight (NLOS) conditions have been carried out. Besides, a procedure for post-processing, channel synthetic generation and experimental MIMO channel analysis based on frequency domain measurements has been proposed and validated. The experimental procedure is based on normalized non-frequency selective channel transfer matrices, estimation of complex covariance matrices (CCM), and the Cholesky factorisation of the CCM to obtain finally the coloring matrix of the MIMO system. Moreover, a validated correction procedure (CP) for synthetic channel generation is presented for MIMO cases with large-scale arrays when the CCM is indefinite. This CP permits the Cholesky factorisation of such CCM. On the other hand, the multivariate characteristics of the MIMO data have been investigated and tested using multivariate complex normal distribution (MCND) analysis. This MCND analysis has indicated both large-scale array and wideband dependency on the normality of the MIMO data.

On the other hand, different channel metrics have been selected for future performance analysis of beamforming, space time block coding (STBC) and spatial multiplexing (SM) in LOS and NLOS for indoor environments. Based on statistical results, all studied metrics showed frequency dependency between 2 and 12 GHz under a high signal to noise ration (SNR), equal electric separation between array elements and isolation of the path loss. Remarkable changes on the magnitude and phase distributions of the complex spatial correlation coefficients (CSCC), distribution of MIMO system eigenvalues, MIMO capacity, and multipath richness were observed for different central frequencies.

Finally, a new channel model useful for wideband MIMO system simulations, which describes frequency-dependent (FD) wideband MIMO channels, has been formulated imposing wide-sense-stationary-uncorrelated-scattering (WSSUS) conditions. The model is a FD-deterministic-Gaussian-uncorrelated-scattering (FD-DGUS) MIMO channel model, which offers useful statistical properties for experimental characterisation. This model considers the effect of both the central frequency and the bandwidth on the space-time-frequency variation of the channel. Besides, environment FD effects are considered within the model by means of homogeneous plane waves (HPW) and inhomogeneous plane waves (IPW), being the first model in the literature using IPWs and applying perfect MIMO channel modelling. The FD-DGUS-MIMO channel model characteristics are analysed, and its 2D-space-time-frequency correlation function (2D-STFCF), power spectral density (PSD) functions, and quantities are closed formulated. Moreover, the perfect MIMO channel modelling strategy is formulated for parameters estimations using measurements, and the simulation model with fixed parameters is presented.

Resumen

La integración de tecnologías de ultra-wideband, radio-cognitiva y MIMO (*multiple-input multiple-output*) representa una herramienta poderosa para mejorar la eficiencia espectral de los sistemas de comunicación inalámbricos. En esta dirección, nuevas estrategias para el modelado de canales MIMO y su caracterización se hacen necesarias si se desea investigar cómo la frecuencia central y el acho de banda afectan el desempeño de los sistemas MIMO. Investigaciones preliminares han enfocado menos atención en cómo estos parámetros afectan las características del canal MIMO. En esta Tesis de Doctorado se presenta una caracterización del canal MIMO en función de la frecuencia, abordándose puntos de vista experimentales y teóricos. Los problemas indicados en esta Tesis tratan cinco áreas principales: medidas, post-procesado de datos, generación sintética del canal, estadística multivariable para datos MIMO y modelado del canal MIMO.

Se ha diseñado y validado un sistema de medida basado en un analizador vectorial de redes (VNA), y se han ejecutado medidas entre 2 y 12 GHz en condiciones estáticas, tanto en línea de vista (LOS) como no línea de vista (NLOS). Además, se ha propuesto y validado un procedimiento confiable para post-procesado, generación sintética de canal, y análisis experimental del canal MIMO basado en medidas en el dominio de la frecuencia. El procedimiento experimental se ha focalizado en matrices de transferencia del canal (normalizadas) para casos no selectivos en frecuencia, estimándose además las matrices complejas de covarianza (CCM), aplicándose la factorización de Cholesky sobre las CCM y obteniéndose finalmente las matrices de coloreado del sistema MIMO. Además, se presenta un procedimiento de corrección (CP) para generación sintética del canal aplicado a casos MIMO de grandes dimensiones y cuando la CCM es indefinida. Este CP permite la factorización de Cholesky de dichas CCM. Por otro lado, las características multivariables de los datos experimentales MIMO han sido investigadas, realizándose además un test de normalidad compleja multivariable (MCND). Este análisis MCND ha indicado una dependencia en la normalidad de acuerdo a las dimensiones del array y el ancho de banda.

Por otro lado, diferentes métricas del canal han sido seleccionadas para futuros análisis de desempeño de técnicas de *beamforming*, *space time block coding* (STBC) y *spatial multiplexing* (SM) en LOS y NLOS para entornos indoor. Basándose en resultados estadísticos, todas las métricas estudiadas mostraron dependencia en frecuencia entre 2 y 12 GHz bajo una elevada relación señal a ruido (SNR), igual separación eléctrica entre elementos del array y aislamiento de las pérdidas por trayectoria. Cambios importantes a diferentes frecuencias centrales fueron observados en las distribuciones magnitud y fase de los coeficientes complejos de correlación espacial (CSCC), en la distribución de lo valores propios del sistema MIMO, en la capacidad MIMO, y en la riqueza multi-camino.

Finalmente, un nuevo modelo de canal, útil para simulaciones de sistemas MIMO de banda ancha, ha sido formulado imponiendo condiciones de estacionariedad en sentido amplio y *scattering* incorrelados (WSSUS). El modelo, denominado FD-DGUS (*frequency-dependent-deterministic-Gaussian-uncorrelated-scattering*), considera el efecto de la frecuencia central y el ancho de banda sobre la variación espacio-tiempo-frecuencia del canal. Además, efectos FD en el entorno son considerados utilizando ondas planas homogéneas (HPW) e in-homogéneas (IPW), siendo el primer modelo en la literatura utilizando IPWs y aplicando modelado perfecto del canal MIMO. Las características del modelo son analizadas, y se han formulado de forma cerrada su función de correlación 2D-STFCF (*2D-space-time-frequency correlation function*), su función de densidad espectral de potencia (PSD), y parámetros del canal. Además, se propone la estrategia de modelado perfecto del canal MIMO para la estimación de parámetros usando medidas, presentándose finalmente el modelo de simulación con parámetros fijos.

Resum

La integració de tecnologies de banda ampla i MIMO (multiple-input multiple-output) representa una ferramenta poderosa per a millorar l'eficiència espectral dels sistemes de comunicació sense fil. En esta direcció, noves estratègies per al modelatge de canals MIMO i la seua caracterització es fan necessaris si es desitja investigar com la freqüència central i l'ample de banda afecten el funcionament dels sistemes MIMO. Investigacions preliminars han prestat menys atenció en com estos paràmetres afecten les característiques del canal MIMO. En esta Tesi de Doctorat es presenta una caracterització del canal MIMO en funció de la freqüència, abordant-se punts de vista experimentals i teòrics. Els problemes indicats en esta Tesi tracten cinc àrees principals: mesures, post-processat de dades, generació sintètica del canal, estadística multivariable per a dades MIMO i modelatge del canal MIMO.

S'ha dissenyat i validat un sistema de mesura basat en un analitzador vectorial de xarxes (VNA), i s'han executat mesures entre 2 i 12 GHz en condicions estàtiques, tant en línia de vista (LOS) com no línia de vista (NLOS). A més, s'ha proposat i validat un procediment confiable per a post-processat, generació sintètica de canal, i anàlisi experimental del canal MIMO basat en mesures en el domini de la freqüència. El procediment experimental s'ha focalitzat en l'ús de matrius de transferència del canal (normalitzades) per a casos no selectius en freqüència, estimant-se a més les matrius complexes de covariació (CCM), aplicant-se la factorització de Cholesky sobre les CCM i obtenint-se finalment les matrius de caracterització del sistema MIMO. A més, es presenta un procediment de correcció (CP) per a la generació sintètica del canal aplicat a casos MIMO de grans dimensions quan la CCM és indefinida. Aquest CP permet la factorització de Cholesky de dites CCM. D'altra banda, les característiques multivariables de les dades experimentals MIMO han sigut investigades, realitzant-se a més un test de normalitat complexa multivariable (MCND). Esta anàlisi MCND hi ha rebel•lat una dependència en la normalitat d'acord amb les dimensions de l'agrupació d'antenes i l'ample de banda.

D'altra banda, diferents mètriques del canal han sigut seleccionades per a futures anàlisis del funcionament de tècniques de beamforming, space estafe block coding (STBC) i spatial multiplexing (SM) en LOS i NLOS per a entorns indoor. Basat en els resultats estadístics, totes les mètriques estudiades van mostrar dependència en freqüència entre 2 i 12 GHz baix una elevada relació senyal a soroll (SNR), la mateixa separació elèctrica entre elements de l'agrupació d'antenes i aïllament de les pèrdues per trajectòria. Canvis importants a diferents freqüències centrals van ser observats en les distribucions magnitud i fase dels coeficients complexos de correlació espacial (CSCC), en la distribució dels valors propis del sistema MIMO, en la capacitat MIMO, i en la riquesa multi-camí.

Finalment, un nou model de canal, útil per a simulacions de sistemes MIMO de banda ampla, ha sigut formulat imposant condicions d'estacionarietat en sentit ampli i scattering incorrelats (WSSUS). El model, denominat FD-DGUS (frequency dependent - deterministic-Gaussianuncorrelated-scattering), considera l'efecte de la freqüència central i l'ample de banda sobre la variació espai-temps-freqüència del canal. A més, efectes FD en l'entorn són considerats utilitzant ones planes homogènies (HPW) i in-homogènies (IPW), sent el primer model en la literatura utilitzant IPWs i aplicant modelatge perfecte del canal MIMO. Les característiques del model són analitzades, i s'han formulat de forma tancada la seua funció de correlació 2D-STFCF (2D-space-time-frequency correlation function), la seua funció de densitat espectral de potència (PSD), i paràmetres del canal. A més, es proposa l'estratègia de modelatge perfecte del canal MIMO per a l'estimació de paràmetres usant mesures, presentant-se finalment el model de simulació amb paràmetres fixos.

CONTENTS

List of Figures ..... **xxiii**

List of Tables ..... **xxix**

Preface ..... **xxxi**

List of abbreviations ..... **xxxiii**

List of notations ..... **xxxvii**

List of Publications ..... **xli**

1. PRELIMINARIES ***3***

1.1. Introduction and motivation **3**

1.2. Relevance **7**

1.3. Objectives of the Dissertation **9**
1.3.1. Main objective 9
1.3.2. Secondary objectives 9

1.4. Problems addressed in the Dissertation **10**
1.4.1. MIMO measurements 10
1.4.2. MIMO data post-processing 11
1.4.3. MIMO channel synthetic generation 11
1.4.4. MIMO channel modelling 12

1.5. Research contributions **13**

1.6. Document structure **14**

References **16**

2. MIMO CHANNEL MEASUREMENTS ***21***

2.1. Introduction **21**

2.2. Environment and scenarios **22**

2.3. Measurement setup **24**
2.3.1. Vector network analyzer (VNA) configuration 24
2.3.2. MIMO array configuration 25
2.3.3. Ultra wideband biconical antennas 27

2.4. Link budget and dynamic range **30**
2.4.1. Link budget 30
2.4.2. Noise floor 31

2.5. Minimum conditions for measurements **32**

2.6. Post-processing of MIMO data **34**
2.6.1. MIMO transfer matrix normalisation 34
2.6.2. FSC MIMO matrix estimation 36

2.7. Conclusions **37**

References **38**

3. SYNTHETIC MIMO CHANNEL ***39***

3.1. Introduction **39**

3.2. FSC MIMO matrix: Cholesky factorisation and limitations **40**

3.3. Alternating projections to find the closest positive definite FSC MIMO matrix **41**

3.4. Performance of the CP **43**

3.4.1. Useful considerations for the CP 46

3.5. MIMO data characteristics and their relationship with estimated covariance matrices **48**

3.5.1. Ergodicity of data 48

3.5.2. Issues in the FSC MIMO matrix estimation 49

3.5.3. Multivariate normal distribution of the MIMO data 53

3.5.3.1. Multivariate normal distribution tests for MIMO data 62

3.5.4. Linearity of the MIMO data entries 69

3.6. FSC matrix estimation techniques under low-sampled data sets **75**

3.7. Conclusions **76**

References **78**

4. EXPERIMENTAL MIMO ANALYSIS ***80***

4.1. Introduction **80**

4.2. Experimental MIMO channel capacity **81**

4.3. MIMO system eigenvalues analysis **88**

4.3.1. Array gain and diversity effects 95

4.3.2. Channel multipath richness 97

4.4. Spatial correlation analysis **98**

4.4.1. Magnitude and phase of the SCCC 100

4.4.2. Angular estimations using ULAs 105

4.5. Validation of the experimental procedure **106**

4.5.1. Isolation of the path loss effect 107

4.5.2. Capacity of the synthetic channel vs. measurements 108

4.5.3. Synthetic channel generator: eigenvalues stability 108

4.6. Conclusions **109**

References **112**

5. PERFECT MIMO CHANNEL MODELLING ***115***

5.1. Introduction **115**

5.2. FD-DGUS-MIMO channel model 116
5.2.1. DG processes for HPWs 131
5.2.2. Random phases for HPWs 138
5.2.3. DG processes for IPWs 140
5.2.4. Random phases for IPWs 143
5.2.5. Uncorrelated-Scattering for HPWs and IPWs 144

5.3. 2D-space-time-frequency correlation functions 145

5.4. Scattering function 148

5.5. Characteristic functions and quantities 149
5.5.1. Characteristic functions 150
5.5.1.1. Delay-Doppler PSD 150
5.5.1.2. Delay-DOA PSD 150
5.5.1.3. Delay-DOD PSD 151
5.5.1.4. DOD-DOA PSD 151
5.5.1.5. Doppler-DOA PSD 152
5.5.1.6. Delay PSD 153
5.5.2. Characteristic Quantities 153
5.5.2.1. Delay average and Delay spread 153
5.5.2.2. Doppler average and Doppler spread 154
5.5.2.3. DOD average and DOD spread 155
5.5.2.4. DOA average and DOA spread 156

5.6. Perfect wideband MIMO channel modelling 158
5.6.1. Measurement vs. model PSDs: perfect and non-perfect 158
5.6.2. Model parameters calculation from PSD measurements 159
5.6.3. Model parameters from non-consistent measurements 165
5.6.4. Parameters estimation based on the 2D-STFCF 166

5.7. FD-DGUS-MIMO channel simulations 167

5.8. Conclusions 170

References 172

6. CONCLUSIONS AND FUTURE RESEARCH 175

6.1. Introduction 175

6.2. Conclusions 175
6.2.1. General conclusions of the Dissertation 175
6.2.2. Particular conclusions of the Dissertation 176
6.2.2.1. Measurement setup and experimental procedure 176
6.2.2.2. Channel synthetic generation 177
6.2.2.3. Alternating projection (AP) method for CCM 177
6.2.2.4. MIMO channel parameter evaluation 178
6.2.2.5. Multivariate and linearity analysis of MIMO data 179
6.2.2.6. FD-DGUS-MIMO model 180

6.3. Future research 180
6.3.1.1. Measurement setup and experimental procedure 180
6.3.1.2. Channel synthetic generation 181
6.3.1.3. Alternating projection (AP) method for CCM 181

6.3.1.4. MIMO channel parameter evaluation....181
6.3.1.5. Multivariate and linearity analysis of MIMO data....182
6.3.1.6. FD-DGUS-MIMO model....183

APPENDIX A. MULTIVARIATE STATISTICS FOR MIMO 185

A.1. Matrix variate complex normal distribution....185

A.2. Matrix variate complex Wishart distribution....187

A.3. Surfaces of constant variance....188

List of Figures

Figure 2.1. Block diagram of the performed experimental procedure for the MIMO channel characterisation.

Figure 2.2. Indoor scenario (Zone A): indoor environment for measurement campaigns in LOS and NLOS conditions at the iTEAM - UPV.

Figure 2.3. Indoor scenario (Zone B): indoor environment for measurement campaigns in LOS and NLOS conditions at the ETSIT - UPV. a) Measurements in LOS, b) Measurements in NLOS.

Figure 2.4. Measurement setup for MIMO channels using a vector network analyzer (VNA) taking into account the isolation of the path loss and a high SNR regime. The parameters *Lx* indicate losses for each component, *Px* powers, and *Gx* gains.

Figure 2.5. Virtual array configuration to perform measurements at different frequency bands using uniform linear arrays (ULAs) at both ends of the link.

Figure 2.6. Measurement equipment in Zone B in NLOS: a) VNA, robotic precise linear positioning system, UWB antenna, and broadband devices at the RX side, b) UWB antenna, precise linear positioning system, amplifiers, power source, and broadband devices at the TX side.

Figure 2.7. Omni-directional UWB antenna EM-6865 characterisation between 2 and 12 GHz using an anechoic chamber: a) antenna EM-6865, b) characterisation at 2 and 2.4 GHz based on two reference horn antennas, and c) characterisation between 4 and 12 GHz based on two reference double ridged horn antennas.

Figure 2.8. EM-6865 antenna gain versus frequency. Values obtained by cubic interpolation using the provided manufacturer information and the data obtained in an anechoic chamber using reference horn antennas between 4 and 18 GHz.

Figure 2.9. EM-6865 antenna gain patter variations between 2 and 12 GHz: a) H plane b) V plane. Note that the V plane shows nulls at 180 and 0º, which correspond to the top and bottom of the biconical antenna.

Figure 2.10. Noise floor for different number of frequency bin samples at 2 GHz. SPAN of 500 MHz and IF filter of 10 kHz.

Figure 2.11. Experimental noise level (average) in the VNA for different span and IF filters.

Figure 2.12. Comparisons on the calculation of the PDP per TX-RX pairs of antennas when the number of time snapshots increases: a) error b) variance

Figure 2.13. Samples and segmentation in the frequency domain used to calculate the entries of $\widehat{\mathbf{H}}$ based on the measured sequences $\widehat{H}_{ij}^{\kappa}[f_l]$ around f_c.

Figure 3.1. CDF of the $\widetilde{\mathbf{R}}_{\mathrm{MIMO}}$ eigenvalues for values lower than 1.5 for different MIMO array configurations, i.e., $N = M = \{2,5,8,9\}$.

Figure 3.2. Impact of a fixed tol and ε on the performance of the CP for different MIMO array configurations, i.e., $N = M = \{2,5,8,9\}$.

Figure 3.3. Impact of tol and ε on the performance of the CP for a 5×5 MIMO array configuration.

Figure 3.4. Impact of ε, with tol =10-15, on the capacity of the generated synthetic MIMO channel for $N = M = \{5,6,7,8\}$.

Figure 3.5. Error between $\widetilde{\mathbf{R}}_{\mathrm{MIMO}}$ and $\widehat{\mathbf{R}}_{\mathrm{MIMO}}$: error between CDFs of the eigenvalues in terms of $\varepsilon_{\min}$ for different $N \times M$ array configurations.

Figure 3.6. CDF of the $\widetilde{\mathbf{R}}_{\mathrm{MIMO}}$ eigenvalues lower that 1.5 for different array configurations, $N = M = \{2,5,8\}$. Impact of the number of samples with SNR higher than 15dB for frequency selective channels.

Figure 3.7. Surfaces of constant variance to test the MND of MIMO data (real part of $\widehat{\mathbf{h}}_{\omega,v}^{[f_{l'},t_{\kappa'}]}$): theoretical and experimental results for $N = 2,\ M = 1$, $f_c = 12$ GHz in NLOS, with a) $B = 2.5$ MHz, b) $B = 5$ MHz, c) $B = 10$ MHz, and d) $B = 100$ MHz.

Figure 3.8. PDF of MND to test the normality of MIMO data (real part of $\widehat{\mathbf{h}}_{\omega,v}^{[f_{l'},t_{\kappa'}]}$): theoretical and experimental results for $N = 2,\ M = 1$, $f_c = 12$ GHz in NLOS, with a) $B = 2.5$ MHz, b) $B = 5$ MHz, c) $B = 10$ MHz, and d) $B = 100$ MHz.

Figure 3.9. Skeweness and Kurtosis for UCND test of $\hat{H}_{ij}^{\kappa,\omega}[f_{l'}]$, with $B = \{2.5,5,10,100\}$ MHz, where $W = \{80,40,20,2\}$ and $I = \{40,80,160,1600\}$, respectively, using entries from configurations $N = M = \{3,4,5,6,7,8\}$: a) CDF of the Skeweness for the $\widehat{\mathbf{H}}_{\omega}$ entries in Zone A, and b) CDF of the Kurtosis for the $\widehat{\mathbf{H}}_{\omega}$ entries in Zone A.

Figure 3.10. Skeweness and Kurtosis for UCND test of $\hat{H}_{ij}^{\kappa,\omega}[f_{l'}]$, with $B = \{2.5,5,10,100\}$ MHz, where $W = \{80,40,20,2\}$ and $I = \{40,80,160,1600\}$, respectively, using entries from configurations $N = M = \{3,4,5,6,7,8\}$: a) CDF of the Skeweness for the $\widehat{\mathbf{H}}_{\omega}$ entries in Zone B, and b) CDF of the Kurtosis for the $\widehat{\mathbf{H}}_{\omega}$ entries in Zone B.

Figure 3.11. Skeweness and Kurtosis for UCND test of the synthetic channel entries, with $B = \{2.5,5,10,100\}$ MHz, where $W = \{80,40,20,2\}$ and $I = \{40,80,160,1600\}$, respectively, and MIMO configurations $N = M = \{3,4,5,6,7,8\}$: a) CDF of the Skeweness and Kurtosis for Zone A, and b) CDF of the Skeweness and Kurtosis for Zone B.

Figure 3.12. Skeweness and Kurtosis for MCND test of $\widehat{\mathbf{H}}_{\omega}$, with $B = \{2.5,5,10\}$ MHz, where $W = \{80,40,20\}$ and $I = \{40,80,160\}$, respectively, and $N = M = \{2,4,5,6,7\}$: a) CDF of the Skeweness, $b_{1,NM}$, for Zone A, and b) CDF of the Kurtosis, $b_{2,NM}$, for Zone A.

Figure 3.13. Skeweness and Kurtosis for MCND test of $\widehat{\mathbf{H}}_{\omega}$, with $B = \{2.5,5,10\}$ MHz, where $W = \{80,40,20\}$ and $I = \{40,80,160\}$, respectively, and $N = M = \{2,4,5,6,7\}$: a) CDF of the Skeweness, $b_{1,NM}$, for Zone B, and b) CDF of the Kurtosis, $b_{2,NM}$, for Zone B.

Figure 3.14. CDF of the envelope correlation coefficients $\tilde{R}_{ij,\ell s}^{env}$ for 2.5 cm among antenna elements, with $B=\{2.5,5,10,100\}$ MHz, where $W=\{80,40,20,2\}$ and $I=\{40,80,160,1600\}$, respectively, and MIMO configurations $N=M=\{3,4,5,6,7,8\}$. a) Zone A, b) Zone B.

Figure 3.15. CDF of the correlation ratio coefficients $\eta_{ij,\ell s}$ for 2.5 cm among antenna elements, with $B=\{2.5,5,10,100\}$ MHz, where $W=\{80,40,20,2\}$ and $I=\{40,80,160,1600\}$, respectively, and MIMO configurations $N=M=\{3,4,5,6,7,8\}$. a) Zone A, b) Zone B.Figure 3.15. CDF of the correlation ratio coefficients $\eta_{ij,\ell s}$ for 2.5 cm among antenna elements, with $B=\{2.5,5,10,100\}$ MHz, where $W=\{80,40,20,2\}$ and $I=\{40,80,160,1600\}$, respectively, and MIMO configurations $N=M=\{3,4,5,6,7,8\}$. a) Zone A, b) Zone B.

Figure 3.16. CDF of the linearity error for 2.5 cm among antenna elements, with $B=\{2.5,5,10,100\}$ MHz, where $W=\{80,40,20,2\}$ and $I=\{40,80,160,1600\}$, respectively, and MIMO configurations $N=M=\{3,4,5,6,7,8\}$. a) Zone A, b) Zone B.

Figure 4.1. CDF of MIMO channel capacity, $\tilde{C}$, for $M=N=2$, SNR=10dB, with one wavelength of elements separation, $f_c=\{2,2.4,6,12\}$ GHz in: a) LOS and NLOS in Zone A, and, b) LOS and NLOS in Zone B.

Figure 4.2. CDF of MIMO channel capacity, $\tilde{C}$, for $M=N=3$, SNR=10dB, with one wavelength of elements separation, $f_c=\{2,2.4,6,12\}$ GHz in: a) LOS and NLOS in Zone A, and, b) LOS and NLOS in Zone B.

Figure 4.3. CDF of MIMO channel capacity, $\tilde{C}$, for $M=N=4$, SNR=10dB, with one wavelength of elements separation, $f_c=\{6,12\}$ GHz in: a) LOS and NLOS in Zone A, and, b) LOS and NLOS in Zone B.

Figure 4.4. Ergodic and 1% outage capacities for $M=N=\{1,2,3,4\}$, SNR=10dB, with one wavelength of elements separation, $f_c=\{2,2.4,6,12\}$ GHz in: a) LOS and NLOS in Zone A, and, b) LOS and NLOS in Zone B.

Figure 4.5. CDF of the $\widetilde{\mathbf{H}}^H\widetilde{\mathbf{H}}$ matrix eigenvalues for $M=N=2$, with one wavelength of elements separation, $f_c=\{2,2.4,6,12\}$ GHz in: a) LOS and NLOS in Zone A, and, b) LOS and NLOS in Zone B.

Figure 4.6. CDF of the $\widetilde{\mathbf{H}}^H\widetilde{\mathbf{H}}$ matrix eigenvalues for $M=N=3$, with one wavelength of elements separation, $f_c=\{2,2.4,6,12\}$ GHz in: a) LOS and NLOS in Zone A, and, b) LOS and NLOS in Zone B.

Figure 4.7. CDF of the $\widetilde{\mathbf{H}}^H\widetilde{\mathbf{H}}$ matrix eigenvalues for $M=N=4$, with one wavelength of elements separation, $f_c=\{6,12\}$ GHz in: a) LOS and NLOS in Zone A, and, b) LOS and NLOS in Zone B.

Figure 4.8. Mean power gain of the $\widetilde{\mathbf{H}}^H\widetilde{\mathbf{H}}$ matrix eigenvalues, $\tilde{\lambda}_1>\tilde{\lambda}_2>\tilde{\lambda}_3$, for $M=N=3$, with one wavelength elements separation, $f_c=\{2,6,12\}$ GHz in LOS and NLOS in Zone A.

Figure 4.9. CDF of $\mathrm{Tr}\left\{\widetilde{\mathbf{H}}^{H}\widetilde{\mathbf{H}}\right\}$ for $M=N=3$, with one wavelength of elements separation, $f_c=\{2,6,12\}$ GHz, in LOS and NLOS at Zone A.

Figure 4.10. PDF of $\left|\tilde{R}_{ij,\ell s}\right|$, $\{\forall j=s; s=\{1,\cdots,M\}; \forall i=(\ell+1); \ell=\{1,\cdots,N\}\}$, and $\{\forall i=\ell; \ell=\{1,\cdots,N\}; \forall j=(s+1); s=\{1,\cdots,M\}\}$, for $N=M=\{2,3,4\}$, with one wavelength of elements separation and $f_c=\{2,2.4,6,12\}$ GHz in: a) LOS and NLOS in Zone A, and, b) LOS and NLOS in Zone B.

Figure 4.11. PDF of $\angle\tilde{R}_{ij,\ell s}$, $\{\forall j=s; s=\{1,\cdots,M\}; \forall i=(\ell+1); \ell=\{1,\cdots,N\}\}$, and $\{\forall i=\ell; \ell=\{1,\cdots,N\}; \forall j=(s+1); s=\{1,\cdots,M\}\}$, for $N=M=\{2,3,4\}$, with one wavelength of elements separation and $f_c=\{2,2.4,6,12\}$ GHz in: a) LOS and NLOS in Zone A, and, b) LOS and NLOS in Zone B.

Figure 4.12. Path loss effect isolation: mean local eigenvalues variations vs. distance for $N=M=4$, with one wavelength element separations, 6 and 12 GHz, in a) LOS and b) NLOS for Zone A.

Figure 4.13. CDF of the MIMO capacity for $N=M=3$, one wavelength elements separation, at 2 GHz, NLOS, for the synthetic MIMO channel $\widetilde{\mathbf{H}}$ and the measured MIMO channel $\widehat{\mathbf{H}}_{\omega}$.

Figure 4.14. Validation of the synthetic channel generator according to the number of samples: CDF of the MIMO system eigenvalues $\tilde{\lambda}_i$ and $\sum\tilde{\lambda}_i$ (trace of $\widetilde{\mathbf{H}}^{H}\widetilde{\mathbf{H}}$) for $N=M=4$, i.i.d channel, and 5x104, 1x105 and 2x105 samples.

Figure 5.1. Homogeneous and In-homogeneous plane waves (HPWs and IPWs, respectively).

Figure 5.2. Transmitter and receiver array geometry for the FD-DGUS-MIMO model.

Figure 5.3. Vector representation used for phase analysis at the receiver array. Black circles depict the array elements.

Figure 5.4. Geometry used at the receiver array for the FD-DG model when the bandwidth and carrier frequency increase.

Figure 5.5. TX and RX geometry used in the FD-DG-MIMO model for, a) waves grouping and, b) space array effects for phase analysis.

Figure 5.6. Variation and trend of the relative wavelength vs. relative bandwidth: geometric series approximation, a) for $f_c=\{4,6,12\}$ GHz and $B=7$ GHz, b) for $f_c=\{6,7,12\}$ GHz and $B=7$ GHz and c) $f_c=\{4,6,12\}$ GHz and $B=1$ GHz.

Figure 5.7. Relative wavelength variations: second-order polynomial approximation, geometric series, and error bounds for $f_c>7$ GHz and $0<B<7$ GHz.

Figure 5.8. PDFs of the theoretical and simulated distributions for, a) AOA spreading with $\sigma_{\phi''}=\{4^{o},6^{o},8^{o}\}$, and b) AOD spreading with $\sigma_{\phi'}=\{4^{o},6^{o},8^{o}\}$, $\phi_{R_{n,\ell}}=30^{o}$ and $\gamma=1.5$.

Figure 5.9. Experimental PDF of $\tau''_{\kappa,\ell}$ for AOA spreading, $\phi''_{R_{\kappa,n,\ell}}$, with $\sigma_{\phi''}=\{4^{o},6^{o},8^{o}\}$.

Figure 5.10. Experimental PDF of $\Omega''_{R_{\kappa,n,\ell}}$, with and without approximations.

Figure 5.11. Experimental PDF of $\measuredangle\exp\left(j\left(u_{\kappa,n,\ell}\right)\right)$ with and without approximations under different bandwidths and central frequencies.

Figure 5.12. Experimental PDF of $\measuredangle\exp\left(j\left(u^{in}_{\kappa',n',\ell'}\right)\right)$ under different B and central f_c.

Figure 5.13. Perfect MIMO channel modelling based on perfect fitting of the PSD characteristics

Figure 5.14. Delay-Doppler PSD experimental matrix.

Figure 5.15. Delay-DOA/DOD PSD experimental matrix.

Figure 5.16. Simulation results of the correlation functions of the FD-DGUS-MIMO model, a) frequency-time correlation function with/without IPWs at 2 GHz and 200 MHz bandwidth, and, b) frequency-time correlation function with/without IPWs at 2 GHz and 700 MHz bandwidth.

Figure 5.17. Simulation results of the correlation function of the FD-DGUS-MIMO model: RX-space-time correlation function with/without IPWs at 2 GHz and 200 MHz bandwidth.

List of Tables

Table 3.1. Median values of the Skeweness, $\overline{b}_{1,NM}$, and Kurtosis, $\overline{b}_{2,NM}$, for MCND test of $\widehat{\mathbf{H}}_{\omega}$, with $B=\{2.5,5,10\}$ MHz, where $W=\{80,40,20\}$ and $I=\{40,80,160\}$, respectively, and $N=M=\{2,3,4,5,6,7\}$ for Zone A and B.

Table 4.1. Mean values of $\left|\tilde{R}_{ij,\ell s}\right|$ and $\measuredangle\tilde{R}_{ij,\ell s}$ with $N=M=\{2,3,4\}$, one wavelength of elements separation for $\{\forall j=s; s=\{1,\cdots,M\}; \forall i=(\ell+1); \ell=\{1,\cdots,N\}\}$, and $\{\forall i=\ell; \ell=\{1,\cdots,N\}; \forall j=(s+1); s=\{1,\cdots,M\}\}$, with $f_c=\{2,2.4,6,12\}$ GHz, in LOS and NLOS in Zone A and B.

Preface

Following the wireless and mobile telecommunications activities that I started at the Electrical, Electronic and Telecommunications Engineering Department at the Industrial University of Santander (Universidad Industrial de Santander, UIS) in 2000 in Bucaramanga, Colombia, I concluded other works related with radio propagation and mobile communications in 2003[1,2]. Afterwards, I continued with similar research works in a MSc at the same University[3], and I finally started a PhD in Telecommunications at the Polytechnical University of Valencia (Universidad Politécnica de Valencia, UPV) at the end of 2004. All of these activities have given me some tools to follow a professional life around wireless communications, and then obtaining some benefits for me and my country.

I started in 2004 a PhD thanks to the support of the AlBan Program (the European Union Programme of High Level Scholarships for Latin America, scholarship No. E04D044088CO), and thanks to the support of both the UPV and UIS, by means of the iTEAM Research Institute and RadioGIS group, respectively. I followed during the last years the planned research activities and proposed this Dissertation as the final step to obtain the PhD degree in Telecommunications.

In this way, the selection of the specific research topics to perform this work took some time due to the main selected topic, i.e., multiple-input multiple-output (MIMO) wireless channels, was in the literature for long time[4], finding about 300 references related with modelling, simulation, measurement and space-time processing for MIMO systems.

Thanks to the experience in wireless channels by my supervisor, Dr. Lorenzo Rubio, my previous experience in radio propagation, and the technological support at the iTEAM (broadband equipment and devices), I was able to focus my research around measurement, characterisation and modelling of MIMO wireless channels.

---

[1] A. P. García, A. Navarro, N. Cardona, and H. Ortega, "Effect of terrain on electromagnetic propagation in urban environments on the andean region, using the COST 231- Walfisch-Ikegami model," *7th Management Committee Meeting COST 273 (Commission of the European Communities and COST Telecommunications, "Towards Mobile Broadband Multimedia Networks")*, 11 p., Paris, 2003.

[2] A. P. García, H. Ortega, A. Navarro and H. Rodríguez, "Effect of terrain on electromagnetic propagation in urban environments on the andean region, using the COST 231- Walfisch-Ikegami model and GIS planning tools," *Twelfth International Conference On Antennas And Propagation (ICAP 2003)*, University of Exeter, UK, pp. 270-275, 2003.

[3] A. P. García, "Análisis de irradiación electromagnética en las inmediaciones de una radio base sectorizada bajo condiciones andinas," *UIS Ingenierías: Revista de la Facultad de Ingenierías Físico-Mecánicas*, Universidad Industrial de Santander, Vol. 3, No. 2, pp. 99-116, 2004, ISSN 1657-4583.

[4] A. P., García, "Sistemas MIMO como alternativa para el control del efecto multitrayectoria y de la interferencia co-canal en sistemas de radio móvil satelital y terrestre," *Revista de la Facultad de Ingeniería "Sistemas y Telemática,"* Icesi, Vol. 2, No.1, pp. 57-94, 2004, ISSN 1692-5238.

I finished a research stage in 2006 with an experimental capacity analysis at different central frequencies[5], and then I focused my activities to experimental MIMO frequency dependent analysis[6] thanks to many ideas treated in international conferences and research networks as COST2100[7] and NEWCOM[8] (Network of Excellence in Wireless COMmunications). Besides of this experimental analysis, a complementary part of the main topic was reached in a research stay in Norway[9], where modelling of frequency dependent MIMO channels was addressed.

Therefore, this PhD Dissertation treats, in my judgment, a wide set of topics related with MIMO channel characterisation, where both new and old theoretical/practical knowledge are reflected. This is a document where the physics, linear algebra, multivariate statistics and signal processing applied to MIMO channels find a common way seeking the characterisation of frequency dependent MIMO channels.

[5] A. P. García, *Memoria del trabajo de investigación para la obtención del Diploma de Estudios Avanzados (DEA): Análisis experimental de la capacidad en sistemas MIMO de interiores en función de la frecuencia*, Universidad Politécnica de Valencia, Doctorado en Telecomunicación, Octubre de 2006.

[6] A. P. García and L. Rubio, "Frequency impact on the indoor MIMO channel capacity between 2 and 12 GHz," IEEE 66th Vehicular Technology Conference - VTC, Baltimore, USA, 30 September-3rd October, 2007. ISBN: 1-4244-0264-6.

[7] Commission of the European Communities and COST Telecommunications, COST2100: "Pervasive Mobile & Ambient Wireless Communications".

[8] Network of Excellence in Wireless COMmunications - NEWCOM, Work Package 2: Research Integration for Department 2 "Radio channel modelling for design optimisation and performance assessment of next generation communication systems". Quarterly Management Reports 9-12, WPR2 (IMCO2-UPV, 1 March 2006 - 28 February 2007).

[9] Topic of the research stay at University of Agder: "Perfect modelling and simulation of MIMO channels using real-world measurement data," 11/04/07-11/07/07, Mobile Communications Group, University of Agder, Grimstad-Norway, under the supervision of Dr. Prof. Matthias Pätzold.

List of abbreviations

2D	2 Dimensions
2D-STFCF	2D-space-time-frequency correlation function
2D-D^3-PSD	2D-direction-Doppler-delay power spectral density function
3D	3 Dimensions
3G	3rd Generation
3GPP	3rd Generation Partnership Project
4G	4th Generation
AOA	Angle Of Arrival
AOD	Angle Of Departure
AP	Alternating Projection
APS	Angular Power Spectrum
BAN	Body Area Networks
BER	Bit Error Rate
CCM	Complex Covariance Matrix
CDF	Cumulative Distribution Function
CDMA	Code Division Multiple Access
CF	Correlation Function
CLT	Central Limit Theorem
COST	Cooperation in the Field of Scientific and Technical Research
CP	Correction Procedure
CRS	Cognitive Radio Systems
CSCC	Complex Spatial Correlation Coefficients

DG	Deterministic Gaussian
DGUS	Deterministic Gaussian Uncorrelated Scattering
DOA	Direction Of Arrival
DOD	Direction Of Departure
ETSIT	Escuela Técnica Superior de Ingenieros de Telecomunicación
ESPRIT	Estimation of Signal Parameters via Rotational Invariance Techniques
FA	Frequency Autocorrelation
FCF	Frequency Correlation Function
FD	Frequency Dependent
FDD	Frequency Division Duplexing
FSC	Full Spatial Correlation
HiperLAN/2	High Performance Radio Local Area Networks version 2
HPW	Homogeneous Plane Wave
IEEE	Institute of Electrical and Electronics Engineers
IF	Intermediate Frequency
IFFT	Inverse Fast Fourier Transformation
i.i.d	Independent Identically Distributed
INLSA	Iterative Nonlinear Least Squares Approximation
IPW	Inhomogeneous Plane Wave
IRR	Infinite Impulse Response
iTEAM	Instituto de Telecomunicaciones y Aplicaciones Multimedia
ITU	International Telecommunication Union
LAN	Local Area Networks
LOS	Line Of Sight
MIMO	Multiple Input Multiple Output
MISO	Multiple Input Single Output

MCND	Multivariate Complex Normal Distribution
MCC	Multivariate Complex Covariance
MCM	Multivariate Complex Mean
ML	Maximum Likehood
MLE	Maximum Likehood Estimator
MMAC	Multimedia Mobile Access Communication Systems
MMW	Millimetre-Waves
MND	Multivariate Normal Distribution
MUSIC	Multiple Signal Classification
MVCND	Matrix Variate Complex Normal Distribution
MVCWD	Matrix Variate Complex Wishart Distribution
NEWCOM	Network of Excellence in Wireless COMmunications
NLOS	Non LOS
OFDMA	Orthogonal Frequency Division Multiple Access
PAN	Personal Area Networks
PC	Personal Computer
PDF	Probability Density Function
PDP	Power Delay Profile
PSD	Power Spectral Density
RF	Radio Frequency
SAGE	Space-Alternating Generalized Expectation-maximization
SCCC	Spatial Complex Correlation Coefficient
SCE	Shrinkage Covariance Estimator
SCF	Space Correlation Function
SCV	Surfaces of Constant Variance
SNR	Signal to Noise Ratio

SIMO	Single Input Multiple Output
SISO	Single Input Single Output
SM	Spatial Multiplexing
ST	Space Time
STBC	Space Time Block Coding
STD	STandard Deviation
TCF	Time Correlation Function
TDD	Time Division Duplexing
TOA	Time Of Arrival
UCND	Univariate Complex Normal Distribution
UMTS	Universal Mobile Telecommunication System
ULA	Uniform Lineal Array
UPV	Universidad Politécnica de Valencia
US	Uncorrelated Scattering
VNA	Vector Network Analyzer
WLAN	Wireless Local Area Networks
WPAN	Wireless Personal Area Networks
WMAN	Wireless Metropolitan Area Networks
WCDMA	Wideband CDMA
WSS	Wide Sense Stationary
WSSUS	Wide Sense Stationary Uncorrelated Scattering

List of notations

Variables

$\mathbf{H}$	bold capitalize indicates matrix (can be random and complex)
$\mathbf{a}$	bold lowercase indicates column or row vector (can be random and complex)
H	italic capitalize indicates entries of a matrix (can be random and complex)
a	italic lowercase indicates entries of a vector or scalar (can be random and complex)

Sets

$\mathbb{R}$	real field
$\mathbb{C}$	complex field
$\mathbb{Z}$	integer field

Indexing

H_{ij}	element in i-th row and j-th column of matrix $\mathbf{H}$
$\eta_{ij,\ell s}$	indicates a result of a multivariable operation using matrix entries at the i-th row and j-th column and the ℓ-th row and s-th column
$H_{ij}^{\kappa,\omega}$	element in i-th row and j-th column of matrix $\mathbf{H}$, for the κ-th snapshot and the ω-th segment
$H_{ij\,/\,\ell s}^{\kappa,\omega}$	element in i-th row and j-th column, or ℓ-th row and s-th column, of matrix $\mathbf{H}$, for the κ-th snapshot and the ω-th segment

Variable cases

$\widetilde{\mathbf{H}}$, $\widehat{\mathbf{H}}$, $\widehat{\mathbf{H}}$	experimental (or simulated) approximation to the original variable $\mathbf{H}$

$\tilde{H}$, $\hat{H}$, $\widehat{H}$	experimental (or simulated) approximation to the original variable H
$\tilde{\lambda}$, $\hat{\lambda}$, $\widehat{\lambda}$	experimental (or simulated) approximation to the original variable λ

Matrix cases

$\mathbf{R} > 0$	means that $\mathbf{R}$ is positive definite
$\mathbf{R} < 0$	means that $\mathbf{R}$ is negative definite
$\mathbf{R} \geq 0$	means that $\mathbf{R}$ is positive semidefinite
$\mathbf{I}_M$	$M \times M$ identity matrix

Operators

$E[\cdot]$	expectation operator
$P[\cdot]$	probability operator
$\mathrm{Re}\{\mathbf{h}\}$	real part of $\mathbf{h}$
$\mathrm{Im}\{\mathbf{h}\}$	imaginary part of $\mathbf{h}$
$\mathrm{Tr}\{\mathbf{H}\}$	trace of $\mathbf{H}$
$\mathrm{rank}\{\mathbf{H}\}$	rank of $\mathbf{H}$
$\det(\mathbf{H})$	determinant of $\mathbf{H}$
$\mathrm{vec}(\mathbf{H})$	stacks $\mathbf{H}$ into a $NM \times 1$ vector columnwise, if $\mathbf{H}$ is a $N \times M$ matrix
$\mathrm{cov}(\mathbf{H})$	gets the covariance matrix of $\mathbf{H}$
$diag\{a_1, \cdots, a_M\}$	$M \times M$ diagonal matrix with $i = j$ -th elements equal a_i
$\min(N, M)$	gets the minimum scalar between N or M
$\max(N, M)$	gets the maximum scalar between N or M
$\|\mathbf{R}\|_F$	Frobenius norm of $\mathbf{R}$
$\|\mathbf{h}\|$	norm of $\mathbf{h}$
$\|a\|$	absolute value of scalar a
$\langle H_{ij}(f,t) \rangle_t$	ensemble-averaged mean of $H(f,t)$ on the domain t
$\mathbf{H}^T$	transpose of $\mathbf{H}$

$\mathbf{H}^H$	conjugate transpose of $\mathbf{H}$
$\mathbf{H}^*$	conjugate of $\mathbf{H}$
$\mathbf{R}^{-1}$	inverse of $\mathbf{R}$
$\otimes$	Kronecker product

Special notations

$\triangleq$	variable definition
$\lceil a / b \rceil$	gets the upper nearest integer
$\lfloor a / b \rfloor$	gets the lower nearest integer
$[a, b)$	set of scalar values from a to $< b$

Statistics

$a \sim N(\mu, \sigma)$	a is univariate normal distributed with mean μ and variance σ (a can be complex)
$\mathbf{h} \sim N_{NM}(\boldsymbol{\mu}, \boldsymbol{\Sigma})$	$\mathbf{h}$ is multivariate normal distributed with mean vector $\boldsymbol{\mu}$ and covariance matrix $\boldsymbol{\Sigma}$ ($\mathbf{h}$ can be complex)
$\mathbf{H} \sim N_{N,M}(\mathbf{M}, \boldsymbol{\Psi})$	$\mathbf{H}$ is matrix variate normal distributed with mean matrix $\mathbf{M}$ and covariance matrix $\boldsymbol{\Psi}$ ($\mathbf{H}$ can be complex)
$W_{NM}(K-1, \boldsymbol{\Sigma})$	Wishart distribution with $K-1$ degrees of freedom
$\Gamma(x)$	gamma function
$\Gamma_{NM}(\mathbf{x})$	multivariate gamma function
$p(x)$	probability density function of random variable x
$p(x_1, \cdots, x_{NM})$	joint probability density function of random variables $x_1, \cdots, x_{NM}$

List of Publications

Publications related to the PhD Dissertation

Publications in international journals

- A. P. García, J. F. Monserrat, and L. Rubio, "Alternating projection method applied to indefinite correlation matrices for generation of synthetic MIMO channels," *AEÜ - International Journal of Electronics and Communications*, Elsevier Ltd., 2008. doi: 10.1016/j.aeue.2008.09.005. In press.
- A. P. García and L. Rubio, "Frequency dependent indoor MIMO channel characterisation between 2 and 12 GHz based on full spatial correlation matrices," *Journal of Communications*, Academy Publisher, Vol. 3, No. 4, pp. 8-15, 2008, ISSN : 1796-2021.

Publications in national journals

- A.P. Garcia, G. Llano, L. Rubio, and J. Reig, "Carrier frequency effect on the MIMO eigenvalues in an indoor environment," *Revista de la Facultad de Ingeniería "Sistemas y Telemática,"* Universidad ICESI, Vol. 6, No. 7, pp. 33-41, 2008. ISSN 1692-5238.
- A. P. García y L. Rubio, "Análisis de la capacidad de sistemas MIMO en escenarios de interiores," *Revista Gerencia Tecnológica Informática*, Vol. 5, No. 11, pp. 37-45, 2006. ISSN. 1657-8236.
- A. P. García y L. Rubio, "Medida, simulación y análisis de eficiencia espectral para canales MIMO en entornos indoor en la banda de 2 GHz," *Revista de la Facultad de Ingeniería "Sistemas y Telemática,"* Universidad ICESI, Vol. 2, No. 7, pp. 13-33, 2006, ISSN 1692-5238.

Publications in international conferences

- A. P. García and L. Rubio, "Frequency impact on the indoor MIMO channel capacity between 2 and 12 GHz," *IEEE 66th Vehicular Technology Conference - VTC*, Baltimore, USA, 30 September-3rd October, 2007. ISBN: 1-4244-0264-6.
- A. P. García, V. M. Rodrigo-Peñarrocha and L. Rubio, "Experimental analysis of the spectral efficiency between 2 and 12 GHz for indoor MIMO channels," *The 18th Annual IEEE International Symposium on*

Personal, Indoor and Mobile Radio Communications - PIMRC'07, Athens, Greece, 3-7 September, 2007. ISBN: 1-4244-1144-0.

- A. P. García, L. Rubio and N. Cardona, "Indoor MIMO channel analysis between 2 and 12 GHz," *North American Radio Science Meeting URSI - CNC/USNC*, Ottawa, Canada, July 22 - 26, 2007. ISBN: 978-0-9738425-2-4. Invited paper.
- A. P. García, L. Rubio and J. A. Díaz, "Experimental analysis of the frequency impact on the MIMO channel capacity between 2 and 12 GHz in an office environment," *IEEE Antennas and Propagation Society International Symposium 2007*, Honolulu, Hawaii, USA, June 10-15, 2007. ISBN: 1-4244-0878-4.
- A. P. García, L. Rubio, J. A. Díaz and N. Cardona, "Eigen/Capacity analysis for indoor correlated MIMO channels between 2 and 4 GHz," *IEEE 3rd International Symposium on Wireless Communication System*, Technical University of Valencia – UPV, Valencia, Spain, 5 - 8 September, 2006, ISBN 1-4244-0398-7.
- A. P. García y L. Rubio, "Análisis de capacidad de un sistema MIMO en entornos indoor," *Congreso Internacional del Area Andina – IEEE 2006, Quito-Ecuador*, 8-10 Noviembre 2006, ISBN-978-9978-45-920-1.
- L. Rubio, A. P. García, D. Argilés, and N. Cardona, "Modelling and simulation of correlated time-variant channels for diversity systems," *The International Symposium on Wireless Personal Multimedia Communications -WPMC'05*, Aalborg University, Denmark, September 17-22, 2005. ISBN: 87-90834-79-8, ISSN: 0908-1224.

Publications in national conferences

- A. P. García, L. Rubio, "Estudio experimental de la capacidad de un sistema MIMO en función de la frecuencia," *XXII Simpósium Nacional de la Unión Científica Internacional de Radio URSI*, Tenerife, España, 19 - 21 de Septiembre de 2007, ISBN-13: 978-84-690-7500-5.
- A. P. García, L. Rubio, J. A. Díaz, "Análisis de capacidad para canales MIMO y efectos de la polarización a 2 y 2.6 GHz," *XXI Simpósium Nacional de la Unión Científica Internacional de Radio URSI*, Oviedo, España, 12 - 15 de Septiembre de 2006, ISBN-13: 978-84-611-2488-6, ISBN-10: 84-611-2488-X.

Temporary Documents (TDs) in Euro COST2100 action

- A. P. Garcia, L. Rubio, and R. S. Thomä, "Multivariate normality of measured wideband MIMO channels", *COST 2100 (Commission of the European Communities and COST Telecommunications) "Pervasive Mobile & Ambient Wireless Communications", 7nd*

Management Committee Meeting, Braunschweig, Germany, 16-18 Feb., 2009, TD(09)768.

- A. P. García, L. Rubio and N. Cardona, "Frequency impact on the MIMO capacity between 2 and 12 GHz in an office environment," *COST 2100 (Commission of the European Communities and COST Telecommunications) "Pervasive Mobile & Ambient Wireless Communications," 2nd Management Committee Meeting*, Lisbon-Portugal, 26-28th Feb., 2007, TD-(07)016.

CHAPTER 1

PRELIMINARIES

1.1. Introduction and motivation

Space-time-frequency techniques are one of the most promising areas of innovation in wireless communications [1],[2]. In this way, multiple antenna systems, also known as multiple-input multiple-output (MIMO) systems, have proved highly efficient in the use of the spectrum [3],[4]. The main limitations in the application of these systems are the restrictions given by spatial correlations and rank deficiency of realistic MIMO channels [5],[6]. Therefore, MIMO channel characterisation is an important issue in order to assess a realistic MIMO system performance. In practice, to perform a MIMO channel characterisation it is often necessary to carry out a large number of measurements of the MIMO channel using slightly displaced arrays [7]-[10]. However, experimental studies based on measurements have usually investigated the MIMO channel characteristics focused on specific frequencies [7]-[15].

The new and constantly growing personal, local and metropolitan area wireless networks that consider MIMO technology will open a wide-band of frequency band options [16]-[21]. Therefore, one challenge is to study how the properties of the MIMO channel change with the frequency. Recently, the impact of frequency has been studied in [22] at 2.55 and 5.25 GHz for indoor scenarios. This work found differences in the directional spread of the multipath components at both ends of the link, but left several questions open and did not show capacity results. In this Dissertation, a MIMO channel experimental characterisation is presented at different frequency bands. Capacity results and other MIMO channel characteristics are compared at 2, 2.4, 6 and 12 GHz in Line-Of-Sight (LOS) and Non-LOS (NLOS) in two different indoor scenarios.

In a practical point of view, as it was referenced above, to perform a realistic MIMO channel characterisation it is often necessary to carry out a large number of measurements of the MIMO channel with slightly displaced arrays and considering temporally varying scatterers [23]. For example, to determine the cumulative distribution function (CDF) of the MIMO channel capacity from measurements, and thereby the outage capacity [1], thousands of MIMO channel samples are necessary. Since each single measurement requires an enormous effort, this

procedure is undesirable. Therefore, another challenge is to improve these experimental procedures taking advantage of linear algebra, statistics and signal processing techniques. This is another issue treated in this Dissertation.

On the other hand, many works have been dedicated to develop new techniques to generate cross-correlated synthetic channels based on Gaussian samples [24]-[30], which is a useful task in the analysis of diversity systems. These works have led the way for practical analysis of MIMO channel characteristics in different environments, propagation conditions and array geometry configurations. One of the first practical works applying these techniques to MIMO was proposed by Kermoal et al. [10].

Habitually, the methods of generation of synthetic MIMO channels are based on the estimation of the covariance or correlation matrix of the MIMO system, which characterise the space-time, or space-time-frequency variation of the propagation channel [23]. The estimation of these matrices can be performed from real measurements in the time or frequency domain [10],[31]. When the complex covariance or correlation matrix is estimated, it is possible to use the Cholesky factorisation [32] to find the coloring matrix of the system [25]. This coloring matrix can be used to generate thousands of synthetic realisations of the space-time MIMO channel transfer matrix [10]. Once it is generated an adequate number of sampled MIMO matrices, it is then possible to perform a reliable study of capacity, channel eigenvalues, and other MIMO channel characteristics, as it was suggested in [10],[31].

The main advantage of the procedure explained above is that it is possible to obtain a high number of samples of the MIMO channel transfer matrix from a limited set of measurements. These measurements are used beforehand to estimate the full spatial correlation (FSC) MIMO matrix required for the Cholesky factorisation. Consequently, the necessary time to carry out both the measurement campaign and the MIMO channel analysis is significantly decreased. The only restriction to use this procedure is that the FSC MIMO matrix must be positive definite to perform the Cholesky factorisation, being another issue to be solved here.

Under realistic propagation conditions, and for a large number of antenna elements at the transmitter and the receiver, the estimated FSC MIMO matrices may be indefinite as consequence of statistical inconsistency among the random variables involved in the estimation process [33],[34]. In such cases, the estimated FSC MIMO matrix may contain zero and negative eigenvalues. Indeed, it is demonstrated in this Dissertation that many FSC MIMO matrices estimated from real data are indefinite. Besides, it is proved that the probability of being indefinite increases for large-scale matrices, i.e., when the number of antenna elements increases. To overcome these limitations, a new iterative algorithm to find the closest positive definite FSC MIMO matrix is presented in this Dissertation.

On the other hand, apart from the topics treated above, ultra-wideband (UWB) techniques, used firstly by Hertz and Marconi in their experiments more than one century ago, started a renewed research interest parallel to MIMO

[35],[36]. Despite of their different system targets in a communication point of view, MIMO and UWB can be complementary for some system solutions, i.e., short-range communications (personal area networks-PANs and body area networks-BANs), radar and imaging [37].

Using MIMO and UWB radio technologies, it is possible to take advantage of both the spatial multipath propagation and the rich scattering with high multipath resolution using ultra-wideband signals. Hence, space-time coding and spatial multiplexing [1] can be exploited with UWB-MIMO, and useful channel characteristics can be used to achieve high data rates and to reduce the multipath fading in the time domain [37]. These advantages can improve the overall capacity and the robustness of communication systems, especially in limited radiated power conditions.

Investigations in this area are recently developed. The application of space-time (ST) coding to UWB [38], and performance analysis of diversity and spatial multiplexing have been carried out [39],[40]. In this way, the study of effects related to the ST channel characteristics, as spatial correlation [8], rank deficiency [6] and time variation [23] are also key issues. For example, it will be especially interesting for UWB to considerate the amount of detected energy at the receiver, which can modify the experimental spatial correlation in indoor environments when multiple antennas are used [37]. This topic is also addressed in this Dissertation including two types of plane waves for channel modelling.

On the other hand, for cognitive radio systems (CRS) [41], the frequency-dependent channel analysis is also a pertinent issue. This is required for testing the expected spectral efficiencies for different cognitive models under frequency reuse scenarios [42] and channel interference [43]. Correlated channel variations could be one of the main challenges in the system design for CRS due to the many band options considered in the cognition process of software radios [41]. Correlated models should be included in this process, since during the system adjustment part of the RF front-end remains constant, e.g., the antennas. These characteristics, including MIMO [42],[44], must be considered for future system performance analysis.

Therefore, for UWB, MIMO and CRS integration, one of the challenges is the realistic channel modelling and characterisation, taking into account possible random space-time-frequency variations of the channel. The waves-arrays-environment interaction, in a frequency-dependent condition and under high multipath resolution, introduces new effects in the complex random channel that should be considered in order to assess a realistic system performance.

Recently, many UWB channel models have been introduced, for instance the IEEE 802.15.3a/4a channel models [45]. These models have been designed for short-range and long-range systems, including typical impulse-response model parameters (path gains, delays, clusters and phases) and classifying different propagation conditions (in LOS and NLOS). Some models have also included the frequency-dependent affects related to propagation mechanisms [45], path gains and antenna patterns [20].

One of the first space-temporal UWB characterisation was presented by Crammer in [46], where the angle-of-arrival (AOA) and the angular spread were included as experimental channel parameters for analysis. Recently, a space-time variant UWB channel model was presented in [21]. This statistical impulse-response model includes AOA (in a two-dimensional – 2D approximation) and temporal variations of the different echoes. In this model, the AOA variations of each ray within a cluster are assumed Laplace distributed, and the rest of parameters are close formulated, allowing a simple implementation for simulations using parameters estimated from measurements.

The physical basis in the formulation of the space-temporal UWB models are the assumption of plane wave propagation with surrounding objects situated far away from the antennas. These assumptions are possible following the modelling strategy of plane wave summations according to the Maxwell's equations [47]. Despite of the described models follow these assumptions, they do not take into account the possible existence of inhomogeneous plane waves in the propagation [48], which could contribute to the whole received energy. The inclusion of these plane waves in a channel model is another challenge and it can improve our physical interpretation of the space-time-frequency-dependency on the MIMO channel.

On the other hand, most of the channel models are based in an impulse-response representation. Another usual way in wideband MIMO channel representation (for modelling and experimental characterisation) is the frequency domain, where is used a set of flat MIMO channels centred at a single frequency component [31]. A matrix representation is also optional to build UWB-MIMO channels [37]. Therefore, frequency-dependent (FD) formulations for channel models offer many advantages, besides allowing us to extend the extensively literature of MIMO channels to UWB-MIMO channels.

A novel FD-MIMO channel model is presented in this Dissertation. This model is derived from a spatial deterministic-Gaussian-uncorrelated-scattering (DGUS) model [49], being extended to MIMO and including inhomogeneous plane waves in the formulation. The proposed model uses simple summations of complex exponential functions and considers typical channel parameters, i.e., angle-of-departure –AOD, AOA, path gains, Doppler frequencies and delays. The aim of the formulation of this model was to consider most of the possible physical propagation effects related to the interaction between waves, arrays and environment, according to both the central frequency and the bandwidth of the signal. Besides, this model was formulated seeking a MIMO application of perfect modelling techniques [50],[51], to be used in conjunction with measurements based on channel sounders [23] or vector network analyzers (VNAs) [31],[52]. Here, it is demonstrated that the proposed FD-DGUS-MIMO channel model can be used for realistic system performance analysis. Besides, the model could be considered for the characterisation of indoor UWB-MIMO channels using measurement campaigns.

As it has been verified in the literature, MIMO is the chosen technology to be used with different wideband techniques for wireless personal area networks

(WPANs), e.g., IEEE 802.15.3c [53], and wireless local area networks (WLANs), e.g., IEEE 802.11 [18], HiperLAN/2 [54] and multimedia mobile access communication systems[10] (MMAC) [54]. Additionally, MIMO is a complementary technology to achieve high data rates in wireless metropolitan area networks (WMANs) developed in frequency bands upper 2 GHz, e.g., IEEE 802.16 [19], and for the future 4G technology, together with Orthogonal Frequency Division Multiple Access (OFDMA) [17],[55]. All of these different technologies open a wide spectrum and range of coverages for MIMO, including wideband systems in the licensed and un-licensed spectrum (i.e., 2.5, 3.5 and 5.2/5.8 GHz). Hence, a compressive and detailed modelling and experimental characterisation of MIMO channels for realistic environments at different frequency bands will have a huge contribution to develop these new technologies.

1.2. Relevance

It has been presented the main motivation to perform this PhD Dissertation, which wraps research activities around measurements, post-processing, multivariate statistics, and modelling techniques, focusing in the characterisation of frequency-dependent MIMO channels.

It is worth to indicate that in literature it has not been found well defined experimental research works focussing on the effects of the central frequency and the frequency bandwidth over MIMO channel characteristics. There are many works carried out at one or two different central frequencies [7]-[15],[22],[23], and with similar array configurations for indoor and outdoor environments. Although there are many works published about MIMO channel measurements, not so much attention has been addressed in MIMO channel parameter analysis for different central frequencies and bandwidths under different propagation conditions in an indoor environment.

An earlier work about single-input single-output (SISO) channels found different channel characteristics between 430 and 5750 MHz in an urban environment [56]. This work showed that the experimental delay spread[11] decreases while the central frequency increases, with results at 50% and 10% outage probabilities.

Recently, as it was introduced in Section 1.1, the impact of the frequency was addressed in [22], where measurements at 2.55 and 5.25 GHz were carried out in an indoor environment. This work found differences in the angular spread at both sides of the link, but no results about spatial correlation, eigenvalues and MIMO capacity were treated. In the same way, the impact of the central frequency is also addressed in [57]-[59], where indoor and outdoor measurements were

[10] Wireless system for transmissions up to 1Gbps in SHF band (3-60GHz), millimetre band (30-300GHz) and other frequency bands. This system can be used for mobile calls, video-calls and high definition television.
[11] The form how is calculated the power delay profile (PDP) could change the expected delay spread, and this calculation has dependence on the dynamic range of the measurement setup and on the used reference levels.

performed for two different central frequencies using similar array configurations. In those works the same electrical separation between antenna elements was never used and the experimental results are discrepant among them.

In [57], when the central frequency was higher the capacity drops for LOS and NLOS. In the same way, for a study carried out in a microcellular scenario [58], the capacity was higher for higher frequencies, which agrees with an increment in the multipath richness for higher central frequencies. However, in the same work, it was anticipated that if the path-loss effect is allowed in the MIMO data, lower central frequencies will then achieve higher MIMO capacities due to the higher signal to noise ratio (SNR) at the receiver side.

On the other hand, the effect of the central frequency in the spatial correlation coefficients at 2.4 and 5.2 GHz in an indoor environment was addressed in [59]. The results showed a similar behaviour at both central frequencies, which contradicts further works [57].

All works presented above have been carried out at different central frequencies and scenarios. Hence, a reliable answer can not be given about the frequency dependency of the MIMO channel parameters based on their results. Besides, these experimental results can not be extrapolated and used for other propagation scenarios; this is only possible with few results from indoor environments. The metrics presented in such works could be considered, but it is therefore necessary an own well defined and reliable experimental research work to get the desire comparative results in a specific environment. This PhD Dissertation deals with this problem and presents a well defined and reliable experimental analysis for indoor scenarios in both LOS and NLOS conditions for comparisons between 2 and 12 GHz.

On the other hand, in MIMO channel literature there are not works related to the solution of the non-positiveness of experimental complex covariance matrices. The non-positiveness has an intrinsic relationship with the central frequency due to such problem increases for higher correlation values [34], and as it is demonstrated in this work, a correlation increment happens (in some cases) when the central frequency increases. In those cases, where usually large arrays are also presented, this problem could limit the MIMO channel stochastic simulation based on covariance matrices [10]. Hence, based on the results presented in the Dissertation, this problem is overcome thanks to a new alternating projection (AP) method to approximate non-positive definite complex covariance matrices to positive definite matrices.

Perhaps one of the most relevant issues addressed in this work is the multivariate statistics of wideband MIMO data for large-scale arrays. This issue is treated from both theoretical and experimental point of views and useful results about the non-multivariate normality of MIMO data are presented. This topic deal the way for new researches about non-stationary multidimensional wireless channels.

In addition, in literature there are not FD MIMO channel models including inhomogeneous plane waves, which could be useful in those cases where high

central frequencies, different bandwidths and small confined areas affect the expected local area size [47], and then the detected energy [37]. This consideration in the MIMO channel modelling offers many advantages for comparisons. Besides, the new proposed FD-DGUS-MIMO model offers to the scientific community a powerful tool for experimental channel modelling based on measurements [50],[51], due to the proposed model follows the desired DGUS characteristics [49].

Finally, it is worth to indicate that in a multi-antenna element system point of view, this PhD Dissertation is relevant for radio researchers at different system layers, due to many results presented here concern different technologies, at different frequency bands, and for systems applying space-time block-coding (STBC), spatial multiplexing (SM), beamforming or diversity techniques [1]. In practice, it will be useful for STBC techniques [60]-[63] the performed evaluation about the impact of the central frequency over the complex spatial correlation at both ends of the link. Besides, for SM systems [65]-[67], it will be useful the performed evaluation about the impact of the central frequency over the spatial correlation, the MIMO system eigenvalues, multipath richness, and the well known MIMO capacity [4], some times called spectral efficiency, and given in bits/s/Hz. On the other hand, for beamforming techniques [68],[69], complex spatial correlations and eigenvalue decomposition of covariance matrices can be useful metrics for its performance evaluation at different central frequencies. On the other hand, for diversity techniques [70] and for MIMO system evaluation, the diversity measure [71] and the spatial correlation [8] are also practical metrics. All of these metrics obtained from measurements, and reflected in both a stochastic and a DGUS model, are used along of this PhD Dissertation giving many comparative results at different central frequencies. As it will be demonstrated, these results have a wide application in the MIMO channel characterisation.

1.3. Objectives of the Dissertation

The objectives of this PhD Dissertation are list below. First, it is presented its main objective, and then the secondary specific objectives are included, which limits the frame work and focus of the research activities included in this Dissertation.

1.3.1. Main objective

Evaluate the central frequency effects on the MIMO channel characteristics in indoor environments from an experimental and theoretical view points.

1.3.2. Secondary objectives

- Identify the MIMO channel parameters which define the channel behaviour in a stochastic point of view, and those parameters being

useful for a MIMO channel experimental characterisation based on measurements and simulations.

- Establish computational conditions for simulation, analysis, and validation of a stochastic MIMO channel model useful for research activities about frequency dependent channels.
- Design and perform measurement campaigns between 2 and 12 GHz to do a reliable evaluation of the MIMO channel characteristics that change with the central frequency, taking into account the bandwidth, antenna characteristics, separation between antenna elements, array dimensions, number of snapshots and stationary of the channel.
- Propose and analyze a new theoretical MIMO channel model useful to study and evaluate the experimental MIMO system performance at different central frequencies and bandwidths, designing as well the MIMO channel simulation model.
- Validate the stochastic and the proposed MIMO models, based on simulations and measurement data.
- Analyze the experimental parameters obtained from measurements, identifying and qualifying their dependence with the central frequency, and taking into account the applicability of this analysis for STBC, SM and beamforming techniques in LOS and NLOS condition for indoor environments.
- Compare the experimental results with published works in open literature.

1.4. Problems addressed in the Dissertation

For the research about frequency dependent MIMO channels, this PhD Dissertation has addressed some specific problems around a main question: Are the MIMO channel parameters dependent on the central frequency and bandwidth for different array dimensions, and even for the same electrical separation? The problems addressed around this question are briefly summarized in 4 main areas of MIMO channel characterisation and modelling which are described in the following sections.

1.4.1. MIMO measurements

The solution to this problem consider a fairly MIMO channel measurement in the frequency domain at different central frequencies between 2 and 12 GHz. The starting point was the available measurement setup: a vector network analyzer (VNA) and broadband devices (antennas, cables, amplifiers, etc.). Besides, the environment and the MIMO parameters to measure/estimate have been taken into account to define the experimental procedure.

Two indoor scenarios are considered, where the spatial correlation, eigenvalues, MIMO capacity, and multipath richness are estimated using measurements. Moreover, it has been taken into account the stationarity of the channel, a high SNR regimen in the system (above 15 dB), equal electric separation at each central frequency (one wavelength), path-loss effect isolation and the calibration of the equipment. The number of samples and resolution (in each MIMO channel domain) were other issues to judge in the design process of the measurement setup, due to the multidimensional characteristic of data and the time consumption needed for acquisitions.

1.4.2. MIMO data post-processing

The solution of this problem covers the normalisation of MIMO data and the achieving of normalized non-frequency selective channel transfer matrices. For this process, segmentation and matrix normalization using a measured bandwidth of 200 MHz (span in the VNA) at each central frequency (i.e., 2, 2.4, 6 and 12 GHz) have been considered.

The channel transfer matrix is achieved based on the available number of segments and samples in the frequency domain, the number of time snapshots (under static conditions), the coherent bandwidth of the channel, and the distance to the scattering objects. The normalized non-frequency selective channel transfer matrices for each central frequency were obtained and stored for the subsequent MIMO channel parameters estimation. The post-processing described above was carried out looking for the isolation of the path-loss effect under a high SNR regimen, obtaining then the useful MIMO information to do reliable comparisons at different central frequencies.

1.4.3. MIMO channel synthetic generation

This problem addresses the efficient and reliable generation of enough synthetic MIMO channel matrices. These matrices are necessary to perform the desired comparisons based on estimations of the selected MIMO parameters, which are useful to judge the performance of STBC, SM, and/or beamforming techniques under realistic conditions at different central frequencies.

To solve this problem, it has been considered the estimation of the complex covariance matrix (CCM) of the MIMO system, i.e., the estimation of the FSC MIMO matrix using the Pearson's product moment correlation, based on a set of normalized non-frequency selective channel transfer matrices obtained from measurements. These CCMs are then considered to obtain the coloring matrix of the MIMO system by means of the Cholesky factorization where it was possible, due to the non-positiveness of some matrices.

The problem where the FSC matrices were non-positive definite was solved. A reliable approximation of such matrix, i.e., the nearest positive definite matrix, was obtained by means of iterative projections in different predefined sub-spaces of matrices (AP method). The problem of non-positiveness was also addressed from a statistical point of view, considering where the multivariate normal

distribution (MND) and the matrix variate complex normal distribution (MVCND) were not satisfied from the MIMO data. As a consequence of non normality, it is mentioned that the matrix variate complex Wishart distribution (MVCWD) of CCMs is not fulfilling. Besides, the non-linearity of MIMO data is also addressed, considered as a potential problem for the correct estimation of correlation coefficients.

When all problems related to the non-positiveness were studied and solved by means of the AP method, obtaining then the positive definite FSC matrices and their decompositions by Cholesky, the synthetic MIMO channel generation has been addressed. Thousands of MIMO matrices were generated based on both zero-mean complex independent identically distributed (i.i.d) random variables and the coloring matrix of the system. These MIMO matrix samples were used to obtain the particular MIMO parameters necessary to do the reliable comparisons at different central frequencies. Complex spatial correlation coefficients (CSCC), MIMO system eigenvalues, MIMO capacity (ergodic and outage capacities), and multipath richness were estimated and used for comparisons of the MIMO channel performance in two different indoor scenarios in LOS and NLOS conditions.

1.4.4. MIMO channel modelling

One of the main problems addressed in this PhD Dissertation, subsequent to the experimental analysis, was the MIMO channel modelling for frequency dependent analysis. The problem has been addressed considering a FD-DGUS reference model.

The closed formulated model includes typical parameters: path and Doppler coefficient gains, delays, Doppler frequencies, angles of departure (AODs) and angles of arrival (AOAs). All of these parameters are obtained for a 2 dimensional (2D) spatial model approximation, with multiple antennas at both ends of the link, non-static receiver, and with homogeneous and inhomogeneous plane waves reaching the receiver array.

In this model it is addressed the frequency dependency in the channel, i.e., different central frequencies and bandwidths. The model includes specific parameters related to the relative bandwidth (normalized to the central frequency) and high resolution scattering components.

The DG and US characteristics, forced in this MIMO model, offered useful statistical properties for closed formulation of its correlations (in space, time and frequency) and power spectral density (PSD) functions. This new model and its characteristic functions were also addressed looking for an experimental application of the model based on correlations functions and PSDs estimated from measurements. This integration of measurements and modelling has been called in literature “perfect channel modelling” and it is the purpose of the DGUS models.

1.5. Research contributions

This PhD Dissertation contributes to different areas related to the MIMO channel characterisation. The main contributions of this research are list below:

- **Measurement setup:** A measurement setup based on a VNA, UWB antennas, a robotic positioning system, wideband devices and a remote control software system was designed, implemented and tested for reliable time or frequency dependent channel measurements at different central frequencies and bandwidths under static channel conditions and the same electrical array element separation.
- **Experimental procedure:** A well defined and reliable experimental procedure including measurements, post-processing, simulation and analysis of MIMO channels (until 13x13 array elements) at different central frequencies is presented and validated. This procedure allows the study of different MIMO channel parameters useful for performance analysis of STBC, SM and beamforming techniques. Besides, this experimental procedure allows a MIMO performance evaluation using different ULA dimensions in an indoor environment in LOS and NLOS conditions.
- **Synthetic channel generation:** A reliable procedure based on a stochastic MIMO channel model and the Cholesky factorization is analysed and validated for MIMO channel synthetic generation. This procedure allows researchers to do analysis of frequency dependent channels considering the isolation of the path-loss effect. The FSC MIMO matrices used in the procedure are analysed. For this synthetic channel generation a new AP method is also proposed to correct the FSC matrices when it is necessary.
- **Alternating projection (AP) method for CCM:** A new method to find the closest positive definite complex matrix to a non-positive definite complex matrix is presented. This method enables to use large-scale arrays for MIMO channel synthetic generation in such cases where the non-positiveness of the FSC matrix prevented the Cholesky factorization. The reasons of non-positiveness are analysed from a statistical point of view. Besides, the AP method is proved and tested for different array dimensions and the non-positiveness of MIMO data is compared for each case. The distribution of being a non-positive definite matrix is calculated at each central frequency and array dimensions, and the success rate of the AP method is also presented from a statistical point of view.
- **MIMO channel parameter evaluation:** A completed statistical analysis of the most important MIMO channel parameters is presented for 4 different central frequencies between 2 and 12 GHz and for LOS and NLOS conditions in two indoor scenarios. CSCC, MIMO system eigenvalues, MIMO capacities, and multipath richness are analysed

and compared based on statistical results (CDF, PDF, mean and median values) at each central frequency.

- **Multivariate and linearity analysis of MIMO data**: Different multivariate and linearity analysis of realistic MIMO data has been performed. The proposed procedure can be applied for verification of multivariate-normality of data (as this characteristic is not always fulfilled), for stationarity statistical analysis in different domains, and for reliability analysis of covariance estimators. Many facts/assumptions considered in MIMO experimental analysis are verified as wrong approximations and useful techniques for reliable analysis are proposed.
- **FD-DGUS-MIMO Model:** A new MIMO channel model for simulation and experimental MIMO channel characterisation under high central frequencies and wideband signals is formulated and analysed. This is the sole FD-DGUS model in literature including both HPWs and IPWs in the formulations. The FD-DGUS-MIMO model is completely defined by steps, explaining its statistical and deterministic parameters, and also its statistical functions. The space-time-frequency correlation and PSD functions are obtained in a closed form and simulations results are presented. The useful statistical characteristics of the FD-DGUS model are explained and its experimental applicability for wideband MIMO channels is introduced.

1.6. Document structure

This PhD Dissertation has been organised in 6 Chapters and one Appendix about multivariate statistics for MIMO (Appendix A). Chapter 2 exposes the performed MIMO channel measurements, Chapter 3 addresses the synthetic MIMO channel generation, Chapter 4 presents the MIMO experimental analysis, Chapter 5 presents the new MIMO channel model for frequency dependent analysis and Chapter 6 addresses the conclusions of this PhD Dissertation and future work. A briefly description of each chapter is given in the list below:

- **Chapter 2:** This chapter describes the environment (two indoor scenarios), the measurement setup, the link budget and dynamic range considerations, and the minimum conditions for measurements. Besides, it is described the measurement procedure and post-processing applied to MIMO data, addressing the sample sequence segmentation, matrix normalisation and FSC MIMO matrix estimation.
- **Chapter 3:** In this chapter, the techniques used for synthetic MIMO channel generation, based on FSC MIMO matrices, and the

formulation used for experimental MIMO channel analysis are shown. The validation of the procedure is presented, a brief description of the FSC MIMO matrices, the Cholesky factorisation and its limitations for synthetic channel generation are also included. The AP method for adjusting indefinite Hermitian correlation matrices is introduced. A case study, based on real measured MIMO data, is used to assess the performance of the AP method, showing the main effects of the AP parameters on the eigenvalues distribution and on the ergodic and outage capacities of the MIMO system. The problem of non-MCND and linearity in the MIMO data is also treated, and some analysis and discussions are presented together with a possible technique for FSC matrix estimation under low data samples, non-linearity and non-MCND conditions.

- **Chapter 4:** This chapter addresses the results analysis, where MIMO channel characteristics are compared for different central frequencies. An experimental statistical analysis of MIMO capacity, system eigenvalues, spatial correlation, and multipath richness are shown. The validation of the experimental procedure is also included, checking the isolation of the path-loss effect, the synthetic channel generator (simulator validation) and the distribution of MIMO parameters compared with measurements.
- **Chapter 5:** This chapter describes de proposed FD-DGUS-MIMO model, given details of its derivation, and presenting closed formulations for its parameters and functions. The principal FD-DGUS-MIMO model characteristics, its correlations functions, and PSD function are formulated and analysed. The simulation model and simulation results with fixed parameters are presented and compared. In this chapter is also introduced the new concept of perfect MIMO channel modelling and the estimation process of channel parameters applied to realistic MIMO channel simulations.
- **Chapter 6:** This chapter concludes with the PhD Dissertation given useful conclusions for the applicability of STBC, SM and beamforming techniques under correlated conditions at different central frequencies, bandwidths and array configurations. The main conclusions about the experimental characterisation and modelling are also addressed in this chapter. Besides, the future research related to the problems indicated in Section 1.4 is presented in this chapter.

Note: Each chapter in this Dissertation includes its own reference list with independent numeration.

References

[1] A. Paulraj, R. Nabar and D. Gore, *Introduction to space-time wireless communications*, Cambridge University Press, 2003.

[2] V. Kühn, *Wireless communications over MIMO channels: applications to CDMA and multiple antenna systems*, John Wiley & Sons Ltd, 2006.

[3] G. J. Foschini, and M.J. Gans, "On limits of wireless communications in a fading environment when using multiple antennas," *Wireless Personal Commun*., Vol. 6, No.3, pp.311-315, 1998.

[4] E. Telatar, "Capacity of multi-antenna gaussian channels". *Euro. Trans. Telecommun*, Vol. 10, pp. 585–595, 1999.

[5] D. Chizhik, F. Rashid-Farrokhi, J. Ling and A. Lozano, "Effect of antenna separation on the capacity of BLAST in correlated channels," *IEEE Commun. Letters*, Vol. 4, No. 11, pp.337-339, 2000.

[6] H. Shin, and J. H. Lee, "Capacity of multiple-antenna fading channels: spatial fading correlation, double scattering, and keyhole," *IEEE Trans. on Information Theory*, Vol. 49, No. 10, pp. 2636-2647, 2003.

[7] D. Chizhik, et al, "Multiple-input-multiple-output measurements and modeling in Manhattan," *IEEE J. on Selected Areas in Commun.*, Vol. 21, No. 3, pp. 321-331. 2003.

[8] P. Kyritsi, D. C. Cox, R. A. Valenzuela, and P. W. Wolniansky, "Correlation analysis based on MIMO channel measurements in an indoor environment," *IEEE J. on Selected Areas in Commun*., Vol. 21, No. 5, pp. 713-720, 2003.

[9] A. F. Molisch, M. Steinbauer, M. Toeltsch, E. Bonek, and R. S. Thomä, "Capacity of MIMO systems based on measured wireless channels," *IEEE J. on Selected Areas in Commun.*, Vol. 20, No. 3, pp. 561-569, 2002.

[10] J. P. Kermoal, L. Schumacher, K. I. Pedersen, P. E. Mogensen, and F. Frederiksen, "A stochastic MIMO radio channel model with experimental validation," *IEEE J. on Selected Areas in Commun.*, Vol. 20, No. 6, pp. 1211-1226, 2002.

[11] D. S. Baum, et al., "Measurements and characterization of broadband MIMO fixed wireless channels at 2.5 GHz," Proceedings of ICPWC'00, Hyderabad, 2000.

[12] J. W. Wallace and M. A. Jensen, "Characteristics of measured 4×4 and 10×10 MIMO wireless channel data at 2.4-GHz," IEEE Antennas and Propagation Society International Symposium, Boston, July 2001.

[13] J. W. Wallace and M. A. Jensen, "Measured characteristics of the MIMO wireless channel," IEEE 54th Vehicular Technology Conference - VTC Fall 2001, Atlantic City, October 2001.

[14] J. P. Kermoal, et. al., "Experimental investigation of correlation properties of MIMO radio channels for indoor picocell scenarios," IEEE 52nd Vehicular Technology Conference - VTC Fall 2000, Boston, September 2000.

[15] J. P. Kermoal, et. al., "Smart antennas cluster year 2000 report," *IST-1999-11729 METRA Project*, In: http://www.ist-imetra.org/metra/papers/

[16] "Multiple-Input Multiple-Output in UTRA," 3GPP TR25.876 V1.8.0., Oct. 2005.

[17] "Spatial channel model for multiple input multiple output (MIMO) simulations," 3GPP TR 25.996 V7.0.0:, June 2007.

[18] "Part 11: Wireless LAN medium access control (MAC) and physical layer (PHY) specifications," IEEE P802.11n, D3.00, Sept. 2007.

[19] "Part 16: Air interface for fixed broadband wireless access systems," IEEE Std 802.16 2004, Oct. 2004.

[20] A. F. Molisch, et all, "A comprehensive standardized model for ultrawideband propagation channels," *IEEE Trans. on Antennas and Propagation,"* Vol. 54, No. 11, pp. 3151-3166, 2006.

[21] P. Pagani, and P. Pajusco, "Modeling the space-and time-variant ultra-wideband propagation channel," IEEE International Conference on Ultra-Wideband, September 2006.

[22] E. Bonek, et al, "Indoor MIMO measurements at 2.55 and 5.25 GHz - a comparison of temporal and angular characteristics." Procc. of the IST Mobile Summit, Myconos, June 2006.

[23] J. W. Wallace. and M.A. Jensen, "Time-varying MIMO channels: measurement, analysis, and modelling," *IEEE Trans. on Antennas and Propagation*, Vol. 54, pp. 3265-3273, 2006.

[24] R. B. Ertel and J.H. Reed, "Generation of two equal power correlated Rayleigh fading envelopes," *IEEE Commun. Letters*, Vol. 2, No. 10, pp. 276-278, 1998.

[25] N. C. Beaulieu, "Generation of correlated Rayleigh fading envelopes," *IEEE Commun. Letters*, Vol. 3, No. 6, pp. 172-174, 1999.

[26] B. Natarajan, C.R. Nassar and V. Chandrasekhar, "Generation of correlated Rayleigh fading envelopes for spread spectrum applications," *IEEE Commun. Letters*, Vol. 4, No. 1, pp. 9-11, 2000.

[27] N. C. Beaulieu and M.L. Merani, "Efficient simulation of correlated diversity channels," IEEE Wireless Commun. and Networking Conference (WCNC), p. 207-10, 2000.

[28] Q. T. Zhang, "A decomposition technique for efficient generation of correlated Nakagami fading channels," *IEEE J. Select. Areas Commun.*, Vol. 18, No. 11, pp. 2385-2392, 2000.

[29] K. Zhang, Z. Song and Y.L. Guan, "Simulation of Nakagami fading channels with arbitrary cross-correlation and fading parameters," *IEEE Trans. on Wireless Commun.*, Vol. 3, No. 5, pp. 1463-1468, 2004.

[30] K. E. Baddour, and N.C. Beaulieu, "Accurate simulation of multiple cross-correlated Rician fading channels," *IEEE Trans. on Commun.*, Vol. 52, No. 11 pp. 1980-1987, 2004.

[31] A. P. García and L. Rubio "Frequency impact on the indoor MIMO channel capacity between 2 and 12 GHz". *IEEE 66th Vehicular Technology Conference – VTC Fall 2007*, Baltimore, October 2007.

[32] C. D. Mayer, *Matrix analysis and applied linear algebra,* Society for Industrial and Applied Mathematics, 2000.

[33] Y.I Abramovich, N.K. Spencer A.Y. and Gorokhov, "Detection-estimation of more uncorrelated Gaussian sources than sensors in nonuniform linear antenna arrays - Part I: Fully augmentable arrays," *IEEE Trans. on Signal Processing*, Vol. 49, No. 5, pp. 959-971, 2001.

[34] S. Sorooshyari and D.G Daut, "On the generation of correlated Rayleigh fading envelopes for accurate simulation of diversity channels," *IEEE Trans. on Commun.*, Vol. 54, No. 8, pp. 1381-1386, 2006.

[35] M.Z. Win and R.A. Scholtz, "Impulse radio: how it works," *IEEE Comm. Letters*, Vol. 2, No. 2, pp. 36-38, 1998.

[36] M.Z. Win and R.A. Scholtz, "Characterization of ultra-wide bandwidth wireless channels: a communication-theoric view," *IEEE Journal on Selected Areas in Communications*, Vol. 20, No. 9, pp. 1613-1627, 2002.

[37] B. Allen, et all, *Ultra-wideband antennas and propagation for communications, radar and imaging*, Jhon Wiley and Sons Inc., West Sussex, UK, 2007.

[38] Liuqing Yang and G.B. Giannakis, "Analog space-time coding for multiantenna ultra-wideband transmissions," *IEEE Transactions on Communications*, Vol. 52, No. 3, pp. 507-517, 2004.

[39] Li-Chun Wang, Wei-Cheng Liu, and Kuan-Jiin Shieh, "On the performance of using multiple transmit and receive antennas in pulse-based ultrawideband systems," *IEEE Transactions on Wireless Communications*, Vol. 4, No. 6, pp. 2738-2750, 2005.

[40] C. Abou-Rjeily, N. Daniele, and J.C.Belfiore, "Diversity-multiplexing tradeoff of single-antenna and multi-antenna indoor ultra-wideband channels," *IEEE International Conference on Ultra-Wideband*, pp. 441-446, Sept. 2006.

[41] J. Mitola, and G. Q- Maguire, "Cognitive radio: making software radios more personal," *IEEE Personal Communications*, Vol. 6, No.4, pp. 13-18, 1999.

[42] O. O. Koyluoglu, H. El Gamal, "On the utility of frequency reuse in cognitive radio channels," IEEE International Symposium on Information Theory - ISIT 2007, pp. 2161-2165, 24-29 June 2007.

[43] N. Devroye, P. Mitran, V. Tarokh, "Achievable rates in cognitive radio channels," *IEEE Transactions on Information Theory*, Vol. 52, No. 5, pp. 1813-1827, 2006.

[44] R. Soundararajan, S. Vishwanath, "Adaptive sum power iterative waterfilling for MIMO cognitive radio channels," IEEE International Conference on Communications - ICC 2008, pp. 1060-1064, 19-23 May 2008.

[45] Molisch, A.F., "Ultrawideband propagation channels-theory, measurement, and modeling," *IEEE Transactions on Vehicular Technology*, Vol. 54, No. 5, pp. 1528-1545, 2005.

[46] J. M. Cramer, R.A. Scholtz, M.Z. Win, "Spatio-temporal diversity in ultra-wideband radio," Proceedings of IEEE Wireless Communication and Networking Conference, Vol. 2, pp. 888-892, 1999.

[47] G. D. Durgin, *Space-Time Wireless Channels*, Pearson Education, Inc., NJ, US, 2003.

[48] M. Born and E. Wolf, *Principles of Optics: Electromagnetic Theory of Propagation, Interference, and Diffraction of Light*, Pergamon Press, New York, 6th edition, 1980. p. 560-564.

[49] M. Pätzold and N. Youssef, "Modelling and simulation of direction-selective and frequency-selective mobile radio channels," *AEÜ-Int. J. Electr. and Commun.*, Vol. 55, No. 6, pp. 433-442, 2001.

[50] M. Pätzold, "Perfect channel modeling and simulation of measured wide-band mobile radio channels," 3G Mobile Communication Technologies, Conference Publication No. 471, IEE, 2000.

[51] M. Pätzold and Q. Yao, "Perfect modelling and simulation of measured spatio-temporal wireless channels," Proc. 5th Int. Symp. on Wireless Personal Multimedia Communications, WPMC '02, Honolulu, Hawaii, 27. - 30. Oct. 2002, pp. 563-567.

[52] J. Molina-García-Pardo, "A MIMO Measurement System Based on Two Network Analyzers," COST 273 TD(04)106, Gothenburg, Sweden, 2004.

[53] R. Fisher, "60 GHz WPAN Standardization within IEEE 802.15.3c," International Symposium on Signals, Systems and Electronics, 2007. ISSSE '07, pp. 103-105, July 30-Aug. 2, 2007.

[54] M. I. Rahman, S. S. Das and F. H.P. Fitzek, "OFDM based WLAN systems," Center for TeleInFrastruktur (CTiF), Aalborg University, Technical Report R-04-1002, v1.2, 18 February 2005.

[55] E. Baccarelli, M. Biagi, C. Pelizzoni, and P. Bellotti, "A novel multi-antenna impulse radio UWB transceiver for broadband high-throughput 4G WLANs," *IEEE Comm.Letters*, Vol. 8, No. 7, pp. 419-421, 2004.

[56] P. Papazian and M. Cotton, "Relative propagation impairments between 430 MHz and 5750 MHz for mobile communication systems in urban environments," *U.S. Department of Commerce, National Telecommunications and Information Administration Report TR-04-407*, December 2003.

[57] B.T. Maharaj, J.W. Wallace, M.A. Jensen, L.P. Linde, "Co-located indoor 2.4- and 5.2-GHz MIMO channel measurement, frequency scaling of capacity and correlation," Proc. of ICT 2005, Cape Town, South Africa, May 2005.

[58] L. Vuokko, P. Suvikunnas, J. Salo, J. Kivinen and P. Vainikainen, (2005, October). Comparison of measured MIMO capacities at 2 and 5 GHz, XXVIIIth URSI General Assembly, New Delhi, India [Online]. Available: http://www.ursi.org/proceedings/ProcGA05/pdf/CBA.8(0741).pdf

[59] B. T. Maharaj, Jon W. Wallace, L. P. Linde, and Michael A. Jensen, "Frequency scaling of spatial correlation from co-located 2.4 GHz and 5.2 GHz wideband indoor MIMO channel measurements," *Electronics Letters, IEE*, vol. 41 No. 6, 2005.

[60] S. M. Alamouti, "A simple transmit diversity technique for wireless communications," *IEEE J. on Selected Areas in Com.*, Vol. 16, No.8, p 1451-1458, 1998.

[61] G. G. Raleigh and J. M. Cioffi, "Spatio-temporal coding for wireless communication," *IEEE Transactions on Communications*, vol. 46, pp. 357–366, 1998.

[62] V. Tarokh, A. Naguib, N. Seshadri, and A. R. Calderbank, "Combined array processing and Space–Time coding," *IEEE Trans. On Information Theory*, Vol. 45, No. 4, pp. 1121-1128, May 1999.

[63] V. Tarokh, H. Jafarkhani, A.R. Calderbank, "Space-time block coding for wireless communications: performance results," *IEEE Journal on Selected Areas in Communications*, Vol. 17, No. 3, pp. 451-460, March 1999.

[64] M. Godbout, and H. Leib, "Space-time modulation and coding over transmit correlated fading channels," *IEEE Transactions on Wireless Communications*, Vol. 3, No. 5, 2004.

[65] G. J. Foschini, "Layered space-time architecture for wireless communication," *Bell Labs Tech. Journal*., Vol. 1, pp. 41–59, 1996.

[66] G.D. Golden, et al. "Detection algorithm and initial laboratory results using the V-BLAST space-time communication architecture," *Elec. Letters*, Vol. 35, No. 1, pp. 14–15, 1999.

[67] J. B. Andersen, "Array gain and capacity for known random channels with multiple element arrays at both ends," *IEEE Journal on Selected Areas in Communications*, Vol. 18, No. 11, 2000.

[68] L. C , Godara, "Applications of antenna arrays to mobile communications, Part II: Beam-Forming and Direction-of-Arrival considerations". *Proceedings of the IEEE*. Vol. 85, No. 8, p. 1195-1245, 1997.

[69] J. W., Wallace, et al, "Power and complex envelope correlation for modeling measured indoor MIMO channels: a beamforming evaluation," *IEEE 58thVehicular Technology Conference*, VTC 2003-Fall, Vol. 1, pp.363-367, 6-9 Oct. 2003.

[70] S. R., Saunders, *Antennas and propagation for wireless communication systems*, West Sussex : John Wiley & Sons, 1999.

[71] Kotterman, W. and Thomä, R., "Testing for Kronecker-separability," COST 2100 TD(07) 017, Lisbon, Portugal, 26-28 February, 2007.

CHAPTER 2

MIMO CHANNEL MEASUREMENTS

2.1. Introduction

This chapter deals with the performed MIMO measurement procedure, addressing the scenario characteristics, measurement setup and post-processing of data. The designed and tested experimental procedure was developed for indoor measurements until 13x13 array elements, with frequency bands between 2 and 12 GHz, centered at 2, 2.4, 6 and 12 GHz.

In Figure 2.1 shows the performed experimental procedure for the MIMO channel characterisation. The experimental MIMO matrix, denoted by $\widehat{\mathbf{H}}$, is acquired by means a VNA, then a personal computer (PC) performs a local post-processing, and the data is then used to estimate the FSC MIMO matrix, denoted by $\mathbf{R}$. Based on $\mathbf{R}$ matrix, it is then applied a stochastic model to generate the synthetic channel matrix, denoted by $\widetilde{\mathbf{H}}$, which is finally used to estimate the MIMO channel metrics used for analysis in this Dissertation.

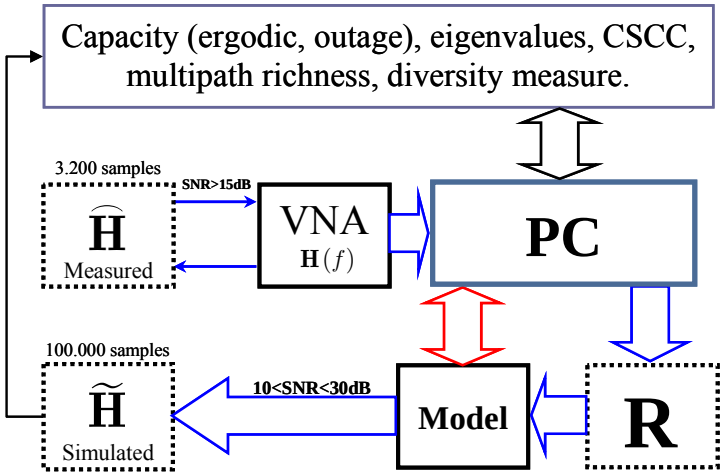

Figure 2.1. Block diagram of the performed experimental procedure for the MIMO channel characterisation.

2.2. Environment and scenarios

For comparisons, two indoor scenarios were chosen for the measurement campaigns: a laboratory area (Figure 2.2), and a hall and corridor area (Figure 2.3), called Zone A and B, respectively, both with LOS and NLOS propagation conditions. In specific, the measurements were carried out at the iTEAM Research Institute, and at the Telecommunications Department ETSIT-UPV. The measurements were performed at nights, in absence of people and guaranteeing static conditions.

The iTEAM scenario (Zone A, Figure 2.2) included a room in LOS condition (laboratory room) and a corridor in NLOS (between an office room and a laboratory room), with wood made walls around, concrete columns and furniture. The receiver array (RX) was placed in the laboratory room and the transmitter array (TX) was placed in both the room and the adjacent corridor to obtain the two conditions with 7 different locations. The TX was located at a height of 1.7 m and the RX at 2 m. The maximum distance from the TX to RX was 12 m in order to guarantee a SNR higher than 15 dB in LOS and NLOS conditions for any frequency band. For convenience, the TX was moved instead of the RX.

The ETSIT scenario (Zone B, Figure 2.3) included two different floors in a hall and corridor area, one in the first floor in LOS conditions, and other in the fourth floor in a corridor in NLOS condition. The ETSIT building is made with brick walls and concrete columns. The Zone B in LOS included one location (denoted by 3*) where the spatial resolution at the TX array was twice in electrical dimensions compared with the spatial resolution of the rest of locations. Besides, it was included a location with 3 different angles at the TX ULA (0º, 45º and 90º orientations), and other location (denoted by 5*) where the TX power was variable, seeking a stable SNR at the RX array for each central frequency.

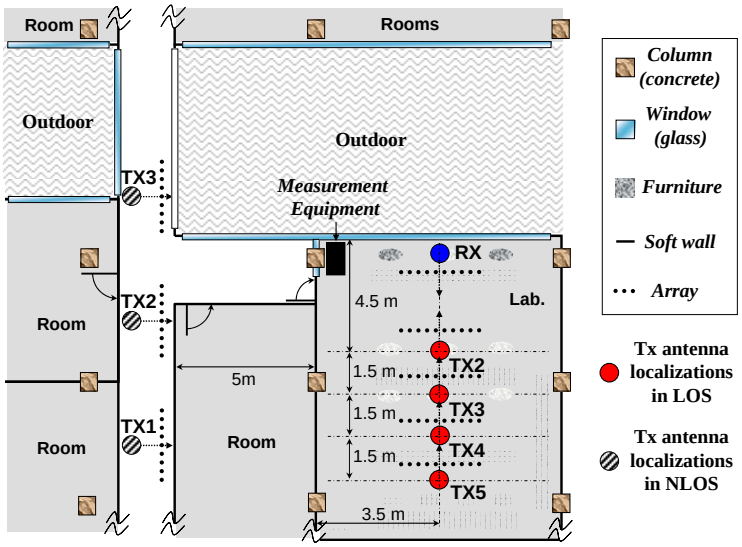

Figure 2.2. Indoor scenario (Zone A): indoor environment for measurement campaigns in LOS and NLOS conditions at the iTEAM - UPV.

The Zone B in NLOS was a corridor with corner, and with both arrays placed in the middle of the corridors. It was included one TX location with higher spatial resolution (denoted by 1*), and other with the TX parallel to the corridor (denoted by 2*). In Zone B, in the same way as Zone A, the TX was located at a height of 1.7 m and the RX at 2 m with a maximum distance of 2 m between the TX and RX.

These different locations in Zone A and B let us comparisons (Chapter 4) for different array configurations and propagation conditions, taking into account two indoor scenarios where the constituent material of buildings were different.

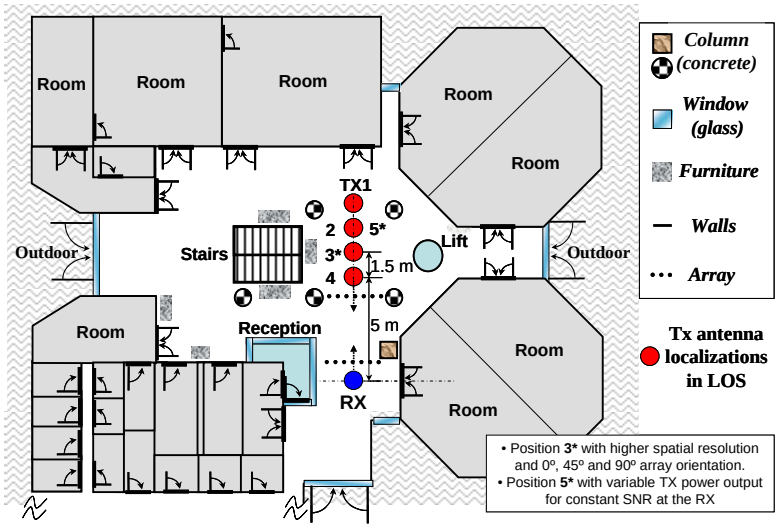

a)

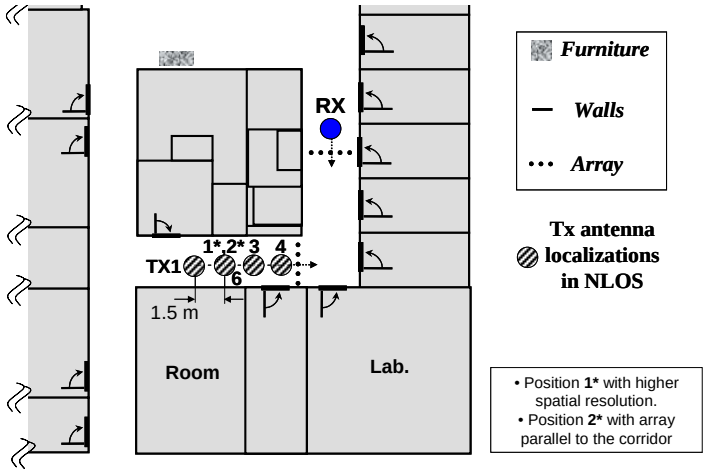

b)

Figure 2.3. Indoor scenario (Zone B): indoor environment for measurement campaigns in LOS and NLOS conditions at the ETSIT - UPV. a) Measurements in LOS, b) Measurements in NLOS.

2.3. Measurement setup

The radio channel sounder was a VNA; the ZVA-24 Rohde & Schwarz (from 10MHz up to 24 GHz) [1]. Besides, UWB antennas EM-6865 [2], and wideband devices were integrated in the measurement setup (Figure 2.4). It is worth to indicate that the measurement chain was calibrated before each measurement in each location inside zones A and B. The collected MIMO data were frequency domain complex samples obtained under a high SNR regimen, equal electric separation between array elements in all frequency bands, and under static indoor channel conditions.

2.3.1. Vector network analyzer (VNA) configuration

To perform the measurement campaigns, it was used a VNA with a dynamic range of about 130 dB [1], omnidirectional wideband biconical antennas (up to 18 GHz [2]) at the TX and the RX side, wideband RF amplifiers at the RX side and very low attenuation cables (Figure 2.4). The system resolution was as follows: 10 μs of acquisition time per frequency bin, 62.5 kHz between frequency bins and a minimum of 2.5 cm between antenna elements (1.25 cm in higher spatial resolution for two locations in Zone B in Figure 2.3).

For notation, it is defined the MIMO channel matrix by $\mathbf{H} \in \mathbb{C}^{N \times M}$, where M and N are the number of antenna elements at the TX and RX, respectively, and $M \geq N$. The matrix $\mathbf{H}$ was measured in the frequency domain. A bandwidth of 250 MHz (SPAN in the VNA) was set around each central frequency, f_c, i.e., $f_c = \{2, 2.4, 6, 12\}$ GHz, with 4000 frequency bin samples and 50 snapshots per

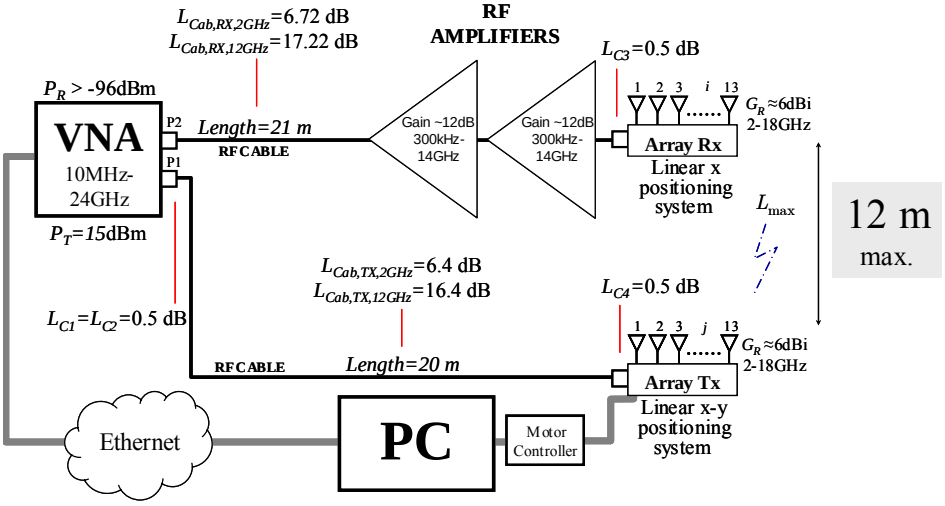

Figure 2.4. Measurement setup for MIMO channels using a vector network analyzer (VNA) taking into account the isolation of the path loss and a high SNR regime. The parameters L_x indicate losses for each component, P_x powers, and G_x gains.

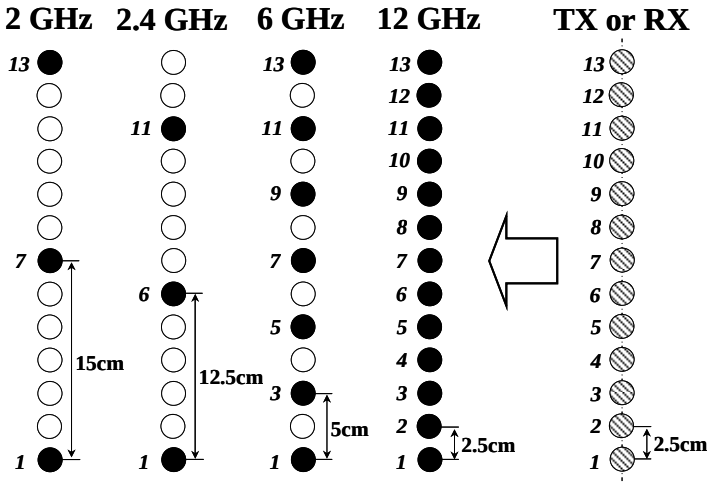

Figure 2.5. Virtual array configuration to perform measurements at different frequency bands using uniform linear arrays (ULAs) at both ends of the link.

location. The analysed bandwidth after post-processing was 200 MHz with 3200 frequency bin samples. The chosen frequency bands are included in the International Telecommunication Union (ITU) distribution frequencies for fixed and mobile terrestrial systems [3]. It is worth to indicate that it has been used 50 snapshots per frequency bin in order to average possible variability introduced by noise, which increased the final SNR.

2.3.2. MIMO array configuration

The antennas were mounted over precise linear positioning systems emulating virtual uniform-lineal-arrays (ULAs) without coupling effects. The virtual ULAs kept the same elements separation in terms of the wavelength, which were one wavelength for all frequencies using the minimum common step of 2.5 cm (Figure 2.5), and ½ wavelength for 1.25 cm (in a similar way than 2.5 cm but only for two locations in Zone B).

In Figure 2.5 the filled black circles, which established one wavelength separation, were obtained by searching the correct elements over all 13 acquired data array elements (indicated as circles with oblique lines). $M = N \leq 4$ was considered for most of the experimental analysis, in agreement with current recommendations [4]-[7]. Nevertheless, in some analysis higher array dimensions were included. It has been established 30 cm as the maximum length for the ULAs (i.e., 2λ at 2 GHz).

The measurement procedure was controlled by a PC connected by LAN to the VNA and the motor controller of the robotic positioning system at the RX. To measure relative effects versus frequency, all frequency bands data were collected simultaneously at the same array element positions. Figure 2.6 shows details of the

MIMO measurement system based on VNA, where the robotic positioning system, antennas and broadband devices at both sides of the link can be seen.

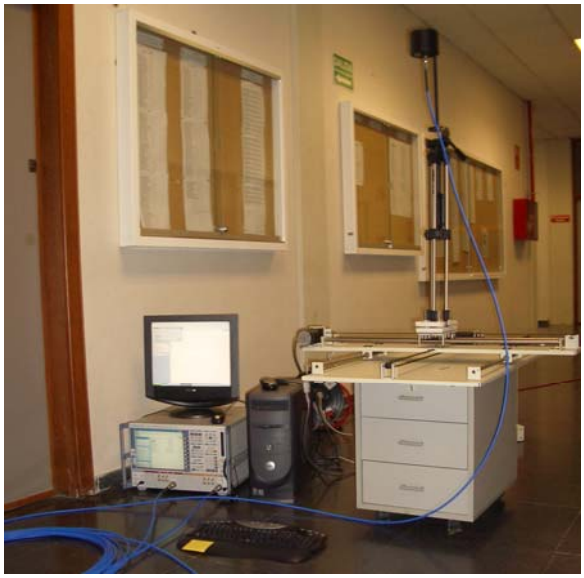

a)

b)

Figure 2.6. Measurement equipment in Zone B in NLOS: a) VNA, robotic precise linear positioning system, UWB antenna, and broadband devices at the RX side, b) UWB antenna, precise linear positioning system, amplifiers, power source, and broadband devices at the TX side.

2.3.3. Ultra wideband biconical antennas

A characterisation of the biconical antennas EM-6865 [2] is presented in this section. The aim was to verify possible pattern variation during the experimental MIMO channel measurements covering a wideband spectrum of about 10 GHz.

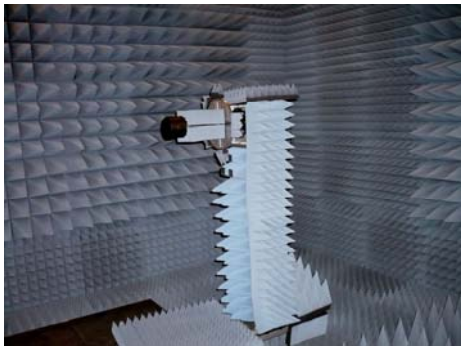

a)

b)

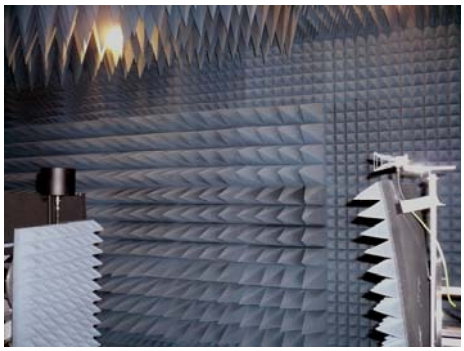

c)

Figure 2.7. Omni-directional UWB antenna EM-6865 characterisation between 2 and 12 GHz using an anechoic chamber: a) antenna EM-6865, b) characterisation at 2 and 2.4 GHz based on two reference horn antennas, and c) characterisation between 4 and 12 GHz based on two reference double ridged horn antennas.

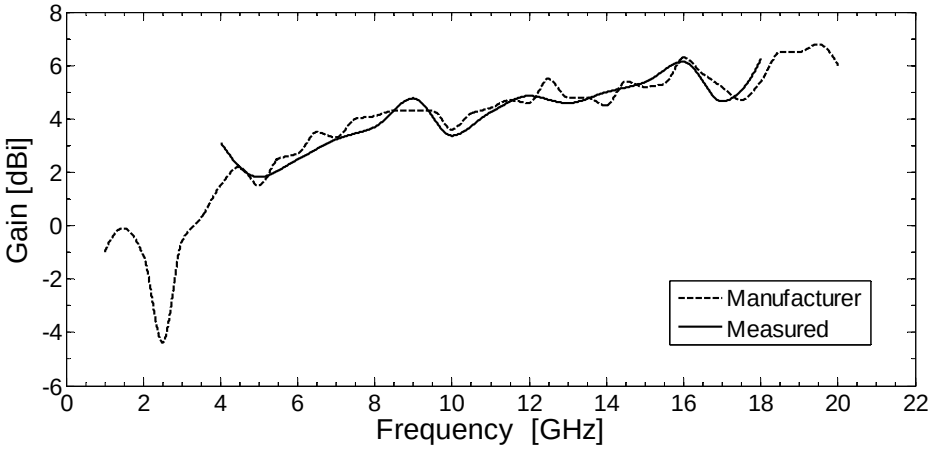

Figure 2.8**.** EM-6865 antenna gain versus frequency. Values obtained by cubic interpolation using the provided manufacturer information and the data obtained in an anechoic chamber using reference horn antennas between 4 and 18 GHz.

The main issue to assess was the variations in the vertical (V)/horizontal (H) patterns and the antenna gain at each central frequency, since these variations are not included in the calibration procedure using a VNA. For this purpose, an anechoic chamber and reference horn antennas were used (Figure 2.7). The goal was to verify the inherent variations in the antenna directivity that may affect the experimental MIMO channel analysis.

Two different reference antennas were used for characterisation: two reference horn antennas at 2 and 2.4 GHz, and two reference horn antennas between 4 and 12 GHz[12]. The 3 GHz band was not tested due to the reference antennas were not available at the facilities.

On the other hand, note from Figure 2.7 that the distance between the EM-6865 antenna and the reference antennas is different for each case. It was chosen 2.95 m for 2 and 2.4 GHz, and 91 cm between 4 and 12 GHz, in the seeking of far field characterisation.

The EM-6865 antenna gain is drawn in Figure 2.8 based on both the manufacturer information (between 1 and 20 GHz) and the measurements done in the anechoic chamber (only between 4 and 18 GHz). It was used cubic interpolation to get values between the provided samples in both cases. It was checked that the antenna gain followed the expected values, and that those values were stable in the desired bands for channel measurements (around the SPAN for the VNA). It is worth to indicate that most of the antenna gain variations were overcame in the segmentation and normalization steps at post-processing, where the path-loss effect was isolated (Section 2.6.1).

[12] Antenna DRH40 - Double Ridged Horn 4 GHz - 40 GHz, by RFspin s.r.o Company.

The EM-6865 gain patter is drawn in Figure 2.9. For the horizontal plane, the manufacturer guaranteed omnidirectionality, and this behaviour was confirmed at 2, 2.4, 4, 6 and 12 GHz. The differences among all H planes were about 10 dB, having 12 and 4 GHz the maximum and minimum values, respectively. For convenience the H plane at 12 GHz was listed first in Figure 2.9.a.

The vertical planes included the biggest differences in the desired

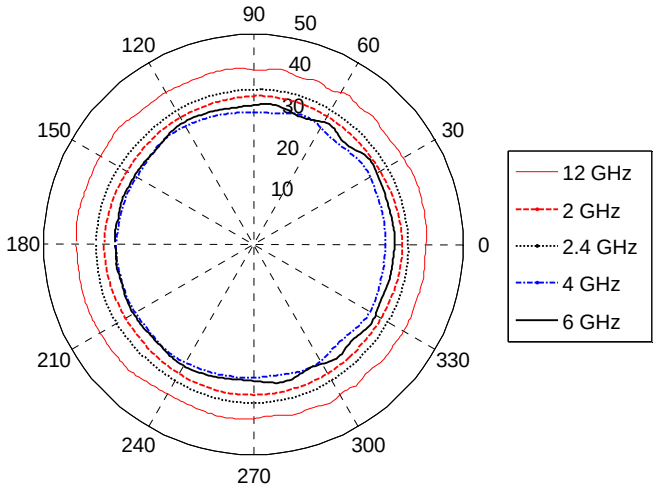

H plane

a)

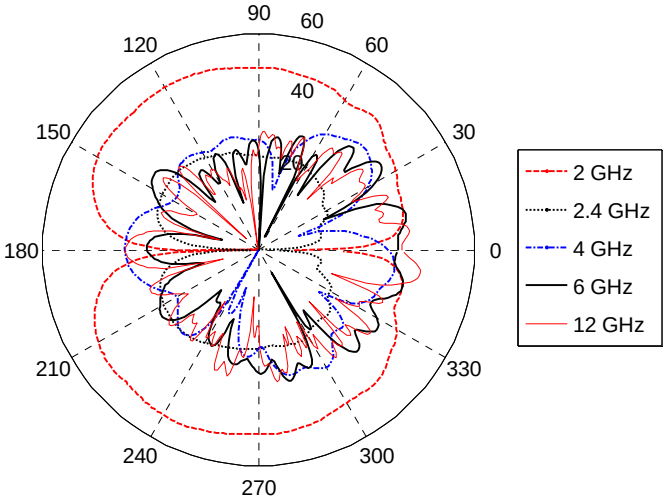

V plane

b)

Figure 2.9**.** EM-6865 antenna gain patter variations between 2 and 12 GHz: a) H plane b) V plane. Note that the V plane shows nulls at 180 and 0º, which correspond to the top and bottom of the biconical antenna.

omnidirectionality of the antenna patter[13]. The Figure 2.9.b shows how the V plane start with two main lobes at 2 and 2.4 GHz (a usual way for biconical antennas) and finish with a multi-lobe V plane at 6 and 12 GHz. The main effect of this pattern variation for the experimental MIMO channel characterisation will be a modification in the CSCC at different central frequencies (see Section 4.4).

2.4. Link budget and dynamic range

It has been checked from current literature that the link noise level affects the reliability of the MIMO channel analysis based on measurements, recommending a SNR higher than 15 dB [8],[9]. For the measurement setup used in this PhD Dissertation the power noise floor was verified by measurements at -130 dBm approximately. Besides, the chain links in the system were designed to keep a SNR higher than 15 dB in all frequency bands (details of the system in Figure 2.4).

2.4.1. Link budget

Based on 10 kHz intermediate frequency (IF) filter (VNA configuration), the noise power at the RX side was calculated in about -134 dBm at 290K [10]. The rest of values used for the link budget calculation are detailed in Figure 2.4, where cables and connectors are included at 2 and 12 GHz. Besides, it was tested the RX noise power variability in about 5.65 dB (standard deviation) with span of 500 MHz. For the used VNA, the minimum detected power at the input port was -125 dBm [1], and the TX power was set to 15 dBm.

With the system configuration presented above, the maximum distance between antenna arrays was then calculated. For the scenarios introduced in Section 2.2 and measurement setup presented in Section 2.3, it has been established a reference maximum distance of 12 m to follow the desired high SNR regime, taking into account the noise values obtained in Section 2.4.2. For that calculation, it has been used an indoor propagation model with fading margins for NLOS [11], and the Friis formula for LOS [10]. The maximum reference distance has been designed based on fading margins calculated at 99% for the fading process, i.e., based in a Rayleigh channel model.

Finally, a maximum allowed power of 15 dBm at RX side was taken into account in the calculations. In this way, the minimum allowed distance between the TX and RX was 3 m, due to the two 12 dB wideband amplifiers in the RX chain (Figure 2.4).

[13] The omnidirectionality is desired for ULA configurations due to its effect in the spatial correlation and the angular spread estimations [12].

2.4.2. Noise floor

The particularity of the wideband measurement setup proposed in this Dissertation implies restrictions about the noise floor level, especially if it is necessary to make experimental comparisons in frequency. For the measurement setup presented in Section 2.3, and based on the results presented in Section 2.4.1, the SNR between 2 and 12 GHz was always higher than 15 dB, assuring it for both LOS and NLOS conditions, but for reliable analysis it is necessary to test the noise level at the RX side.

In this way, the performance of the VNA used for measurements was tested. It was checked the noise level (mean) with an IF filter bandwidth of both 1 and 10 kHz (Figure 2.10 and Figure 2.11), and with different number of frequency bin samples for spans of both 5 and 500 MHz. It was found different noise levels for different frequency bin samples with 500 MHz of span and an IF filter of 10 kHz (see Figure 2.10), without cables, antennas and connectors included. It is worth to indicate that 10 kHz bandwidth at the IF filter was chosen looking for an acquisition time per frequency bin lower than 10 μs, ensuring stationary conditions in the tested channel.

Figure 2.10 shows that the VNA guarantee a noise level between -119 and -126 dBm for frequency bins samples from 401 to 2001. These values are higher than the theoretical value obtained in Section 2.4.1. The experimental noise floor was about -130 dBm for higher number of frequency bin samples. These different noise floor level has been considered for the calculation of the maximum distance between TX and RX in Section 2.4.1, taking into account 3200 frequency bin samples, 10 kHz IF filter and 200 MHz of span for the measurement setup.

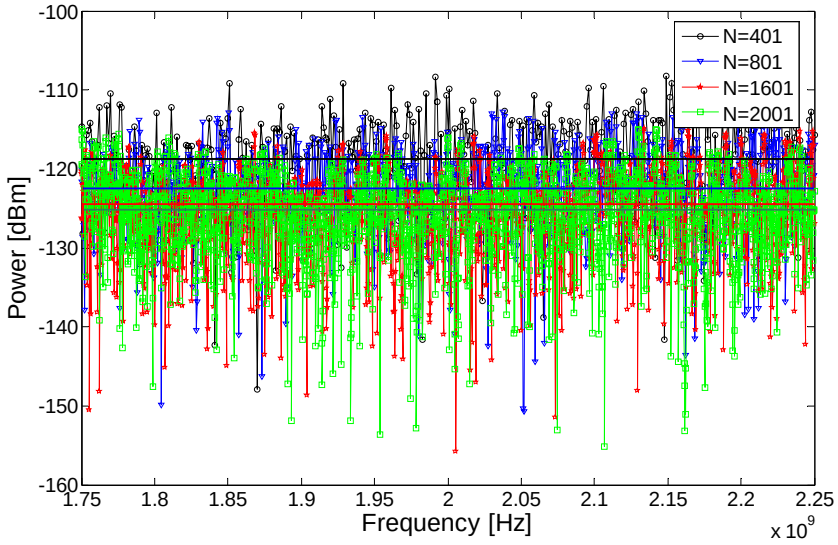

Figure 2.10. Noise floor for different number of frequency bin samples at 2 GHz. SPAN of 500 MHz and IF filter of 10 kHz.

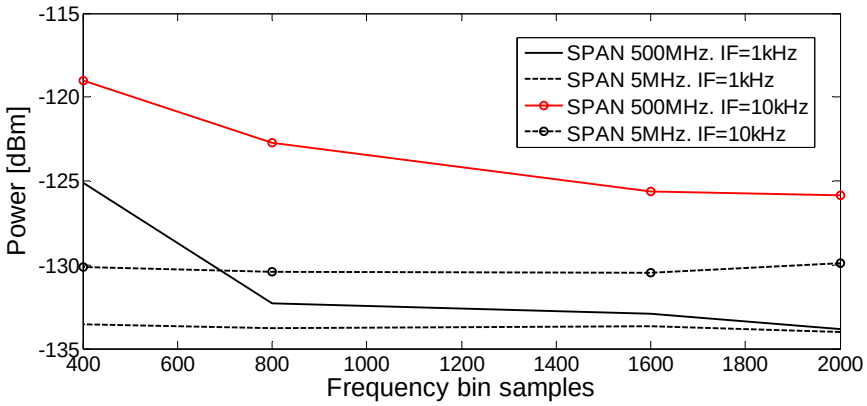

Figure 2.11**.** Experimental noise level (average) in the VNA for different span and IF filters.

In Figure 2.11 is included the experimental noise level (mean) for different SPAN and IF filters at the VNA. It was confirmed that the noise floor was always between -119 and -130 dBm if the IF filter bandwidth was set to 10 kHz, even for lower SPAN and higher frequency bin samples. Of course, the noise values are lower for 1 kHz IF filter, but the time for acquisition increases, which is undesired in the experimental procedure.

2.5. Minimum conditions for measurements

To guarantee the reliability of the measurement campaign, it was chosen a minimum number of time snapshots per TX-RX pairs of antenna elements. This value was obtained according to the error and variance calculated comparing different experimental power delay profiles (PDP) [10]. The maximum reference number of time snapshots was 500, decreasing until cero to perform comparisons.

It was verified that the desired minimum number of time snapshots is 50, due to the low error and stable variance achieved in the PDP comparisons (Figure 2.12). This number of time snapshots allowed both faster measurement campaigns and stationarity in the MIMO data. For the measurement setup, the acquisition time was lower than the coherent time of the channel, since the measurements were performed in static conditions, at nights, and without people around. The 50 time snapshots also enabled to reach higher SNR in post-processing based on averages of those samples.

On the other hand, the acquisition time of each frequency sweep at the VNA was established from its datasheet [1]. The time duration per frequency sweep for 3200 frequency bin samples and 200 MHz of span is about 100 ms for an IF filter of 10 kHz. Note that if a Doppler component of around 1 Hz is considered due to

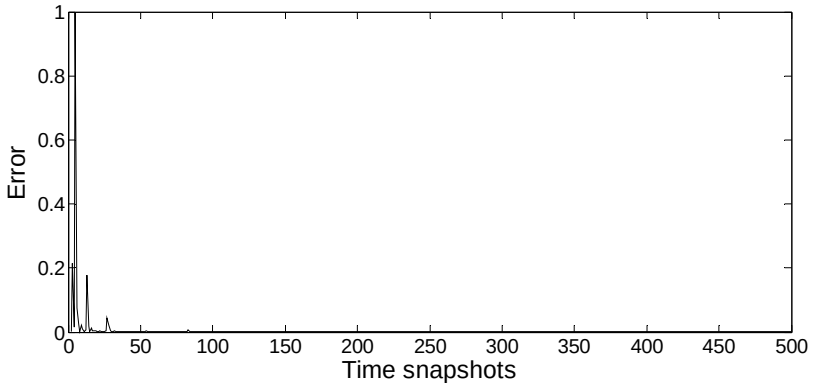

a)

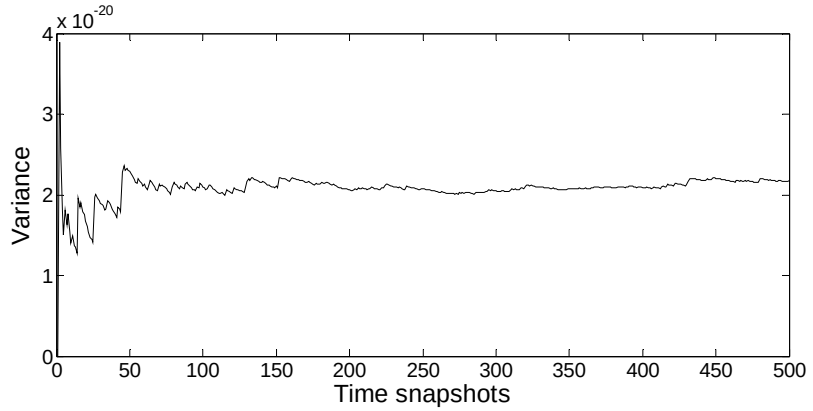

b)

Figure 2.12. Comparisons on the calculation of the PDP per TX-RX pairs of antennas when the number of time snapshots increases: a) error b) variance

environment variations, this can contribute with a coherent time of about 180 ms [10], which can be resolved with this measurement setup.

Moreover, based on PDP results, it was tested for Zone A that the closer scatterer objects were at 40 ns in the NLOS scenario. This value gives a distance 90% higher than the ULA array lengths (i.e., 2 wavelengths at 2 GHz), fulfilling the wide sense stationary (WSS) and local area conditions [12] for most of the measurement locations in this zone. Zone B was less restrictive compared with Zone A, having higher electrical dimensions.

Based on the analysis presented in last sections, the measurement setup and chosen scenarios offered the desired conditions for a reliable characterisation of the MIMO channel between 2 and 12 GHz, fulfilling WSS conditions during measurements and assuring a high SNR regime within the MIMO data [8]. These necessary conditions guarantee the statistical validity and accuracy of the MIMO analysis presented in this Dissertation with a minimal noise influence [9].

2.6. Post-processing of MIMO data

In this section the post-processing applied to MIMO data, i.e., normalization, segmentation and FSC matrix estimation is described. With both the chosen scenarios and the measurement setup described in Sections 2.2 and 2.3, and applying the Frobenius norm [13] to the measured MIMO channel matrix, denoted by $\widehat{\mathbf{H}} \in \mathbb{C}^{N\times M}$, it is possible to eliminate the path loss effects for every frequency band and then to apply the estimation procedures. It is assumed that the MIMO channel transfer matrix elements have identical average power [14].

2.6.1. MIMO transfer matrix normalisation

The normalised non-frequency-selective stationary frequency domain MIMO channel, denoted by $\widehat{\mathbf{H}} \in \mathbb{C}^{N\times M}$, is obtained using 40 consecutive windows of 5 MHz per frequency band and 50 snapshots (see Figure 2.13). Primarily, it is found in 200 MHz the stationary frequency selective channel coefficients $\widehat{H}_{ij}(f) \in \mathbb{C}$, where f indicates frequency domain. These coefficients are the entries of the matrix $\widehat{\mathbf{H}}$, in this case, the complex gain transmission coefficients from the *j*-th transmitting antenna to the *i*-th receiving antenna (see Figure 2.4). It is worth to indicate that for the considered static indoor environment, it has been verified a coherent bandwidth for both LOS and NLOS conditions about 16.4 and 4.67 MHz (mean), respectively, with a correlation coefficient of 0.75 [15]. It is used here a value close to the minimum bandwidth to obtain the stationary non-frequency selective channel coefficients $\hat{H}_{ij} \in \mathbb{C}$ from $\widehat{H}_{ij}(f)$.

To obtain $\widehat{\mathbf{H}}$, it has been used all l-th frequency bins and κ-th snapshots of the measured base-band discrete-complex sequences, $\widehat{H}_{ij}^{\kappa}[f_l]$ (see Figure 2.13), where $f_l = -B_m/2 + l\Delta f$, $l = \{0,1,\cdots,I_m - 1\}$, and $\kappa = \{0,1,\cdots,K_m - 1\}$. Here, B_m and Δf are the total bandwidth (200 MHz) and the system frequency domain resolution (62.5 kHz), respectively. I_m is the total number of frequency bin samples and K_m is the total number of snapshot samples, i.e., I_m=3200 and

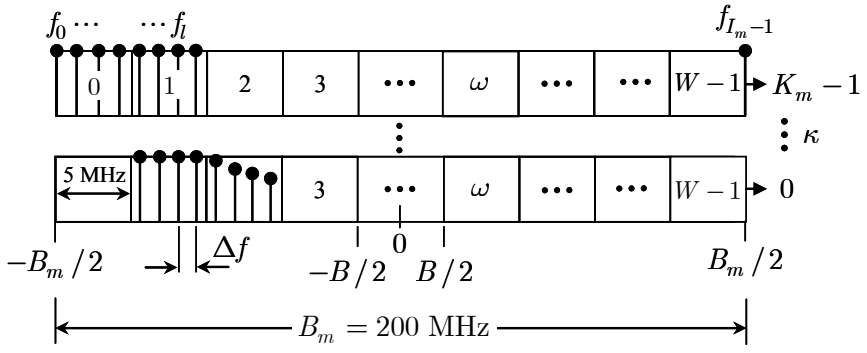

Figure 2.13. Samples and segmentation in the frequency domain used to calculate the entries of $\widehat{\mathbf{H}}$ based on the measured sequences $\widehat{H}_{ij}^{\kappa}[f_l]$ around f_c.

K_m=50.

It is then divided $\widehat{H}_{ij}^{\kappa}[f_l]$ in W=40 frequency segments of B=5 MHz. This procedure was carried out by applying to $\widehat{H}_{ij}^{\kappa}[f_l]$ a sampled version of the rectangular unitary window

$$w(f)=\begin{cases}1, & -B/2\le f\le B/2,\\ 0, & otherwise,\end{cases} \tag{2.1}$$

as follows

$$\widehat{H}_{ij}^{\kappa,\omega}[f_{l'}]=\widehat{H}_{ij}^{\kappa}[f_{\omega R+l'}]\,w[f_{l'}], \tag{2.2}$$

where $f_{l'}=-B/2+l'\Delta f$, $l'=\{0,1,\cdots,I-1\}$, $I=\lfloor I_m/W\rfloor$, $\omega=\{0,1,\cdots,W-1\}$, $i=\{1,2,\cdots,N\}$, $j=\{1,2,\cdots,M\}$ and choosing $R=I$ to obtain consecutive segments.

For $\widehat{H}_{ij}^{\kappa,\omega}[f_{l'}]$, $f_{l'}$ is the l'-th frequency bin sample inside of the ω-th frequency segment at the κ-th snapshot sample.

Using (2.2), the ω-th averaged and normalised non-frequency selective MIMO channel transfer matrix, denoted by $\widehat{\mathbf{H}}_{\omega}^{[f_{l'}]}\in\mathbb{C}^{N\times M}$, is obtained calculating its entries as follows

$$\widehat{H}_{ij}^{\omega}[f_{l'}]=\left\langle\frac{\left(\widehat{H}_{ij}^{\kappa,\omega}[f_{l'}]-\left\langle\widehat{H}_{ij}^{\kappa,\omega}[f_{l'}]\right\rangle_{f_{l'}}\right)}{\sqrt{\mathrm{var}_{f_{l'}}\left(\widehat{H}_{ij}^{\kappa,\omega}[f_{l'}]\right)}}\right\rangle_{\kappa}, \tag{2.3}$$

where $\langle\cdot\rangle_{f_{l'}}$ and $\langle\cdot\rangle_{\kappa}$ denote sampled mean in $f_{l'}$ and κ domains, respectively, and $\mathrm{var}_{f_{l'}}(\cdot)$ denotes variance operator in $f_{l'}$ domain. By means of (2.3), the ω-th normalised non-frequency selective MIMO channel transfer matrix without path loss effects, denoted by $\widehat{\mathbf{H}}_{\omega}\in\mathbb{C}^{N\times M}$, is given by the square Frobenius norm [13] of $\widehat{\mathbf{H}}_{\omega}^{[f_{l'}]}$, applied to each l'-th frequency bin

$$\widehat{\mathbf{H}}_{\omega}^{[f_{l'}]}=\left((1/MNI)\sum_{l'=0}^{I-1}\left\|\widehat{\mathbf{H}}_{\omega}^{[f_{l'}]}\right\|_F^2\right)^{-1/2}\widehat{\mathbf{H}}_{\omega}^{[f_{l'}]}, \tag{2.4}$$

where

$$\left\|\widehat{\mathbf{H}}_{\omega}^{[f_{l'}]}\right\|_F^2 = Tr\left[\left(\widehat{\mathbf{H}}_{\omega}^{[f_{l'}]}\right)^H\left(\widehat{\mathbf{H}}_{\omega}^{[f_{l'}]}\right)\right] = \sum_{i=1}^{N}\sum_{j=1}^{M}\left|\widehat{H}_{ij}^{\omega}\left[f_{l'}\right]\right|^2. \tag{2.5}$$

In (2.5) $Tr[\cdot]$ denotes trace and the superscript H indicates conjugate transpose. Note that in (2.4) the total channel components of the $\widehat{\mathbf{H}}_{\omega}$ matrix have unit power.

2.6.2. FSC MIMO matrix estimation

The FSC MIMO matrix, denoted henceforth by $\mathbf{R}_{\text{MIMO}}$, is theoretically defined by [16]

$$\mathbf{R}_{\text{MIMO}} \triangleq E\left[vec(\mathbf{H})vec(\mathbf{H})^H\right], \tag{2.6}$$

where

$$vec(\mathbf{H})_{NM\times 1} = \left(H_{11}, H_{21}, .., H_{N1}, .., H_{1M}, H_{2M}, .., H_{NM}\right)^T, \tag{2.7}$$

$E[\cdot]$ is the expectation operator, and the superscript T indicates transpose. Note that $\mathbf{H} \in \mathbb{C}^{N\times M}$, with $M \geq N$. In (2.6) $\mathbf{R}_{\text{MIMO}} \in \mathbb{C}^{NM\times NM}$ is by definition a Hermitian and positive semidefinite matrix [13], and its entries, denoted by $R_{q,r}$, with $q = \{1,2,\cdots NM\}$ and $r = \{1,2,\cdots NM\}$, follow

$$\left|R_{ij,\ell s}\right| = \left|E\left[H_{ij}H_{\ell s}^*\right]\right| \leq 1,\ \forall ij \neq \ell s \tag{2.8}$$

If it is fulfilled linearity between the MIMO channel entries, H_{ij}, stationary conditions, non-frequency selectivity, and a local area channel condition [12], the $\mathbf{R}_{\text{MIMO}}$ matrix can be then estimated by means of the Pearson's product moment correlation [13]. Hence, using (2.4), for each frequency band, around of f_c, the $\mathbf{R}_{\text{MIMO}}$ matrix can be estimated by

$$\widetilde{\mathbf{R}}_{\text{MIMO}} = \frac{1}{WI}\sum_{\omega=0}^{W-1}\sum_{l'=0}^{I-1} vec\left(\widehat{\mathbf{H}}_{\omega}^{[f_{l'}]}\right)vec\left(\widehat{\mathbf{H}}_{\omega}^{[f_{l'}]}\right)^H, \tag{2.9}$$

where $\widetilde{\mathbf{R}}_{\text{MIMO}}$ denotes the estimated FSC MIMO matrix, W=40, and I=80. Take into account that SNR>15 dB is guaranteed in all cases [8].

It is worth to indicate that the $\widetilde{\mathbf{R}}_{\text{MIMO}}$ matrix will be the focal point for the synthetic channel generation and the new correction methods detailed in Chapter 3.

2.7. Conclusions

A measurement campaign in two indoor scenarios following WSS conditions, high SNR regimen, and isolation of the path-loss effect for the acquisition of reliable MIMO data between 2 and 12 GHz has been designed and performed. The measurement setup was proposed, the robotic linear positioning system and control software were implemented, the UWB antennas were characterized, the minimum conditions for measurements were defined, and the performance of the VNA was verified. Subsequently, a post-processing of data to obtain the normalized non-frequency selective MIMO channel matrix was proposed, which allowed a reliable estimation of the FSC MIMO matrices of the system.

References

[1] Vector Network Analyzer Data Sheet, ZVA, "High-end network analyzer up to 8 GHz /24 GHz with two or four test ports," Rohde&Schwarz, V.1.0, 2005.

[2] Instruction Manual, "Omni-directional wideband antenna model EM-6865: 2 GHz-18 GHz," Electro-Metrics Corporation, 2005.

[3] "ITU Radio Regulations Article 8 (RR 8)," 1990, and 1995.

[4] "Multiple-Input Multiple-Output in UTRA," 3GPP TR25.876 V1.8.0., Oct. 2005.

[5] "Spatial channel model for multiple input multiple output (MIMO) simulations," 3GPP TR 25.996 V7.0.0:, June 2007.

[6] "Part 11: Wireless LAN medium access control (MAC) and physical layer (PHY) specifications," IEEE P802.11n, D3.00, Sept. 2007.

[7] "Part 16: Air interface for fixed broadband wireless access systems," IEEE Std 802.16 2004, Oct. 2004.

[8] P. Kyritsi, D. C. Cox, R. A. Valenzuela, and P. W. Wolniansky, "Correlation analysis based on MIMO channel measurements in an indoor environment," *IEEE J. on Selected Areas in Commun.*, vol. 21, no. 5, pp. 713-720, June 2003.

[9] J.W. Wallace, M.A. Jensen, A.L. Swindlehurst, and B.D. Jeffs, "Experimental characterization of the MIMO wireless channel: data acquisition and analysis," *IEEE Trans. on Wireless Communications*, Vol. 2, No. 2, pp.335-343, 2003.

[10] S. R., Saunders, *Antennas and propagation for wireless communication systems*, West Sussex : John Wiley & Sons, 1999.

[11] International Telecommunication Union, ITU-R Recommendation P.1238-2: Propagation data and prediction models for the planning of indoor radiocommunications systems and radio local area networks in the frequency range 900MHz to 100GHz, Geneva, 2001.

[12] G. D. Durgin, *Space-Time Wireless Channels*, Pearson Education, Inc., NJ, US, 2003.

[13] C. D. Mayer, *Matrix analysis and applied linear algebra*, Society for Industrial and Applied Mathematics, 2000.

[14] D. Chizhik, et al, "Multiple-input-multiple-output measurements and modeling in Manhattan," *IEEE J. on Selected Areas in Commun.*, vol. 21, no. 3, pp. 321-331. April 2003.

[15] J. A. Díaz, A. P. García, and L. Rubio, "Time dispersion characterization for UWB mobile radio channels between 3.1 and 10.6 GHz," IEEE Antennas and Propagation Society International Symposium 2007, Honolulu, Hawaii, USA, June 10-15, 2007.

[16] A. Paulraj, R. Nabar and D. Gore, *Introduction to space-time wireless communications*, Cambridge University Press, 2003.

CHAPTER 3

SYNTHETIC MIMO CHANNEL

3.1. Introduction

Once it was obtained the reliable experimental FSC MIMO matrix from the MIMO data (Chapter 2), the next proposed step for the channel characterisation was the synthetic MIMO channel generation. This procedure is based on the coloring matrix of the MIMO system, which is obtained by the Cholesky factorisation of a positive definite FSC MIMO matrix.

Under realistic propagation conditions, and for a large number of antenna elements at the TX and the RX, the estimated FSC MIMO matrices may be indefinite as a consequence of statistical inconsistency among the random variables involved in the estimation process [1],[2], besides, the MIMO data becomes in non multivariate normal. In such cases, the estimated FSC MIMO matrix may contain zero and negative eigenvalues. Indeed, in this PhD Dissertation, it is demonstrated that many FSC MIMO matrices estimated from real data are indefinite, and the MIMO data becomes in non-multivariate normal in many wideband multi-antenna cases. Besides, it has been proved that the probability of being indefinite and non-normal increases for large-scale matrices, i.e., when the number of antenna elements increases, and the loss of normality increases with the bandwidth.

In order to carry out a synthetic generation of the MIMO channel using the coloring matrix of the system, the FSC MIMO matrix must be positive definite, i.e., the correlation matrix can not contain both zero and negative eigenvalues. If this is not the case, the nearest Hermitian positive definite matrix has to be computed. Sorooshyari and Daut proposed an approximation to solve the non-positiveness of a matrix [2], addressing an optimisation problem and finding the necessary positive eigenvalues to construct a new correlation matrix. Although this work offers a starting point considering a searching in a subspace of matrices, it neither analyses the performance of the procedure nor assesses its effect on both the eigenvalues distribution and the structure of the FSC MIMO matrix. The effect of the matrix transformation on the correlation matrix structure (i.e., Hermitian with unit diagonal) and on the eigenvalues distribution has a special interest on MIMO systems, because channel spatial characteristics are mapped in the eigenvalues and eigenvectors of the FSC MIMO matrix.

Therefore, the main contribution of this chapter is as follows: given an indefinite Hermitian matrix, a novel correction procedure (CP) [3] based on the alternating projection (AP) method [4] is proposed to find the closest Hermitian and positive definite matrix with unit diagonal. Moreover, this chapter demonstrates that the resulting FSC MIMO matrix is valid to generate the large number of synthetic samples of the MIMO channel transfer matrix needed to perform a reliable MIMO channel analysis, as for example an outage capacity analysis. To conclude this chapter, the MIMO data used for the FSC MIMO matrix estimation is also verified. Both the normality (univariate and multivariate) and the linearity of the MIMO data (measured and synthetic) are tested, guaranteed the reliability of the MIMO channel analysis addressed in Chapter 4.

3.2. FSC MIMO matrix: Cholesky factorisation and limitations

From estimations of the FSC MIMO matrix, as in (2.9), denoted by $\widetilde{\mathbf{R}}_{\text{MIMO}}$, it is possible to generate by simulation different realisations of $\mathbf{H}$ [5]. This procedure uses the Cholesky factorisation to decompose $\widetilde{\mathbf{R}}_{\text{MIMO}}$ as [6]:

$$\widetilde{\mathbf{R}}_{\text{MIMO}} = \mathbf{C}\mathbf{C}^{H} \tag{3.1}$$

If the $\widetilde{\mathbf{R}}_{\text{MIMO}}$ matrix is positive definite, the $\mathbf{C}_{NM\times NM}$ matrix is a lower complex triangular matrix with real positive diagonal entries. Besides, this matrix is the unique lower triangular matrix satisfying (3.1).

The $\mathbf{C}$ matrix is the coloring matrix [7] of the MIMO system and can be used to generate by simulation as many realisations of the MIMO channel, denoted by $\widetilde{\mathbf{H}}$, as desired following [5],[8]-[13]:

$$vec(\widetilde{\mathbf{H}}) = \mathbf{C}\mathbf{a} \tag{3.2}$$

where $\widetilde{\mathbf{H}} \in \mathbb{C}^{N\times M}$, with $M \geq N$, is the synthetic MIMO channel transfer matrix,

$$vec(\widetilde{\mathbf{H}})_{NM\times 1} = \left(\tilde{H}_{11}, \tilde{H}_{21}, .., \tilde{H}_{N1}, .., \tilde{H}_{1M}, \tilde{H}_{2M}, .., \tilde{H}_{NM}\right)^{T},$$

$$\mathbf{a}_{NM\times 1} = \left(\alpha_{11}, \alpha_{21}, \ldots, \alpha_{N1}, \ldots, \alpha_{1M}, \alpha_{2M}, \ldots, \alpha_{NM}\right)^{T},$$

and α_{ij} are zero-mean complex independent identically distributed random variables. Note that $\mathbf{C}$ could be expressed as an upper triangular matrix with positive diagonal entries; therefore $\widetilde{\mathbf{R}}_{\text{MIMO}} = \mathbf{C}^{H}\mathbf{C}$, and $vec(\widetilde{\mathbf{H}}) = \mathbf{C}^{H}\mathbf{a}$.

Equations (3.1) and (3.2) permit to generate the cross-correlated $N \times M$ complex normal random variables of the entries of $\widetilde{\mathbf{H}}$, which have the specific correlation matrix $\widetilde{\mathbf{R}}_{\text{MIMO}}$.

The main limitation of this procedure is that the experimental correlation matrix $\widetilde{\mathbf{R}}_{\mathrm{MIMO}}$ must be a Hermitian positive definite matrix to apply the Cholesky factorisation and then find only one coloring matrix. Provided that correlation matrices derived from measurements or synthetic samples are not always guaranteed to be positive definite (see e.g., [1],[2]), the $\mathbf{C}$ matrix does not always exist, making the Cholesky factorisation unsuitable.

Finally, it is worth to indicate that the Cholesky factorisation can be applied if and only if the $\widetilde{\mathbf{R}}_{\mathrm{MIMO}}$ matrix is both Hermitian and positive definite, or both Hermitian and positive semidefinite. If $\widetilde{\mathbf{R}}_{\mathrm{MIMO}}$ is a Hermitian positive semidefinite matrix, the $\mathbf{C}$ matrix is a lower complex triangular matrix with no strictly real positive diagonal entries and there exist several $\mathbf{C}$ matrices satisfying the Cholesky factorisation [6]. For the sake of simplicity and under the assumption that zero eigenvalues can be replaced by small enough eigenvalues, it is considered here the case where only one $\mathbf{C}$ matrix exists. Therefore, in this PhD Dissertation, the $\widetilde{\mathbf{R}}_{\mathrm{MIMO}}$ matrix is forced to be Hermitian positive definite.

3.3. Alternating projections to find the closest positive definite FSC MIMO matrix

In this PhD Dissertation, it is proposed a CP [3] based on the AP method [4] to solve the problem of non-positiveness of some experimental FSC MIMO matrices. To access the problem, note that a complex spatial correlation matrix is always Hermitian with unit diagonal (equations (2.6) and (2.8)). Thus, we must only care if such matrix is positive definite. Here for the CP is proposed to use iteratively two different projections to find the closest positive definite FSC MIMO matrix in the intersection of two target subspaces. In this way, the subspaces of interest and the projection rules are defined below.

Let D be the subspace of Hermitian and positive definite matrices, and U the subspace of Hermitian matrices with unit diagonal:

$$D = \left\{ \mathbf{R} = \mathbf{R}^H \in \mathbb{C}^{NM \times NM} : \mathbf{x}_q^H (\mathbf{R}) \mathbf{x}_q > 0, \forall \mathbf{x}_q \in \mathbb{C}^{NM \times 1} \neq 0 \right\},$$

$$U = \left\{ \mathbf{R} = \mathbf{R}^H \in \mathbb{C}^{NM \times NM} : R_{q,q} = 1, q = 1 : NM \right\}.$$

Given one experimental correlation matrix $\widetilde{\mathbf{R}}_{\mathrm{MIMO}} \in U$, with a set of eigenvalues $\left\{ \tilde{\xi}_q \right\}$, where $q = \{1, 2, \cdots, NM\}$ and $\tilde{\xi}_1 > \tilde{\xi}_2 > \cdots > \tilde{\xi}_{NM}$, the CP performs a search of the Hermitian and positive definite matrix $\widehat{\mathbf{R}}_{\mathrm{MIMO}} \in \{D \cap U\}$ that is the closest to $\widetilde{\mathbf{R}}_{\mathrm{MIMO}}$ in the Frobenius norm. The search of the $\widehat{\mathbf{R}}_{\mathrm{MIMO}}$ matrix is carried out through iterative projections onto the subspaces D and U of an auxiliary matrix, $\widehat{\mathbf{R}} \in \mathbb{C}^{NM \times NM}$.

The projections of $\widehat{\mathbf{R}}_k$ onto subspace D is denoted by $\widehat{\mathbf{R}}'_k = P_D\left(\widehat{\mathbf{R}}_k, \varepsilon\right)$, where k refers to the current iteration and $\varepsilon \in \mathbb{R}_+$. It is considered that $\left\{\widehat{\xi}_p\right\}$, with $\widehat{\xi}_1 > \widehat{\xi}_2 > \cdots > \widehat{\xi}_{NM}$, is the set of eigenvalues of $\widehat{\mathbf{R}}_k$, which has a total of P zero and/or negative eigenvalues $\left\{\widehat{\xi}_p^-\right\}$, given by $\widehat{\xi}_p^- = \widehat{\xi}_{p+NM-P}$, where $p = \{1,2,\cdots,P\}$. Hence, the projection onto the subspace D consists in removing the negative and zero eigenvalues of $\widehat{\mathbf{R}}_k$, by substituting them for a small enough value ε, so that $\widehat{\xi}_p^- = \varepsilon, \forall p$.

On the other hand, in order to project $\widehat{\mathbf{R}}'_k$ onto the subspace U, denoted by $\widehat{\mathbf{R}}''_k = P_U\left(\widehat{\mathbf{R}}'_k, 1\right)$, all the elements in its main diagonal are set to 1, $\widehat{R}'^k_{q,q} = 1$. The subspace U projection entails a new modification in the matrix eigenvalues and therefore a new projection onto the subspace D should be carried out, and so on until the distance between $\widehat{\mathbf{R}}''_k$ and $\widehat{\mathbf{R}}''_{k-1}$ is lower than a specified tolerance.

The CP can be summarised by the following equations, taking into account that $\mathbf{E}^k$ is the difference matrix between $\widehat{\mathbf{R}}'_k$ and $\widehat{\mathbf{R}}_k$ at the k-th iteration, and s_k is the relative distance between matrices $\widehat{\mathbf{R}}''_k$ and $\widehat{\mathbf{R}}''_{k-1}$:

$$\widehat{\mathbf{R}}_k = \widehat{\mathbf{R}}''_{k-1} - \mathbf{E}^{k-1} \tag{3.3}$$

$$\widehat{\mathbf{R}}'_k = P_D\left(\widehat{\mathbf{R}}_k, \varepsilon\right) \tag{3.4}$$

$$\mathbf{E}^k = \widehat{\mathbf{R}}'_k - \widehat{\mathbf{R}}_k \tag{3.5}$$

$$\widehat{\mathbf{R}}''_k = P_U\left(\widehat{\mathbf{R}}'_k, 1\right) \tag{3.6}$$

$$s_k = \frac{\left\|\widehat{\mathbf{R}}''_k - \widehat{\mathbf{R}}''_{k-1}\right\|_F}{\left\|\widehat{\mathbf{R}}''_k\right\|_F} \tag{3.7}$$

where $\widehat{\mathbf{R}}''_0 = \widetilde{\mathbf{R}}_{\text{MIMO}}$, $\mathbf{E}^0 = \mathbf{0}$, and $\|\cdot\|_F$ is the Frobenius norm. This iterative method runs until the relative distance between the resulting matrices of two consecutive iterations is lower than a defined tolerance, tol, i.e., while $s_k \geq tol$. The work of Boyle and Dykstra [3] demonstrates that, with the CP based on the AP method, the $\widehat{\mathbf{R}}''_k$ matrix converges to the desired FSC MIMO matrix, $\widehat{\mathbf{R}}_{\text{MIMO}}$, which is the nearest positive definite matrix to the original $\widetilde{\mathbf{R}}_{\text{MIMO}}$ matrix.

3.4. Performance of the CP

To validate the procedure explained in the last sections, a large set of FSC MIMO matrices were estimated using (2.9) from the frequency-domain MIMO data obtained in Zone A (see Figure 2.2). For the chosen stationary indoor environment [14], it has been verified the coherent bandwidths, for both LOS and NLOS conditions, with values about 20 and 10 MHz (mean), respectively, for a correlation level of 0.5 [15]. For the experimental analysis presented here, the non-frequency selective channel (in NLOS) was achieved using 40 segments of 5 MHz inside the measured bandwidth (equation (2.4)). Besides, in order to estimate the FSC MIMO matrices, it has been assumed ergodicity and linearity between the MIMO channel entries, stationary conditions, non-frequency selectivity, and a local area channel condition [16].

As it was addressed in Section 2.6.2, the FSC MIMO matrix was estimated by means of the Pearson's product moment correlation [6]. The estimated complex correlation matrix is the same as the complex covariance matrix calculated from standardised Gaussian random variables using the maximum likelihood estimator [17]. The segmentation and number of samples were chosen to approximate the estimator to an unbiased and consistent estimator.

Once the $\widetilde{\mathbf{R}}_{\mathrm{MIMO}}$ matrices were estimated, it was verified whether they were effectively positive definite for different array configurations, i.e., $N = M = \{2,5,8,9\}$. Figure 3.1 shows the CDF of the $\widetilde{\mathbf{R}}_{\mathrm{MIMO}}$ eigenvalues lower than 1.5. It can be observed that the higher the number of antenna elements involved in the array configuration, the higher the probability of $\widetilde{\mathbf{R}}_{\mathrm{MIMO}}$ not being positive definite, and higher negative eigenvalues are introduced. Specifically, for the 2×2 array configuration this probability is lower than 1%, whereas for 5×5, 8×8, and 9×9 is between 20% and 35%, with a probable maximum negative eigenvalue around -1 for 9×9. These experimental results are in agreement with the work presented by Sorooshyari and Daut for a correlation level from 0.1 to 0.4 between Gaussian variables [2]. This issue will be verified in Table 4.1, Chapter 4.

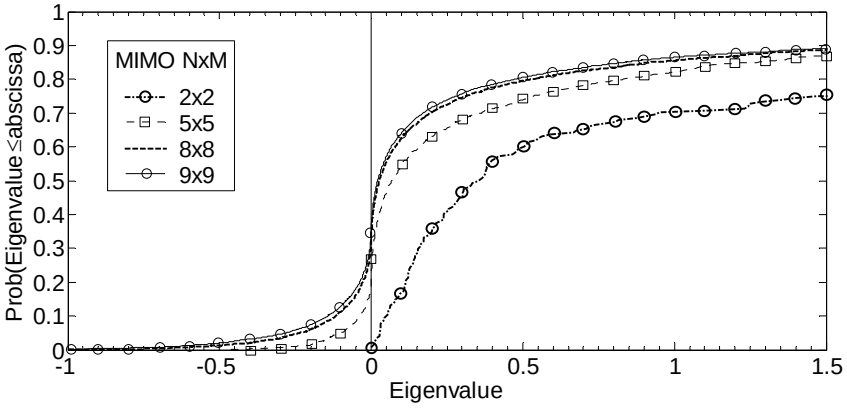

Figure 3.1. CDF of the $\widetilde{\mathbf{R}}_{\mathrm{MIMO}}$ eigenvalues for values lower than 1.5 for different MIMO array configurations, i.e., $N = M = \{2,5,8,9\}$.

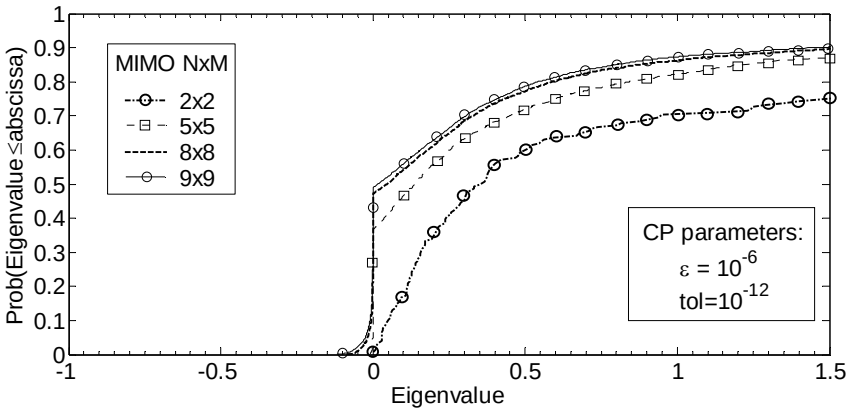

Figure 3.2. Impact of a fixed tol and ε on the performance of the CP for different MIMO array configurations, i.e., $N = M = \{2,5,8,9\}$.

Subsequently, the procedure proposed in Section 3.3 it has been used to adjust all matrices detected as non-positive definite. Note that the term 'adjust' is used to indicate the search procedure followed to find the closest Hermitian and positive definite matrix with unit diagonal.

Figure 3.2 depicts the same eigenvalue distribution than Figure 3.1 after the CP using ε=10^{-6}, tol=10^{-12}, and 40 iterations (maximum). In general, applying the CP, only small differences between the eigenvalue distributions of $\widetilde{\mathbf{R}}_{\text{MIMO}}$ and $\widehat{\mathbf{R}}_{\text{MIMO}}$ were detected for eigenvalues lower than 1 with $N = M > 2$. Take into account that for $N = M = 2$, the differences between the distributions are almost null because the CP has been applied only in few cases. The good fit among distributions means that the CP preserves the MIMO channel characteristics, not modifying the results of the subsequent MIMO analysis.

Besides, in Figure 3.2, the curves show that almost all matrices are adjusted correctly for each MIMO configuration, with a good approximation of the eigenvalues distribution compared with the positive eigenvalues of Figure 3.1. Only small changes in the distribution are detected for eigenvalues lower than 1 for $N = M > 2$, and the probable maximum negative eigenvalue is around -0.1 for 9×9. Once the CP is performed, the probability of getting a non-positive definite matrix with smaller negative eigenvalues is lower than 25% for $N = M = \{5,8,9\}$, whereas for $N = M = 2$ the few detected indefinite matrices were all appropriately adjusted.

On the other hand, the results shown in Figure 3.2 indicate that the success rate of the procedure to reach the $\widehat{\mathbf{R}}_{\text{MIMO}}$ matrix depends on the CP parameters (tol and ε) and on the number of antenna elements $N \times M$. According to the results presented in other trials for $N = M > 2$, the procedure requires lower values of tol and ε to obtain a success rate of 100%, and more iterations to reach $\widehat{\mathbf{R}}_{\text{MIMO}}$.

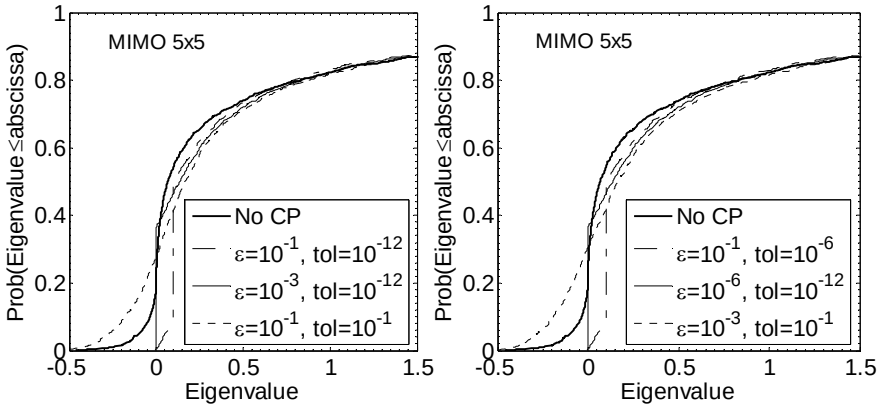

Figure 3.3. Impact of tol and ε on the performance of the CP for a 5×5 MIMO array configuration.

Therefore, it is interesting to further assess how tol and ε affect the eigenvalues distribution and the success rate of the CP. For this purpose, a 5×5 array configuration has been chosen. ε has been set equal to 10^{-1}, 10^{-3} and 10^{-6}, whereas tol has been set equal to 10^{-1}, 10^{-6} and 10^{-12}. In Figure 3.3 (left) it is shown how a value of ε and tol equal to 0.1 changes the eigenvalues distribution as compared with the eigenvalue distribution of the original $\widetilde{\mathbf{R}}_{\text{MIMO}}$ (referred in the figure as "No CP"). Besides, even higher negative eigenvalues appear. This behaviour is even noticeable for $\varepsilon = 10^{-3}$ and $tol = 10^{-1}$ (right).

On the other hand, in Figure 3.3 (left and right) it is observed that the success rate of the CP increases with lower tolerance values. Besides, a greater ε value results in a higher change in the distribution. Such modification on the distribution affects small positive eigenvalues, increasing slightly the distance between the $\widehat{\mathbf{R}}_{\text{MIMO}}$ and $\widetilde{\mathbf{R}}_{\text{MIMO}}$ matrices. However, even with $\varepsilon = 10^{-1}$ and $tol \leq 10^{-6}$, the success rate is 100%. In consequence, provided this 5×5 array configuration, tol should be at least equal to 10^{-6} to guarantee $\widehat{\mathbf{R}}_{\text{MIMO}}$ positiveness, whereas ε should be at least equal to 10^{-3} and $tol = 10^{-12}$ to modify at a minimum the eigenvalue distribution. For $tol < 10^{-12}$ the performance of the CP can be slightly improved, but at the expense of more iterations to reach $\widehat{\mathbf{R}}_{\text{MIMO}}$.

Finally, different MIMO channel metrics can be performed using the realisations of the synthetic MIMO channel, $\widetilde{\mathbf{H}}$, as it is suggested in [5], obtaining $\widetilde{\mathbf{H}}$ from (3.2), and after applying the CP over $\widetilde{\mathbf{R}}_{\text{MIMO}}$ if it is necessary. For example, the MIMO channel capacity was calculated for the performance analysis of the CP, using (3.1) and (3.2) to produce 10^5 realisations of $\widetilde{\mathbf{H}}$ when $\widetilde{\mathbf{R}}_{\text{MIMO}}$ was indefinite for the array configurations $N = M = \{5, 6, 7, 8\}$.

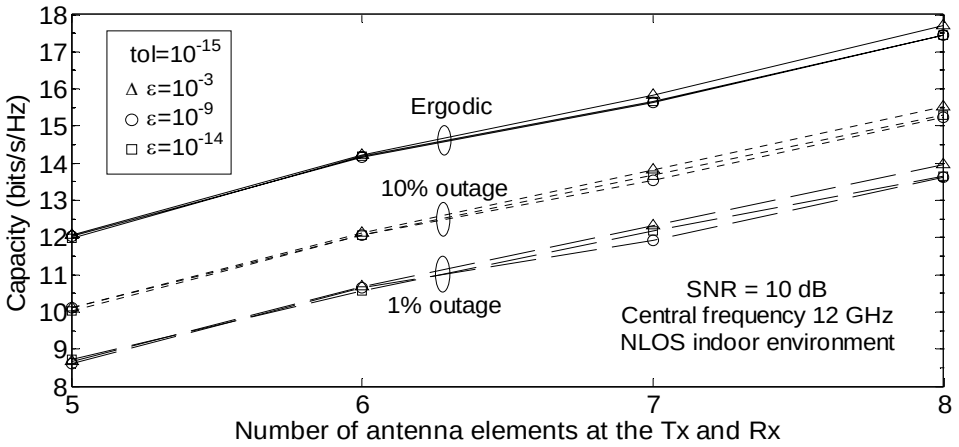

Figure 3.4. Impact of ε, with tol =10^{-15}, on the capacity of the generated synthetic MIMO channel for $N = M = \{5,6,7,8\}$.

Figure 3.4 shows the ergodic and the outage (at 1% and 10%) capacities [18] at 12 GHz in NLOS for the MIMO configurations $N = M = \{5,6,7,8\}$. It has been used tol =10^{-15} and ε equal to 10^{-3}, 10^{-9} and 10^{-14}. Note that a value of tol =10^{-15} was chosen to guarantee a 100% success rate in all configurations.

Figure 3.4 proves the little effect of ε on the MIMO capacity results, being increased these effects at 1% outage capacity. The modifications of the $\widehat{\mathbf{R}}_{\mathrm{MIMO}}$ eigenvalues, due to not small enough ε values, cause only slight variations on the capacity, which are lower than 0.5 bits/s/Hz at 1% outage capacity for all array configurations. These results confirm that the CP [3], based on the AP method [4], is useful for MIMO channel characterisation when $\widetilde{\mathbf{R}}_{\mathrm{MIMO}}$ is indefinite. Besides, these results prove that very small values of ε are not necessary, because modifications of the smallest eigenvalues do not affect practically the characteristics of the original $\widetilde{\mathbf{R}}_{\mathrm{MIMO}}$ matrix.

3.4.1. Useful considerations for the CP

The projections onto subspace D (equation (3.4)), can be also performed by

$$\widehat{\mathbf{R}}'_k = P_D\left(\widehat{\mathbf{R}}_k, \{\varepsilon_p\}\right), \tag{3.8}$$

which consists in removing the negative and zero eigenvalues of $\widehat{\mathbf{R}}'_k$, $\{\widehat{\xi}_p^-\}$, by substituting them for a set of positive and small enough numbers $\{\varepsilon_p\} \in \mathbb{R}$ as follows

$$\widehat{\xi}_{p+NM-P} = \varepsilon_p = \widehat{\xi}_{NM-P} - \left(\left(\widehat{\xi}_{NM-P} - \varepsilon_{\min}\right)/P\right) p \;,\; \forall \varepsilon_{\min} \le \widehat{\xi}_{NM-P} \tag{3.9}$$

where $\widehat{\xi}_{NM-P}$ is the smallest positive eigenvalue from $\left\{\widehat{\xi}_q\right\}$, and $\varepsilon_{\min} \in \mathbb{R}$ is the substituting smallest positive value (in the same way that ε in (3.4)). Note that in (3.9) $\widehat{\xi}_{NM-P} < \varepsilon_p \leq \varepsilon_{\min}$. This new point of view, permit us to keep, by default, the eigenvalues structure $\hat{\xi}_1 > \hat{\xi}_2 > \cdots > \hat{\xi}_{NM}$ in the adjusted FSC MIMO matrix, increasing the performance of the CP.

Figure 3.5 shows the error between the $\widetilde{\mathbf{R}}_{\text{MIMO}}$ and $\widehat{\mathbf{R}}_{\text{MIMO}}$ matrices, i.e., the error between the CDFs of the eigenvalues of both matrices. It has been included array configurations between 2×2 and 9×9. In this case, $tol = 10^{-15}$ and $\varepsilon_{\min}$ from 10^{-3} to 10^{-12} have been established. Note that $\varepsilon_{\min}$ could be set according to the $\widetilde{\mathbf{R}}_{\text{MIMO}}$ dimensions, how it already was addressed. Besides, it is observed that there is an optimum value for $\varepsilon_{\min}$ according to the matrix dimensions, i.e., $\varepsilon_{\min} = 10^{-12}$ for $N = M = \{2,3,4\}$, $\varepsilon_{\min} = 10^{-11}$ for $N = M = \{5,6\}$, $\varepsilon_{\min} = 10^{-10}$ for $N = M = 7$, $\varepsilon_{\min} = 10^{-9}$ for $N = M = 8$ and $\varepsilon_{\min} = 10^{-8}$ for $N = M = 9$.

Note that the $\varepsilon_{\min}$ values chosen for the projections onto the D subspace, which have not effect in the higher positive eigenvalues (see (3.9)), could increase the error when the projections onto the U subspace are carried out, which modifies the eigenvalues distribution. However, the reached error is always lower than -20 dB, which prevents undesirable effects on the MIMO channel characterisation using the CP. Besides, as it was shown in Figure 3.3, the error is always focused around the smallest $\widetilde{\mathbf{R}}_{\text{MIMO}}$ eigenvalues, which was also proved in Figure 3.4.

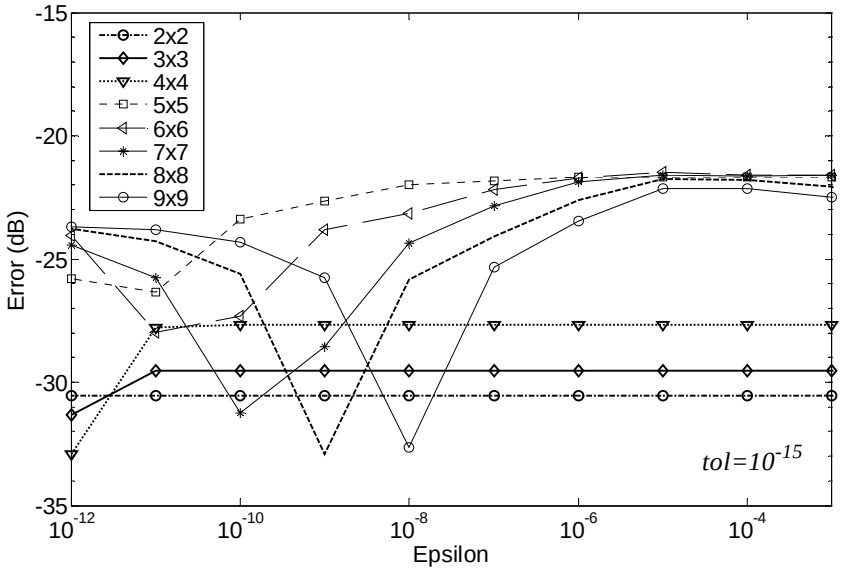

Figure 3.5. Error between $\widetilde{\mathbf{R}}_{\text{MIMO}}$ and $\widehat{\mathbf{R}}_{\text{MIMO}}$: error between CDFs of the eigenvalues in terms of $\varepsilon_{\min}$ for different $N \times M$ array configurations.

Based on both the synthetic channel generation and the proposed CP, the MIMO channel capacity and other channel metrics will be analysed in Chapter 4. As it was addressed in last sections, the CP will allow accessing the desired experimental MIMO channel characterisation between 2 and 12 GHz for different array configurations based on the estimated FSC MIMO matrices.

3.5. MIMO data characteristics and their relationship with estimated covariance matrices

Before to deal with the experimental MIMO channel characterisation and comparisons in Zones A and B, in this chapter it will be finally addressed the intrinsic relationship between MIMO data, and its characteristics, with the estimated covariance matrices. As it was commented above, under realistic propagation conditions, and for a large number of antenna elements at the TX and the RX, the estimated FSC MIMO matrices may be indefinite as a consequence of statistical inconsistency among the random variables involved in the estimation process [1],[2]. Here, besides, it will be taken into account the MIMO data ergodicity, its multivariate distribution, linearity characteristics and their relationship with the non-positiveness of the FSC MIMO matrices, seeking a test of the reliability of the MIMO data (measured and synthetic), and building a reference frame for future research works in this field.

Beforehand, consider the characteristics of the acquired MIMO data. According to Section 2.3, the system resolutions were: 10 μs per frequency bin, 62.5 kHz in the frequency domain and different wavelengths in the space domain, with a minimum distance among antenna elements of 2.5 cm in Zone A, and 2.5 and 1.25 cm in Zone B. For next sections, it is selected a time-variant channel from a sounding point of view, and from a VNA point of view (due to the based VNA data) a stationary non-frequency selective and frequency selective channel using different number of windows (5 MHz width) inside of the measured bandwidth.

3.5.1. Ergodicity of data

To perform the estimation of the FSC MIMO matrix consider the ergodicity of the normalized channel (equation (2.4)). A statistic is said to be ergodic if, when measured by averaging a single realization of a stochastic ensemble, it is equal to the ensemble average. Therefore, from a sounding point of view, the time-varying frequency response of each MIMO channel transfer matrix entry, denoted by $\hat{H}_{ij}(f,t)$, is mean-ergodic if the frequency, f, and time, t, averaged mean of a single realization equals the ensemble-averaged mean [16]:

$$\left\langle \left\langle \hat{H}_{ij}(f,t) \right\rangle_f \right\rangle_t \equiv E\left[\hat{H}_{ij}(f,t)\right] \tag{3.10}$$

This condition is only followed for the power ergodicity

$$\left\langle \left| \hat{H}_{ij}(f,t) \right|^2 \right\rangle_t = \left\langle \left| \hat{H}_{ij}(f,t) \right|^2 \right\rangle_f \tag{3.11}$$

when the discrete Doppler frequencies, and time delays, involved in the channel element $\hat{H}_{ij}(f,t)$, are different among them. From a VNA point of view, the channel is only frequency dependent $\hat{H}_{ij}(f)$, and the snapshot samples are only used for averages (see equation (2.3)). Hence, there is not care about the power ergodicity between the frequency, f, and time, t, domains for VNA measurements.

On the other hand, for power ergodicity in the space domain, the spatial averaged power must be the same received power averaged as a function of frequency and equal to the assemble-averaged power

$$\left\langle \left| \hat{H}_{ij}(f,t) \right|^2 \right\rangle_i = \left\langle \left| \hat{H}_{ij}(f,t) \right|^2 \right\rangle_j = \left\langle \left| \hat{H}_{ij}(f,t) \right|^2 \right\rangle_f \equiv E\left[\hat{H}_{ij}(f,t) \right] \tag{3.12}$$

when the discrete outgoing directions, and incident directions, of the propagated plane waves are different among them. These definitions of power ergodicity are regarding with heterogeneous scattering [16], which describes a condition where no two multipath waves arrive with precisely the same time delay or direction of arrival. For the chosen environments, there exist elevated scattering conditions, and both the local area size and WSS conditions were followed for the measurements. Besides, according to (2.4), the condition shown in (3.12) is fulfilled. Note that the time domain is not considered for the VNA measurements.

It is worth to indicate that (3.12) presents the property for determining ergodicity, and ergodicity is a property for determining measurability of a channel. Hence, the heterogeneous scattering determines how statistics may be calculated from real-world channel measurements.

3.5.2. Issues in the FSC MIMO matrix estimation

To perform the non-frequency-selective stationary frequency domain MIMO channel, from a sounding point of view, it can be considered a measured base-band discrete-complex sequence, $\widehat{H}_{ij}[f_l, t_\kappa]$, where $f_l = -B_m/2 + l\Delta f$, $t_\kappa = \kappa \Delta t$, $l = \{0,1,\cdots,I_m - 1\}$, $\kappa = \{0,1,\cdots,K_m - 1\}$. B_m, Δf and Δt are the total bandwidth, the system time and frequency resolutions, respectively. See Figure 2.13 for comparisons with the process performed for VNA data (for static measurements).

These sequences with I_m frequency bin samples in the measured bandwidth B_m, around of f_c, with K_m time snapshot samples in the measured time interval T_m, can be divided in W frequency segments of B MHz, with I frequency bin

samples (in the same way that in (2.2)), and V time segments of T seconds, with K time snapshot samples. This procedure is carried out by applying to $\widehat{H}_{ij}[f_l, t_\kappa]$ a sampled version of the rectangular unitary window

$$w(f,t) = \begin{cases} 1, & -B/2 \le f \le B/2, \quad 0 \le t \le T \\ 0, & otherwise, \end{cases} \tag{3.13}$$

which uses smaller lengths than the coherent bandwidth and coherent time. The procedure in the sampled domains is as follows

$$\widehat{H}_{ij}^{\omega,v}[f_{l'}, t_{\kappa'}] = \widehat{H}_{ij}\left[f_{\omega R+l'}, t_{vQ+\kappa'}\right] w[f_{l'}, t_{\kappa'}], \tag{3.14}$$

where $l' = \{0,1,\cdots,I-1\}$, $\kappa' = \{0,1,\cdots,K-1\}$, $\omega = \{0,1,\cdots,W-1\}$, $v = \{0,1,\cdots,V-1\}$, $i = \{1,2,\cdots,N\}$, $j = \{1,2,\cdots,M\}$, $R = I$, and $Q = K$.

In (3.14) $f_{l'}$ is the l'-th frequency bin sample in the ω-th frequency segment (window), $t_{\kappa'}$ is the κ'-th time snapshot sample in the v-th time segment, $B_m = B * W$, $T_m = T * V$, $I = \lfloor I_m / W \rfloor$ and $K = \lfloor K_m / V \rfloor$. Note that T_m is the total time to perform a sampled version of $\widehat{H}_{ij}(f,t)$, and due to $R = I$ and $Q = K$ the frequency and time domain segments are contiguous. Besides, T and K are considered as the process stationary time interval and the total time snapshot samples in such interval, respectively. If it is assumed stationary conditions in the measurements, then $T = T_m$, $K = K_m$ and V =1, in the same way than in (2.2).

Based on (3.14), the resulting normalised non-frequency selective MIMO channel transfer matrix with isolation of the path loss effect, denoted by $\widehat{\mathbf{H}}_{\omega,v}$, for each location area and f_c, is given by the square Frobenius norm of $\widehat{\mathbf{H}}_{\omega,v}^{[f_{l'}, t_{\kappa'}]}$, whose entries are given by

$$\widehat{H}_{ij}^{\omega,v}[f_{l'}, t_{\kappa'}] = \frac{\left(\widehat{H}_{ij}^{\omega,v}[f_{l'}, t_{\kappa'}] - \left\langle \widehat{H}_{ij}^{\omega,v}[f_{l'}, t_{\kappa'}] \right\rangle_{f,t}\right)}{\sqrt{\mathrm{var}\left(\widehat{H}_{ij}^{\omega,v}[f_{l'}, t_{\kappa'}]\right)}} \tag{3.15}$$

The normalisation is applied to each frequency bin and time snapshot samples:

$$\widehat{\mathbf{H}}_{\omega,v}^{[f_{l'}, t_{\kappa'}]} = \left((1/MNIK) \sum_{\kappa'=0}^{K-1} \sum_{l'=0}^{I-1} \left\| \widehat{\mathbf{H}}_{\omega,v}^{[f_{l'}, t_{\kappa'}]} \right\|_F^2 \right)^{-1/2} \widehat{\mathbf{H}}_{\omega,v}^{[f_{l'}, t_{\kappa'}]} \tag{3.16}$$

where

$$\left\|\widehat{\mathbf{H}}_{\omega,v}^{[f_{l'},t_{\kappa'}]}\right\|_F^2 = Tr\left[\left(\widehat{\mathbf{H}}_{\omega,v}^{[f_{l'},t_{\kappa'}]}\right)^H\left(\widehat{\mathbf{H}}_{\omega,v}^{[f_{l'},t_{\kappa'}]}\right)\right] = \sum_{i=1}^{N}\widehat{\lambda}_{\omega,v}^{[f_{l'},t_{\kappa'}]}, \tag{3.17}$$

or

$$\left\|\widehat{\mathbf{H}}_{\omega,v}^{[f_{l'},t_{\kappa'}]}\right\|_F^2 = \sum_{i=1}^{N}\sum_{j=1}^{M}\left|\widehat{H}_{ij}^{\omega,v}\left[f_{l'},t_{\kappa'}\right]\right|^2 = \left(vec\left(\widehat{\mathbf{H}}_{\omega,v}^{[f_{l'},t_{\kappa'}]}\right)\right)^H\left(vec\left(\widehat{\mathbf{H}}_{\omega,v}^{[f_{l'},t_{\kappa'}]}\right)\right). \tag{3.18}$$

In (3.17), $\widehat{\lambda}_{\omega,v}^{[f_{l'},t_{\kappa'}]}$ is the *i*-th eigenvalue of $\left(\widehat{\mathbf{H}}_{\omega,v}^{[f_{l'},t_{\kappa'}]}\right)^H\left(\widehat{\mathbf{H}}_{\omega,v}^{[f_{l'},t_{\kappa'}]}\right)$. Besides, note that (3.15) and (3.16) can be applied to different array MIMO configurations, chosen the correct measurement setup, in time, frequency and space. Also, note from (3.16) that the total channel components of the $\widehat{\mathbf{H}}_{\omega,v}$ matrix have unit power.

The definitions given between (3.13) and (3.17) are not only a mathematic aspect for MIMO data processing. In this section this equations permit to asses an important issue related to the non-positiveness of FSC MIMO matrices, in those cases where the measurement setup is wrong defined. Note that the formulations presented above are defined for data obtained by channel sounders, but it can be used for VNA data assuming time snapshots only for averages, as in Section 2.6.1.

If the ergodicity and linearity between the MIMO channel entries are fulfilled, and under stationary conditions, non-frequency selectivity, and a local area channel condition, the experimental complex covariance MIMO matrix, $\widetilde{\mathbf{R}}_{\text{MIMO}}^{[\nu,\tau']}$, is estimated for each frequency band, around of f_c, by average $W*V$ windowed covariance MIMO matrices, using K time snapshot samples and I frequency bin samples of $\widehat{\mathbf{H}}_{\omega,v}$:

$$\widetilde{\mathbf{R}}_{\text{MIMO}}^{[\nu,\tau']} = \frac{1}{WVKI}\sum_{\omega=0}^{W-1}\sum_{v=0}^{V-1}\sum_{l'=0}^{I-1}\sum_{\kappa'=0}^{K-1} vec\left(\widehat{\mathbf{H}}_{\omega,v}^{[f_{l'},t_{\kappa'}]}\right)vec\left(\widehat{\mathbf{H}}_{\omega,v}^{[f_{l'}+\nu,t_{\kappa'}+\tau']}\right)^H \tag{3.19}$$

where τ' and ν indicate time and frequency domain displacements, respectively: $\tau' = \left(-(K-1),\cdots,0,\cdots,(K-1)\right)\Delta t$, and $\nu = \left(-(I-1),\cdots,0,\cdots,(I-1)\right)\Delta f$. For low errors, it must followed $|\tau'| = \tau'_{\max} \ll K\Delta t$, and $|\nu| = \nu_{\max} \ll I\Delta f$.

Note that the estimated covariance matrix given in (3.19) characterises completely the MIMO channel, since it is included space, time and frequency in the covariance matrix estimation. On the other hand, the FSC MIMO matrix, $\widetilde{\mathbf{R}}_{\text{MIMO}}$, is then obtained from (3.19) by averaging all frequency and time samples:

$$\widetilde{\mathbf{R}}_{\text{MIMO}} = \frac{1}{4\lceil\tau'_{\max}/\Delta t\rceil\lceil\nu_{\max}/\Delta f\rceil}\sum_{\nu=-\nu_{\max}}^{\nu_{\max}}\sum_{\tau'=-\tau'_{\max}}^{\tau'_{\max}}\widetilde{\mathbf{R}}_{\text{MIMO}}^{[\nu,\tau']}. \tag{3.20}$$

Note that $\lceil\cdot\rceil$ indicates selection of the upper nearest integer.

The last FSC MIMO matrix estimation can be applied if the MIMO data are obtained from a channel sounder. Though this is not the case addressed in this PhD Dissertation, the estimator given in (3.19) is useful for space-time-frequency analysis, and it can be used for synthetic MIMO channel generation. The same generation process proposed in Section 3.2 can be followed, but taking into account all domains at the same iteration. The main limitation is the size of the obtained multidimensional covariance MIMO matrix, requiring new strategies to generate the correlated samples in all domains. The CP can be also used for this purpose if the resulting matrix is non-positive definite.

If the MIMO data is obtained from a VNA, the time domain, and then the time displacement τ', can not be included in the covariance structure. Hence, the estimation of the FSC MIMO matrix can be performed by (2.9). Of course, if the frequency displacement, ν, is included, the estimation can be improved. Take into account that a high SNR regime, 80 samples per window, and 40 windows were used for the estimation, increasing the performance of the estimator in that way.

On the other hand, the estimators (2.9) and (3.19) use a limited set of samples from the frequency domain, and from both frequency and time domains, respectively. From a VNA point of view, the only way to get more samples is increasing the number of frequency bin samples per window, or using a window larger than the coherent bandwidth (using samples from a frequency selective channel). The last option will be addressed here for the available MIMO dada, and the estimator given in (2.9) will be applied. This option permits some comparisons of the FSC MIMO matrix eigenvalues under frequency selective channels (see Figure 3.6). It has been selected 160, 1600 and 3200 samples in the frequency domain, which include 10, 100 and 200 MHz of the measured bandwidth, respectively. From Figure 3.6, slightly effects of the measured bandwidth appear on the eigenvalues distributions for different MIMO array dimensions. If larger frequency windows and higher number of samples are used (but lower number of

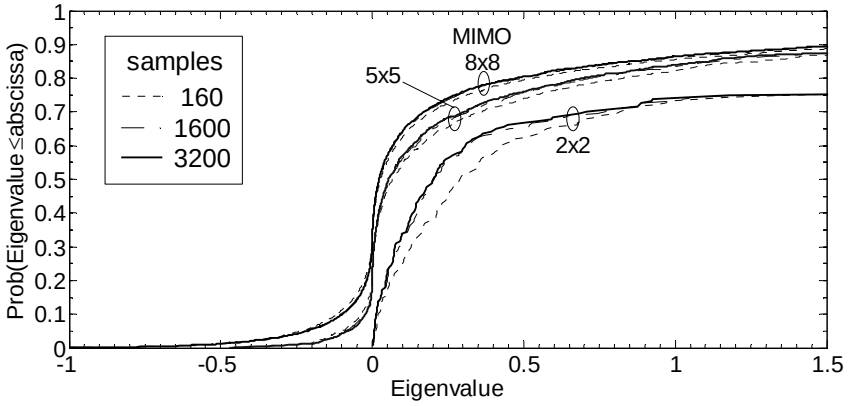

Figure 3.6. CDF of the $\widetilde{\mathbf{R}}_{\mathrm{MIMO}}$ eigenvalues lower that 1.5 for different array configurations, $N = M = \{2,5,8\}$. Impact of the number of samples with SNR higher than 15dB for frequency selective channels.

windows, W), the probability of being non-positive definite is slightly reduced for higher array dimensions. This behaviour obeys to a reduction of the correlation between distant samples in the frequency domain. For these frequency selective cases, it is also possible the application of the CP to perform a MIMO channel analysis. Note that even with 3200 samples the non-positiveness of the FSC MIMO matrix remains almost constant and with the same probabilities for all MIMO configurations compared with the results presented in Figure 3.1 for 80 samples per window.

Finally, it is worth to indicate that another possible improving for the estimators (2.9) and (3.19) can be reached using a different window shape for the segmentation [19]. So far in this PhD Dissertation, the averaged FSC MIMO matrices were reached using a rectangular unitary window for both (2.9) and (3.19). In the case of a channel sounder, if the process does not follow a rigorous stationary condition, the average applied in (3.19) must be carried out by a better segmentation in the time domain. Besides, the stationary interval, T, and number of samples, K, of the time domain segments can be obtained checking the process stationary using a multivariate normal distribution (MND) test over $\widehat{\mathbf{H}}_{\omega,v}$ [19]-[22]. A similar way can be followed for VNA measurements, taking into account that only frequency domain segmentation is performed. In next section it will be addressed the MND of data based on the unitary window. Besides, it is introduced the theoretical concepts of MND for measurements based on channel sounders.

3.5.3. Multivariate normal distribution of the MIMO data

The complex MIMO channel transfer matrix, $\widehat{\mathbf{H}}_{\omega,v}$ (from equation (3.15)), has complex coefficients entries, $\widehat{H}_{ij}^{\omega,v}$. These coefficients are completely characterised, in a first-order statistics level, using probability density functions (PDF) describing fluctuations of their envelopes in a small-scale variation point of view [16]. Such envelopes, $\left|\widehat{H}_{ij}^{\omega,v}\left[f_{l'},t\right)\right|$, can be Rayleigh distributed in NLOS, Rice distributed in LOS or Nakagami distributed for a wide range of fading conditions [23]. On the other hand, the phases of these channel coefficients are defined uniformly distributed as a result of the summation of many homogeneous plane waves that are arriving from different directions in the local area. This definition allows us to suppose that the channel coefficients are complex Gaussian distributed in NLOS indoor environments. However, the univariate complex normal distribution (UCND, sometimes called univariate complex Gaussian distribution), for each channel coefficient does not imply that the sampled observation matrix, $\widehat{\mathbf{H}}_{\omega,v}$, must be multivariate complex normal distributed (MCND). In some cases, multivariate observations are approximately normal distributed [24].

Considering the central limit theorem (CLT), sampling distributions of certain statistics can be approximated by normal distributions, even if the data is not multivariate normal, but such approximations should be checked to apply the procedures proposed for MIMO generation/analysis used in this PhD Dissertation.

For the analysed space-frequency-time process (from a sounder point of view), the complex channel gains $\widehat{H}_{ij}^{\omega,v}\left[f_{l'},t_{\kappa'}\right]$, for a single frequency bin $f_{l'}$ at the time sample $t_{\kappa'}$, could follow a MCND in space, x (i,j samples), frequency, f, and time, t. In this case, the process is completely characterized by the multivariate complex mean (MCM) vector, $\boldsymbol{\mu}_{f,t,x}$, and the multivariate complex covariance (MCC), $\boldsymbol{\Sigma}_{f,t,x}$. For the sampled versions, the entries of these two parameters are respectively given by:

$$\mu_{ij}^{[f_{l'},t_{\kappa'}]}=E\left[\widehat{H}_{ij}^{\omega,v}\left[f_{l'},t_{\kappa'}\right]\right] \tag{3.21}$$

$$\begin{aligned}&\Sigma_{ij,\ell s}^{[f_{l'},\nu][t_{\kappa'},\tau']}=\\&=E\left[\left(\widehat{H}_{ij}^{\omega,v}\left[f_{l'},t_{\kappa'}\right]-\mu_{ij}^{[f_{l'},t_{\kappa'}]}\right)\left(\widehat{H}_{\ell s}^{\omega,v}\left[f_{l'}+\nu,t_{\kappa'}+\tau'\right]-\mu_{\ell s}^{[f_{l'}+\nu,t_{\kappa'}+\tau']}\right)^{*}\right]\end{aligned} \tag{3.22}$$

For non-frequency-selective channels and stationary conditions, $\boldsymbol{\mu}_{f,t,x}$ and $\boldsymbol{\Sigma}_{f,t,x}$ are not a function of f and t. Besides, in such conditions, take into account that the MCC is only a function of both the frequency and temporal displacements, ν and τ', respectively.

In this section the analysis will be focused on the MCND of the space sampled variables of $\widehat{\mathbf{H}}_{\omega,v}$ (see also Appendix A.1), which could affect the correct estimation of $\mathbf{R}_{\text{MIMO}}$. Thus, consider a space dimension vector of the space-frequency-time sampled observation matrix, $\widehat{\mathbf{H}}_{\omega,v}$, as

$$\widehat{\mathbf{h}}_{\omega,v}^{[f_{l'},t_{\kappa'}]}=vec\left(\widehat{\mathbf{H}}_{\omega,v}^{[f_{l'},t_{\kappa'}]}\right)\in\mathbb{C}^{NM\times 1}. \tag{3.23}$$

Under the assumption of non-frequency-selectivity and total stationarity process, it then said that the vector $\widehat{\mathbf{h}}_{\omega,v}^{[f_{l'},t_{\kappa'}]}$ is a NM-dimensional MCND if and only if all linear combinations (in a space of $I\times K$ size) of that vector are univariate complex normal [20]:

$$\begin{aligned}&\widehat{\mathbf{h}}_{\omega,v}^{[f_{l'},t_{\kappa'}]}\sim N_{NM}\left(\boldsymbol{\mu}_x,\boldsymbol{\Sigma}_x^{[\nu,\tau']}\right)\Leftrightarrow\mathbf{b}^T\widehat{\mathbf{h}}_{\omega,v}^{[f_{l'},t_{\kappa'}]}\sim N\left(\mathbf{b}^T\boldsymbol{\mu}_x,\mathbf{b}^T\boldsymbol{\Sigma}_x^{[\nu,\tau']}\mathbf{b}\right),\\&\qquad\qquad\forall\mathbf{b}\in\mathbb{R}^{NM\times 1},\end{aligned} \tag{3.24}$$

where $N_{NM}\left(\boldsymbol{\mu}_x,\boldsymbol{\Sigma}_x^{[\nu,\tau']}\right)$ denote MCND with mean vector $\boldsymbol{\mu}_x\in\mathbb{C}^{NM\times 1}$ and covariance matrix $\boldsymbol{\Sigma}_x^{[\nu,\tau']}\in\mathbb{C}^{NM\times NM}$. The PDF in such case, $p_{\widehat{\mathbf{h}}_{\omega,v}^{[f_{l'},t_{\kappa'}]}}\left(\widehat{H}_{11}^{\omega,v},\cdots,\widehat{H}_{NM}^{\omega,v}\right)$, is given by [24]:

$$p_{\widehat{\mathbf{h}}_{\omega,v}^{[fl',t_{\kappa}']}}\left(\widehat{H}_{11}^{\omega,v},\widehat{H}_{21}^{\omega,v},\ldots,\widehat{H}_{N1}^{\omega,v},\widehat{H}_{12}^{\omega,v},\widehat{H}_{22}^{\omega,v}\ldots,\widehat{H}_{N2}^{\omega,v},\ldots,\widehat{H}_{1M}^{\omega,v},\widehat{H}_{2M}^{\omega,v},\ldots,\widehat{H}_{NM}^{\omega,v}\right)=$$
$$=(2\pi)^{-\frac{NM}{2}}\det\left(\boldsymbol{\Sigma}_x^{[\nu,\tau']}\right)^{-\frac{1}{2}}\exp\left\{Tr\left[-\frac{1}{2}\left(\boldsymbol{\Sigma}_x^{[\nu,\tau']}\right)^{-1}\left(\widehat{\mathbf{h}}_{\omega,v}^{[fl',t_{\kappa}']}-\boldsymbol{\mu}_x\right)\left(\widehat{\mathbf{h}}_{\omega,v}^{[fl',t_{\kappa}']}-\boldsymbol{\mu}_x\right)^H\right]\right\},\quad(3.25)$$
$$\widehat{\mathbf{h}}_{\omega,v}^{[fl',t_{\kappa}']}\in\mathbb{C}^{NM\times 1},\boldsymbol{\mu}_x\in\mathbb{C}^{NM\times 1},\boldsymbol{\Sigma}_x^{[\nu,\tau']}>0,\boldsymbol{\Sigma}_x^{[\nu,\tau']}\in\mathbb{C}^{NM\times NM},$$

where $\det(\cdot)$ denotes determinant. Equation (3.25) can be simplified to

$$p_{\widehat{\mathbf{h}}_{\omega,v}^{[fl',t_{\kappa}']}}\left(\widehat{H}_{11}^{\omega,v},\cdots,\widehat{H}_{NM}^{\omega,v}\right)=$$
$$=(2\pi)^{-\frac{NM}{2}}\det\left(\boldsymbol{\Sigma}_x^{[\nu,\tau']}\right)^{-\frac{1}{2}}\exp\left\{-\frac{1}{2}\left(\widehat{\mathbf{h}}_{\omega,v}^{[fl',t_{\kappa}']}-\boldsymbol{\mu}_x\right)^H\left(\boldsymbol{\Sigma}_x^{[\nu,\tau']}\right)^{-1}\left(\widehat{\mathbf{h}}_{\omega,v}^{[fl',t_{\kappa}']}-\boldsymbol{\mu}_x\right)\right\}.\quad(3.26)$$

On the other hand, $\boldsymbol{\mu}_x$ and $\boldsymbol{\Sigma}_x^{[\nu,\tau]}$ can be estimated using all frequency bins and time snapshot samples as follows

$$\hat{\boldsymbol{\mu}}_x=\frac{1}{KI}\sum_{\kappa'=0}^{K-1}\sum_{l'=0}^{I-1}\widehat{\mathbf{h}}_{\omega,v}^{[fl',t_{\kappa}']}\quad(3.27)$$

$$\widehat{\boldsymbol{\Sigma}}_x^{[\nu,\tau']}=\frac{1}{KI}\sum_{l'=0}^{I-1}\sum_{\kappa'=0}^{K-1}\left(\widehat{\mathbf{h}}_{\omega,v}^{[fl',t_{\kappa}']}-\hat{\boldsymbol{\mu}}_x\right)\left(\widehat{\mathbf{h}}_{\omega,v}^{[fl'+\nu,t_{\kappa}'+\tau']}-\hat{\boldsymbol{\mu}}_x\right)^H.\quad(3.28)$$

Take into account that $\boldsymbol{\Sigma}_x^{[\nu,\tau']}$ is a Hermitian positive definite matrix, and its properties should be followed by $\widehat{\boldsymbol{\Sigma}}_x^{[\nu,\tau']}$. Besides, $\widehat{\boldsymbol{\Sigma}}_x^{[\nu,\tau']}$ is a complex random matrix with a Wishart distribution [24] (see also Appendix A.2), hence $\boldsymbol{\Sigma}_x^{[\nu,\tau']}=E\left[\widehat{\boldsymbol{\Sigma}}_x^{[\nu,\tau']}\right]$, which indicates that the complex covariance matrix can be estimated by sample average using all time and frequency windows (W and V), in the same way than in (3.19) for $\widetilde{\mathbf{R}}_{\text{MIMO}}^{[\nu,\tau']}$.

Based on (3.27) and (3.28), it is then tested the MCND (3.26) of the vector $\widehat{\mathbf{h}}_{\omega,v}^{[f_{l'},t_{\kappa'}]}$ obtained from VNA measurements (from equations (2.2), (2.3), and (3.23)). The MCND given in (3.26) can be represented as surfaces of constant variance, σ^2, which correspond to surfaces of equal probability for MCND vectors satisfying (see Appendix A.1 and A.3)

$$\left(\widehat{\mathbf{h}}_{\omega,v}^{[fl',t_{\kappa}']}-\hat{\boldsymbol{\mu}}_x\right)^H\left(\widehat{\boldsymbol{\Sigma}}_x^{[\nu,\tau']}\right)^{-1}\left(\widehat{\mathbf{h}}_{\omega,v}^{[fl',t_{\kappa}']}-\hat{\boldsymbol{\mu}}_x\right)=\sigma^2.\quad(3.29)$$

These constant variance surfaces are NM-dimensional ellipsoids centered at $\hat{\boldsymbol{\mu}}_x$, with exes of symmetry given by the eigenvectors of $\widehat{\boldsymbol{\Sigma}}_x^{[\nu,\tau']}$, and major and minor

axes given by its eigenvalues. Thus, for $(N=2,\ M=1)$ or $(N=1,\ M=2)$ there exist 2-dimensional ellipsoids (ellipses) centered at $\hat{\boldsymbol{\mu}}_x$. It is worth to indicate if it is desired a single 2 or 3D perceptive visual test of (3.26), only the MISO/SIMO configurations $(N=2,\ M=1)$, $(N=1,\ M=2)$, $(N=1,\ M=3)$ or $(N=3,\ M=1)$ can be performed, e.g., a bivariate normal distribution visual test for $(N=2,\ M=1)$ or $(N=1,\ M=2)$ can be represented by ellipses.

For the MCND visual test using the MIMO data, in Figure 3.7 are presented the 2-dimensional ellipsoids, here, surfaces of constant variance for the real part of $\widehat{\mathbf{h}}_{\omega,v}^{[f_{l'},t_{\kappa'}]}$. They are obtained from the eigenvectors and eigenvalues of the estimated $\widehat{\boldsymbol{\Sigma}}_x^{[\nu,\tau']}$ (equation (3.28)), centered at $\hat{\boldsymbol{\mu}}_x$ (equation (3.27)), and applying (3.29) to get the range of σ^2 for the current multivariate MIMO vector data $\widehat{\mathbf{h}}_{\omega,v}^{[f_{l'},t_{\kappa'}]}$. Each sample of σ^2 defines, for each ellipse, the different size of the major and minor axes together with the eigenvalues of $\widehat{\boldsymbol{\Sigma}}_x^{[\nu,\tau']}$. Note that for the visual MND test, it is also plotted the samples of $\mathrm{Re}\left\{\widehat{\mathbf{h}}_{\omega,v}^{[f_{l'},t_{\kappa'}]}\right\}$, where $\mathrm{Re}\{\cdot\}$ indicates real component. The configurations used for Figure 3.7 were: $N=2,\ M=1$, $f_c=12$ GHz, and $B=\{2.5,5,10,100\}$ MHz, in NLOS. These plots, based on different segmentation of data (different window widths in the frequency domain), permit a simple 2D visual test of the MND of $\mathrm{Re}\left\{\widehat{\mathbf{h}}_{\omega,v}^{[f_{l'},t_{\kappa'}]}\right\}$ for each case. As it was expected, the early conclusion is that $B=2.5$ MHz offers the better fit to MND (Figure 3.7.a), and the worst case is obtained for $B=100$ MHz (Figure 3.7.d). This conclusion is reached due to the samples are well distributed inside of the constant variance surfaces for $B=2.5$ MHz. Note that h_{11} and h_{12} are the entries of the MND vector. Similar results were visualized for the imaginary part.

Although there exist a good fit for $B=2.5$ MHz using the 2D visual test presented in Figure 3.7, the data plotted in these graphics do not include the associate probability value, for both the samples and the surfaces. In Figure 3.8, it is then plotted the surfaces of constant variance with the associated probability density values obtained from (3.26). Besides, it is also included the data samples of $\mathrm{Re}\left\{\widehat{\mathbf{h}}_{\omega,v}^{[f_{l'},t_{\kappa'}]}\right\}$ based on (3.26) and (3.29). The 3D visual analysis of these new results indicates that $B=2.5$ MHz is not the bets option to follow a MND in the MIMO data (and then use the data for covariance estimations), and therefore $B=5$ MHz can be the best option, which still follows a non-frequency selective channel for the analysed indoor scenarios.

Finally, if it is desired a reliable test of the frequency segmentation effects on the experimental MCND of MIMO data and for higher matrix dimensions, the multidimensional axes of NM-dimensional ellipsoids make difficult the visual test, and then more efficient techniques should be applied (addressed shortly).

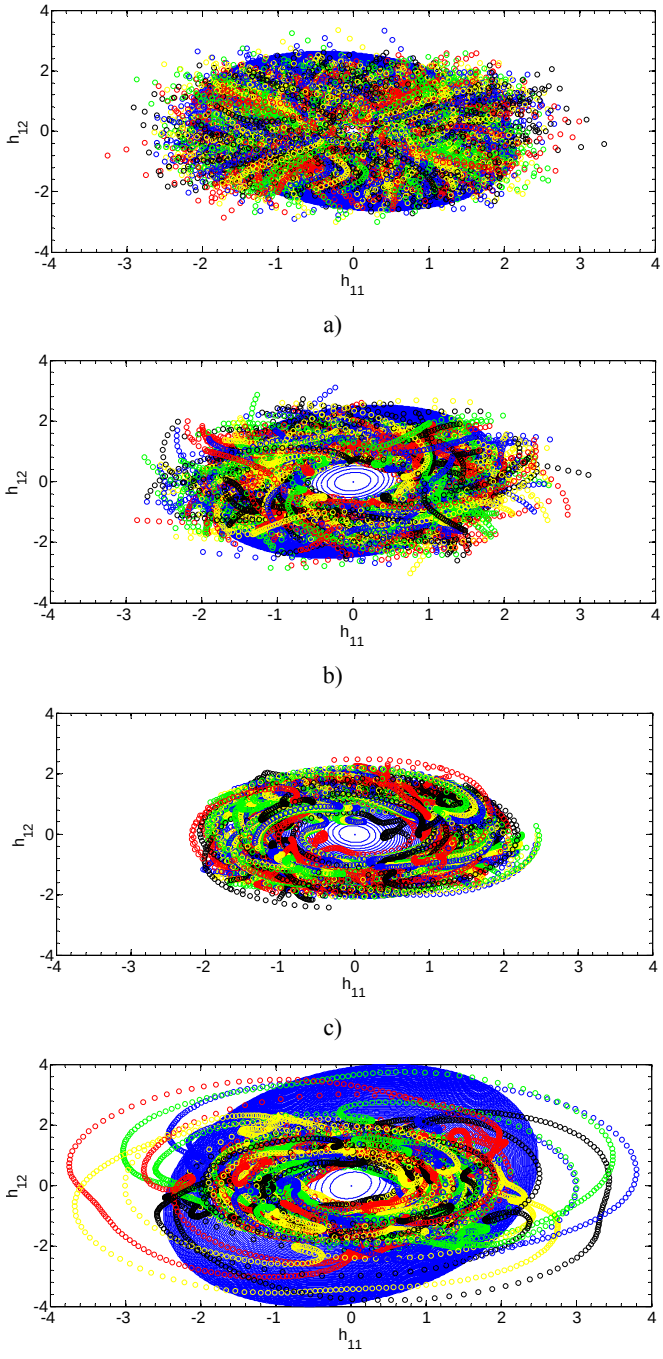

Figure 3.7. Surfaces of constant variance to test the MND of MIMO data (real part of $\widetilde{\mathbf{h}}_{\omega,v}^{[f_i,t_{\kappa'}]}$): theoretical and experimental results for $N=2$, $M=1$, $f_c=12$ GHz in NLOS, with a) $B=2.5$ MHz, b) $B=5$ MHz, c) $B=10$ MHz, and d) $B=100$ MHz.

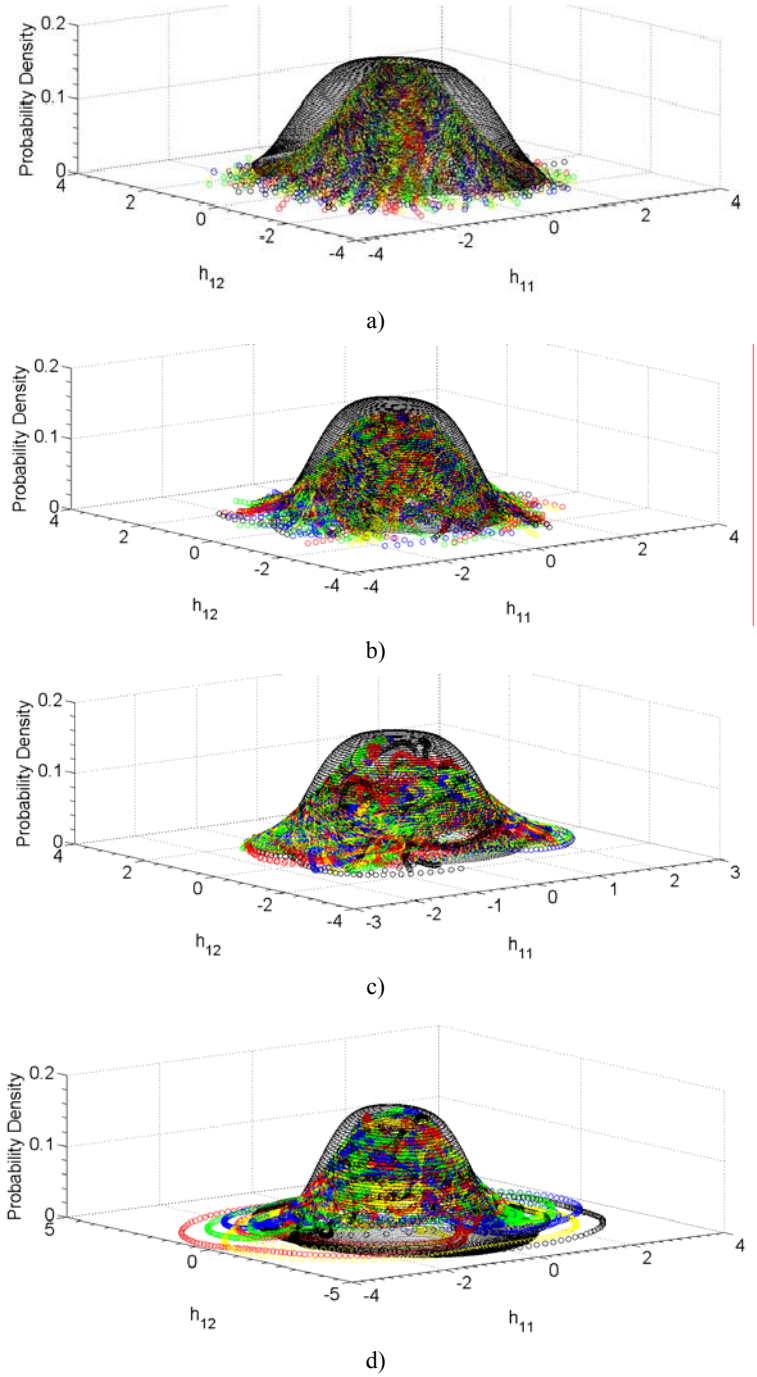

Figure 3.8. PDF of MND to test the normality of MIMO data (real part of $\widehat{\mathbf{h}}_{\omega,v}^{[f_l,t_\kappa]}$): theoretical and experimental results for $N=2,\ M=1$, $f_c=12$ GHz in NLOS, with a) $B=2.5$ MHz, b) $B=5$ MHz, c) $B=10$ MHz, and d) $B=100$ MHz.

On the other hand, for complex normal distribution analysis (in a sounder point of view), it will be also introduced the notation for the matrix variate complex normal distribution (MVCND) [24]. The complex random matrix $\widehat{\mathbf{H}}_{\omega,v}^{[f_{l'},t_{\kappa'}]} \in \mathbb{C}^{N\times M}$ is said to have a MVCND,

$$\widehat{\mathbf{H}}_{\omega,v}^{[f_{l'},t_{\kappa'}]} \sim N_{N,M}\left(\mathbf{M}_x, \boldsymbol{\Sigma}_{x_R}^{[\nu,\tau']} \otimes \boldsymbol{\Sigma}_{x_T}^{[\nu,\tau']}\right) \tag{3.30}$$

with complex mean matrix $\mathbf{M}_x \in \mathbb{C}^{N\times M}$ and complex covariance matrix $\boldsymbol{\Sigma}_{x_R}^{[\nu,\tau']} \otimes \boldsymbol{\Sigma}_{x_T}^{[\nu,\tau']}$, where $\boldsymbol{\Sigma}_{x_R}^{[\nu,\tau']} > 0$ and $\boldsymbol{\Sigma}_{x_T}^{[\nu,\tau']} > 0$, if

$$vec\left(\widehat{\mathbf{H}}_{\omega,v}^{[f_{l'},t_{\kappa'}]}\right) \sim N_{NM}\left(vec\left(\mathbf{M}_x\right), \boldsymbol{\Sigma}_{x_R}^{[\nu,\tau']} \otimes \boldsymbol{\Sigma}_{x_T}^{[\nu,\tau']}\right) \tag{3.31}$$

being $\boldsymbol{\Sigma}_{x_R}^{[\nu,\tau']} \in \mathbb{C}^{N\times N}$ and $\boldsymbol{\Sigma}_{x_T}^{[\nu,\tau']} \in \mathbb{C}^{M\times M}$ the complex covariance matrices at the RX and TX sides, respectively. The primary implication of this definition is the Kronecker separability of the MIMO channel, which is not a proper approximation in some electromagnetic propagation conditions [25]. Under the Kronecker assumption, the PDF of $\widehat{\mathbf{H}}_{\omega,v}^{[f_{l'},t_{\kappa'}]}$ is given by [24]:

$$\begin{aligned} p\left(\widehat{\mathbf{H}}_{\omega,v}^{[f_{l'},t_{\kappa'}]}\right) &= (2\pi)^{-\frac{NM}{2}} \det\left(\boldsymbol{\Sigma}_{x_R}^{[\nu,\tau']}\right)^{-\frac{M}{2}} \det\left(\boldsymbol{\Sigma}_{x_T}^{[\nu,\tau']}\right)^{-\frac{N}{2}} \cdot \\ &\cdot \exp\left\{Tr\left[-\frac{1}{2}\left(\boldsymbol{\Sigma}_{x_R}^{[\nu,\tau']}\right)^{-1}\left(\widehat{\mathbf{H}}_{\omega,v}^{[f_{l'},t_{\kappa'}]} - \mathbf{M}_x\right)\left(\boldsymbol{\Sigma}_{x_T}^{[\nu,\tau']}\right)^{-1}\left(\widehat{\mathbf{H}}_{\omega,v}^{[f_{l'},t_{\kappa'}]} - \mathbf{M}_x\right)^H\right]\right\}, \end{aligned} \tag{3.32}$$

which is derived from (3.25) using

$$\boldsymbol{\Sigma}_{x}^{[\nu,\tau']} = \boldsymbol{\Sigma}_{x_R}^{[\nu,\tau']} \otimes \boldsymbol{\Sigma}_{x_T}^{[\nu,\tau']}, \tag{3.33}$$

$$\det\left(\boldsymbol{\Sigma}_{x_R}^{[\nu,\tau']} \otimes \boldsymbol{\Sigma}_{x_T}^{[\nu,\tau']}\right)^{-\frac{1}{2}} = \det\left(\boldsymbol{\Sigma}_{x_R}^{[\nu,\tau']}\right)^{-\frac{M}{2}} \det\left(\boldsymbol{\Sigma}_{x_T}^{[\nu,\tau']}\right)^{-\frac{N}{2}}, \tag{3.34}$$

and

$$\left(\boldsymbol{\Sigma}_{x_R}^{[\nu,\tau']} \otimes \boldsymbol{\Sigma}_{x_T}^{[\nu,\tau']}\right)^{-1} = \left(\boldsymbol{\Sigma}_{x_R}^{[\nu,\tau']}\right)^{-1} \otimes \left(\boldsymbol{\Sigma}_{x_T}^{[\nu,\tau']}\right)^{-1}. \tag{3.35}$$

If the Kronecker separability is assumed, the $\boldsymbol{\Sigma}_{x}^{[\nu,\tau']}$ eigenvalues, denoted by $\left\{\vartheta_q\right\}$, with $q = \{1,2,\cdots,NM\}$ and $\vartheta_1 > \vartheta_2 \cdots > \vartheta_{NM}$, are given by the product between the eigenvalues of $\boldsymbol{\Sigma}_{x_R}^{[\nu,\tau']}$, $\left\{\vartheta_i^{x_R}\right\}$, and the eigenvalues of $\boldsymbol{\Sigma}_{x_T}^{[\nu,\tau']}$, $\left\{\vartheta_j^{x_T}\right\}$, hence

$$\vartheta_q = \vartheta_i^{x_R} \vartheta_j^{x_T} \tag{3.36}$$

where $j = \{1,2,\cdots,N\}$ and $j = \{1,2,\cdots,M\}$.

As it was earlier indicated in (2.9) and (3.19), if the covariance matrix estimation is based on the Pearson's product moment correlation method [6], the complex correlation matrix is the same as the complex covariance matrix calculated from standardised random variables, this means that (3.15) is then given by $\widehat{\overline{H}}_{ij}^{\omega,v}[f_{l'},t_{\kappa'}] = \widehat{H}_{ij}^{\omega,v}[f_{l'},t_{\kappa'}] / \sqrt{\mathrm{var}(\widehat{H}_{ij}^{\omega,v}[f_{l'},t_{\kappa'}])}$, and then used in (3.19) by mean of (3.16). Hence, the new estimated complex covariance matrix, $\widehat{\mathbf{\Sigma}}_x^{[\nu,\tau']}$ from (3.28), denoted from now on by $\widehat{\overline{\mathbf{\Sigma}}}_x^{[\nu,\tau']}$, is exactly the FSC MIMO matrix, $\widetilde{\mathbf{R}}_{\mathrm{MIMO}}^{[\nu,\tau']}$ from (3.19) using all W and V windows, which is a Hermitian positive 'semidefinite' matrix. This implies that $\widehat{\mathbf{H}}_{\omega,v}^{[f_{l'},t_{\kappa'}]}$, denoted from now on by $\widehat{\overline{\mathbf{H}}}_{\omega,v}^{[f_{l'},t_{\kappa'}]}$, has a singular MVCND [24], and both the PDF of $\widehat{\overline{\mathbf{h}}}_{\omega,v}^{[f_{l'},t_{\kappa'}]}$, from (3.25), and the PDF of $\widehat{\overline{\mathbf{H}}}_{\omega,v}^{[f_{l'},t_{\kappa'}]}$, from (3.32), do not exist, because $\widehat{\overline{\mathbf{\Sigma}}}_x^{[\nu,\tau']} \geq 0$, being impossible to compute $\left(\overline{\mathbf{\Sigma}}_x^{[\nu,\tau']}\right)^{-1}$. Based on the CP proposed in this Chapter, this problem is overcome since $\widehat{\mathbf{R}}_{\mathrm{MIMO}}^{[\nu,\tau']} > 0$, which is the closest to $\widehat{\overline{\mathbf{\Sigma}}}_x^{[\nu,\tau']} \geq 0$, being possible to obtain $p\left(\widehat{\overline{\mathbf{H}}}_{\omega,v}^{[f_{l'},t_{\kappa'}]}\right)$ from (3.32).

Consider now the case where no CP is applied. For $\widehat{\overline{\mathbf{H}}}_{\omega,v}^{[f_{l'},t_{\kappa'}]}$, $E\left[\widehat{\overline{\mathbf{H}}}_{\omega,v}^{[f_{l'},t_{\kappa'}]}\right] = \overline{\mathbf{M}}_x \in \mathbb{C}^{N\times M}$, and $\mathrm{cov}\left(\widehat{\overline{\mathbf{H}}}_{\omega,v}^{[f_{l'},t_{\kappa'}]}\right) = \overline{\mathbf{\Sigma}}_{x_R}^{[\nu,\tau']} \otimes \overline{\mathbf{\Sigma}}_{x_T}^{[\nu,\tau']}$, where $\overline{\mathbf{\Sigma}}_{x_R}^{[\nu,\tau']} \geq 0$ and $\overline{\mathbf{\Sigma}}_{x_T}^{[\nu,\tau']} \geq 0$ with $\mathrm{rank}\left(\overline{\mathbf{\Sigma}}_{x_R}^{[\nu,\tau']}\right) = N_r < N$ and $\mathrm{rank}\left(\overline{\mathbf{\Sigma}}_{x_T}^{[\nu,\tau']}\right) = M_t < M$ ($\mathrm{rank}(\cdot)$ denotes rank). Under these conditions, $\widehat{\overline{\mathbf{H}}}_{\omega,v}^{[f_{l'},t_{\kappa'}]}$ has a singular MVCND [24], denoted by

$$\widehat{\overline{\mathbf{H}}}_{\omega,v}^{[f_{l'},t_{\kappa'}]} \sim N_{N,M}\left(\overline{\mathbf{M}}_x, \overline{\mathbf{\Sigma}}_{x_R}^{[\nu,\tau']} \otimes \overline{\mathbf{\Sigma}}_{x_T}^{[\nu,\tau']} \middle| N_r, M_t\right), \tag{3.37}$$

if there exist matrices $\mathbf{X} \in \mathbb{R}^{N\times N_r}$ and $\mathbf{Y} \in \mathbb{R}^{M_t \times M}$ with ranks N_r and M_t respectively such that

$$\widehat{\overline{\mathbf{H}}}_{\omega,v}^{[f_{l'},t_{\kappa'}]} = \mathbf{X}\mathbf{J}_{\omega,v}^{[f_{l'},t_{\kappa'}]}\mathbf{Y} + \overline{\mathbf{M}}_x \tag{3.38}$$

for some random matrix $\mathbf{J}_{\omega,v}^{[f_{l'},t_{\kappa'}]} \sim N_{N_r,M_t}\left(0,\mathbf{Q}_{x_R}^{[\nu,\tau']}\otimes\mathbf{Q}_{x_T}^{[\nu,\tau']}\right)$, with $\mathbf{Q}_{x_R}^{[\nu,\tau']}\in\mathbb{C}^{N_r\times N_r}>0$ and $\mathbf{Q}_{x_T}^{[\nu,\tau']}\in\mathbb{C}^{M_t\times M_t}>0$. In this conditions

$$\overline{\mathbf{\Sigma}}_{x_R}^{[\nu,\tau']}=\mathbf{X}\mathbf{Q}_{x_R}^{[\nu,\tau']}\mathbf{X}^H, \tag{3.39}$$

$$\overline{\mathbf{\Sigma}}_{x_T}^{[\nu,\tau']}=\mathbf{Y}\mathbf{Q}_{x_T}^{[\nu,\tau']}\mathbf{Y}^H. \tag{3.40}$$

Note that the analysis of this distribution is reduced to find the matrices $\mathbf{X}$, $\mathbf{Y}$, and $\mathbf{Q}_{x_R}^{[\nu,\tau']}$. These matrices can be reached by mean of an eigendecomposition of a positive semidefinite matrix [6].

According to the definition of singular MVCND given in (3.37), if either at the TX or at the RX the rank deficiency happens, i.e., $N_r=N$ with $M_t<M$, or $N_r<N$ with $M_t=M$, then $\widehat{\overline{\mathbf{\Sigma}}}_x^{[\nu,\tau']}\geq 0$ and $\widehat{\overline{\mathbf{H}}}_{\omega,v}^{[f_{l'},t_{\kappa'}]}$ has a singular MVCND. Hence, for rank deficient MIMO channels, the singular MVCND is the most suitable distribution for MIMO data analysis.

On the other hand, going back to the algebraic form given in (3.33), besides of its implicit propagation approximation, it can introduce propagated errors when the estimation of the CCMs are performed independently at both ends of the link, which could increase the probability of $\mathbf{\Sigma}_x^{[\nu,\tau']}\geq 0$ or $\mathbf{\Sigma}_x^{[\nu,\tau']}\leq 0$. This error is avoided if the normality data analysis is carried out checking (3.26) and applying the CP to estimate $\widehat{\mathbf{R}}_{\text{MIMO}}^{[\nu,\tau']}$, as it was presented in Figure 3.7 and Figure 3.8, but with the visual limitations already addressed for higher channel matrix dimensions.

From a signal processing point of view, the MCND test is also useful to perform a reliable power spectral density (PSD) analysis. If a multidimensional process is MCND (a stationary process), the PSD can be then calculated by the Fourier transform of the covariance matrix of the system [17]. For the MIMO case, if the process $\widehat{\mathbf{H}}_{\omega,v}^{[f_{l'},t_{\kappa'}]}$ is MCND, the PSD matrix entries, for a PSD matrix denoted by $\mathbf{S}_{\tau,f_d,\Omega}$, can be obtained by mean of the Fourier transform of the $\mathbf{\Sigma}_{f,t,x}$ entries:

$$S_{ij,\ell s}=\int_{-\infty}^{\infty}\int_{-\infty}^{\infty}\int_{-\infty}^{\infty}\Sigma_{ij,\ell s}^{[\nu,\tau',\varsigma]}e^{j2\pi\nu\tau}e^{-j2\pi\tau' f_d}e^{-j\frac{2\pi}{\lambda_0}\varsigma\Omega}d\nu d\tau' d\varsigma \tag{3.41}$$

where ς is the spatial displacement according to $|\varsigma|=\varsigma_{\max}\ll(M\Delta x_T,N\Delta x_R)$, Δx_T and Δx_R are the distances among antenna elements at the TX and RX arrays, respectively, Ω is the 2D-directional information introduced by the space domain, and λ_0 is the free space wavelength. If the MCND is not fulfilled in the

matrix $\widehat{\mathbf{H}}_{\omega,v}^{[f_{l'},t_{\kappa'}]}$, the estimation of $\mathbf{S}_{\tau,f_d,\Omega}$, based on the estimated $\widehat{\boldsymbol{\Sigma}}_{f,t,x}$, can give wrong spectral information.

Summarizing, if the stationary conditions of the process $\widehat{\mathbf{H}}_{\omega,v}^{[f_{l'},t_{\kappa'}]}$ is not fulfilled, it is necessary to consider a channel with slowly variations in time (in a channel sounder point of view), which is reached applying a correct windowed average to calculate the mean and the covariance [19]. Therefore, the assumption of multivariate normality is a key point for MIMO data analysis, but not so much works have been focused in this issue. The understanding of the effects of the non-normality, its relationship with non-positiveness of experimental FSC MIMO matrices, and the theoretical multivariate and matrix variate distributions discussed in this section deal the way for new researches in MIMO analysis based on experimental data.

3.5.3.1. Multivariate normal distribution tests for MIMO data

The analysis of the constant variance surfaces (equation (3.29)), and the experimental PDF multivariate distribution test (see Figure 3.8), are not enough to determine MCND of MIMO data, being required reliable tests and not only visual limited examination. Recently it has been studied and classified some of the many of procedures to test the multivariate normality of data [20], which have not limitations as the multidimensional axes of the NM-dimensional ellipsoids in (3.29). The work of Mecklin and Mundfrom recommend many tests, including the Mahalanobis distances, multivariate Skeweness and Kurtosis, the Shapiro-Wilk test, and the Henze-Zirkler test [21]. The Shapiro-Wilk and Henze-Zirkler test has been used by Svantesson and Wallace over indoor MIMO measurements [22], being a powerful test against distributions with heavy tails. Svantesson and Wallace found that large MIMO systems show strong evidence of non-normality but each channel coefficient can be close to a complex normal distribution. This effect confirms the close relationship between the non-normality of MIMO data with the non-positiveness of some FSC MIMO matrices in the case of large MIMO channels and then large-scale covariance matrices.

Here, to test the normality of data for different frequency window widths, the Skeweness and Kurtosis were first calculated to test the UCND of MIMO data, i.e., to test the UCND of the $\widehat{\mathbf{H}}_{\omega}$ entries, $\hat{H}_{ij}^{\kappa,\omega}\left[f_{l'}\right]$. The CDFs of Skeweness and Kurtosis using the data obtained for all frequency bands were calculated for Zones A and B and are presented in Figure 3.9 and Figure 3.10, respectively. It has been included four different window widths, i.e., $B=\{2.5,5,10,100\}$ MHz, where $W=\{80,40,20,2\}$ and $I=\{40,80,160,1600\}$, respectively, taking into account univariate data from configurations $N=M=\{3,4,5,6,7,8\}$. It is worth to indicate that a Skeweness around cero indicates good symmetry of the normal distribution (for real or complex part), and the Kurtosis around 3 confirms the normality of the data (also for real or complex part). The conclusion from Figure 3.9 and Figure 3.10 is that the experimental data has a close UCND (in both

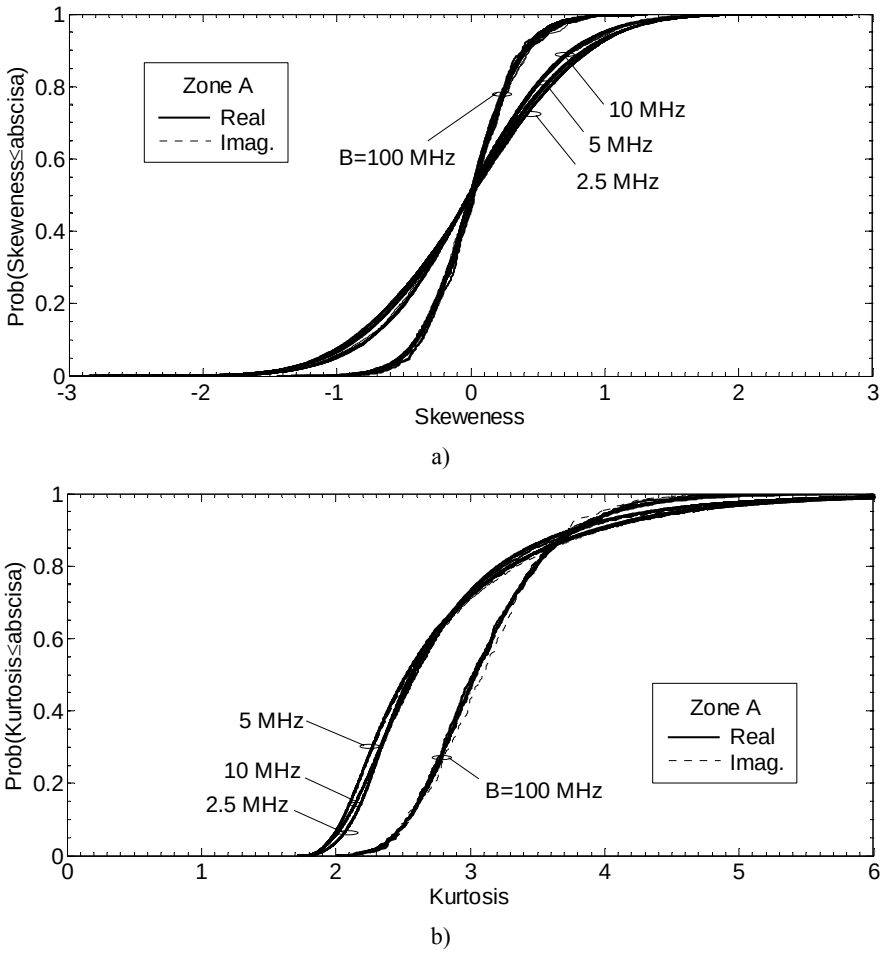

Figure 3.9. Skeweness and Kurtosis for UCND test of $\hat{H}_{ij}^{\kappa,\omega}[f_{l'}]$, with $B=\{2.5,5,10,100\}$ MHz, where $W=\{80,40,20,2\}$ and $I=\{40,80,160,1600\}$, respectively, using entries from configurations $N=M=\{3,4,5,6,7,8\}$: a) CDF of the Skeweness for the $\widehat{\mathbf{H}}_{\omega}$ entries in Zone A, and b) CDF of the Kurtosis for the $\widehat{\mathbf{H}}_{\omega}$ entries in Zone A.

Zones), and there exist a closer UCND in data if the frequency window width is higher. Note that the real and imaginary parts of $\hat{H}_{ij}^{\kappa,\omega}[f_{l'}]$ follow approximately the same distributions, which guarantee the closer UCND. The results presented in Figure 3.9 and Figure 3.10 also indicate that the assumption of univariate normality for experimental data is not always fulfilled, but could be a good approximation for higher bandwidths using VNAs. Despite these results, as it will be addressed in Section 3.5.4, the higher frequency window is not the most suitable option for correlation analysis due to linearity inconsistencies, becoming in a trade-off between normality, linearity and number of samples.

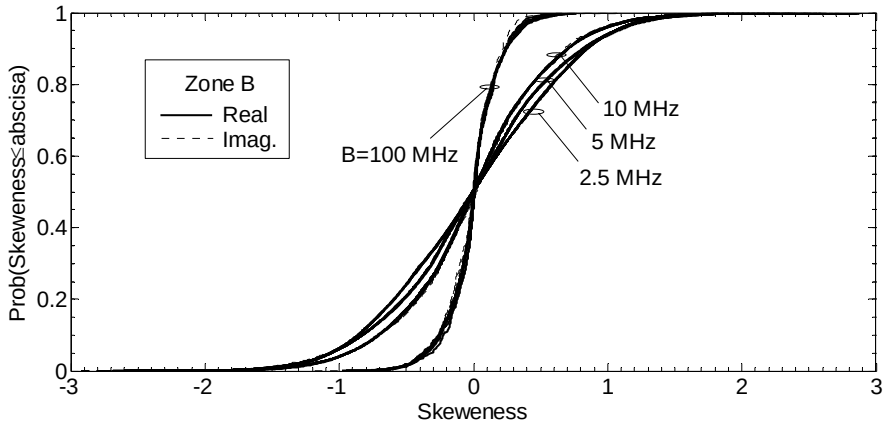

a)

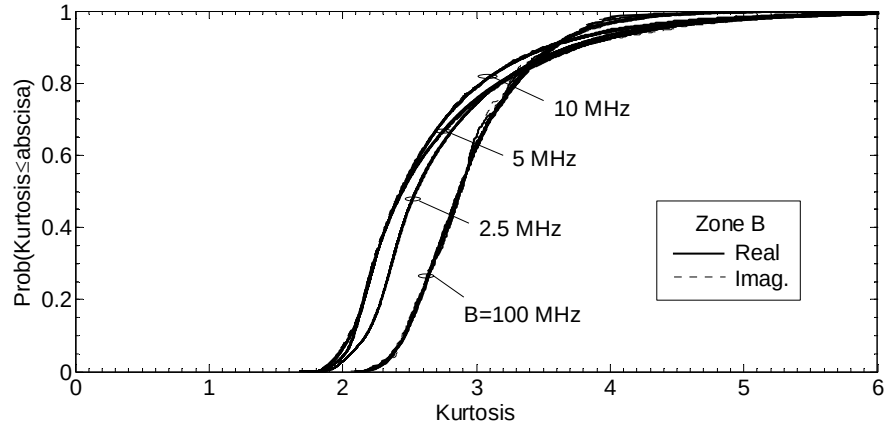

b)

Figure 3.10. Skeweness and Kurtosis for UCND test of $\hat{H}_{ij}^{\kappa,\omega}[f_{l'}]$, with $B=\{2.5,5,10,100\}$ MHz, where $W=\{80,40,20,2\}$ and $I=\{40,80,160,1600\}$, respectively, using entries from configurations $N=M=\{3,4,5,6,7,8\}$: a) CDF of the Skeweness for the $\widehat{\mathbf{H}}_{\omega}$ entries in Zone B, and b) CDF of the Kurtosis for the $\widehat{\mathbf{H}}_{\omega}$ entries in Zone B.

On the other hand, for the synthetic channel $\widetilde{\mathbf{H}}$, the UCND of its entries was also tested. In Figure 3.11 is presented the CDF of the Skeweness and Kurtosis for Zones A and B. It was used 10^5 realisations of the channel (see equation (3.2)) based on the estimation of $\mathbf{R}_{\mathrm{MIMO}}$ (the CP was applied where it was necessary) and taking into account the same configurations from the experimental data used in Figure 3.9 and Figure 3.10. Note that the synthetic channels follow a close UCND for all possibilities analysed here. The results presented in Figure 3.11 also indicate that the assumption of univariate normality for synthetic data is not always fulfilled, but it is an exceptional good approximation for the correlated random generator used in this work (based on the coloring matrix of the system).

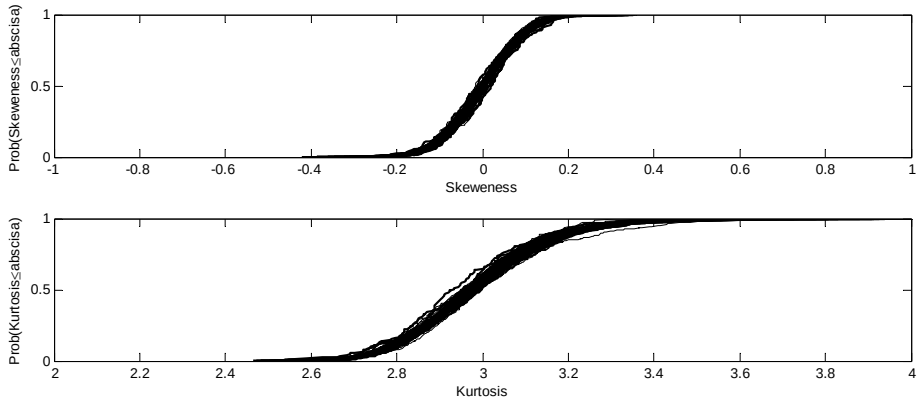

a)

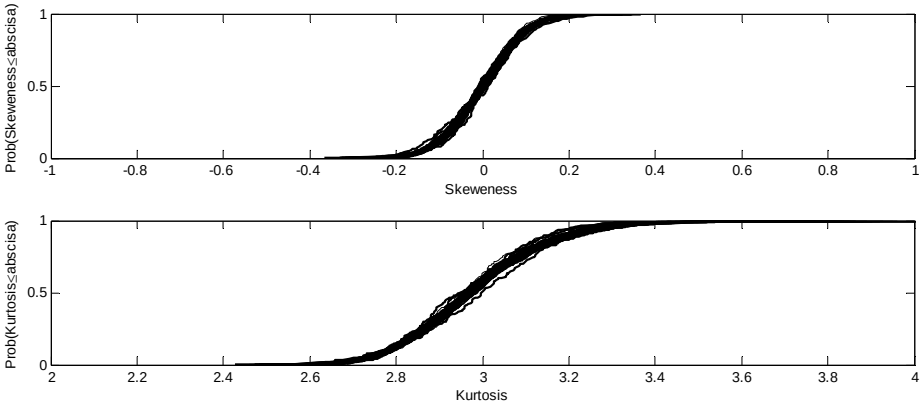

b)

Figure 3.11. Skeweness and Kurtosis for UCND test of the synthetic channel entries, with $B=\{2.5,5,10,100\}$ MHz, where $W=\{80,40,20,2\}$ and $I=\{40,80,160,1600\}$, respectively, and MIMO configurations $N=M=\{3,4,5,6,7,8\}$: a) CDF of the Skeweness and Kurtosis for Zone A, and b) CDF of the Skeweness and Kurtosis for Zone B.

Finally, a multivariate normal test has been performed to verify the MCND of MIMO data. This test permits us to confirm the array dimension dependency on the MCND. Here, the multivariate Skeweness and Kurtosis for MIMO channels

$$b_{1,NM}=\frac{1}{I^2K^2}\sum_{\kappa'=0}^{K-1}\sum_{\zeta'=0}^{K-1}\sum_{l'=0}^{I-1}\sum_{\gamma'=0}^{I-1}\left[\left(\widehat{\mathbf{h}}_{\omega,v}^{[f_{l'},t_{\kappa'}]}-\hat{\boldsymbol{\mu}}_x\right)^T\left(\widehat{\boldsymbol{\Sigma}}_x^{[\nu,\tau']}\right)^{-1}\left(\widehat{\mathbf{h}}_{\omega,v}^{[f_{\gamma'},t_{\zeta'}]}-\hat{\boldsymbol{\mu}}_x\right)\right]^3, \quad (3.42)$$

$$b_{2,NM}=\frac{1}{IK}\sum_{\kappa'=0}^{K-1}\sum_{l'=0}^{I-1}\left[\left(\widehat{\mathbf{h}}_{\omega,v}^{[f_{l'},t_{\kappa'}]}-\hat{\boldsymbol{\mu}}_x\right)^T\left(\widehat{\boldsymbol{\Sigma}}_x^{[\nu,\tau']}\right)^{-1}\left(\widehat{\mathbf{h}}_{\omega,v}^{[f_{l'},t_{\kappa'}]}-\hat{\boldsymbol{\mu}}_x\right)\right]^2, \quad (3.43)$$

respectively, were calculated for $\widehat{\mathbf{H}}_\omega$ (see equation (2.4)), where $\widehat{\boldsymbol{\Sigma}}_x^{[\nu,\tau']}$ and $\hat{\boldsymbol{\mu}}_x$ can be obtained from (3.27) and (3.28). The CP was applied to $\widehat{\boldsymbol{\Sigma}}_x^{[\nu,\tau']}$ when it was

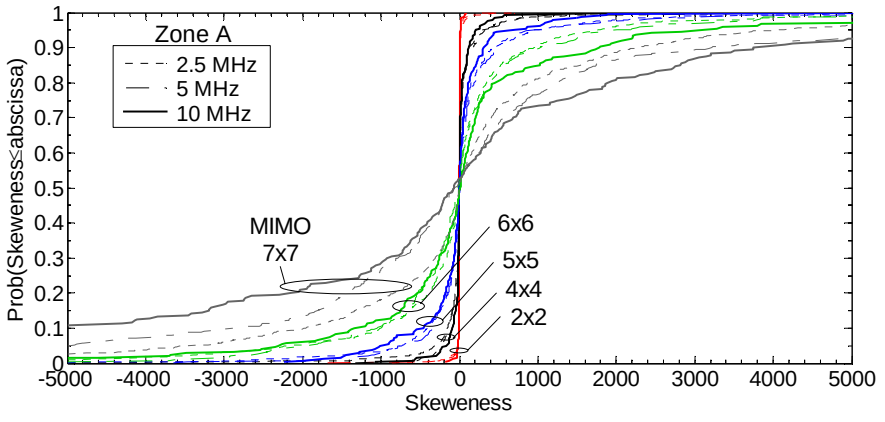

a)

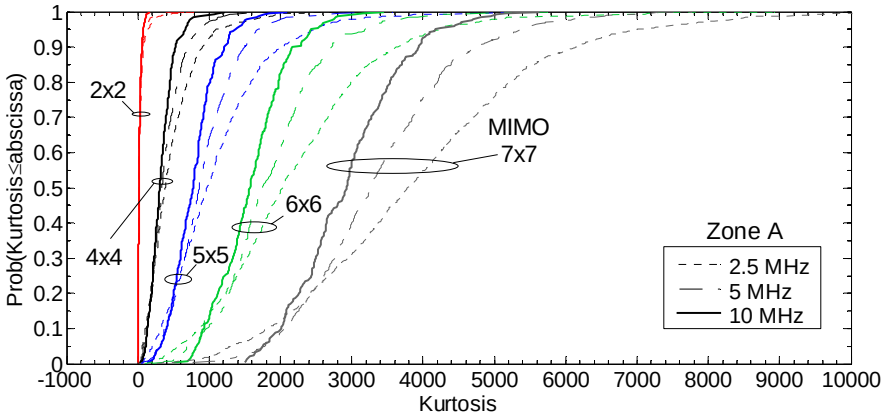

b)

Figure 3.12. Skeweness and Kurtosis for MCND test of $\widehat{\mathbf{H}}_{\omega}$, with $B=\{2.5,5,10\}$ MHz, where $W=\{80,40,20\}$ and $I=\{40,80,160\}$, respectively, and $N=M=\{2,4,5,6,7\}$: a) CDF of the Skeweness, $b_{1,NM}$, for Zone A, and b) CDF of the Kurtosis, $b_{2,NM}$, for Zone A.

necessary to fulfil $\widehat{\boldsymbol{\Sigma}}_x^{[\nu,\tau']}>0$ [3]. Note that equations (3.42) and (3.43) can be applied if and only if $\widehat{\boldsymbol{\Sigma}}_x^{[\nu,\tau']}>0$. On the other hand, if VNA data is used, the temporal variables and their indexes must be avoided in (3.42) and (3.43).

The MCND test has been performed for $B=\{2.5,5,10\}$ MHz, and then $W=\{80,40,20\}$, $I=\{40,80,160\}$, respectively. The MIMO configurations $N=M=\{2,3,\cdots,7\}$ have been considered. Note that $B=100$ MHz was not included, since visual results in Figure 3.7 and Figure 3.8 proved its deviation from multivariate normality. Besides, this window width does not fulfil the linearity conditions required for the MIMO data entries (to be addressed in Section 3.5.4). The CDF of the multivariate Skeweness and Kurtosis for the cases described above are shown in Figure 3.12 and Figure 3.13. Besides, Table 3.1 presents the theoretical and experimental median values for both parameters in the same cases.

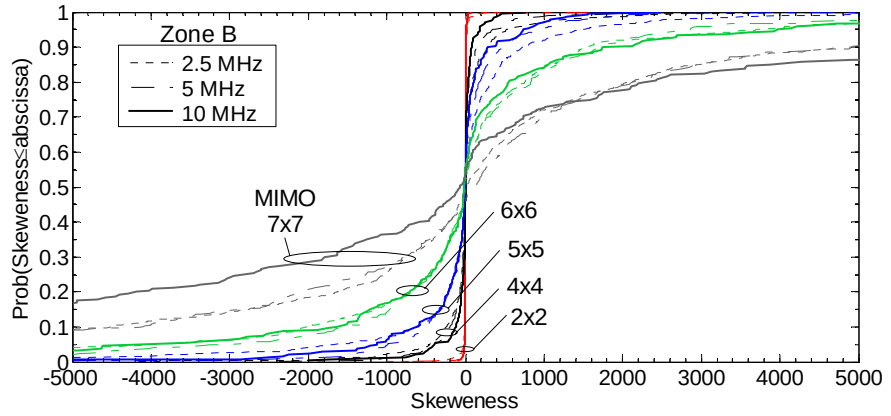

a)

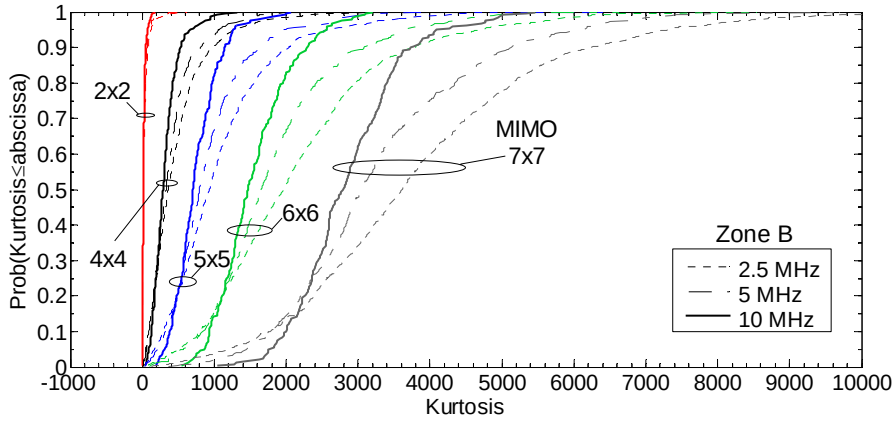

b)

Figure 3.13. Skeweness and Kurtosis for MCND test of $\widehat{\mathbf{H}}_{\omega}$, with $B=\{2.5,5,10\}$ MHz, where $W=\{80,40,20\}$ and $I=\{40,80,160\}$, respectively, and $N=M=\{2,4,5,6,7\}$: a) CDF of the Skeweness, $b_{1,NM}$, for Zone B, and b) CDF of the Kurtosis, $b_{2,NM}$, for Zone B.

Under multivariate normality, it is expected $b_{1,NM}=0$ and $b_{2,NM}=NM(NM+1)$ for the real and imaginary parts of $\widehat{\mathbf{H}}_{\omega}$. Therefore, based on the multivariate Skeweness results in Figure 3.12.a and Figure 3.13.a, it is then proved that, if larger MIMO channel matrices, higher the probability of non-normality in the MIMO data. It is worth to indicate that Figure 3.12 and Figure 3.13 depict CDFs only for the real part, the imaginary part followed similar distributions, in the same way that UCND in Figure 3.9 and Figure 3.10. From Figure 3.12.a and Figure 3.13.a, the MIMO configuration $N=M=2$ follows the closer distribution around cero for any B, even at lower outage values, i.e., <10%. There exist also a good approximation up to $N=M=4$, with closer values to cero up to 20% outage. $N=M=3$ was not included in the figures because readability. From Table 3.1, it is confirmed that $\overline{b}_{1,NM}$ (the median value of $b_{1,NM}$)

is closer to 'cero' only for $B=\{2.5,5\}$ MHz up to $N=M=4$. For higher dimensions, only $B=2.5$ MHz shows $\overline{b}_{1,NM}\approx 0$, but $\overline{b}_{2,NM}$ is not longer closer to $NM(NM+1)$. From Figure 3.12.b and Figure 3.13.b, it is proved that B has a higher perturbation on $b_{2,NM}$ than on $b_{1,NM}$, depicting wider dispersion for larger arrays. Therefore, the MCND is not completely fulfilled for $N=M>4$, since it is increased the test deviation. If departures from $\overline{b}_{1,NM}\approx 0$ and $\overline{b}_{2,NM}\approx NM(NM+1)$, in Table 3.1, are taken into account up to $N=M=4$ for $B=\{2.5,5,10\}$ MHz (Zones A and B), it is then proved that $B=5$ MHz is the most suitable option for MCND channel characterisation based on the current data obtained with a VNA. Note that these results differ from the UCND test depicted in Figure 3.9 and Figure 3.10, where the matrix dimension did not affect the test, being $B=100$ MHz the best option only for SISO channels. According to the MCND test, the parameters $B=5$ MHz, $W=40$, $I=80$, and $N=M=\{2,3,4\}$ offer a reliable experimental MIMO channel analysis. These configurations are used in Chapter 4 for metric comparisons between 2 and 12 GHz

Finally, note that the multivariate normality of MIMO channel matrices and the positiveness of FSC MIMO matrices have strong liaison. If larger channel matrices, higher the probability of non-normality in the MIMO data and higher the

Table 3.1. Median values of the Skeweness, $\overline{b}_{1,NM}$, and Kurtosis, $\overline{b}_{2,NM}$, for MCND test of $\widehat{\mathbf{H}}_{\omega}$, with $B=\{2.5,5,10\}$ MHz, where $W=\{80,40,20\}$ and $I=\{40,80,160\}$, respectively, and $N=M=\{2,3,4,5,6,7\}$ for Zone A and B.

Zone A								
MIMO ***N×M***	**Theoretical**		**B=2.5 MHz**		**B=5 MHz**		**B=10 MHz**	
	Kurtos.	Skewe.	Kurtos.	Skewe.	Kurtos.	Skewe.	Kurtos.	Skewe.
2×2	20	0	15.820	*-0.0099*	16.763	*0.0006*	16.353	*-0.0313*
3×3	90	0	108.53	*0.0207*	104.72	*-0.1515*	96.601	*0.2119*
4×4	272	0	386.35	*-0.1626*	342.29	*-0.1836*	306.49	*0.3708*
5×5	650	0	972.10	*1.2574*	858.46	*0.6715*	774.96	*-5.4930*
6×6	1372	0	2035.8	*0.7920*	1749.2	*-16.765*	1570.5	*11.486*
7×7	2450	0	3784.3	*2.512*	3268.3	*-66.511*	2927.0	*-73.281*
Zone B								
2×2	20	0	17.943	*0.0016*	16.450	*0.0111*	15.983	*0.0012*
3×3	90	0	103.40	*0.0022*	95.196	*-0.0153*	84.746	*0.1395*
4×4	272	0	359.01	*-0.0379*	332.44	*-0.2759*	291.77	*0.2615*
5×5	650	0	935.92	*0.7855*	798.70	*-2.9097*	704.68	*-5.2130*
6×6	1372	0	1963.3	*-4.1867*	1656.5	*-1.7340*	1468.5	*-18.396*
7×7	2450	0	3614.0	*16.224*	3047.6	*115.47*	2793.5	*-65.657*

probability of being non-positive definite for the FSC MIMO matrices (see Figure 3.1, Figure 3.12, and Figure 3.13). This behaviour was observed in the two scenarios studied in this Dissertation.

3.5.4. Linearity of the MIMO data entries

Consider a non-frequency selective MIMO channel fulfilling MCND and linear relationship between the channel entries. In such conditions, from a VNA point of view, the $\widetilde{\mathbf{R}}_{\text{MIMO}}^{env}$ entries, denoted by $\tilde{R}_{q,r}^{env} = \tilde{R}_{ij,\ell s}^{env}$, where env indicate envelope, can be calculated by the Pearson's product moment correlation using the windowed samples $\left|\widehat{H}_{ij}^{\kappa,\omega}\left[f_{l'}\right]\right|$, from (2.2), as follows

$$\tilde{R}_{ij,\ell s}^{env} = \frac{1}{W}\sum_{\omega=0}^{W-1}\tilde{R}_{ij,\ell s}^{env,\omega}, \tag{3.44}$$

$$\tilde{R}_{ij,\ell s}^{env,\omega} = \left\langle \frac{\sum_{l=0}^{I-1}\left[\left|\widehat{H}_{ij}^{\kappa,\omega}\left[f_{l'}\right]\right| - \left\langle\left|\widehat{H}_{ij}^{\kappa,\omega}\left[f_{l'}\right]\right|\right\rangle_f\right]\left[\left|\widehat{H}_{\ell s}^{\kappa,\omega}\left[f_{l'}\right]\right| - \left\langle\left|\widehat{H}_{\ell s}^{\kappa,\omega}\left[f_{l'}\right]\right|\right\rangle_f\right]}{\sqrt{\text{var}\left(\left|\widehat{H}_{ij}^{\kappa,\omega}\left[f_{l'}\right]\right|\right)}\sqrt{\text{var}\left(\left|\widehat{H}_{\ell s}^{\kappa,\omega}\left[f_{l'}\right]\right|\right)}}\right\rangle_{\kappa}, \tag{3.45}$$

$$\text{var}\left(\left|\widehat{H}_{ij/\ell s}^{\kappa,\omega}\left[f_{l'}\right]\right|\right) = \frac{1}{I}\sum_{l=0}^{I-1}\left[\left|\widehat{H}_{ij/\ell s}^{\kappa,\omega}\left[f_{l'}\right]\right| - \left\langle\left|\widehat{H}_{ij/\ell s}^{\kappa,\omega}\left[f_{l'}\right]\right|\right\rangle_f\right]^2, \tag{3.46}$$

$$\left\langle\left|\widehat{H}_{ij/\ell s}^{\kappa,\omega}\left[f_{l'}\right]\right|\right\rangle_f = \frac{1}{I}\sum_{l=0}^{I-1}\left|\widehat{H}_{ij/\ell s}^{\kappa,\omega}\left[f_{l'}\right]\right|. \tag{3.47}$$

Note that (3.45) denote a usual estimator for envelope correlation coefficients [26]. The CDF of the envelope correlation coefficients for Zone A and B with $\Delta x_T = \Delta x_R = 2.5$ cm for all frequency bands is shown in Figure 3.14. It is included four different window widths, i.e., $B = \{2.5, 5, 10, 100\}$ MHz, where $W = \{80, 40, 20, 2\}$ and $I = \{40, 80, 160, 1600\}$, with $N = M = \{3, 4, 5, 6, 7, 8\}$.

A first inspection shows a clear bandwidth dependence in the correlation coefficients, which are reduced if the frequency window width B increases. How it was addressed before in this chapter, these results are usual because the correlation between frequency bin samples reduces with the bandwidth.

On the other hand, MIMO matrix dimension effects are also found if the window width is constant, which is a clear multidimensional effect, since the same spatial reference for all frequency bands was used. For $\Delta x_T = \Delta x_T = 2.5$ the CDF were calculated using simultaneous acquired data. Note that an abrupt change around higher correlations values (around 0.9) in the distributions happened for lower array dimensions, i.e., $M = N = 3$. These variations are a consequence of the lower available samples with such array dimensions, which increase the probability to reach high correlation values.

Comparing distributions for individual B values, the differences are reduced for frequency flat channels, i.e., 2.5 and 5 MHz, which are within the coherence bandwidth for the environments tested in this Dissertation. Hence, narrow window widths show desirable characteristics for MIMO channel analysis. Note that Figure 3.14 presents a single correlation analysis using $\tilde{R}_{ij,\ell s}^{env}$ elements, which not include

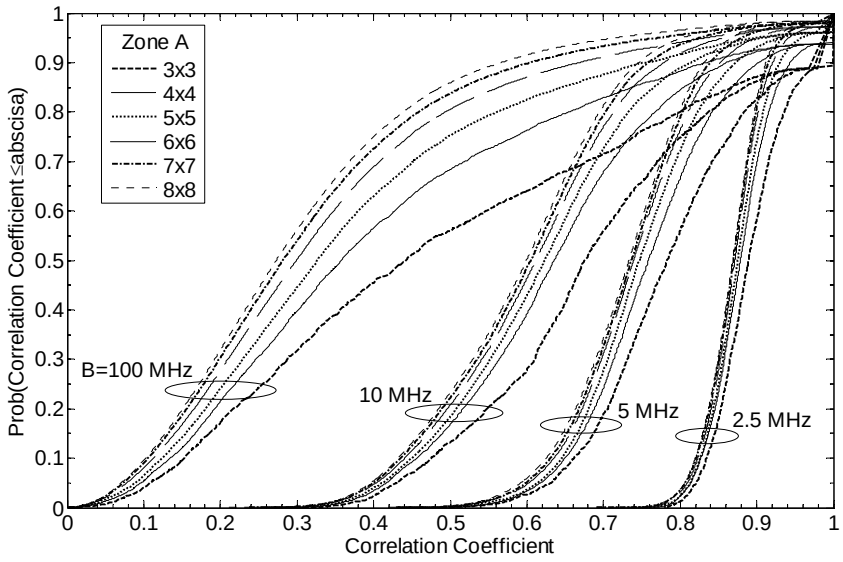

a)

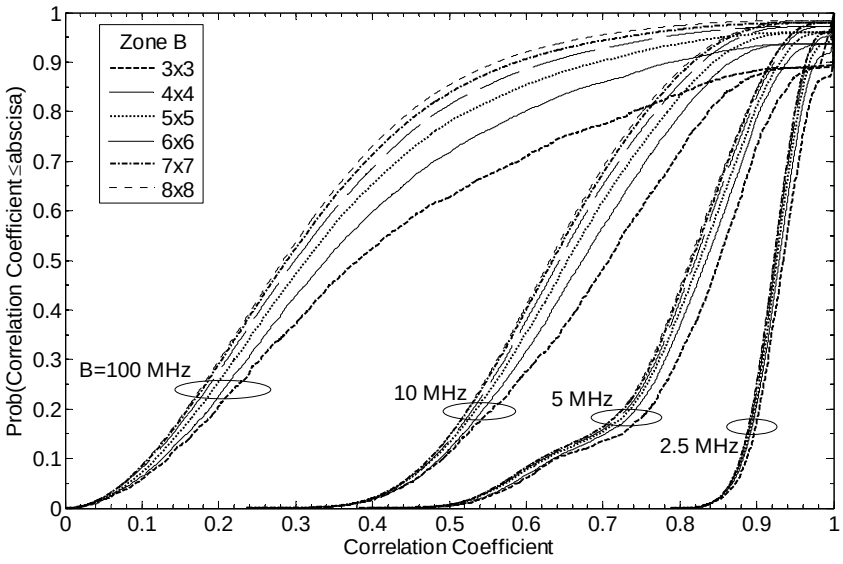

b)

Figure 3.14. CDF of the envelope correlation coefficients $\tilde{R}_{ij,\ell s}^{env}$ for 2.5 cm among antenna elements, with $B = \{2.5, 5, 10, 100\}$ MHz, where $W = \{80, 40, 20, 2\}$ and $I = \{40, 80, 160, 1600\}$, respectively, and MIMO configurations $N = M = \{3, 4, 5, 6, 7, 8\}$: a) Zone A, b) Zone B.

the multivariate behaviour of the channel matrix as it was analysed in Section 3.5.3. Therefore, for the MIMO data used in this Dissertation, B equal to 5 MHz is still the most suitable bandwidth for MIMO channel analysis following MCND in this scenario. Note that 2.5 MHz and 100 MHz were discarded from Figure 3.8, and 10 MHz did not fulfil at all the text from Table 3.1.

On the other hand, if the MCND and the linearity are fulfilled, $\tilde{R}_{ij,\ell s}^{env}$ should be the most approximated coefficient to $R_{ij,\ell s}^{env}$. Otherwise, if it is considered a non-MCND, or a non-linear relationship between $\left|\widehat{H}_{ij}^{\kappa,\omega}[f_{l'}]\right|$ and $\left|\widehat{H}_{\ell s}^{\kappa,\omega}[f_{l'}]\right|$, $\forall \ell s \neq ij$, the Pearson's product moment correlation can gives wrong coefficients. Therefore, once it has been tested the MCND of the MIMO data in Section 3.5.3, the next step is then to test the linear relationship between the entries of $\widehat{\mathbf{H}}_{\omega}$ to be sure about the results presented in Figure 3.14. This analysis is performed with the correlation ratio [27], denoted by $\eta_{ij,\ell s}$. This coefficient is estimated in the same way that the Pearson's product moment correlation, using the frequency bin samples per window, with averages in the time domain, and finally averaging using all frequency windows:

$$\eta_{ij,\ell s}^{\omega} = \left\langle \left(\frac{I\left(\left(\left\langle \left|\widehat{H}_{ij}^{\kappa,\omega}\right|\right\rangle_f - \left\langle \left|\widehat{H}_{ij,\ell s}^{\kappa,\omega}\right|\right\rangle_f \right)^2 + \left(\left\langle \left|\widehat{H}_{\ell s}^{\kappa,\omega}\right|\right\rangle_f - \left\langle \left|\widehat{H}_{ij,\ell s}^{\kappa,\omega}\right|\right\rangle_f \right)^2 \right)}{\sum_f \left(\left|\widehat{H}_{ij}^{\kappa,\omega}\right| - \left\langle \left|\widehat{H}_{ij,\ell s}^{\kappa,\omega}\right|\right\rangle_f \right)^2 + \sum_f \left(\left|\widehat{H}_{\ell s}^{\kappa,\omega}\right| - \left\langle \left|\widehat{H}_{ij,\ell s}^{\kappa,\omega}\right|\right\rangle_f \right)^2} \right)^{1/2} \right\rangle_{\kappa}, \quad (3.48)$$

$$\eta_{ij,\ell s} = \frac{1}{W} \sum_{\omega=0}^{W-1} \eta_{ij,\ell s}^{\omega}, \quad (3.49)$$

where $\left|\widehat{H}_{ij,\ell s}^{\kappa,\omega}\right|$ contents all samples both the $\left|\widehat{H}_{ij}^{\kappa,\omega}[f_{l'}]\right|$ sequence and the $\left|\widehat{H}_{\ell s}^{\kappa,\omega}[f_{l'}]\right|$ sequence. Note that $\left|\widehat{H}_{ij}^{\kappa,\omega}[f_{l'}]\right|$ and $\left|\widehat{H}_{\ell s}^{\kappa,\omega}[f_{l'}]\right|$ have the same number of samples, I, and $\eta_{ij,\ell s}$ is calculated between couples of the $\widehat{\mathbf{H}}_{\omega}$ entries.

If the relationship between $\left|\widehat{H}_{ij}^{\kappa,\omega}[f_{l'}]\right|$ and $\left|\widehat{H}_{\ell s}^{\kappa,\omega}[f_{l'}]\right|$ is linear, then $\eta_{ij,\ell s} = \tilde{R}_{ij,\ell s}^{env}$, otherwise $\tilde{R}_{ij,\ell s}^{env} < \eta_{ij,\ell s} < 1$. In Figure 3.15, it is shown the CDF of the correlation ratio coefficients, $\eta_{ij,\ell s}$, for the same cases presented in Figure 3.14. The results in Figure 3.15 show a frequency window width dependence in $\eta_{ij,\ell s}$, in the same way than in $\tilde{R}_{ij,\ell s}^{env}$ coefficients. The main differences in Figure 3.15 compared with Figure 3.14 is that always is estimated a $\eta_{ij,\ell s}$ higher than 0.8, even with $B = \{10,100\}$ MHz, which follows the restriction $\tilde{R}_{ij,\ell s}^{env} < \eta_{ij,\ell s} < 1$.

These results also indicate that the most reliable coefficients $\tilde{R}_{ij,\ell s}^{env}$ are calculated with $B = \{2.5, 5\}$ MHz. Note as well that the distributions for $B = 100$ MHz follow a different shape, and that $\eta_{ij,\ell s}$ also has MIMO matrix dimension dependence.

Finally, to test the linearity for the measured MIMO channel transfer matrix entries, using $\widehat{\mathbf{H}}_{\omega}$ from (2.3), the mean square error between $\eta_{ij,\ell s}$ and $\tilde{R}_{ij,\ell s}^{env}$ is calculated. The CDF of the linearity error for all obtained MIMO data in Zones A and B, for the same configurations presented in Figure 3.14 and Figure 3.15, is shown in Figure 3.16.

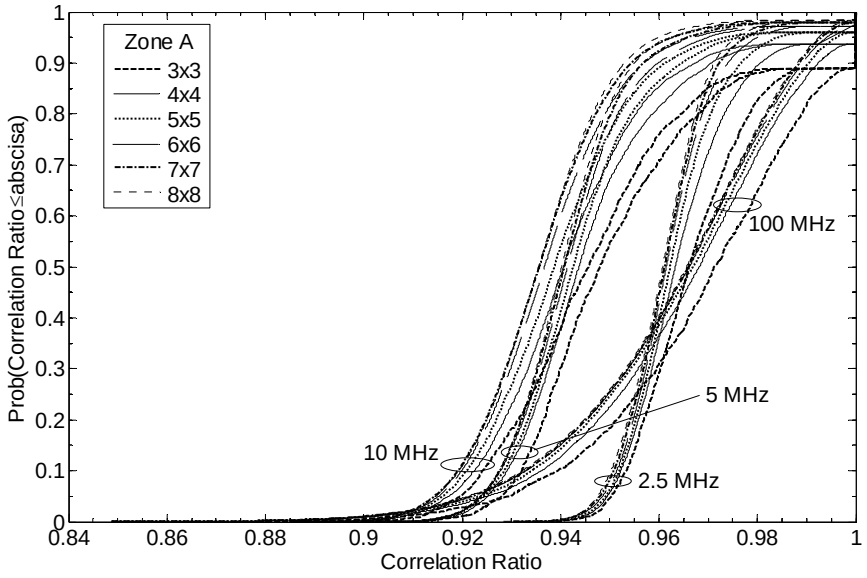

a)

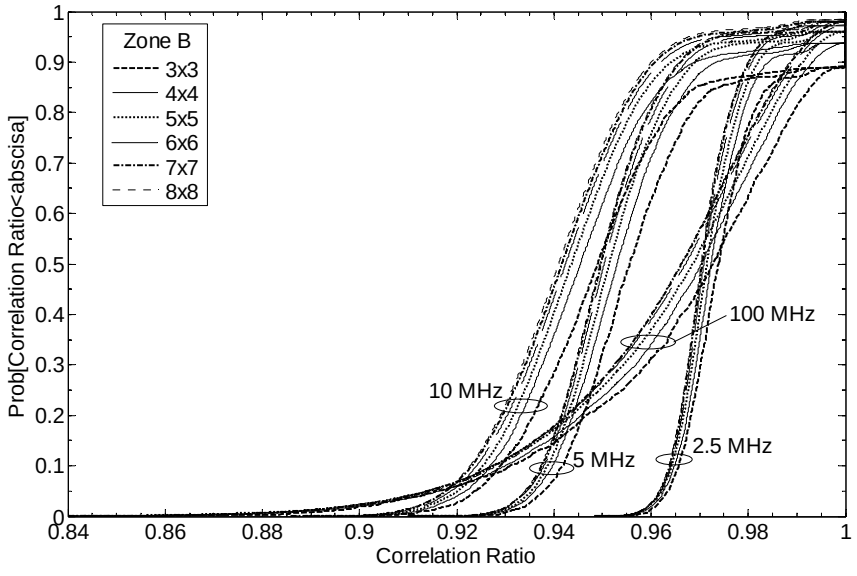

b)

Figure 3.15. CDF of the correlation ratio coefficients $\eta_{ij,\ell s}$ for 2.5 cm among antenna elements, with $B=\{2.5,5,10,100\}$ MHz, where $W=\{80,40,20,2\}$ and $I=\{40,80,160,1600\}$, respectively, and MIMO configurations $N=M=\{3,4,5,6,7,8\}$: a) Zone A, b) Zone B.

Based on these results, it is proved the lost of linearity according to the MIMO matrix dimensions for the measured MIMO data, and also according to the frequency window width used for the segmentation of the spectrum around each central frequency f_c. If larger MIMO channel matrices are included in the analysis, higher is the lost of linearity. Moreover, if wider frequency windows are used for

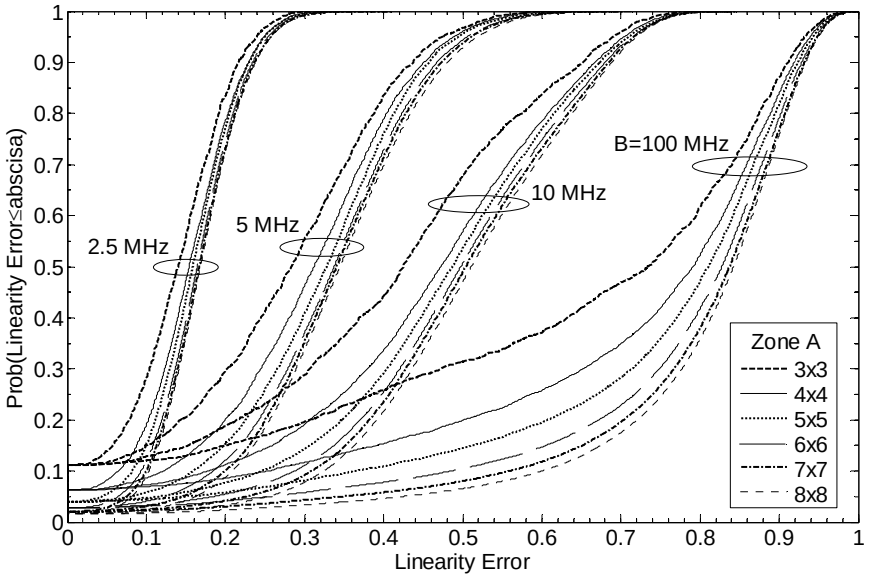

a)

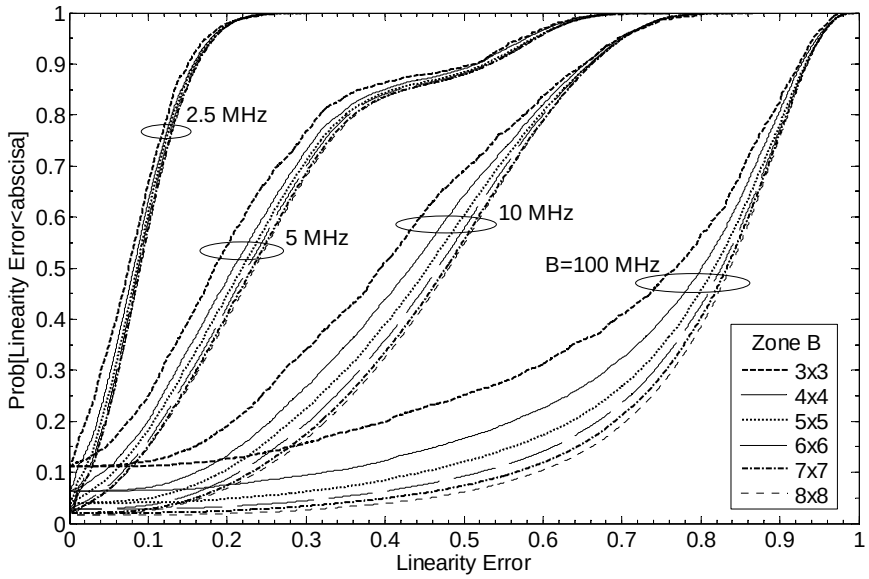

b)

Figure 3.16. CDF of the linearity error for 2.5 cm among antenna elements, with $B = \{2.5, 5, 10, 100\}$ MHz, where $W = \{80, 40, 20, 2\}$ and $I = \{40, 80, 160, 1600\}$, respectively, and MIMO configurations $N = M = \{3, 4, 5, 6, 7, 8\}$: a) Zone A, b) Zone B.

segmentation, higher is the lost of linearity.

From the proposed set of window widths $B = \{2.5, 5, 10, 100\}$ MHz, the conclusion from Figure 3.16 is that 5 MHz is still the most suitable window width for reliable MIMO channel analysis, as 2.5 MHz is not the closest to the MCND for $N = M < 5$ (see Table 3.1). The mean linearity error for $B = 5$ MHz is about 0.25, with lower values for $N = M < 5$ (for zones A and B). Of course, other window width alternatives can be proposed between 2.5 and 5 MHz, but taking into account the samples restrictions, i.e., the 2.5 MHz include lower samples than 5 MHz in each segment. This issue is addressed in Section 3.6.

The results presented above, and in the last section, indicate that both the MCND and the linearity tests should be performed for all type of MIMO data if a reliable channel analysis is desired [28]. Besides, for the application of multivariate normality tests, the positiveness of the experimental covariance matrices is a mandatory characteristic for Skeweness and Kurtosis (also for Mahalanobis distances [20]). In cases where this characteristic is not fulfilled, the CP is a useful tool. It is worth to indicate that there is enough room to continue a research in this issue, where it is observed a strong relationship between non-normality of MIMO data and non-positiveness of FSC MIMO matrices.

Finally, let me indicate that many of the problems treated in this chapter are linked with how the FSC MIMO matrices were estimated from the MIMO data, i.e., using the well know Pearson's product moment correlation. Hence, this Dissertation open a question about the possibility to use new estimation techniques for large-scale MIMO complex correlation/covariance matrices obtained from real world measurement data. This question should be followed taking into account the realistic measurement channel problem, where it is used non-perfect (and non-linear) measurement devices to sense electromagnetic plane waves (homogeneous and inhomogeneous) propagating in frequency-dependent complex environments.

3.6. FSC matrix estimation techniques under low-sampled data sets

A novel possible solution for the estimation of correlation/covariance matrices using low-sampled data sets is the shrinkage covariance estimator (SCE) for large-scale covariance matrices where sparse data are presented [29]. This method guarantee a minimum mean squared error, well-conditioned, and always positive definite FSC MIMO matrix, even for small sample sizes, i.e., when $I < M \times N$. As it is addressed in [29], even with $I \approx M \times N$ the covariance matrix obtained by the Pearson's product moment correlation presents eigenvalues out of the expected values. Note that this possibility was already analysed in this chapter for the array configurations 9×9 with $I = 80$ (see Figure 3.1). The eigenvalues distribution of the experimental FSC MIMO matrices for this configuration showed the highest probability of being non-positive definite.

The SCE for large-scale covariance matrices can be a promising method for experimental MIMO analysis, complementing the CP proposed in this PhD Dissertation. In the same way that the CP [3], all the resulting covariance matrices calculated with SCE are always positive definite, even with $I < M \times N$, which become it in a interesting method for measurement/sounding of MIMO channels. These two novel techniques can reduce vastly the time to perform a MIMO channel measurement campaign. The main implication of this method is the distribution of the FSC MIMO matrices, which follow the Wishart distribution under MCND (see Appendix A.2) for cases with K or $I > M \times N$.

3.7. Conclusions

In this chapter, it has been introduced a reliable synthetic generation procedure for MIMO channels based on real MIMO data obtained from VNA measurements. For the synthetic generation, it has been proposed the well know coloring matrix method. This method is carried out performing the Cholesky factorisation of the estimated FSC MIMO matrix, obtaining then the coloring matrix of the MIMO system, which is finally used for the generation of thousands realisations of the MIMO channel.

Based on experimental results, it has been also proved that a complex FSC MIMO matrix estimated from real measurement data can be indefinite, being the Cholesky factorisation unsuitable. Moreover, it has been demonstrated that this effect is more probable for large-scale MIMO arrays, appearing higher negative eigenvalues.

In order to make the estimated FSC MIMO matrix positive definite and useful to apply Cholesky, a simple and iterative CP based on the AP method has been proposed. Using specific parameters and number of iterations according to the MIMO matrix dimensions, this procedure finds the Hermitian positive definite FSC MIMO matrix with unit diagonal which is the closest in the Frobenius norm to the original FSC MIMO matrix. In this sense, the proposed procedure can reduce the overall time to carry out a measurement campaign, and then the channel analysis, due to the reduced number of samples that it is possible to use to calculate the experimental FSC MIMO matrices.

The performance of the CP has been investigated for different array configurations. It has been checked the eigenvalue distribution of all estimated FSC MIMO matrices, following an adjustment of all matrices detected as non-positive definite. Results suggest a careful selection of the CP parameters (tol and ε) in order to guarantee a 100% success rate and a minimum impact on the CDF of the eigenvalues of the FSC MIMO matrix. Lower values of tol and more iterations are required for large-scale arrays. Besides, optimum values for $\varepsilon_{\min}$ were found for different array dimensions, which can increase the performance of the CP.

Once ensured the positiveness of all FSC MIMO matrices, the Cholesky factorisation has been used to generate as many MIMO channel samples as necessary to assess the ergodic and outage (at 1% and 10%) capacities. Results have proved that the MIMO capacity is not significantly sensitive to the parameter ε once the positiveness is assured. These results guarantee the reliability of the MIMO channel characterisation presented along this PhD Dissertation.

In this chapter, the intrinsic relationship between the non-positiveness of the FSC MIMO matrices with the non multivariate normality of the MIMO data for large-scale channel matrices has been also addressed. The non multivariate normality is increased with the array sizes, even when the normality of the MIMO channel entries is guaranteed (SISO case). This chapter has presented the theory about MCND and MVCND, being as well tested the UCND and MCND of the MIMO data for different array sizes and frequency window widths, being found the most suitable configuration for experimental analysis. The MVCND was not tested due to the current PDF function considers a Kronecker assumption for the covariance matrix, which is not entirely correct for realistic MIMO channels.

As a possible source of inaccuracy for the covariance estimator applied in this Dissertation, it has been also tested the linearity of the MIMO data entries. This characteristic was verified for different array sizes and segmentations. Matrix size and frequency window width dependency were observed in the linearity of the MIMO data. If larger window widths and arrays sizes are used, higher non-linearity is found.

For reliable experimental MIMO channel analysis there exist a trade-off between normality, linearity and number of samples. It was observed in this chapter that the assumption of multivariate normality and linearity is a key point for MIMO data analysis, but not so much works have been focused in this issue. The understanding of the effects of the non-normality and non-linearity, and its relationship with non-positiveness of experimental FSC MIMO matrices, deal the way for new researches in MIMO analysis based on experimental data.

References

[1] Y. I. Abramovich, N. K. Spencer and A. Y. Gorokhov, "Detection-estimation of more uncorrelated Gaussian sources than sensors in nonuniform linear antenna arrays - Part I: Fully augmentable arrays". *IEEE Trans. on Signal Processing*, Vol 49, No. 5, pp. 959-971, 2001.

[2] S. Sorooshyari and D. G. Daut, "On the generation of correlated Rayleigh fading envelopes for accurate simulation of diversity channels," *IEEE Trans. on Commun.*, Vol. 54, No. 8, pp. 1381-1386, 2006.

[3] A. P. García, J. F. Monserrat, and L. Rubio, "Alternating projection method applied to indefinite correlation matrices for generation of synthetic MIMO channels," *AEÜ - International Journal of Electronics and Communications, Elsevier Ltd*., 2008. doi: 10.1016/j.aeue.2008.09.005. In press.

[4] J. P. Boyle and R. L. Dykstra, "A method for finding projections onto the intersection of convex sets in Hilbert spaces," *Lect. Notes in Statist.*, 1986; Vol. 37, pp. 28-47, 1986.

[5] J. P. Kermoal, L. Schumacher, K. I. Pedersen, P. E. Mogensen, and F. Frederiksen, "A stochastic MIMO radio channel model with experimental validation," *IEEE J. on Selected Areas in Commun.*, Vol. 20, No. 6, pp. 1211-1226, August 2002.

[6] C. D Mayer, *Matrix Analysis and Applied Linear Algebra*, Society for Industrial and Applied Mathematics, 2000.

[7] N. C. Beaulieu, "Generation of correlated Rayleigh fading envelopes," *IEEE Commun. Letters*, Vol. 3, No. 6, pp. 172-174, 1999.

[8] R. B. Ertel and J.H. Reed, "Generation of two equal power correlated Rayleigh fading envelopes," *IEEE Commun. Letters*, Vol. 2, No. 10, pp. 276-278, 1998.

[9] B. Natarajan, C.R. Nassar and V. Chandrasekhar, "Generation of correlated Rayleigh fading envelopes for spread spectrum applications," *IEEE Commun. Letters*, Vol. 4, No. 1, pp. 9-11, 2000.

[10] N. C. Beaulieu and M.L. Merani, "Efficient simulation of correlated diversity channels," *IEEE Wireless Commun. and Networking Conference (WCNC)*, p. 207-10, 2000.

[11] Q. T. Zhang, "A decomposition technique for efficient generation of correlated Nakagami fading channels," *IEEE J. Select. Areas Commun.*, Vol. 18, No. 11, pp. 2385-2392, 2000.

[12] K. Zhang, Z. Song and Y.L. Guan, "Simulation of Nakagami fading channels with arbitrary cross-correlation and fading parameters," *IEEE Trans. on Wireless Commun.*, Vol. 3, No. 5, pp. 1463-1468, 2004.

[13] K. E. Baddour, and N.C. Beaulieu, "Accurate simulation of multiple cross-correlated Rician fading channels," *IEEE Trans. on Commun.*, Vol. 52, No. 11 pp. 1980-1987, 2004.

[14] A. P. García and L. Rubio, "Frequency dependent indoor MIMO channel characterisation between 2 and 12 GHz based on full spatial correlation matrices," *Journal of Communications*, *Academy Publisher*, Vo. 3, No. 4, 2008.

[15] J. A. Díaz, A. P. García, and L. Rubio, "Time dispersion characterization for UWB mobile radio channels between 3.1 and 10.6 GHz," IEEE Antennas and Propagation Society International Symposium 2007, Honolulu, Hawaii, USA, June 10-15, 2007.

[16] G. D. Durgin, *Space-Time Wireless Channels*, Pearson Education, Inc., NJ, US, 2003.

[17] J. Parker, D. G. Luenberger and D. L. Wenger, "Estimation of structured covariance matrices," *Proceedings of The IEEE*, Vol. 70, No. 9, pp. 963-974, 1982.

[18] A. Paulraj, R. Nabar and D. Gore, *Introduction to space-time wireless communications*, Cambridge University Press, 2003.

[19] J. M Wallace and M. A Jensen, "Time-varying MIMO channels: measurement, analysis, and modelling," *IEEE Trans. on Antennas and Propagation*, Vol. 54, No. 11, pp. 3265-3273, 2006.

[20] C. J. Mecklin, and D. J. Mundfrom, "An appraisal and bibliography of tests for multivariate normality," *Internat. Statist. Rev.*, Vol. 72, No. 1, pp. 123-138, 2004.

[21] N. Henze, and B. Zirkler, "A class of invariant consistent tests for multivariate normality," *Commun. Statist.-Theor Meth.*, Vol. 19, No. 10, pp. 3595-3618, 1990.

[22] T. Svantesson, J. W. Wallace, "Tests for assessing multivariate normality and the covariance structure of MIMO data," *Proc. of IEEE International Conference on Acoustics, Speech, and Signal Processing*, 6-10 April, 2003.

[23] L. Rubio, J. Reig, and N. Cardona, "Evaluation of Nakagami fading behaviour based on measurements in urban scenarios," *Int. J. Electron. Commun. (AEÜ)*, Vol. 61, No. 2, pp. 135-138, 2007.

[24] A. K. Gupta, and D. K. Nagar, *Matrix variate distributions*, Chapman & Hall/CRC, US, 2000.

[25] W. Kotterman, and R. Thomä, "Testing for Kronecker-separability," COST 2100 TD(07) 017, Lisbon, Portugal, 26-28 February, 2007.

[26] P. Kyritsi, D. C. Cox, R. A. Valenzuela, and P. W. Wolniansky, "Correlation analysis based on MIMO channel measurements in an indoor environment," *IEEE J. on Selected Areas in Commun.*, vol. 21, no. 5, pp. 713-720, June 2003.

[27] J. F. Kenney, and E. S. Keeping, *Mathematics of Statistics*, 2nd ed. Princeton, NJ. Van Nostrand, 1951.

[28] A. P. Garcia, L. Rubio, and R. S. Thomä, "Multivariate normality of measured wideband MIMO channels", COST 2100 (Commission of the European Communities and COST Telecommunications) "Pervasive Mobile & Ambient Wireless Communications", 7nd Management Committee Meeting, Braunschweig, Germany, 16-18 Feb., 2009

[29] J. Schäfer, and K. Strimmer, "A Shrinkage approach to large-scale covariance matrix estimation and implications for functional genomics', *Statistical Applications in Genetics and Molecular Biology*, Vol. 4, No. 1, Article 32, 2005.

CHAPTER 4

EXPERIMENTAL MIMO ANALYSIS

4.1. Introduction

Chapters 2 and 3 have been addressed the MIMO channel measurements and the synthetic MIMO channel generation, respectively. These chapters provided the tools for a reliable MIMO channel experimental analysis, which is presented here. The parameters to be addressed are the experimental MIMO channel capacity, MIMO system eigenvalues, multipath richness, and complex spatial correlation.

It is worth to indicate that the goal of the analysis performed here is a reliable statistical comparison of the MIMO channel characteristics among different central frequencies in different propagation conditions. In this way, it has been considered equal electric separation among antennas elements and a high SNR regimen, as it was addressed in Chapters 2. These analyses are useful for different standards applying MIMO techniques [1]-[4], and also for the future cognitive radio systems (CRS) [5]. The frequency-dependent channel variations could be one of the main challenges in the system design for CRS due to the many band options and strategies considered in the cognition process of software radios [5]-[7]. Take into account that during the system adjustment, part of the RF front-ends remain constant, e.g., the antennas. These characteristics, including MIMO [6],[8], must be considered for future system performance analysis.

On the other hand, in order to do a reliable MIMO channel characterisation using the performed measurements, two independent sets of MIMO data, obtained with the same system configuration (see Section 2.3), and in different indoor scenarios (Section 2.2), will be considered. These characteristics provide comparative results from channels in LOS and NLOS conditions, where different materials (with different constitutive parameters) have been included. As it will be verified in this chapter, the channel characteristics at $f_c = \{2, 2.4, 6, 12\}$ GHz present remarkable tendencies between the two chosen scenarios for MIMO configurations $N = M = \{2, 3, 4\}$. Note that these MIMO configurations fulfil MCND (Section 3.5.3.1), and follow the physical designs given at one wavelength for the ULAs (see Figure 2.5) and the specified array sizes for current standards applying MIMO [1]-[4].

In this chapter, to determine the cumulative distribution function (CDF) of the MIMO channel capacity, eigenvalues, complex spatial correlation and other channel characteristics, and thereby the outage values, thousands of MIMO channel samples were obtained following the procedure proposed in Section 3.2, and applying the CP (Section 3.3) where it was necessary. Moreover, once both the measured and the synthetic MIMO data have been tested in Section 3.5, this chapter addresses: channel characteristics results, a comparative analysis, validation of the software implementation and validation of the applied comparative procedure. A full theoretical frequency dependent analysis for wideband MIMO channels will be addressed in Chapter 5, where a new frequency-dependent MIMO channel model is developed.

4.2. Experimental MIMO channel capacity

The capacity (or mutual information) analysis addressed in this section is related to the capacity found by means of the normalized non-frequency-selective stationary MIMO synthetic channel, $\widetilde{\mathbf{H}} \in \mathbb{C}^{N\times M}$ (from equation (3.2)). Comparative results between $\widehat{\mathbf{H}}_{\omega} \in \mathbb{C}^{N\times M}$ (equation (2.4)) and $\widetilde{\mathbf{H}}$ will be also performed in order to validate the procedure. Take into account that $M \geq N$, $E\left[\left|\tilde{H}_{ij}\right|^2\right] = 1$, and $E\left[\left|\hat{H}_{ij}\right|^2\right] = 1$ are followed.

One hundred thousands samples of $\widetilde{\mathbf{H}}$ has been generated to compare the performance of the MIMO system in different propagation conditions and frequency bands. The analysis is restricted to non-frequency-selective channels by means of the 5 MHz segmentation introduced in Section 2.6. Besides, the channel is assumed unknown at the TX and perfectly known at the RX. Under these conditions, the experimental MIMO channel capacity, denoted by $\tilde{C}$, is given by [9]-[12]

$$\tilde{C} = \log_2\left(\det\left(\mathbf{I}_M + \frac{P_{TX}}{M\sigma_n^2}\widetilde{\mathbf{H}}^H\widetilde{\mathbf{H}}\right)\right), \tag{4.1}$$

where P_{TX} is the total transmit power, σ_n^2 is the noise power at the receiver and $\mathbf{I}_M$ is a $M \times M$ identity matrix. The ergodic capacity, $\tilde{C}_{erg}$, of the MIMO channel can be found by $\tilde{C}_{erg} = E\left[\tilde{C}\right]$, and the outage capacity at $x\%$, $\tilde{C}_{out,x\%}$, by $\mathrm{P}\left[\tilde{C} \leq \tilde{C}_{out,x\%}\right] = x\%$, where $\mathrm{P}[\cdot]$ indicates probability. Note that the capacity analysis presented in this section is restricted to the experimental values found using (4.1). For a theoretical analysis, close-forms of ergodic capacities for different MIMO channels can be found in [12], where ideal i.i.d, spatial correlated, double scattering and keyhole MIMO channels are analysed.

In this section an ideal synthetic uncorrelated MIMO channel, i.e., an i.i.d synthetic channel, will be used as reference for comparisons. The first analysis among the chosen frequency bands is performed by means of the CDF of $\tilde{C}$ obtained for all matrix samples using (4.1).

In Zone A and B, the measured MIMO channel at different frequency bands has shown changes (reductions compared with the i.i.d channel) in $\tilde{C}$ for every $M \times N$ case in LOS and NLOS; see Figure 4.1, Figure 4.2, and Figure 4.3 for 2×2, 3×3, and 4×4 MIMO configurations, respectively. Note that 4×4 is only reached for $f_c = \{6,12\}$ GHz due to the length restrictions at ULAs.

A fast inspection of the depicted curves shows a remarkable difference in the capacity distributions between LOS and NLOS conditions, which is usual due to the different correlation among the MIMO channel entries. For all analysed array configurations and indoor scenarios, the experimental $\tilde{C}$ increases for NLOS cases, being closer to the i.i.d channel in Zone B. This higher $\tilde{C}$ can be explained due to the different constitutive materials (different permittivity and permeability) of the building in Zone B. In this zone, the pillars were built of reinforced concrete (see Figure 2.3), with concrete and brick based walls, which offer a desired rich scattering environment for MIMO communications, increasing the system modes and reducing the correlation among multipath components (this affirmations will be verified in Sections 4.3 and 4.4).

On the other hand, for all $M \times N$ cases and scenarios, $\tilde{C}$ depicts frequency dependency in the CDF. In Zone A, when the frequency increases, the capacity drops. This reduction happens in both propagation conditions, with smaller differences for NLOS. Besides, the reduction between the nearest frequency bands, i.e., 2 and 2.4 GHz, is not noticeable for NLOS cases in 2×2 and 3×3 configurations (see Figure 4.1.a and Figure 4.2.a). In Zone B, the capacity reductions do not follow the same behaviour than in Zone A. For all MIMO configurations in this zone, the lowest capacity is reached at $f_c = 6$ GHz, but the highest capacity is reached at $f_c = 2$ GHz in the same way than in Zone A. This indicates that the constitutive materials for both indoor scenarios affect in a different way the multipath propagation at higher frequencies, i.e., different reflectivity and absorption at higher frequencies. For all MIMO configurations and propagation conditions a higher capacity for $f_c = \{6,12\}$ GHz is reached in Zone B compared with Zone A.

It is worth to indicate that the possible path loss effects over $\tilde{C}$ at different frequencies are overcame based on the matrix normalization performed in (2.4), which is verified in Section 4.5.1. Besides, effects of the antenna gains (see Figure 2.8) are overcame based on the segmentation and normalisation performed in (2.2) and (2.3). The only remaining effect is the antenna pattern variation (see Figure 2.9), which could be overcame using a full complex antenna measurement and using it at the synthetic generation step. Despite these limitations, the comparisons performed for the two different scenarios using the same measurement setup, antennas and ULAs, verify a frequency dependency on the MIMO channel.

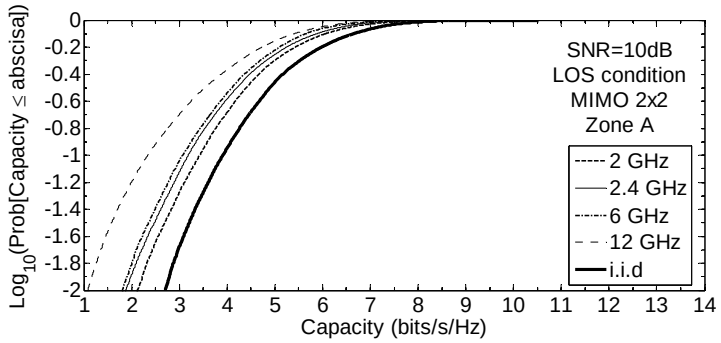

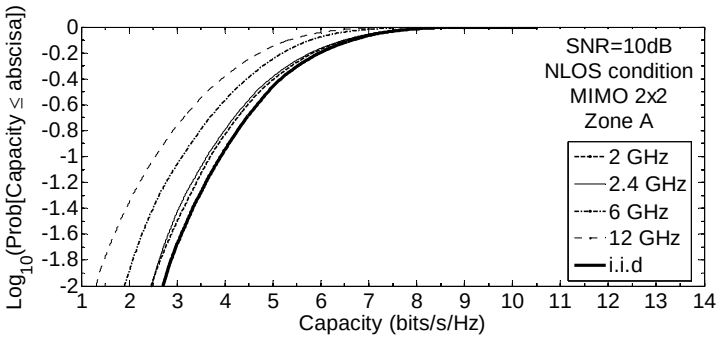

a)

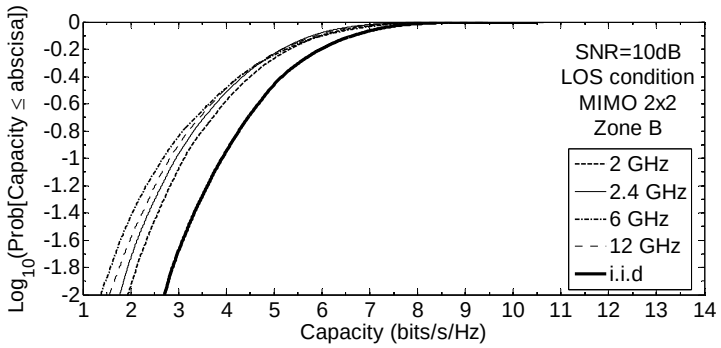

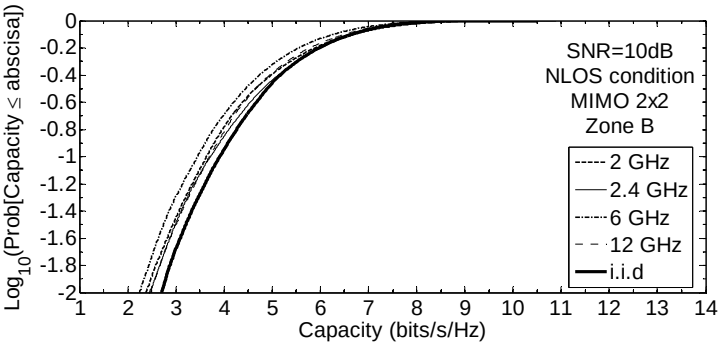

b)

Figure 4.1. CDF of MIMO channel capacity, $\tilde{C}$, for $M = N = 2$, SNR=10dB, with one wavelength of elements separation, $f_c = \{2, 2.4, 6, 12\}$ GHz in: a) LOS and NLOS in Zone A, and, b) LOS and NLOS in Zone B.

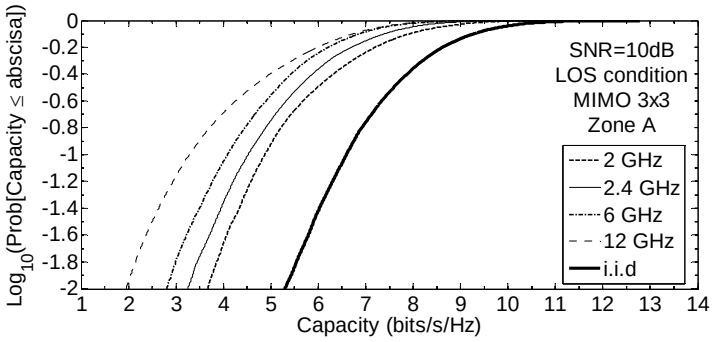

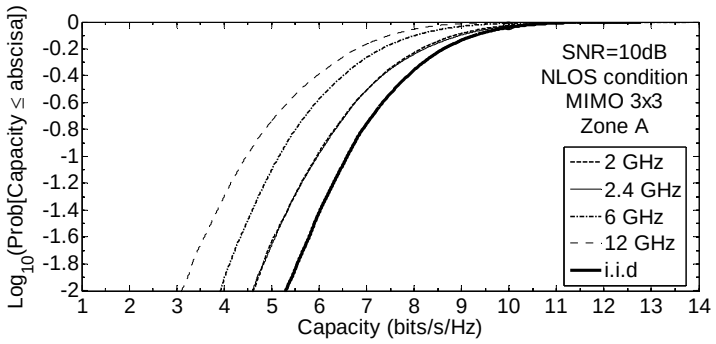

a)

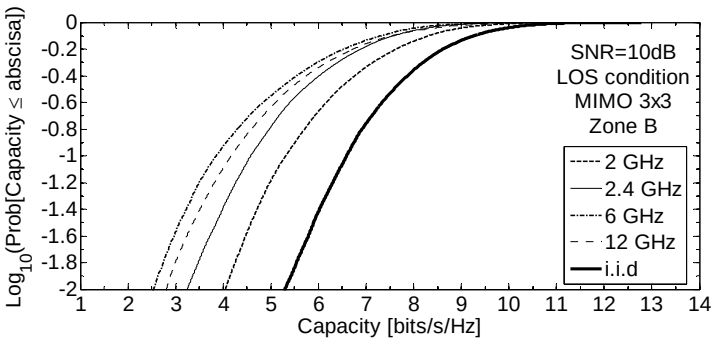

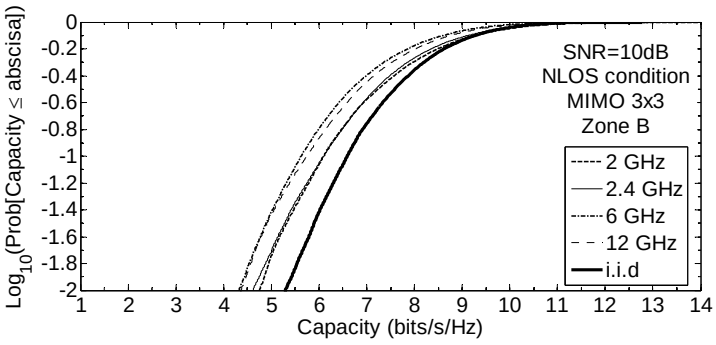

b)

Figure 4.2. CDF of MIMO channel capacity, $\tilde{C}$, for $M = N = 3$, SNR=10dB, with one wavelength of elements separation, $f_c = \{2, 2.4, 6, 12\}$ GHz in: a) LOS and NLOS in Zone A, and, b) LOS and NLOS in Zone B.

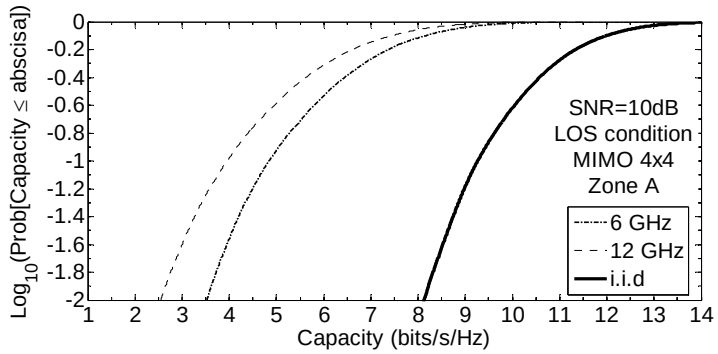

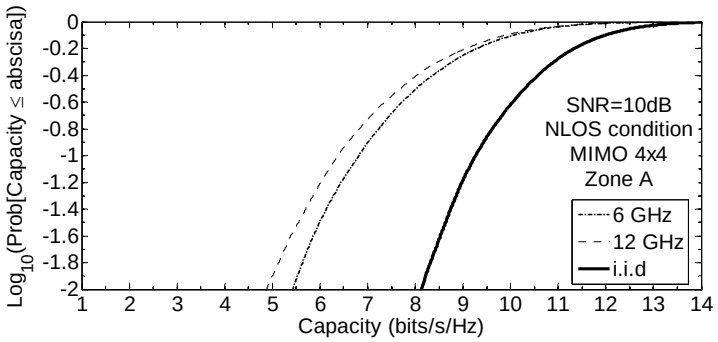

a)

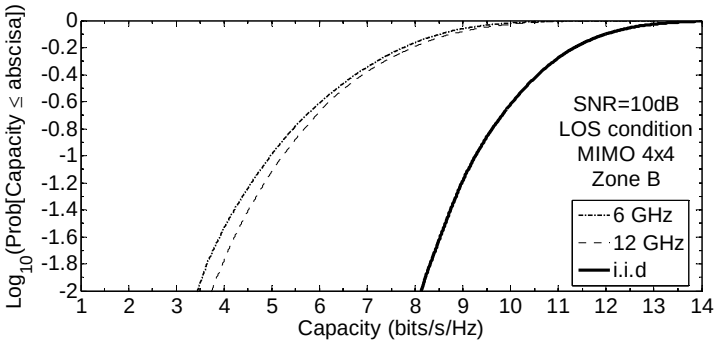

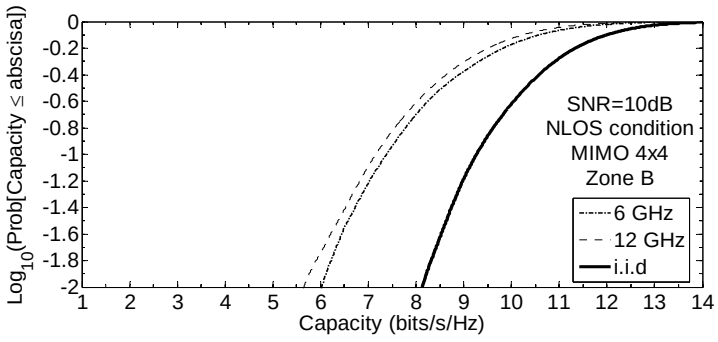

b)

Figure 4.3. CDF of MIMO channel capacity, $\tilde{C}$, for $M = N = 4$, SNR=10dB, with one wavelength of elements separation, $f_c = \{6,12\}$ GHz in: a) LOS and NLOS in Zone A, and, b) LOS and NLOS in Zone B.

If it is compared the capacities at 2×2, 3×3, and 4×4 from Figure 4.1, Figure 4.2, and Figure 4.3, respectively, a non-linear reduction (rising) is found for larger arrays, compared with the expected capacity for i.i.d channels at the same array dimensions. For example, for 4×4 at $f_c=\{6,12\}$ GHz the capacity distributions in Zone A and B depict close distributions to 2×2 ideal cases in LOS, and to 3×3 ideal cases in NLOS. This means, despite of the higher array dimensions, the low multipath richness at those frequencies (as it will be addressed in Section 4.3.2), and the higher spatial correlation (Section 4.4), affect the experimental capacity and then it is never reached the ideal capacity of i.i.d channels. Even lower capacities than the i.i.d channels for larger arrays are found. Similar theoretical results were found in [12] for spatial correlated MIMO channels, where a 4×6 MIMO configuration, with correlation levels around 0.9, shows ergodic capacities to such levels as 2×3 configurations.

To simplify the analysis, in Figure 4.4 the $\tilde{C}_{erg}$ and $\tilde{C}_{out,1\%}$ capacities for $M=N=\{1,2,3,4\}$, within the available frequency bands, for both indoor scenarios and propagation conditions are depicted. The $\tilde{C}_{erg}$ and $\tilde{C}_{out,1\%}$ capacities were always higher in Zone B than in Zone A, as it was addressed above based on the CDFs. Besides, the differences between $\tilde{C}_{erg}$ and $\tilde{C}_{out,1\%}$ are around 3 bits/s/Hz for both scenarios and propagation conditions.

In Zone A there are remarkable differences in the $\tilde{C}_{erg}$ between the ideal case (i.i.d) and measurements in LOS and NLOS for all $M\times N$ cases. In LOS, these differences are between 0.5 and 1.5 bits/s/Hz for 2×2, between 1.5 and 2.5 bits/s/Hz for 3×3, and between 4 and 5 bits/s/Hz for 4×4. In NLOS, the relative capacity reductions are slightly smaller than LOS, and the differences among frequency bands are smaller. Thus, the reductions were between 0.2 and 1.2 bits/s/Hz for 2×2, 0.5 and 1.5 bits/s/Hz for 3×3, and between 1.7 and 2.2 bits/s/Hz for 4×4. For $\tilde{C}_{out,1\%}$ the relatives capacity reductions were slightly higher compared with $\tilde{C}_{erg}$ at the same configurations. Note that for both propagation conditions the highest capacities were found at $f_c=2$ GHz and the smallest at $f_c=12$ GHz, which verifies the frequency dependence in the capacity, even at low probabilities. For Zone B, reductions in $\tilde{C}_{erg}$ and $\tilde{C}_{out,1\%}$ were also depicted when both the frequency and the arrays dimension increased. The main difference was at $f_c=12$ GHz, which has the highest relative reduction only for 4×4 in NLOS. Otherwise, $f_c=6$ GHz has the highest relative reduction.

The major conclusion from Figure 4.4 is that the experimental $\tilde{C}_{erg}$ and $\tilde{C}_{out,1\%}$ show relative reductions with frequency in a non-linear tendency when the number of antenna elements increase [13]. Besides, the capacity reduction among the nearest frequency bands (at low centre frequencies) is not noticeable for NLOS cases, even for different array configurations. It is worth to indicate that similar relative capacity reductions and tendencies were found for $\tilde{C}_{out,10\%}$ capacities [14].

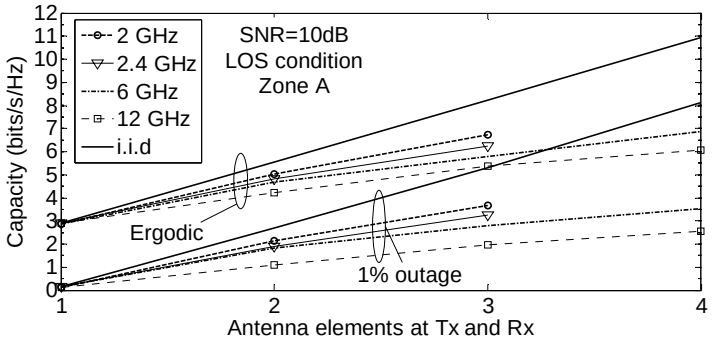

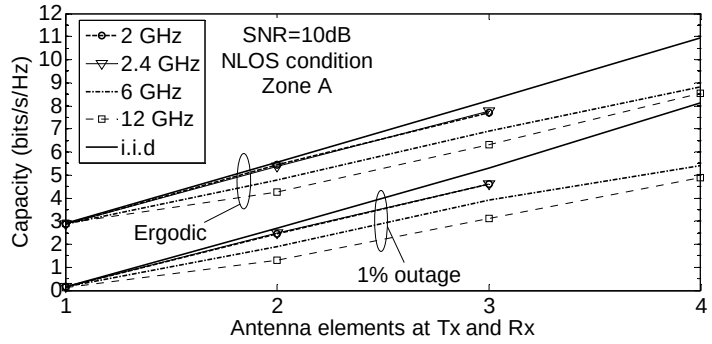

a)

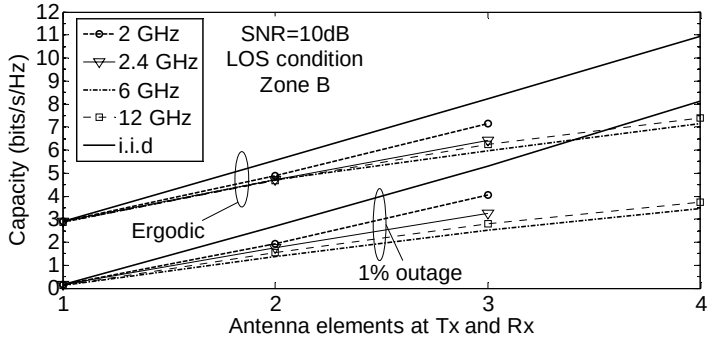

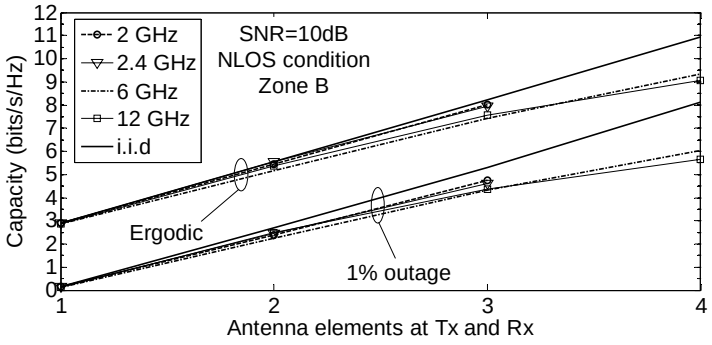

b)

Figure 4.4. Ergodic and 1% outage capacities for $M = N = \{1,2,3,4\}$, SNR=10dB, with one wavelength of elements separation, $f_c = \{2,2.4,6,12\}$ GHz in: a) LOS and NLOS in Zone A, and, b) LOS and NLOS in Zone B.

4.3. MIMO system eigenvalues analysis

From (4.1), the eigenvalue decomposition of the $\widetilde{\mathbf{H}}^H\widetilde{\mathbf{H}} \in \mathbb{C}^{M\times M}$ matrix (a Hermitian positive semi-definite matrix) is given by

$$\widetilde{\mathbf{H}}^H\widetilde{\mathbf{H}} = \widetilde{\mathbf{U}}\widetilde{\mathbf{D}}\widetilde{\mathbf{U}}^H, \tag{4.2}$$

where $\widetilde{\mathbf{D}} = diag\left\{\tilde{\lambda}_1, \tilde{\lambda}_2, \cdots, \tilde{\lambda}_{\mathrm{k}}\right\}$ is the diagonal matrix of eigenvalues $\tilde{\lambda}_i \in \mathbb{R}_+$ (the eigenvalues of $\widetilde{\mathbf{H}}^H\widetilde{\mathbf{H}}$) and $\widetilde{\mathbf{U}} \in \mathbb{C}^{M\times \mathrm{k}} = [\tilde{\mathbf{u}}_1 \tilde{\mathbf{u}}_2 \cdots \tilde{\mathbf{u}}_{\mathrm{k}}]$ the orthogonal matrix of the corresponding eigenvectors $\tilde{\mathbf{u}}_i \in \mathbb{C}^{M\times 1}$. This decomposition is a useful tool for MIMO system performance analysis [15]. While the number of the non-zero eigenvalues, k (rank of $\widetilde{\mathbf{H}}^H\widetilde{\mathbf{H}}$), reflects the spatial multiplexing gain, the eigenvalues $\tilde{\lambda}_i$ represent the power gain of each spatial sub-channel (channel modes). Under a spatial multiplexing (SM) scheme, and with equal power allocation strategy (no water-filling techniques applied [11]), the channel capacity can be also given as the sum of the achieved capacities by each spatial sub-channel. Thereby, the channel capacity, $\tilde{C}$, can be given by [9]-[11]

$$\tilde{C} = \sum_{i=1}^{\mathrm{k}} \log_2\left(1 + \frac{P_{TX}}{M\sigma_n^2}\tilde{\lambda}_i\right). \tag{4.3}$$

Note that if $M \geq N$ then k=N.

From an array signal processing point of view, $\tilde{\lambda}_i$ is the mean energy of the received signal when applying the vector $\tilde{\mathbf{u}}_i$ as spatial filter at the arrays [15], being $\tilde{\mathbf{u}}_i$ the corresponding eigenvector for $\tilde{\lambda}_i$. Hence, the entries of the principal eigenvector, $\tilde{\mathbf{u}}_1$, are the spatial filter weights that maximize the mean energy of the received signal, and $\tilde{\lambda}_1$ (the highest eigenvalue) is the maximum (in average) of the received energy that can be achieved by spatial filtering.

On the other hand, one of the main advantages of the eigenvalue decomposition (4.2) is that its eigenvectors are unit norm and mutually orthogonal, hence

$$\tilde{\mathbf{u}}_i^H\left(\widetilde{\mathbf{H}}^H\widetilde{\mathbf{H}}\right)\tilde{\mathbf{u}}_\ell = 1, \forall i = \ell \tag{4.4}$$

$$\tilde{\mathbf{u}}_i^H\left(\widetilde{\mathbf{H}}^H\widetilde{\mathbf{H}}\right)\tilde{\mathbf{u}}_\ell = 0, \forall i \neq \ell \tag{4.5}$$

which guarantees that the different modes of the MIMO channel are uncorrelated, and therefore, signals in such modes are uncorrelated. This characteristic gives more sense to the well known MIMO channel capacity (4.3).

Besides, these orthogonal modes lead the way for the study of spatial correlations effects, which have influence in the amount of energy carried by each mode of the MIMO channel, i.e., the random values of each $\tilde{\lambda}_i$, being an useful analysis for array processing. In the case of spatial filtering, each mode contributes to the 2D angular power spectrum (APS) due to its directional characteristics [15]. Each MIMO channel mode is stronger in a specific direction, being $\tilde{\lambda}_1$ the highest directive due to the associated eigenvector, $\tilde{\mathbf{u}}_1$, has all degrees of freedom.

In case of diversity techniques, where uncorrelated branches are necessary, $\tilde{\mathbf{u}}_i$ are perfect diversity branches, and $\tilde{\lambda}_i$ denotes the power of these diversity branches. This is possible due to the eigenvalue decomposition of $\widetilde{\mathbf{H}}^H\widetilde{\mathbf{H}}$ permit us to use the k uncorrelated branches to obtain an uncorrelated channel, $\widetilde{\mathbf{H}}_{un}$, as follows

$$\widetilde{\mathbf{H}}_{un} = \widetilde{\mathbf{H}}\widetilde{\mathbf{U}}^H \tag{4.6}$$

Of course, the described useful characteristics on the application of MIMO techniques require a complete or partial knowledge of the channel at the RX or at both the TX and the RX, and usually can not be applied together.

Therefore, once we discussed all of these useful characteristics given by the eigendecomposition of $\widetilde{\mathbf{H}}^H\widetilde{\mathbf{H}}$, this section deals the effect of the frequency band on each $\tilde{\lambda}_i$ as a measured of the MIMO system performance for the applicability of SM, beamforming and diversity techniques. Note that each $\tilde{\lambda}_i \in \mathbb{R}_+$ is a random coefficient, which reflects any of the particular MIMO channel characteristics, including channel degenerations as the space-frequency degeneration at higher frequencies.

In Figure 4.5, Figure 4.6, and Figure 4.7 the CDFs of the eigenvalues $\tilde{\lambda}_i$ are depicted for the same cases presented in Figure 4.1, Figure 4.2, and Figure 4.3, respectively. Note that reference lines for the 50%, 10%, and 1% of outage eigenvalues, and the 0 dB eigenvalue (in the abscissa), are included. Besides, all curves follow $\tilde{\lambda}_1 > \tilde{\lambda}_2 > \cdots \tilde{\lambda}_{\mathrm{k}}$ for the eigenvalue decomposition of $\widetilde{\mathbf{H}}^H\widetilde{\mathbf{H}}$.

From the depicted CDFs, and comparing with the eigenvalues for an i.i.d channel, significant reductions in the smallest eigenvalues at 50% are a general tendency for all MIMO configurations. For lower probabilities (1 and 10 %) these reductions happen for all eigenvalues, but with stronger reductions for the smallest eigenvalues. Other general tendency is a stronger reduction in all eigenvalues for LOS cases, which agrees with the capacity results presented in Section 4.2. In the same way, strongest reductions in Zone A are at 12 GHz, and in Zone B at 6 GHz. In Zone B there exists a stronger reduction at 12 GHz in the smallest eigenvalue for 3×3 in NLOS (see Figure 4.6). For the same scenario, stronger reductions at 12 GHz happen for all smallest eigenvalues in NLOS for 4×4 (Figure 4.7), which follows the capacity results presented in Figure 4.3 for the same NLOS case. The

3×3 case in Figure 4.2 for NLOS does not show the lowest capacity at 12 GHz because $\tilde{\lambda}_3$ has the lowest contribution to the whole capacity (4.3).

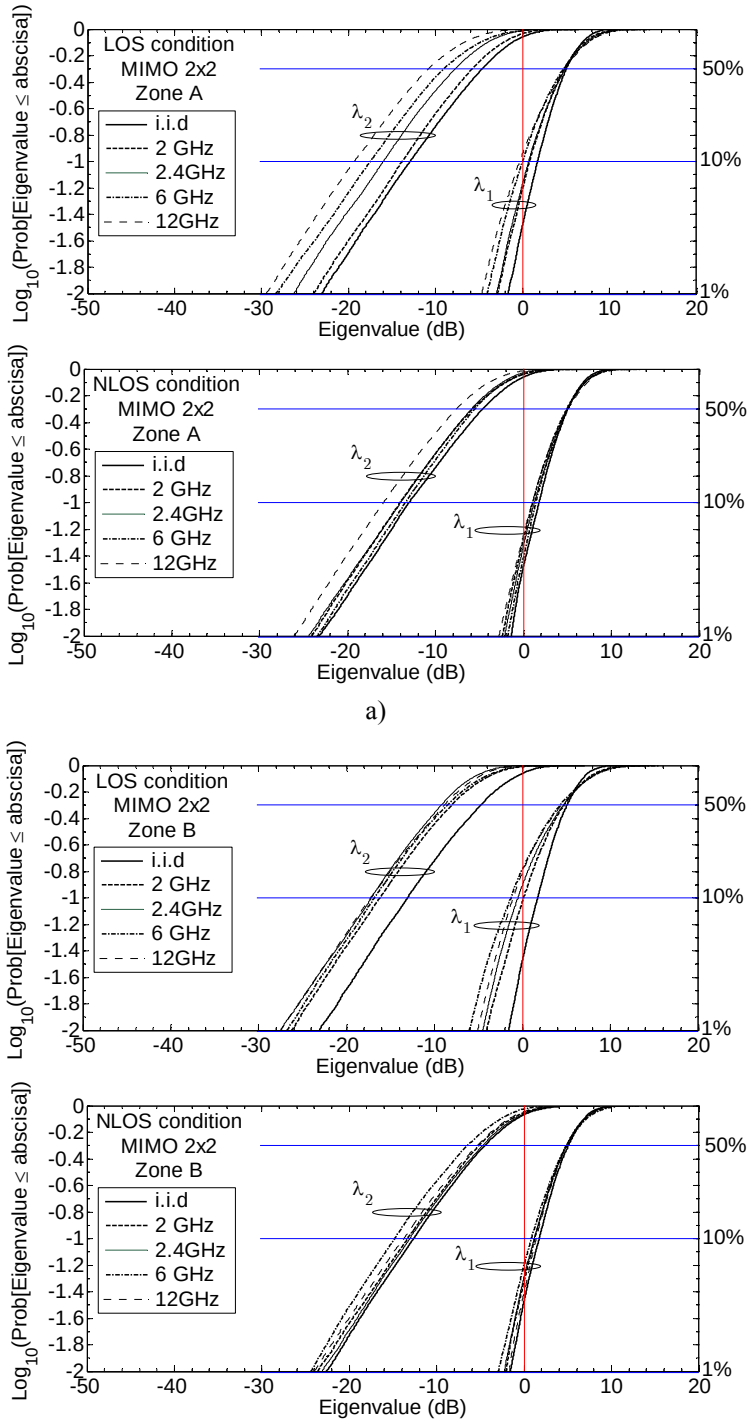

a)

b)

Figure 4.5. CDF of the $\widetilde{\mathbf{H}}^{H}\widetilde{\mathbf{H}}$ matrix eigenvalues for $M = N = 2$, with one wavelength of elements separation, $f_c = \{2, 2.4, 6, 12\}$ GHz in: a) LOS and NLOS in Zone A, and, b) LOS and NLOS in Zone B.

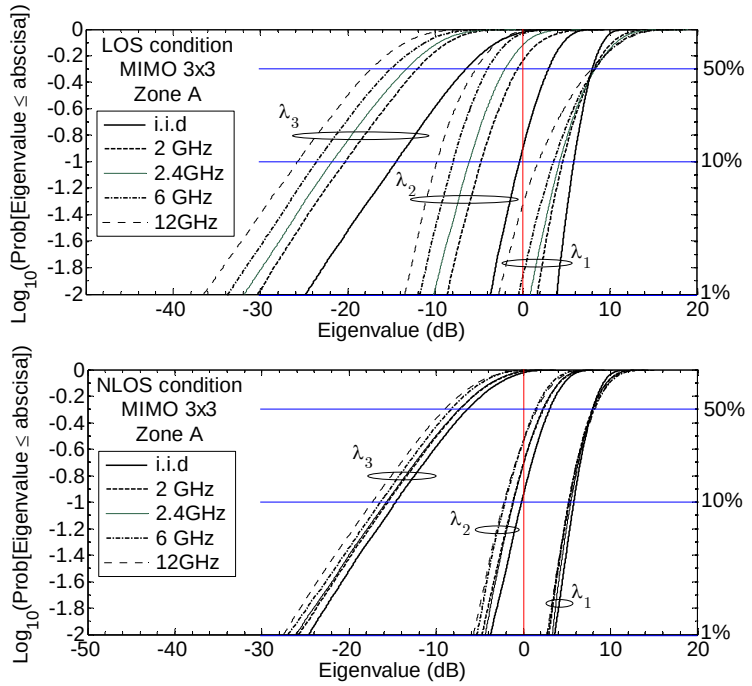

a)

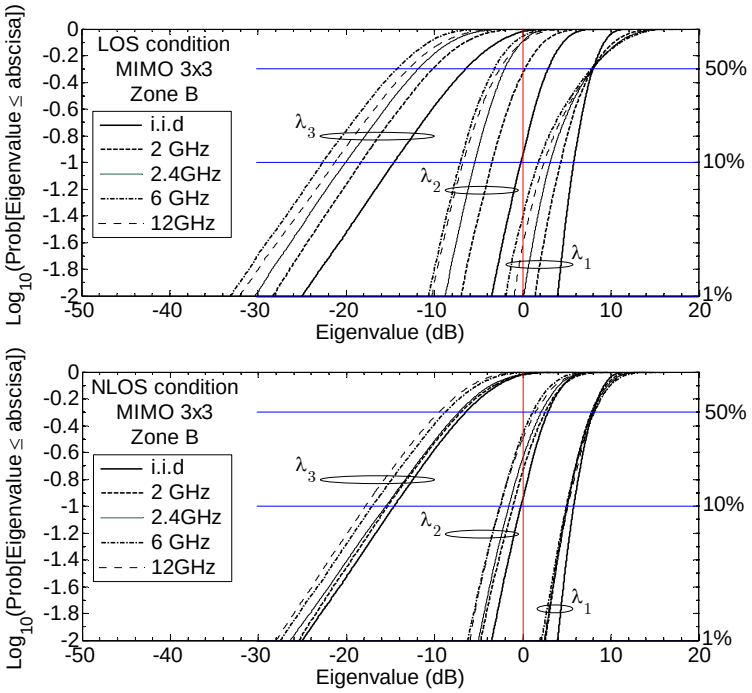

b)

Figure 4.6. CDF of the $\widetilde{\mathbf{H}}^{H}\widetilde{\mathbf{H}}$ matrix eigenvalues for $M = N = 3$, with one wavelength of elements separation, $f_c = \{2, 2.4, 6, 12\}$ GHz in: a) LOS and NLOS in Zone A, and, b) LOS and NLOS in Zone B.

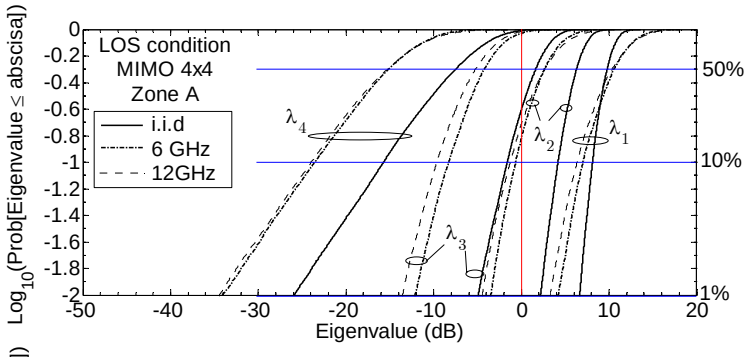

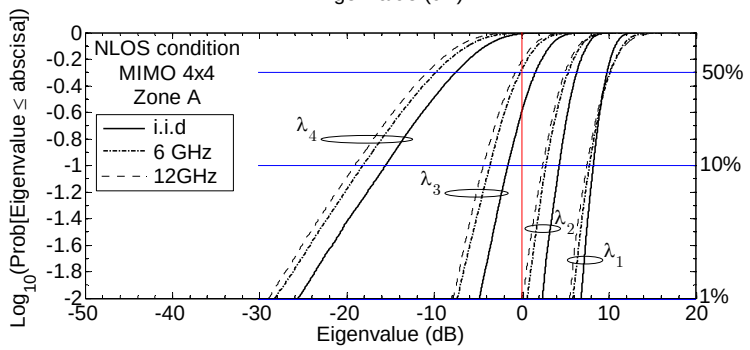

a)

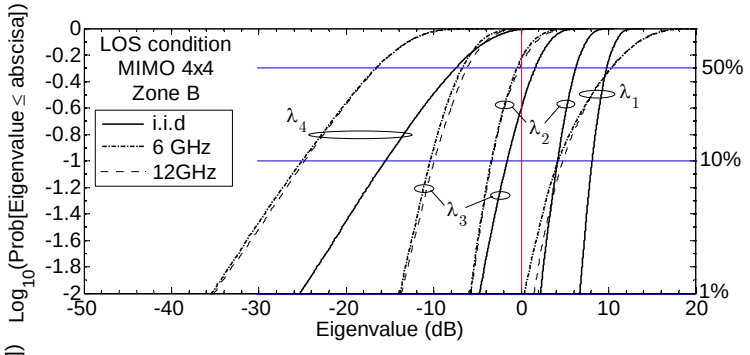

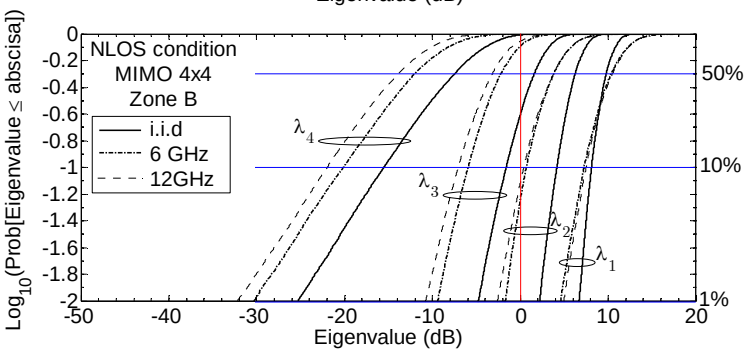

b)

Figure 4.7. CDF of the $\widetilde{\mathbf{H}}^{H}\widetilde{\mathbf{H}}$ matrix eigenvalues for $M = N = 4$, with one wavelength of elements separation, $f_c = \{6,12\}$ GHz in: a) LOS and NLOS in Zone A, and, b) LOS and NLOS in Zone B.

From a MIMO system point of view, the most suitable indoor scenario for the application of SM techniques should follow a rich multipath environment where many spatial sub-channels with high gains are available. This case is followed by Zone B, which depicts higher eigenvalues for all MIMO configurations. This means, in Zone B there are spatial sub-channels with higher power gains, even at higher frequencies. This behaviour agrees with the capacity results addressed in Figure 4.4.

Despite these useful results, note that in the 2×2, 3×3, and 4×4 cases, the smallest eigenvalues, $\tilde{\lambda}_2$, $\tilde{\lambda}_3$, and $\tilde{\lambda}_4$, respectively, have the lowest contribution in (4.3). For 2×2 case, the eigenvalue $\tilde{\lambda}_2$ is around 18 dB lower than $\tilde{\lambda}_1$ at 10% outage, and this difference is increased if the central frequency grows, which is verified in all propagation conditions and scenarios. These reductions are even higher at 1% outage values. It is worth to indicate that all eigenvalues comparisons were performed at 1 wavelength separation among antenna elements.

If the 3×3 and 4×4 cases are also compared, higher differences are found between the lowest and the largest eigenvalue. At 1% outage for 3×3, these differences reach up to 32 and 40 dB for NLOS and LOS cases, respectively. For 4×4 at 1% outage values, these differences reach up to 36 and 44 dB for NLOS and LOS cases, respectively. These results agree with the ergodic and 1% outage capacity results presented in Figure 4.4.

The advantages of larger arrays are the new modes introduced in the MIMO channel, i.e., $\tilde{\lambda}_2$ for 3×3, and $\tilde{\lambda}_2$ and $\tilde{\lambda}_3$ for 4×4, and an always bigger $\tilde{\lambda}_1$. Besides, this useful modes increase their benefit within the MIMO system for higher power gains, which can increase the whole capacity and diversity gains. The drawback is that the ideal channel is never reached (for example at 10% outage), and for 4×4 configurations $\tilde{\lambda}_1$ and $\tilde{\lambda}_2$ go down to the power levels of $\tilde{\lambda}_2$ and $\tilde{\lambda}_3$, respectively (see Figure 4.7, LOS cases), reducing the applicability of SM at higher frequencies in LOS conditions. Perhaps, the only option in such cases is to increase the electrical separation between antenna elements, which at higher frequencies can be easily reached, but with some limitation at the RF front-end owing to the higher losses.

On the other hand, if it is considered the 1 % outage values, the 2×2 cases are not suitable for SM, and for 3×3 and 4×4 the applicability of this technique can be achieved based on the largest eigenvalues and applying water-filling techniques [11] (needs channel knowledge at TX). Note that a possible assigned power to $\tilde{\lambda}_3$ for 3×3, or to $\tilde{\lambda}_4$ for 4×4, could not contribute to increase the capacity of the system, and they also have the worst performance at higher frequencies. As it was addressed in Section 4.2, this behaviour is a result of an increment of the correlation between the spatial sub-channels, and due to a lower scattering at higher frequencies. These issues will be addressed in Sections 4.3.2 and 4.4. Finally, other important result from Figure 4.5, Figure 4.6, and Figure 4.7 is that the distribution depicted by $\tilde{\lambda}_1$ changes with frequency. This eigenvalue

remains mostly constant for all array configurations in LOS and NLOS only around 50% outage (mean value).

4.3.1. Array gain and diversity effects

In Figure 4.8 the mean power gain of the eigenvalues $\tilde{\lambda}_1 > \tilde{\lambda}_2 > \tilde{\lambda}_3$, for $M = N = 3$ in LOS (left) and NLOS (right) conditions at Zone A is shown. Note that only $f_c = \{2, 6, 12\}$ GHz have been included simplifying the view between 2 and 12 GHz. For comparisons, the mean power gain of the eigenvalues for an i.i.d MIMO channel has also plotted. Note that for $M = N = 3$ the diversity order is 9, indicating 9.54 dB of power gain, which is followed by the sum of the eigenvalues of the i.i.d channel [16].

As it was addressed above, the results show that the mean power gain associated to the largest eigenvalue, $\tilde{\lambda}_1$, remains constant while the central frequency increases, which happens in LOS and NLOS conditions [17]. Therefore, the effect of the central frequency on the array gain [16], given by $\tilde{\lambda}_1$, is negligible, being this value almost constant around $10\log_{10} E\left(\tilde{\lambda}_1\right) \approx 7.9\,\mathrm{dB}$ for $M = N = 3$ (1.64 dB lower that the diversity gain). Note that ideal channels for larger arrays are not addressed with the analysed scenarios and ULAs, and then the upper bond array gain $\left(\sqrt{M} + \sqrt{N}\right)^2$ [16], i.e., $10.79\,\mathrm{dB}$, is never reached. Despite, the array gain remains mostly constant and close to this value (the rest of energy is carried by the other modes), even at higher frequencies, and only slightly reductions are found for 2×2 (see Figure 4.5). For 3×3 and 4×4 slightly increases are perceived at 6 and 12 GHz (see Figure 4.6, Figure 4.7 and Figure 4.8 in NLOS). Similar results for other configurations and propagation conditions can be easily obtained from Figure 4.5, Figure 4.6, and Figure 4.7.

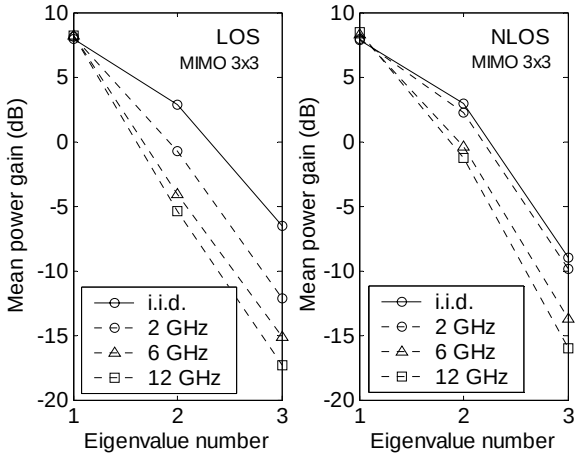

Figure 4.8. Mean power gain of the $\widetilde{\mathbf{H}}^H \widetilde{\mathbf{H}}$ matrix eigenvalues, $\tilde{\lambda}_1 > \tilde{\lambda}_2 > \tilde{\lambda}_3$, for $M = N = 3$, with one wavelength elements separation, $f_c = \{2, 6, 12\}$ GHz in LOS and NLOS in Zone A.

On the other hand, the mean power gain associated to the second and third eigenvalues in Figure 4.8 decreases considerably with the central frequency, with less proportion in NLOS conditions, how it was also described above for other array dimensions. The lower values, compared with the i.i.d. case, indicate an increment of the spatial correlation among the spatial sub-channels, which is related to a reduction of multipath richness. This result indicates higher directionality at higher central frequencies, which also indicates lower spread of the double-directional APS [15]. It is then concluded that higher central frequencies reduce the diversity gain (the sum of the experimental eigenvalues) and depict a clear increment in the double directionality of the channel, i.e., $\tilde{\lambda}_1$ is the most predominant value and then the highest directive associated eigenvector, $\tilde{\mathbf{u}}_1$, governs the channel propagation.

The eigenvalue analysis from the $\widetilde{\mathbf{H}}^H\widetilde{\mathbf{H}}$ matrix also indicates some restrictions for the applicability of SM techniques at higher frequencies due to the low power of some orthogonal modes of the MIMO channel at both propagation conditions and scenarios. On the other hand, for the applicability of beamforming techniques [11],[15] restrictions are not found. If a central frequency around 6 or 12 GHz is considered, the eigenvalue $\tilde{\lambda}_1$ remains constant for all analysed cases at the same levels than 2 and 2.4 GHz. Besides, at 12 GHz slightly improvements are found for $\tilde{\lambda}_1$ (see Figure 4.8 in NLOS), indicating better performance for the applicability of beamforming due to the higher correlation among the spatial sub-channels. If beamforming is applied, it is worth to indicate that the TX must know perfectly the channel to achieve both diversity and the depicted array gains, being the array gain independent of the degree of correlation among antenna elements [18]. The results presented in Figure 4.8 and a reliability test of the estimated covariance matrices can be useful for future analysis of beamforming performance [19].

On the other hand, the noticeable correlation increment characteristics (low power carried by lower eigenvalues) in the curves at Figure 4.8, will be a drawback for diversity systems and the application of ST coding [18],[20], particularly in LOS conditions, and where no channel knowledge is necessary. Note that if ST coding is applied no array gain is achieved due to $\tilde{\mathbf{u}}_1$ is unknown at the TX. In Section 4.4 is addressed the correlation effects by means of a complex spatial correlation analysis of the experimental MIMO channel, which verify the results presented in this section.

Finally, based on the results presented in Figure 4.8, and in the CDFs depicted in Figure 4.5, Figure 4.6, and Figure 4.7, it is clear that water-filling techniques are necessary at higher frequencies for SM. Applying water-filling, improvements of the channel capacity and array gain are achieved. Again, this implies a complete knowledge of the channel at the TX side.

4.3.2. Channel multipath richness

Following the eigenvalue analysis of the MIMO system, Figure 4.9 shows the CDF of the trace of $\widetilde{\mathbf{H}}^{H}\widetilde{\mathbf{H}}$, i.e., $\sum\tilde{\lambda}_i$, as a measure of multipath richness. Again the $M=N=3$ MIMO configuration is chosen at Zone A just for comparisons. This zone was selected because depicted the worst performance in the previous eigenvalue analysis (see Figure 4.5, Figure 4.6, and Figure 4.7).

In Figure 4.9 it is noticeable the differences in terms of the central frequency, where higher differences are found for lower probabilities. Smaller power gain eigenvalues dispersion means higher multipath richness, and this happens in NLOS condition, as it was expected. Note that at 50%, $\sum\tilde{\lambda}_i$ remains close to 9.54 dB of the diversity gain described in Section 4.3.1 for i.i.d channels, but lower values are found at higher frequencies.

The results confirm that at higher central frequencies the multipath richness of the channel is reduced, in this case about 4.5 dB between 2 and 12 GHz in LOS condition at 99% of reliability. Even in NLOS conditions the multipath richness is lower at higher frequencies, but in a less proportion, i.e., 2.5 dB between 2 and 12 GHz. These differences indicate about 50% less multipath richness at 12 GHz in NLOS compared with 2 GHz, and much lower in LOS. For 6 GHz, these differences are 2 and 1 dB for LOS and NLOS conditions, respectively, at 99% of reliability.

From a system performance point of view, the reduction in the multipath richness is a drawback for SM and diversity techniques, and in this specific case (the worst) the performance can be reduced in more than 50% for both propagation conditions at 12 GHz, and in more than 10% at 6 GHz. Note that 2 GHz is used as reference at 99% of reliability.

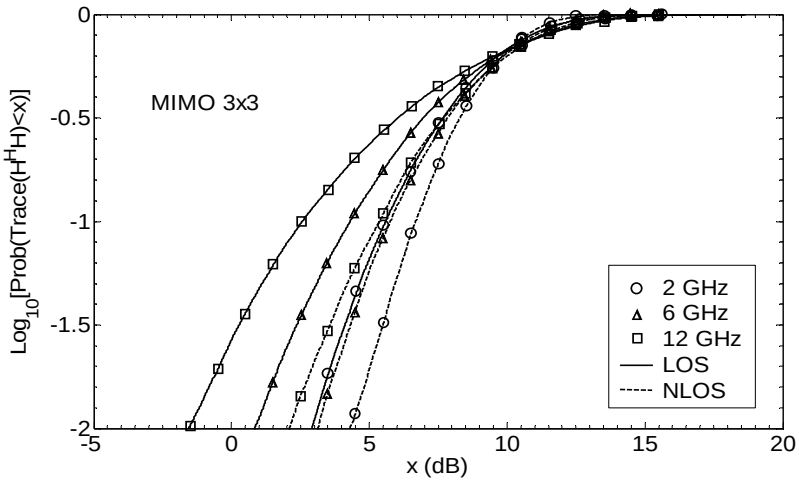

Figure 4.9. CDF of $\mathrm{Tr}\left\{\widetilde{\mathbf{H}}^{H}\widetilde{\mathbf{H}}\right\}$ for $M=N=3$, with one wavelength of elements separation, $f_c=\{2,6,12\}$ GHz, in LOS and NLOS at Zone A.

It is worth to indicate that the reduction in the experimental multipath richness is not only a consequence of the multipath propagation at each frequency. For all cases analysed in this Dissertation, it should be taken into account that the vertical antenna patterns of the UWB antennas change its shape between central frequencies (see Section 2.3.3), which also modify the perceived multipath. At 6 and 12 GHz many side narrower lobes appear, and then the multipath contributions in those directions are higher correlated. This behaviour is also perceived in the performed channel analysis. Despite these differences, the goal of the analysis done in the last sections, and the subsequent channel analysis, is a complete characterisation of the realistic experimental radio channel and its frequency dependency at different scenarios. This experimental characterisation allows us a complete understanding of the frequency dependent propagation phenomenon including components at the RF front-ends that can not be modified, e.g., in case of CRS.

4.4. Spatial correlation analysis

Frequency dependent effects on the eigenvalues of the MIMO system (and capacity) are also reflected on the spatial complex correlation coefficients (SCCC), denoted by $R_{ij,\ell s}$ (see equation (2.8)). For the analysis and reliable comparisons between different frequency bands, the SCCC was estimated at one wavelength of separation among antenna elements at both the TX and RX, i.e., $\{\forall j = s; i = (\ell+1); \ell = \{1,\cdots,N\}\}$, and $\{\forall i = \ell; j = (s+1); s = \{1,\cdots,M\}\}$, respectively (SNR > 15 dB). The Pearson's product moment correlation was also used for the estimations, in the same way than equation (3.44):

$$\tilde{R}_{ij,\ell s} = \frac{1}{W}\sum_{\omega=0}^{W-1} \tilde{R}^{\omega}_{ij,\ell s}, \tag{4.7}$$

$$\tilde{R}^{\omega}_{ij,\ell s} = \left\langle \frac{\sum_{l=0}^{I-1}\left[\widehat{H}^{\kappa,\omega}_{ij}[f_{l'}] - \left\langle \widehat{H}^{\kappa,\omega}_{ij}[f_{l'}]\right\rangle_f\right]\left[\widehat{H}^{\kappa,\omega}_{\ell s}[f_{l'}] - \left\langle \widehat{H}^{\kappa,\omega}_{\ell s}[f_{l'}]\right\rangle_f\right]^*}{\sqrt{\mathrm{var}(\widehat{H}^{\kappa,\omega}_{ij}[f_{l'}])}\sqrt{\mathrm{var}(\widehat{H}^{\kappa,\omega}_{\ell s}[f_{l'}])}} \right\rangle_{\kappa}, \tag{4.8}$$

$$\begin{aligned} &\mathrm{var}\left(\widehat{H}^{\kappa,\omega}_{ij/\ell s}[f_{l'}]\right) = \\ &= \frac{1}{I}\sum_{l=0}^{I-1}\left[\widehat{H}^{\kappa,\omega}_{ij/\ell s}[f_{l'}] - \left\langle \widehat{H}^{\kappa,\omega}_{ij/\ell s}[f_{l'}]\right\rangle_f\right]\left[\widehat{H}^{\kappa,\omega}_{ij/\ell s}[f_{l'}] - \left\langle \widehat{H}^{\kappa,\omega}_{ij/\ell s}[f_{l'}]\right\rangle_f\right]^*, \end{aligned} \tag{4.9}$$

$$\left\langle \widehat{H}^{\kappa,\omega}_{ij/\ell s}[f_{l'}]\right\rangle_f = \frac{1}{I}\sum_{l=0}^{I-1}\widehat{H}^{\kappa,\omega}_{ij/\ell s}[f_{l'}]. \tag{4.10}$$

Note that these complex coefficients, $\tilde{R}_{ij,\ell s}$, can be compared in magnitude and phase. Besides, these coefficients are estimated from complex sequences, i.e., $\widehat{H}_{ij}^{\kappa,\omega}[f_{l'}]$ and $\widehat{H}_{\ell s}^{\kappa,\omega}[f_{l'}]$, that can be represented by the complex vectors $\widehat{\mathbf{h}}_{ij}^{\kappa,\omega} \in \mathbb{C}^{I\times 1}$ and $\widehat{\mathbf{h}}_{\ell s}^{\kappa,\omega} \in \mathbb{C}^{I\times 1}$ as follows

$$\widehat{\mathbf{h}}_{ij}^{\kappa,\omega} = \left[\widehat{H}_{ij}^{\kappa,\omega}[f_1], \widehat{H}_{ij}^{\kappa,\omega}[f_2], \cdots, \widehat{H}_{ij}^{\kappa,\omega}[f_I]\right]^T, \tag{4.11}$$

$$\widehat{\mathbf{h}}_{\ell s}^{\kappa,\omega} = \left[\widehat{H}_{\ell s}^{\kappa,\omega}[f_1], \widehat{H}_{\ell s}^{\kappa,\omega}[f_2], \cdots, \widehat{H}_{\ell s}^{\kappa,\omega}[f_I]\right]^T. \tag{4.12}$$

This representation permits to extrapolate the plane wave propagation phenomenon by means of a geometrical interpretation:

$$\begin{aligned}
&\sum_{l=0}^{I-1}\left[\widehat{H}_{ij}^{\kappa,\omega}[f_{l'}] - \left\langle \widehat{H}_{ij}^{\kappa,\omega}[f_{l'}]\right\rangle_f\right]\left[\widehat{H}_{\ell s}^{\kappa,\omega}[f_{l'}] - \left\langle \widehat{H}_{\ell s}^{\kappa,\omega}[f_{l'}]\right\rangle_f\right]^* = \\
&\quad = \left(\widehat{\mathbf{h}}_{ij}^{\kappa,\omega} - \left\langle \widehat{H}_{ij}^{\kappa,\omega}[f_{l'}]\right\rangle_f\right)^H \left(\widehat{\mathbf{h}}_{\ell s}^{\kappa,\omega} - \left\langle \widehat{H}_{\ell s}^{\kappa,\omega}[f_{l'}]\right\rangle_f\right) \\
&\quad = \left(\widehat{\mathbf{h}}_{ij}^{\kappa,\omega} - \left\langle \widehat{H}_{ij}^{\kappa,\omega}[f_{l'}]\right\rangle_f\right) \bullet \left(\widehat{\mathbf{h}}_{\ell s}^{\kappa,\omega} - \left\langle \widehat{H}_{\ell s}^{\kappa,\omega}[f_{l'}]\right\rangle_f\right),
\end{aligned} \tag{4.13}$$

$$\begin{aligned}
&\sqrt{\sum_{l=0}^{I-1}\left[\widehat{H}_{ij/\ell s}^{\kappa,\omega}[f_{l'}] - \left\langle \widehat{H}_{ij/\ell s}^{\kappa,\omega}[f_{l'}]\right\rangle_f\right]\left[\widehat{H}_{ij/\ell s}^{\kappa,\omega}[f_{l'}] - \left\langle \widehat{H}_{ij/\ell s}^{\kappa,\omega}[f_{l'}]\right\rangle_f\right]^*} = \\
&\quad = \sqrt{\left(\widehat{\mathbf{h}}_{ij/\ell s}^{\kappa,\omega} - \left\langle \widehat{H}_{ij/\ell s}^{\kappa,\omega}[f_{l'}]\right\rangle_f\right)^H \left(\widehat{\mathbf{h}}_{ij/\ell s}^{\kappa,\omega} - \left\langle \widehat{H}_{ij/\ell s}^{\kappa,\omega}[f_{l'}]\right\rangle_f\right)} \\
&\quad = \left\|\widehat{\mathbf{h}}_{ij/\ell s}^{\kappa,\omega} - \left\langle \widehat{H}_{ij/\ell s}^{\kappa,\omega}[f_{l'}]\right\rangle_f\right\|,
\end{aligned} \tag{4.14}$$

where $(\bullet)$ and $\|.\|$ indicate dot product and Euclidean norm (or Euclidean distance), respectively. Under this geometrical interpretation, the angle $\phi_{ij,\ell s}^{\omega}$ between the vectors $\widehat{\mathbf{h}}_{ij}^{\kappa,\omega}$ and $\widehat{\mathbf{h}}_{\ell s}^{\kappa,\omega}$ can be calculated based on

$$\begin{aligned}
\tilde{R}_{ij,\ell s}^{\omega} &= \cos\left(\phi_{ij,\ell s}^{\omega}\right) = \\
&= \left\langle \frac{\left(\widehat{\mathbf{h}}_{ij}^{\kappa,\omega} - \left\langle \widehat{H}_{ij}^{\kappa,\omega}[f_{l'}]\right\rangle_f\right) \bullet \left(\widehat{\mathbf{h}}_{\ell s}^{\kappa,\omega} - \left\langle \widehat{H}_{\ell s}^{\kappa,\omega}[f_{l'}]\right\rangle_f\right)}{\left\|\widehat{\mathbf{h}}_{ij}^{\kappa,\omega} - \left\langle \widehat{H}_{ij}^{\kappa,\omega}[f_{l'}]\right\rangle_f\right\| \left\|\widehat{\mathbf{h}}_{\ell s}^{\kappa,\omega} - \left\langle \widehat{H}_{\ell s}^{\kappa,\omega}[f_{l'}]\right\rangle_f\right\|} \right\rangle_{\kappa}.
\end{aligned} \tag{4.15}$$

Hence, equation (4.15), equivalent to equation (4.8), is the simplest way to do a preliminary analysis of the directionality and spatial correlation at the TX and RX arrays for a measured MIMO channel based on VNA. It is worth to indicate that for non-synchronous measurement set-ups only power correlations can be calculated.

In this section, the PDF of both the magnitude $\left|\tilde{R}_{ij,\ell s}^{\omega}\right|$ and phase $\measuredangle\tilde{R}_{ij,\ell s}^{\omega}=\phi_{ij,\ell s}^{\omega}$, for Zone A and B, with $\Delta x_T=\Delta x_R=2.5$ cm (see Figure 2.5), for all frequency bands, are calculated. The data fulfilled $B=5$ MHz, $W=40$, $I=80$, and $N=M=\{2,3,4\}$. Besides, all possible virtual array combinations within the current ULAs were used for calculations, where up to 13x13 elements were available to achieve $N=M=\{2,3,4\}$.

4.4.1. Magnitude and phase of the SCCC

Figure 4.10 and Figure 4.11 depict the PDF of the magnitude and phase of the SCCC, respectively, for zones A and B in LOS and NLOS. Note that $\left|\tilde{R}_{ij,\ell s}^{\omega}\right|$ and $\measuredangle\tilde{R}_{ij,\ell s}^{\omega}=\phi_{ij,\ell s}^{\omega}$ were calculated for both the TX and RX, i.e.,

$$\left\{\forall j=s; s=\{1,\cdots,M\}; \forall i=(\ell+1); \ell=\{1,\cdots,N\}\right\},$$

$$\left\{\forall i=\ell; \ell=\{1,\cdots,N\}; \forall j=(s+1); s=\{1,\cdots,M\}\right\}, \text{ respectively.}$$

For Zone A, the LOS condition depicts high median correlation values for both the TX and the RX (see Figure 4.10.a), which is usual in this propagation condition. Besides, if the central frequency increases, the achieved median correlation value increases as well. For fair comparisons see Table 4.1, where the mean and median values of the magnitude, and the mean phase, of the SCCC are shown. Note that two statistics for the magnitude of SCCC are included due to the non-symmetric distributions obtained in some cases (see Figure 4.10).

On the other hand, correlation comparisons between the TX and RX show that the mean and median values are higher at the RX side than at the TX side for Zone A in LOS conditions. Besides, for both sides of the link, the mean and median correlation values at 2 and 2.5 GHz are similar, and remarkable increments up to 12 GHz are found. Only at the TX side the correlation at 6 GHz depicts similar values than 2 GHz.

Useful comparisons based on previous analysis from Sections 4.2 and 4.3 and the current correlation results can be done. The capacity and eigenvalues distributions depicted from Figure 4.1.a to Figure 4.3.a, and from Figure 4.5.a to Figure 4.7.a, respectively, for LOS in Zone A, agree with the correlation values at different central frequencies in Figure 4.10.a and Table 4.1. When the correlation increases, the capacity and eigenvalues drop. Besides, if the NLOS and LOS cases are compared, capacity and eigenvalues distributions reach higher values in NLOS than LOS and show lower differences between frequency bands, which also agree with the correlation distributions from Figure 4.10.a (NLOS case) and the mean/median values from Table 4.1. Note that for this specific scenario in NLOS, the correlation distributions (and mean/median values) at the RX show elevated correlation values, even higher or similar than LOS for 2 and 2.4 GHz, which indicates low angular spread and high directivity on the multipath components.

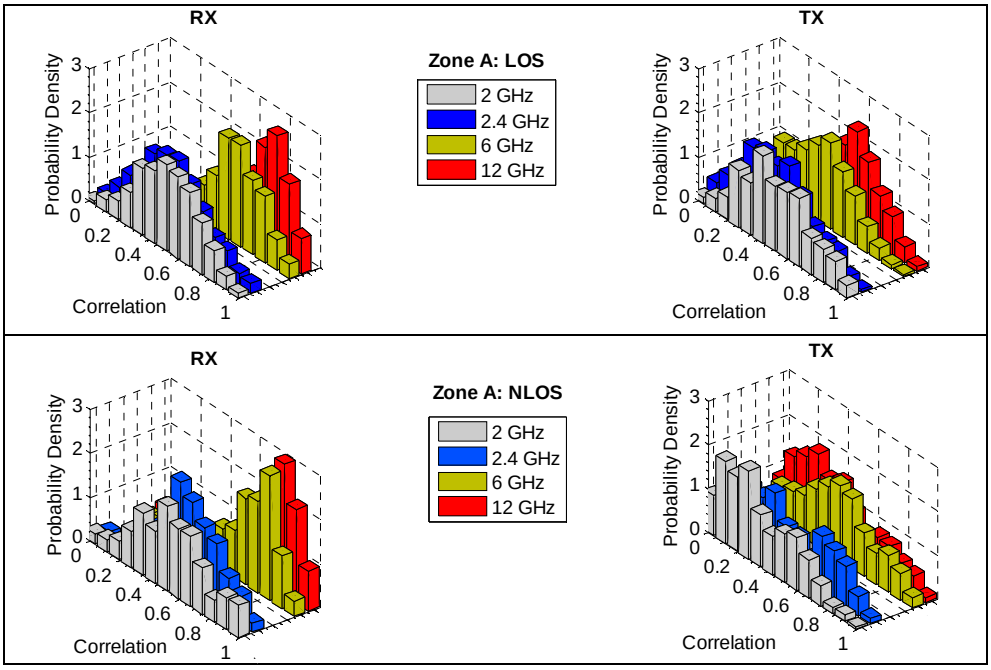

a)

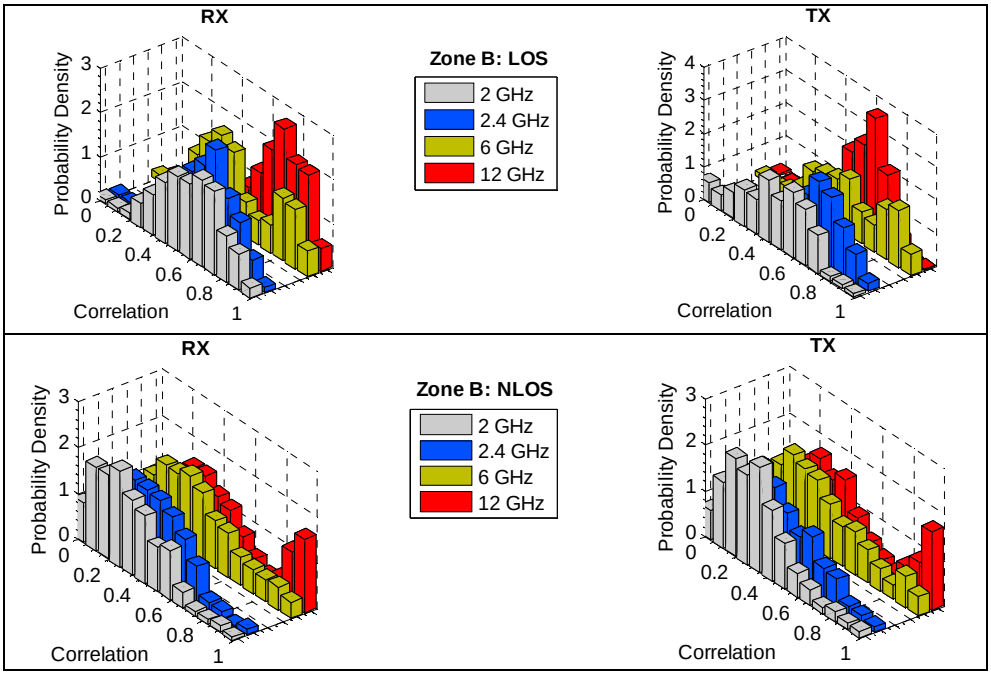

b)

Figure 4.10. PDF of $\left|\tilde{R}_{ij,\ell s}\right|$, $\{\forall j = s; s = \{1,\cdots,M\}; \forall i = (\ell+1); \ell = \{1,\cdots,N\}\}$, and $\{\forall i = \ell; \ell = \{1,\cdots,N\}; \forall j = (s+1); s = \{1,\cdots,M\}\}$, for $N = M = \{2,3,4\}$, with one wavelength of elements separation and $f_c = \{2, 2.4, 6, 12\}$ GHz in: a) LOS and NLOS in Zone A, and, b) LOS and NLOS in Zone B.

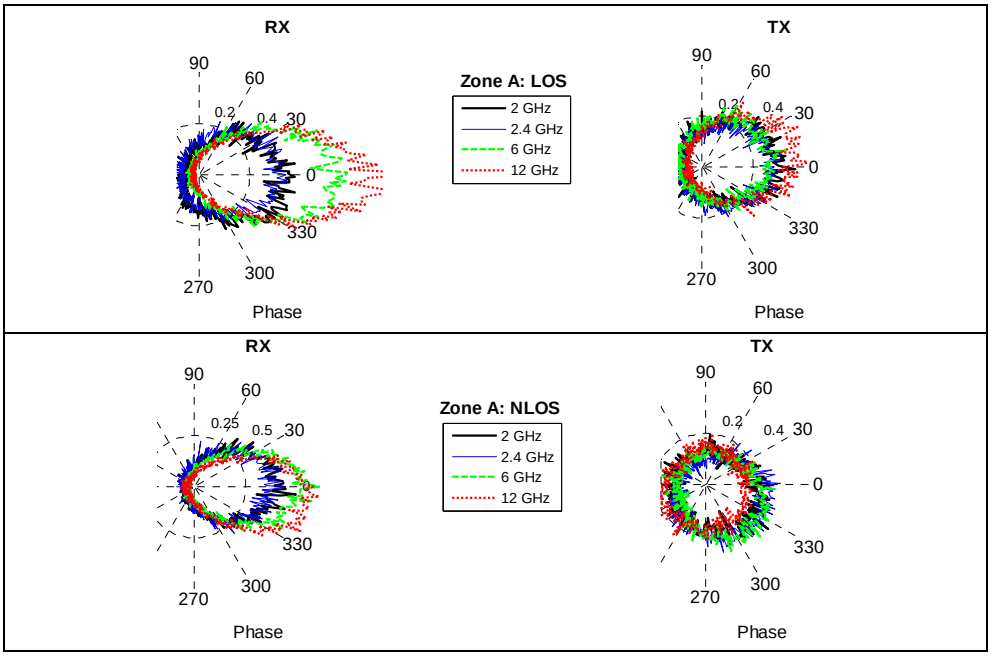

a)

b)

Figure 4.11. PDF of $\angle\tilde{R}_{ij,\ell s}$, $\{\forall j = s; s = \{1,\cdots,M\}; \forall i = (\ell+1); \ell = \{1,\cdots,N\}\}$, and $\{\forall i = \ell; \ell = \{1,\cdots,N\}; \forall j = (s+1); s = \{1,\cdots,M\}\}$, for $N = M = \{2,3,4\}$, with one wavelength of elements separation and $f_c = \{2, 2.4, 6, 12\}$ GHz in: a) LOS and NLOS in Zone A, and, b) LOS and NLOS in Zone B.

Table 4.1. Mean values of $\left|\tilde{R}_{ij,\ell s}\right|$ and $\angle\tilde{R}_{ij,\ell s}$ with $N = M = \{2,3,4\}$, one wavelength of elements separation for $\{\forall j = s; s = \{1,\cdots,M\}; \forall i = (\ell+1); \ell = \{1,\cdots,N\}\}$, and $\{\forall i = \ell; \ell = \{1,\cdots,N\}; \forall j = (s+1); s = \{1,\cdots,M\}\}$, with $f_c = \{2, 2.4, 6, 12\}$ GHz, in LOS and NLOS in Zone A and B.

Zone A									
SCCC		**2 GHz**		**2.4 GHz**		**6 GHz**		**12 GHz**	
		LOS	NLOS	LOS	NLOS	LOS	NLOS	LOS	NLOS
Magn. RX	Mean	0.38	0.46	0.33	0.42	0.59	0.56	0.65	0.58
	Median	0.81	0.90	0.86	0.86	0.92	0.41	0.96	0.85
***Phase.* RX**	*Mean*	*-7.6º*	*1.46º*	*2.81º*	*2.6º*	*-0.22º*	*0.22º*	*-0.18*	*-6.88º*
Magn. TX	Mean	0.29	0.13	0.25	0.22	0.26	0.18	0.40	0.05
	Median	0.89	0.87	0.73	0.23	0.80	0.92	0.88	0.42
***Phase* TX**	*Mean*	*10.69º*	*-38.09º*	*0.97º*	*-42.51º*	*17.8º*	*-38.96º*	*10.8º*	*-87.38º*
Zone B									
Magn. RX	Mean	0.39	0.08	0.31	0.11	0.26	0.14	0.45	0.12
	Median	0.93	0.88	0.12	0.36	0.87	0.92	0.72	0.66
***Phase.* RX**	*Mean*	*-1.61º*	*-41.41º*	*3.41º*	*-110º*	*-4.26º*	*-47.14º*	*22.53º*	*-35.51º*
Magn. TX	Mean	0.51	0.13	0.50	0.10	0.50	0.17	0.79	0.19
	Median	0.46	0.17	0.94	0.37	0.93	0.47	0.96	0.03
***Phase* TX**	*Mean*	*16.59º*	*-15º*	*0.49º*	*-7.2º*	*-1.94º*	*-13.91º*	*5.41º*	*-14.75º*

This angular multipath behaviour in NLOS for Zone A means that strong power multipath contributions in a specific direction are reaching the RX. These characteristics can be verified from the phase distribution of the SCCC in Figure 4.11, where 0º indicates the aperture direction for the ULAs. Noticeable directionality for NLOS condition at the RX side is shown (see Figure 4.11.a), mainly at higher frequencies. Note that for LOS conditions similar characteristics are followed. Besides, for NLOS at the TX, the phase distribution shows lower directionality, with remarkable differences between LOS and NLOS. For fair comparisons, the mean phase of the SCCC at the TX and at the RX, i.e., the mean multipath AOD and AOA, respectively, are included in Table 4.1 for LOS and NLOS conditions.

Note that for Zone A the TX and RX arrays were in alignment for LOS (see Figure 2.2), and then angles around cero were found at both the TX and RX (see Table 4.1). For NLOS, strong multipath components were travelling from one side

of the environment (propagation from corridor to the laboratory room), and then large negative angles were found at the TX (see Table 4.1 for NLOS conditions in Zone A). Hence, the angular results from Figure 4.11.a and Table 4.1 agree with the geometrical TX and RX positions in Zone A. Based on the multi-spectral results in Figure 4.11.a (Zone A), higher frequencies show higher directionality in the multipath components, and then higher spatial correlation is found, which also agree with the results of mean power gain of the MIMO system eigenvalues in Figure 4.8. It is worth to indicate that all locations in Zone A were used for SCCC calculations based on (4.15), and then enough data were available for the magnitude and phase PDF calculations.

On the other hand, if the magnitude and phase distributions for Zone B are compared (see Figure 2.3, Figure 4.10.b and Figure 4.11.b) and the mean/median values in Table 4.1 as well, it is then verified that this scenario offer better conditions for the applicability of MIMO techniques, even at 12 GHz. As it was depicted from Figure 4.1.b to Figure 4.3.b, the capacity in Zone B, compared with Zone A, is enhanced, which agrees with the correlation reductions found in Table 4.1, mainly in NLOS at the RX side. As it was addressed in Section 4.3.2, these results indicate higher multipath richness in this environment, which is verified in Figure 4.11.b where different angular characteristics were found at different central frequencies, principally in LOS. This frequency dependent channel characteristic will be modelled in Chapter 5. Note that high directionality at 6 and 12 GHz is a remaining characteristic in zones A and B. On the other hand, for Zone B in NLOS, the TX/RX antenna locations (see Figure 2.3) agree with the angular values found in Figure 4.11.b and Table 4.1. Negative mean angular values were found at the RX, and more probable values were found around the aperture direction at the TX array, which indicates strong effects on the propagation due to the corridor brick walls in Zone B. Note that corridor effects at the TX in Zone A were almost imperceptible, where the walls were wood made.

Based on the correlation and angular results presented above for both zones, and the channel results addressed in Section 4.2 and 4.3, it is then verified that beamforming techniques can offer better performance in LOS cases and higher central frequencies (particularly in Zone A) due to the higher correlation between the antenna elements, which enhances the largest eigenvalue of the MIMO channel. On the other hand, these increments in the spatial correlation are a drawback for SM and ST coding, since lower power is carried by the rest of orthogonal modes of the MIMO channel if the central frequency increases. In these high correlated and high frequency cases, water-filling techniques must be mandatory for SM, but perfect knowledge of the channel is required at the TX. For ST coding, the unknown channel it is becoming in a loss of performance at higher frequencies, and according to the correlation results at 12 GHz for Zone A, this MIMO technique for LOS conditions in this kind of scenarios can be prohibitive. In these specific indoor environments, the application of orthogonal polarized antennas is a possible solution for ST coding at high central frequencies. From the previous channel analysis, it is then concluded that Zone B offers better conditions for the applicability of SM and ST techniques between 2 and 12 GHz.

To conclude this section, note that the mean phase results in Table 4.1 show useful characteristics for angular channel parameter estimations between 2 and 12 GHz (or above). The multi-spectral MIMO channel measurements capture angular information with different spatial resolution and fine scattering propagation at higher frequencies, which can be exploited by parameter estimation techniques.

4.4.2. Angular estimations using ULAs

Sophisticate spectral or parametric methods can be applied for angular estimations using ULAs [15]. If the current VNA data is used for that purpose, the multiple signal classification (MUSIC) algorithm is a possible choice within the spectral methods. This algorithm assumes that the signal and noise can be separated in two orthogonal subspaces. Besides, for estimations, the Kronecker separability has to be assumed (see equation (3.30)). Hence, the estimated CCM at both ends of the link can be modelled by

$$\widehat{\mathbf{\Sigma}}_{x_T}^{[\nu,\tau']} = \mathbf{\Sigma}_{x_T}^{[\nu,\tau']} + \sigma_n^2 \mathbf{I}_M, \tag{4.16}$$

$$\widehat{\mathbf{\Sigma}}_{x_R}^{[\nu,\tau']} = \mathbf{\Sigma}_{x_R}^{[\nu,\tau']} + \sigma_n^2 \mathbf{I}_N, \tag{4.17}$$

where σ_n^2, $\mathbf{I}_M$, and $\mathbf{I}_N$, are the noise power, and the identity matrices of dimensions $M \times M$ and $N \times N$, respectively. It is worth to indicate that all spectral methods assume spatial filtering either at the TX or the RX side, denoted by $\mathbf{x}_{TX}\left(\phi_T\right) \in \mathbb{C}^{M\times 1}$ and $\mathbf{x}_{RX}\left(\phi_R\right) \in \mathbb{C}^{N\times 1}$, respectively, where ϕ_T and ϕ_R are the AOD and AOA, respectively. In this way, an angular spectral channel power estimator, denoted by $\hat{P}\left(\phi_{T/R}\right)$, can follow the form [15]:

$$\hat{P}\left(\phi_{T/R}\right) = \mathbf{x}_{TX/RX}^T\left(\phi_{T/R}\right) \widehat{\mathbf{\Sigma}}_{x_{T/R}}^{[\nu,\tau']} \mathbf{x}_{TX/RX}^*\left(\phi_{T/R}\right), \tag{4.18}$$

which can be used for azimuth angular estimations at the TX or RX sides based on ULAs. Thus, for the MUSIC angular spectrum, the following spatial filers can be applied [15]

$$\hat{\mathbf{x}}_{TX/RX}\left(\phi_{T/R}\right) = \frac{\left(\widehat{\mathbf{\Sigma}}_{x_{T/R}}^{[\nu,\tau']}\right)^{-1} \boldsymbol{a}^H\left(\phi_{T/R}\right) \sqrt{\boldsymbol{a}^H\left(\phi_{T/R}\right)\boldsymbol{a}\left(\phi_{T/R}\right)}}{\sqrt{\chi}\sigma_{\boldsymbol{n}}\boldsymbol{a}^H\left(\phi_{T/R}\right)\left(\widehat{\mathbf{\Sigma}}_{x_{T/R}}^{[\nu,\tau']}\right)^{-1}\boldsymbol{a}\left(\phi_{T/R}\right)}, \tag{4.19}$$

where $\boldsymbol{a}(\phi_T)$ and $\boldsymbol{a}(\phi_R)$ are the steering vectors at the TX and RX arrays, respectively, and χ is a parameter for adjustment the signal to noise subspace suppression. The ULA steering vectors are given as follows [21]

$$\boldsymbol{a}\left(\phi_T\right) = \left[1, e^{jk\sin(\phi_T)}, \cdots, e^{jk(M-1)\sin(\phi_T)}\right]^T, \tag{4.20}$$

$$\boldsymbol{a}\left(\phi_R\right)=\left[1,e^{jk\sin\left(\phi_R\right)},\cdots,e^{jk(N-1)\sin\left(\phi_R\right)}\right]^T, \tag{4.21}$$

where $k\in\mathbb{R}_+$ is the wave number for plane waves propagation, which offer multi-spectral resolution for angular estimations based on the current VNA data, i.e., different wavelengths are available and then different angular components can be detected as it was verified in Figure 4.11 and Table 4.1.

Thus, based on (4.18) and (4.19), the MUSIC angular spectrum is given as follows

$$\hat{P}\left(\phi_{T/R}\right)=\frac{\boldsymbol{a}^H\left(\phi_{T/R}\right)\boldsymbol{a}\left(\phi_{T/R}\right)}{\chi\sigma_n^2\boldsymbol{a}^H\left(\phi_{T/R}\right)\left(\widehat{\boldsymbol{\Sigma}}_{x_{T/R}}^{[\nu,\tau']}\right)^{-1}\boldsymbol{a}\left(\phi_{T/R}\right)}. \tag{4.22}$$

Note that equations (4.19) and (4.22) impose the restrictions $\widehat{\boldsymbol{\Sigma}}_{x_T}^{[\nu,\tau']}>0$ and $\widehat{\boldsymbol{\Sigma}}_{x_R}^{[\nu,\tau']}>0$, where the CP could be useful in some cases. Besides, note that the power estimation in (4.22) assumes continuous angular information, which becomes into a sampled version as limited spatial samples are available using the antennas elements at ULAs.

On the other hand, parametric methods can be also applied for angular estimations [15]. These methods assume finite plane wave multipath components, which are usually modelled by plane wave summations including angular, gain, delay, and Doppler discrete parameters [21]. In this way, the limitations of these methods are related to the complexity of the implemented models and the ambiguity convergences according to the initial parameters assumed for the models. For the current ULA configuration and VNA data, the well known estimation-of-signal-parameters via rotational-invariance-techniques (ESPRIT) or the space-alternating generalized-expectation-maximization (SAGE) algorithms are possible alternatives for this purpose [15],[21].

Since the objectives of this PhD. Dissertation are not focused in channel parameter estimation, these techniques are not addressed here. The only affinity to this field is addressed in Chapter 5, where a new FD-DGUS MIMO channel model is proposed, principally aimed to include multi-spectral resolution and wideband characteristics within the discrete channel parameters. This new channel model can be adapted to super-resolution channel parameter estimations based on parametric methods.

4.5. Validation of the experimental procedure

Once different MIMO channel parameters were statistically compared based on both the VNA data and the synthetic channel generation for different central

frequencies, the intention of this section is to validate the applied experimental procedure. First the isolation of the path loss is analysed, and then the synthetic channel generator is verified based on both experimental and simulated data.

4.5.1. Isolation of the path loss effect

To assure a fair comparison at different central frequencies with isolation of the path loss effect, Figure 4.12 shows the mean variation of the MIMO system eigenvalues, i.e., $\langle \tilde{\lambda}_i \rangle$, while the distance increases, for 6 and 12 GHz and array configurations $N = M = 4$ in LOS and NLOS in Zone A. Note that 6 and 12 GHz were chosen due to their higher path loss dependence. As it was expected, the eigenvalues remain mostly constant versus distance, with slightly reductions in the smallest eigenvalues for longer distances in NLOS condition. This result confirms the reliable normalization of the MIMO channel, performed in (2.4), which assures the isolation of the path loss effect within the experimental data, and then in the synthetic channel (3.2) used for parameters comparisons.

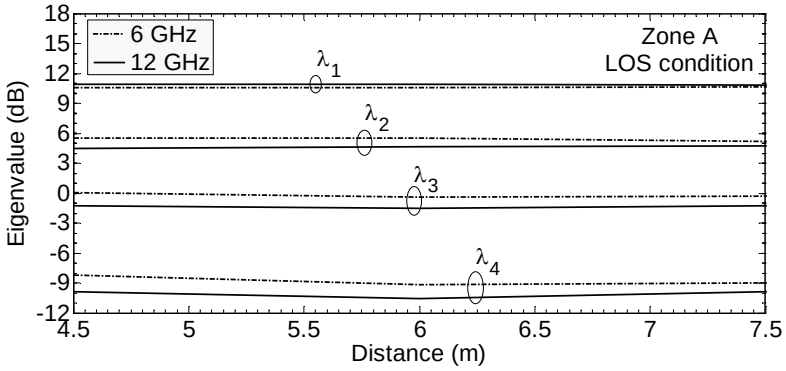

a)

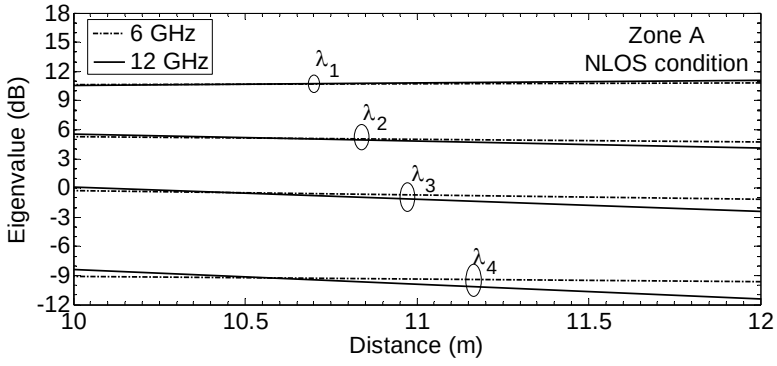

b)

Figure 4.12. Path loss effect isolation: mean local eigenvalues variations vs. distance for $N = M = 4$, with one wavelength element separations, 6 and 12 GHz, in a) LOS and b) NLOS for Zone A.

4.5.2. Capacity of the synthetic channel vs. measurements

Figure 4.13 shows comparative results of the experimental CDF MIMO capacity, for both the synthetic MIMO channel, $\widetilde{\mathbf{H}}$, and the normalised experimental MIMO channel $\widehat{\mathbf{H}}_{\omega}$. The MIMO configuration $N = M = 3$ in NLOS at 2 GHz with a SNR of 30 dB was used for comparisons. All snapshot samples, K_m, locations in NLOS, windows, W, and frequency bin samples, I, were used for computation of $\widehat{\mathbf{H}}_{\omega}$, and one hundred thousands samples have been used for $\widetilde{\mathbf{H}}$. It is worth to indicate that Zone A has been chosen for this analysis as in Figure 4.12.

From Figure 4.13, a good fit between the CDF capacities of $\widetilde{\mathbf{H}}$ and $\widehat{\mathbf{H}}_{\omega}$ has been verified, which indicates a good performance of the synthetic channel generator based on the coloring matrix of the MIMO system (see Section 3.2) and the experimental samples. It is worth to indicate that similar results for other synthetic SNR values, array configurations and frequencies were found.

4.5.3. Synthetic channel generator: eigenvalues stability

Since the synthetic channel generator based on the coloring matrix of the MIMO system used a limited number of samples (see equation (3.2)), the MIMO system eigenvalues variation is a mandatory analysis for validations.

This analysis is required due to the random variables α_{ij} in equation (3.2) were computed based on software code taking into account a limited number of samples, i.e., $1x10^5$ samples for channel comparisons. Hence, for the test of the effects of the number of samples, the CDFs of the eigenvalues of $\widetilde{\mathbf{H}}^H\widetilde{\mathbf{H}}$ for

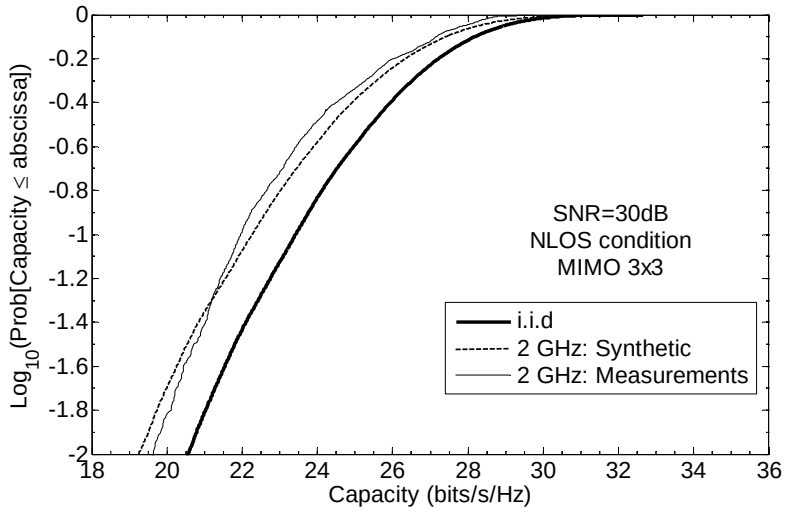

Figure 4.13. CDF of the MIMO capacity for $N = M = 3$, one wavelength elements separation, at 2 GHz, NLOS, for the synthetic MIMO channel $\widetilde{\mathbf{H}}$ and the measured MIMO channel $\widehat{\mathbf{H}}_{\omega}$.

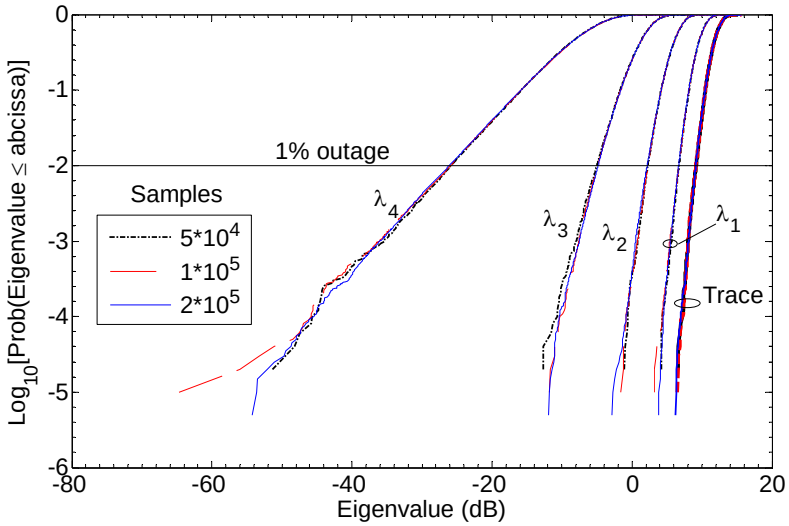

Figure 4.14. Validation of the synthetic channel generator according to the number of samples: CDF of the MIMO system eigenvalues $\tilde{\lambda}_i$, and $\sum \tilde{\lambda}_i$ (trace of $\widetilde{\mathbf{H}}^H \widetilde{\mathbf{H}}$) for $N = M = 4$, i.i.d channel, and $5\text{x}10^4$, $1\text{x}10^5$ and $2\text{x}10^5$ samples.

$N = M = 4$, using $5\text{x}10^4$, $1\text{x}10^5$ and $2\text{x}10^5$ samples, for an i.i.d channel, were calculated. These results are depicted in Figure 4.14. The CDFs of $\tilde{\lambda}_i$ and $\sum \tilde{\lambda}_i$ confirm that one hundred thousands samples are enough for MIMO channel analysis up to 1% outage values.

To conclude, the results presented in Section 3.5, Figure 4.12, Figure 4.13, and Figure 4.14 validate both the procedures proposed in this Dissertation for synthetic MIMO channel generation (Chapter 3) and the experimental channel analysis performed in this chapter. Therefore, the MIMO channel parameter results addressed in previous sections contain reliable remarks for MIMO systems designs between 2 and 12 GHz.

4.6. Conclusions

The impact of frequency on the MIMO channel characteristics for two different indoor scenarios has been investigated based on experimental multi-spectral measurements between 2 and 12 GHz. The synthetic channel generation proposed in Chapter 3 has been applied and validated, doing fair comparisons in four different central frequencies under a high SNR regime. The results presented in this chapter have shown useful remarks for designs and deployment of wireless systems using MIMO techniques as beamforming, SM, and ST coding, operating at 2, 2.4, 6 and 12 GHz.

The results have shown that the CDFs of the MIMO capacity, eigenvalues, multipath richness, spatial correlation (TX and RX), and the AOA and AOD for two indoor environments have a strong frequency dependence. Besides, these results have indicated that Zone B, which represented a high multipath richness environment, depicts better characteristics for the applicability of SM and ST coding up to 12 GHz. On the other hand, beamforming techniques can be applied up to 12 GHz regardless the indoor scenario due to the high directivity of radio channels at elevated frequencies.

The MIMO system performance analysis have shown remarkable differences between 2 and 12 GHz. Compared with the i.i.d channel for $M = N = \{2, 3, 4\}$ cases, the 1%, 10% and 50% outage capacities were reduced while the frequency was increased. The maximum relative capacity reduction was for $M = N = 4$ at 12 GHz. These results were found in LOS and NLOS conditions. These changes versus frequency were related to a RX/TX spatial correlation increment and due to a reduction of the angular spread, which caused a reduction in the MIMO system eigenvalues while the frequency grows. Reductions in eigenvalues power were stronger for the smallest eigenvalues, showing modifications with frequency in the distribution of the largest eigenvalue. The differences in capacity, eigenvalues, spatial correlation, and angular characteristics, were lower between 2 and 2.4 GHz, and for NLOS cases.

Experimental results confirm that at higher central frequencies the multipath richness is reduced, even in NLOS conditions. The performed analysis indicates up to 50% less multipath richness at 12 GHz in NLOS compared with 2 GHz, and much lower in LOS. From a system performance point of view, the reduction in the multipath richness is a drawback for SM and diversity techniques, and in the worst case (Zone A) the performance could be reduced in more than 50% for both propagation conditions at 12 GHz, and in more than 10% at 6 GHz.

Based on correlation and angular results, it was verified that beamforming techniques can offer better performance in LOS cases and higher central frequencies (particularly in Zone A) due to the higher correlation between antenna elements. On the other hand, these increments in the spatial correlation are a drawback for SM and ST coding, since lower power is carried by the rest of orthogonal modes of the MIMO channel. In these cases, water-filling techniques must be mandatory for SM, but perfect knowledge of the channel is required at the TX. For ST coding, the unknown channel become in a loss of performance at higher frequencies, and according to the correlation results at 12 GHz for Zone A, this MIMO technique for LOS conditions in this kind of scenarios (with low multipath richness) can be prohibitive.

The AOA and AOD analysis based on the phase of the complex spatial correlation coefficients shown different angular characteristics at different central frequencies, mainly in LOS in Zone B, which have proved a strong frequency dependence on the indoor multipath propagation. According to the phase distributions, the multi-spectral MIMO measurements addressed useful characteristics for angular channel parameter estimations. The MIMO channel

measurements between 2 and 12 GHz captured angular information with different spatial resolution and fine scattering propagation at higher frequencies. These characteristics can be exploited by super-resolution channel parameter estimations based on parametric methods. In this way, the formulation of new MIMO channel models including multi-spectral resolution and wideband characteristics is a promising research area.

References

[1] "Multiple-Input Multiple-Output in UTRA," 3GPP TR25.876 V1.8.0., Oct. 2005.

[2] "Spatial channel model for multiple input multiple output (MIMO) simulations," 3GPP TR 25.996 V7.0.0:, June 2007.

[3] "Part 11: Wireless LAN medium access control (MAC) and physical layer (PHY) specifications," IEEE P802.11n, D3.00, Sept. 2007.

[4] "Part 16: Air interface for fixed broadband wireless access systems," IEEE Std 802.16 2004, Oct. 2004.

[5] J. Mitola, and G. Q- Maguire, "Cognitive radio: making software radios more personal," *IEEE Personal Communications*, Vol. 6, No.4, pp. 13-18, 1999.

[6] O. O. Koyluoglu, H. El Gamal, "On the utility of frequency reuse in cognitive radio channels," IEEE International Symposium on Information Theory - ISIT 2007, pp. 2161-2165, 24-29 June 2007.

[7] N. Devroye, P. Mitran, V. Tarokh, "Achievable rates in cognitive radio channels," *IEEE Transactions on Information Theory*, Vol. 52, No. 5, pp. 1813-1827, 2006.

[8] R. Soundararajan, S. Vishwanath, "Adaptive sum power iterative waterfilling for MIMO cognitive radio channels," IEEE International Conference on Communications - ICC 2008, pp. 1060-1064, 19-23 May 2008.

[9] E. Telatar, "Capacity of multi-antenna gaussian channels". *Euro. Trans. Telecommun*, Vol. 10, pp. 585–595, 1999.

[10] G. J. Foschini, and M.J. Gans, "On limits of wireless communications in a fading environment when using multiple antennas," *Wireless Personal Commun*., Vol. 6, No.3, pp.311-315, 1998.

[11] A. Paulraj, R. Nabar and D. Gore, *Introduction to space-time wireless communications*, Cambridge University Press, 2003.

[12] H. Shin, and J. H. Lee, "Capacity of multiple-antenna fading channels: spatial fading correlation, double scattering, and keyhole," *IEEE Trans. on Information Theory*, Vol. 49, No. 10, pp. 2636-2647, October 2003.

[13] A. P. García and L. Rubio, "Frequency dependent indoor MIMO channel characterisation between 2 and 12 GHz based on full spatial correlation matrices," *Journal of Communications*, Academy Publisher, Vol. 3, No. 4, pp. 8-15, 2008.

[14] A. P. García and L. Rubio, "Frequency impact on the indoor MIMO channel capacity between 2 and 12 GHz," IEEE 66th Vehicular Technology Conference - VTC, Baltimore, USA, 30 September-3rd October, 2007.

[15] W. Weichselberger, "Spatial Structure of Multiple Antenna Radio Channels: A Signal Processing Viewpoint," PhD. Dissertation, Technische Universtät Wien, 2003.

[16] J. B. Andersen, "Array gain and capacity for known random channels with multiple element arrays at both ends," *IEEE J. Selected Areas in Communications*, Vol. 18, No. 11, 2000.

[17] A.P. Garcia, G. Llano, L. Rubio, and J. Reig, "Carrier frequency effect on the MIMO eigenvalues in an indoor environment," *Revista de la Facultad de Ingeniería "Sistemas y Telemática," Universidad ICESI*, Vol. 6, No. 7, pp. 33-41, 2008.

[18] C. Oestges and B. Clerckx, *MIMO wireless communications: from real-world propagation to space-time code design*, Academic Press, 2007.

[19] J. W., Wallace, et al, "Power and complex envelope correlation for modeling measured indoor MIMO channels: a beamforming evaluation," *IEEE 58thVehicular Technology Conference*, VTC 2003-Fall, Vol. 1, pp.363-367, 6-9 Oct. 2003.

[20] M. Godbout, and H. Leib, "Space-time modulation and coding over transmit correlated fading channels," *IEEE Trans. on Wireless Communications*, Vol. 3, No. 5, 2004.

[21] G. D. Durgin, *Space-time wireless channels*, Pearson Education, Inc., NJ, US, 2003.

CHAPTER 5

PERFECT MIMO CHANNEL MODELLING

5.1. Introduction

The experimental characterisation performed in Chapter 4 has shown particular characteristics of the indoor MIMO channel between 2 and 12 GHz. Since the aim of this PhD Dissertation is the assessment of the frequency dependent MIMO channel from both an experimental and theoretical point of views, to conclude this research, in this chapter a novel MIMO channel model is proposed.

The physical basis in the formulation of the new model is the assumption of plane wave propagation with surrounding objects. This assumption is possible following the modelling strategy of plane wave summations according to the Maxwell's equations [1]. Despite most of models follow these assumptions, they do not take into account the possible existence of inhomogeneous plane waves in the propagation [2]-[4], which could contribute to the whole received energy in the proximity of scatterers. The inclusion of these plane waves in a channel model can improve our physical interpretation of the observed frequency-dependency.

On the other hand, most of the current channel models are based in an impulse-response representation. Another usual way in wideband MIMO channel representation (for modelling and experimental characterisation) is the frequency domain, where it is used a set of flat MIMO channels centered at a single frequency component. This representation is also optional to build UWB-MIMO channels [5]. Thus, frequency domain formulations for channel models offer many advantages, besides allowing to extend the extensively literature of MIMO channels to UWB-MIMO.

The proposed model in this chapter is a frequency-dependent (FD) MIMO channel model. This model is derived from a spatial deterministic-Gaussian-uncorrelated-scattering (DGUS) model [6], being extended to MIMO, and including inhomogeneous plane waves in the formulation. The proposed model uses simple summations of complex exponential functions and considers typical channel parameters (i.e., AOD, AOA, path gains, Doppler frequencies and delays).

The aim in the formulation of this model is to consider most of the possible physical propagation effects related with the interaction between waves, arrays and environments, according to both the carrier frequency and the bandwidth of the signal. Besides, this model is formulated seeking the application of perfect modelling techniques [6],[7], thanks to the closed form expression obtained for its scattering function. Moreover, this model is useful for super-resolution methods [8], e.g., ESPRIT and SAGE, for the estimation of MIMO channel parameters, and for the channel simulation/emulation based on the channel correlation functions [9]-[11]. Hence, this new FD-DGUS-MIMO channel model can be used in conjunction with measurements based on channel sounders or VNAs for realistic system performance analysis, being easily extended for the characterisation of UWB-MIMO channels in indoor environments.

5.2. FD-DGUS-MIMO channel model

For realistic assumptions, the input in a radio RX is considered a scalar voltage, instead electric or magnetic field [1]. The scalar voltage includes all possible effects related to the antenna (pattern, polarization, etc.). Three vectors have been established to model the channel under this approximation: $\vec{\gamma}_R$, $\vec{E}(\vec{\gamma}_R)$ and $\vec{p}_R$. $\vec{\gamma}_R \in \mathbb{R}$ indicates the real-valued spatial translation at the RX side $\vec{\gamma}_R = (vt)\hat{\nu}_R$ (m), where v and t are the speed of the RX translation and the temporal reference, respectively, and $\hat{\nu}_R$ is the unitary spatial vector pointing in the direction of translation. $\vec{E}(\vec{\gamma}_R) \in \mathbb{C}$ represents a complex time-harmonic electromagnetic wave $\vec{E}(\vec{\gamma}_R) = E(\vec{\gamma}_R)\hat{k}$ (V/m), and $\vec{p}_R \in \mathbb{C}$ the complex antenna gain $\vec{p}_R = G\hat{p}$ (m), with $|\vec{p}_R| \triangleq G_R$, where G_R is the RX antenna gain in the direction of the incoming wave, and $\hat{k}$ and $\hat{p}$ are the unitary vectors pointing in the direction of wave propagation and direction of antenna orientation, respectively. $\vec{p}_R \in \mathbb{C}$ enables us to model gain, phase changes and polarization mismatch due to the antenna orientation. Under this definition, for single wave propagation in free-space, the complex scalar channel can be modelled by the dot product

$$\tilde{h}(\vec{\gamma}_R) \triangleq \vec{E}(\vec{\gamma}_R) \bullet \vec{p}_R = \left(E(\vec{\gamma}_R)G\right)\hat{k} \bullet \hat{p}. \quad \text{(V)} \tag{5.1}$$

Note that $\tilde{h}(\vec{\gamma}_R) \in \mathbb{C}$ is a baseband representation of the channel and has twice the total power as its pass band representation [1].

In the case of multipath propagation, the complex scalar channel (in volts) can be modelled as a summation of different dot products between each wave and different antenna vectors.

$$\tilde{h}(\vec{\gamma}_R) \triangleq \sum_i \left(E_i(\vec{\gamma}_R) G_i\right) \hat{k}_i \bullet \hat{p}_i. \quad \text{(V)} \tag{5.2}$$

For this formulation, the baseband received voltage at the antenna terminals has been assumed as the result of waves propagating in a bounded region of linear free-space. Hence, the normalised complex scalar channel can be described by means of a summation of all possible plane waves, i.e., a solution basis satisfying Maxwell's equations [1],[2]:

$$\tilde{h}(\vec{\gamma}_R) = \sum_i \tilde{b}_i \exp\left(j\left(\theta_i - \vec{k}_i \bullet \vec{\gamma}_R\right)\right), \tag{5.3}$$

where $\vec{k}_i \bullet \vec{k}_i = k_0^2$ ($\forall i$ -th wave), $k_0 = 2\pi/\lambda_0$ is the free-space wavenumber, λ_0 is the free-space wavelength, $\left\{\vec{k}_i\right\}$ is the set of constant wavevectors, $\left\{\tilde{b}_i\right\}$ represents the set of path gains ($\tilde{b}_i \in \mathbb{R}_+, \forall i$), and $\{\theta_i\}$ a set of random phases which model the random interaction with every realistic material.

The condition $\vec{k}_i \bullet \vec{k}_i = k_0^2$ restricts (5.3) to plane waves [1], whose wavevectors $\left\{\vec{k}_i\right\}$ are real or complex-valued. This condition divides the plane waves in two groups: homogeneous[14] and inhomogeneous[15] plane waves [1]-[4] (see Figure 5.1). Homogeneous plane waves (HPW) have only real-valued wavevectors, and inhomogeneous plane waves (IPW) have only complex-valued wavevectors. It is worth to indicate that IPWs are caused by scatterers or sources in the propagation medium outside the bounded free-space [1], and they also satisfy Maxwell's equations [3].

If it is assumed that an indoor wideband MIMO system does not follow perfectly the local area size, L_A, restricted at the TX/RX side as $L_A/\lambda_0 < f_c/B$ [1], both types of plane waves should be included at the model. This is a consequence of large bandwidths, B, high central frequencies, f_c, and possible close objects to the array (the antenna arrays inclusive).

Using the real-valued set $\left\{\vec{k}_\ell\right\} = \left\{(2\pi/\lambda_0)\hat{k}_\ell\right\}$ of wavevectors, and the complex-valued set $\left\{\vec{k}'_{\ell'}\right\} = \left\{\left(2\pi/\lambda_{eff_{\ell'}}\right)\hat{k}'_{\ell'} + j(\alpha_{\ell'})\hat{i}_{\ell'}\right\}$, the complex scalar channel can be given by

[14] The envelope of a homogeneous plane wave is a constant value that does not depend on position in space and the equiamplitude and equiphase planes coincide. Besides, all homogeneous plane waves propagate at the same speed with the same wavenumber [2].
[15] The envelope of an inhomogeneous plane wave (also known as evanescent waves) is not a constant value and equiamplitude and equiphase planes do not coincide [2]. Besides, an inhomogeneous plane wave has wavenumber always greater than the free-space wavenumber, and then the effective wavelength is always smaller than the free-space wavelength [1].

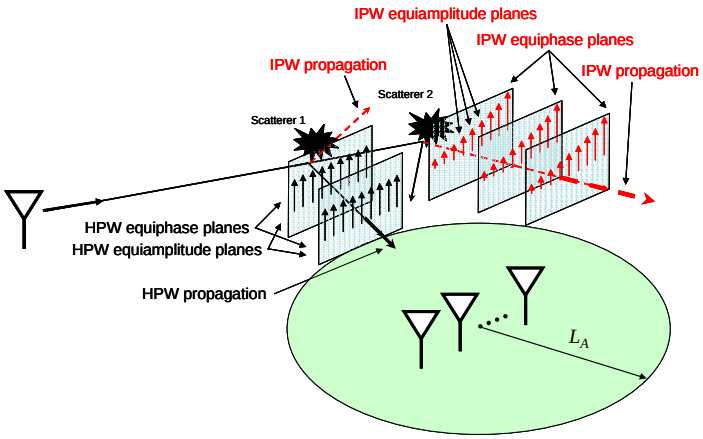

Figure 5.1. Homogeneous and In-homogeneous plane waves (HPWs and IPWs, respectively).

$$\tilde{h}(\vec{\gamma}_R) = \overbrace{\sum_{\ell} \tilde{b}_\ell \exp\left(j\left(\theta_\ell - (2\pi/\lambda_0)\hat{k}_\ell \bullet \vec{\gamma}_R\right)\right)}^{\text{HPWs}} + \overbrace{\sum_{\ell'} \exp\left(-(\alpha_{\ell'})\hat{i}_{\ell'} \bullet \vec{\gamma}_R\right) \exp\left(j\left(\theta_{\ell'}^{in} - \left(2\pi/\lambda_{eff_{\ell'}}\right)\hat{k}'_{\ell'} \bullet \vec{\gamma}_R\right)\right)}^{\text{IPWs}}, \tag{5.4}$$

where the first summation term models HPWs multipath, the second term models IPWs multipath, and $\{\theta_{\ell'}\}$ and $\{\theta_{\ell'}^{in}\}$ are the set of random phases for HPWs and IPWs, respectively. In (5.4), $\hat{k}_\ell$ is a unit vector that points in the direction of propagation of the ℓ-th HPW (in interaction with the ℓ-th scatterer). On the other hand, $\hat{i}_{\ell'}$ and $\hat{k}'_{\ell'}$ are, respectively, the imaginary and real unit vectors of the ℓ'-th IPW (in interaction with the ℓ'-th scatterer), which indicate the direction of amplitude decay and direction of phase propagation, respectively (see Figure 5.2). Note that ℓ and ℓ' are used for differentiation between HPWs and IPWs. The constants $\alpha_{\ell'}$ and $\lambda_{eff_{\ell'}}$ are, respectively, the rate of amplitude decay and the effective wavelength of the ℓ'-th IPW. Based on the restriction $\vec{k}'_{\ell'} \bullet \vec{k}'_{\ell'} = k_0^2$, the unit vectors $\hat{i}_{\ell'}$ and $\hat{k}'_{\ell'}$ should follow $\hat{i}_{\ell'} \bullet \hat{k}'_{\ell'} = 0$.

If we want to assume the effect of IPWs in 2D propagation (plane in azimuth), it is possible to suppose that the ℓ'-th IPW propagates orthogonal to the ℓ-th HPW:

$$\hat{k}'_{\ell'} \bullet \hat{k}_\ell = 0, \quad \forall \ell' = \ell,$$
$$\hat{i}_{\ell'} \bullet \hat{k}_\ell = 1, \quad \forall \ell' = \ell.$$

It is worth to indicate that this assumption fulfils physical statements proposed in the literature [3].

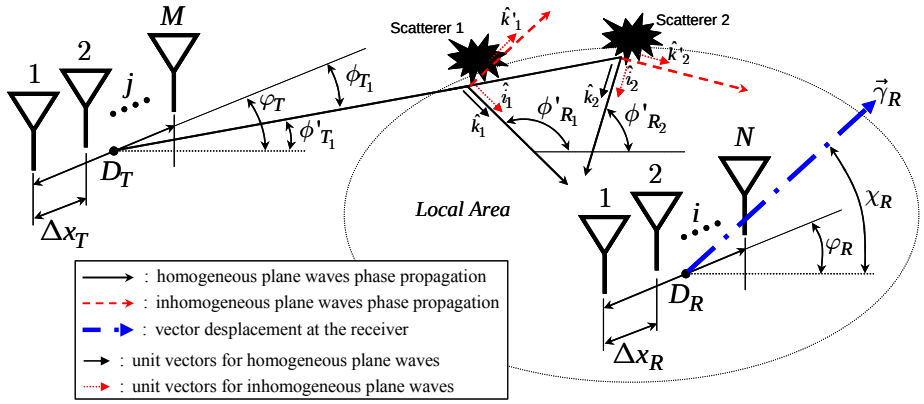

Figure 5.2. Transmitter and receiver array geometry for the FD-DGUS-MIMO model.

If we assume 2D propagation in (5.4), the detected signals are the result of waves propagated away from the scatterers (in a plane formed by arrays and scatterers) and the direction of decay $\hat{i}_{\ell'}$ points parallel to the ℓ-th HPW.

In this way, the IPWs must fulfil

$$k_0^2 = \left(2\pi/\lambda_{eff_{\ell'}}\right)^2 - {\alpha_{\ell'}}^2, \tag{5.5}$$

where $k_{eff_{\ell'}} = 2\pi/\lambda_{eff_{\ell'}}$ is the wavenumber for the ℓ'-th IPW, following $k_{eff_{\ell'}} > k_0$, and

$$\alpha_{\ell'} = \sqrt{k_{eff_{\ell'}}^2 - k_0^2}, \tag{5.6}$$

which restrict $\alpha_{\ell'} \in \mathbb{R}_+, \forall \ell'$. Therefore, it can be possible to model $\alpha_{\ell'}$ as a local area size dependent function

$$\alpha_{\ell'}\left(\lambda_0, \tau_\ell, \Omega_{R_\ell}\right), \quad \forall\ \ell'=\ell$$

where $\{\tau_\ell\}$ are the set of delays ($\tau_\ell \in \mathbb{R}_+, \forall \ell$) for HPW, and $\left\{\Omega_{R_\ell}\right\}$ the set of direction of arrivals ($\Omega_{R_\ell} \in \mathbb{R}_+, \forall \ell$) for HPW as well. With this hypothesis, the space-time-frequency channel can be modelled using (5.4), assuming HPWs and IPWs. It is worth do indicate that this hypothesis fulfil the affirmation given in [3] about the space-time dependency for the complex wavevectors defined in (5.4).

On the other hand, the direction of propagation of the IPWs should be taken into account according to the scatterers and array positions, since it is possible that some of these waves point to the TX and RX arrays, forming multipath propagation with less contribution of HPWs. This hypothesis could confirm the possibility of dominant plane waves arriving with a wavelength shorter than the free-space

wavelength, i.e., $\lambda_{eff_{\ell'}} < \lambda_0$. This possibility is interesting for wideband MIMO systems operating at high central frequencies.

Based on the previous definitions, note that the summation of HPWs and IPWs in (5.4) can be a result of a single scatterer, or several scatterers in the environment; see Figure 5.2. Besides, we can use the complex scalar representation in (5.4) to consider the array geometry, scatterers distribution and the motion at the RX side.

Note that in (5.4) the phase terms $\theta_{\ell'}^{in} \neq \theta_\ell$, $\forall\ \ell' = \ell$, are the random phase changes due to the scatterers and antenna interaction. On other hand, if we consider motion at the RX, the phase terms $(2\pi/\lambda_0)\hat{k}_\ell \bullet \vec{\gamma}_R$ and $\left(2\pi/\lambda_{eff_{\ell'}}\right)\hat{k}'_{\ell'} \bullet \vec{\gamma}_R$, and the amplitude terms $(\alpha_{\ell'})\hat{i}_{\ell'} \bullet \vec{\gamma}_R$, are not constant quantities.

Thus, for phase analysis take into account the vector representation in Figure 5.3 (left and right). Note that the vector displacement direction $\vec{\gamma}_R$ have a relative angle, χ_R, and magnitude, (vt), besides, $\vec{\mathrm{I}}_{\ell'} = \alpha_{\ell'}\hat{i}_{\ell'}$ and $\vec{\Gamma}_{\ell'} = \left(2\pi/\lambda_{eff_{\ell'}}\right)\hat{k}'_{\ell'}$. Hence, this geometry representation (Figure 5.2 and Figure 5.3) let us to include a relative orientation at the arrays: φ_T for the TX and φ_R for the RX side. Besides, the AOD, ϕ_{T_ℓ}, and AOA, ϕ_{R_ℓ}, are included, taking into account the array orientation. For modelling, it will be considered the relative AODs, ϕ'_{T_ℓ}, and AOAs, ϕ'_{R_ℓ}, by means of:

$$\phi_{T_\ell} = \phi'_{T_\ell} - \varphi_T, \tag{5.7}$$

$$\phi_{R_\ell} = \phi'_{R_\ell} - \varphi_R. \tag{5.8}$$

On the other hand, the Figure 5.3 (left) shows the distance differences in the $\hat{k}_\ell$ directions, denoted by $\Delta_{\vec{k}_\ell}$, due to the spatial translation, denoted by $\Delta_{\vec{\gamma}_R} = v\Delta_t$. These differential distances follow:

$$\Delta_{\vec{k}_\ell} = v\Delta_t \cos\left(\phi'_{R_\ell} - \chi_R\right), \tag{5.9}$$

where Δ_t is the differential time for the differential translation $\Delta_{\vec{\gamma}_R}$. These displacements introduce phase changes, $\Delta\psi_\ell$, in the HPWs, which are given by

$$\Delta\psi_\ell = k_0\Delta_{\vec{k}_\ell} = \frac{2\pi}{\lambda_0} v\Delta_t \cos\left(\phi'_{R_\ell} - \chi_R\right), \tag{5.10}$$

and then the resulting Doppler frequencies for HPWs, $\left\{f_{d_\ell}\right\}$, are described by

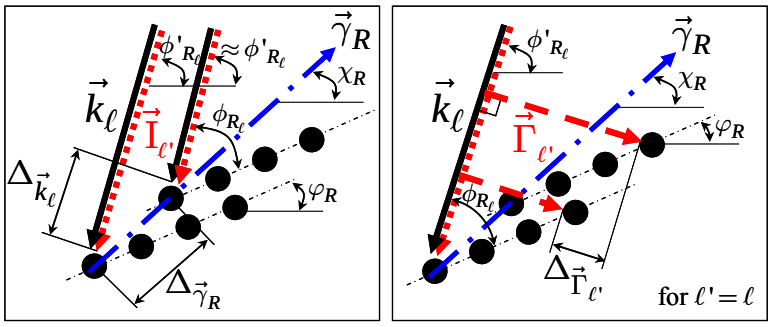

Figure 5.3. Vector representation used for phase analysis at the receiver array. Black circles depict the array elements.

$$f_{d_\ell} = \frac{v}{\lambda_0}\cos\left(\phi_{R_\ell} + \varphi_R - \chi_R\right), \tag{5.11}$$

Hence, the phase terms $(2\pi/\lambda_0)\hat{k}_\ell \bullet \vec{\gamma}_R$ in (5.4) follow

$$\begin{aligned}(2\pi/\lambda_0)\hat{k}_\ell \bullet \vec{\gamma}_R &= 2\pi\cos\left(\phi_{R_\ell} + \varphi_R - \chi_R\right) f_{d_{\max}} t,\\ (2\pi/\lambda_0)\hat{k}_\ell \bullet \vec{\gamma}_R &= 2\pi f_{d_\ell} t,\end{aligned} \tag{5.12}$$

where the maximum Doppler frequency is $f_{d_{\max}} = v/\lambda_0$. In the same way, we can include the amplitude terms $(\alpha_{\ell'})\hat{i}_{\ell'} \bullet \vec{\gamma}_R$, as result of the dot product:

$$(\alpha_{\ell'})\hat{i}_{\ell'} \bullet \vec{\gamma}_R = \alpha_{\ell'} f_{d_{\ell'}} \lambda_0 t. \tag{5.13}$$

Note that $\hat{i}_{\ell'} \bullet \hat{k}_\ell = 1, \ \forall \ell' = \ell$. On the other hand, regarding with $\hat{i}_{\ell'} \bullet \hat{k}'_{\ell'} = 0$, the phase terms $\left(2\pi/\lambda_{eff_{\ell'}}\right)\hat{k}'_{\ell'} \bullet \vec{\gamma}_R$, from equation (5.4), are obtained as follows (see Figure 5.3 right):

$$\Delta_{\vec{\Gamma}_{\ell'}} = v\Delta_t \sin\left(\phi'_{R_\ell} - \chi_R\right), \tag{5.14}$$

$$\Delta\psi'_\ell = \frac{2\pi}{\lambda_{eff_{\ell'}}}\Delta_{\vec{\Gamma}_{\ell'}}, \tag{5.15}$$

$$f_{d_{\ell'}}^{in} = \frac{v}{\lambda_{eff_{\ell'}}}\sin\left(\phi_{R_{\ell'}} + \varphi_R - \chi_R\right), \tag{5.16}$$

$$\left(2\pi/\lambda_{eff_{\ell'}}\right)\hat{k}'_{\ell'} \bullet \vec{\gamma}_R = 2\pi f_{d_{\ell'}}^{in} t, \tag{5.17}$$

where $\left\{ f_{d_{\ell'}}^{in} \right\}$ are the resulting Doppler frequencies for IPWs.

Using the last formulations, the new version of the model (5.4) is as follows

$$\begin{aligned} \tilde{h}(t) = & \sum_{\ell} \tilde{b}_{\ell} \exp j\left(\theta_{\ell} - 2\pi f_{d_{\ell}} t\right) \\ & + \sum_{\ell'} \exp\left(-\alpha_{\ell'} f_{d_{\ell'}} \lambda_0 t\right) \exp j\left(\theta_{\ell'}^{in} - 2\pi f_{d_{\ell'}}^{in} t\right), \quad \forall \ell' = \ell. \end{aligned} \tag{5.18}$$

The model in (5.18) is the result of a 2D space geometry, where the phase propagation of HPWs and IPWs, for the same $\ell' = \ell$-th scatterer, are orthogonal, and the phase variations are a consequence of the speed at the RX. Besides, note that the model in (5.18) represents the summation of two complex deterministic-Gaussian (DG) processes [6].

If the total path length that the HPWs travel from TX to the RX is taken into account, new phase terms should be included in (5.18). Hence, the total path length from the TX array to the RX array via ℓ-th scatterer is defined as follows

$$R_{\ell} = R_{T_{\ell}} + R_{R_{\ell}}, \tag{5.19}$$

where $R_{T_{\ell}}$ and $R_{R_{\ell}}$ are the path lengths from the TX to the ℓ-th scatterer and from the ℓ-th scatterer to the RX, respectively. Using (5.19) the DG time-variant channel model given in (5.18) is updated by

$$\begin{aligned} \tilde{h}(t) = & \sum_{\ell} \tilde{b}_{\ell} \exp j\left(\theta_{\ell} - 2\pi f_{d_{\ell}} t - \left(2\pi/\lambda_0\right) R_{\ell}\right) \\ & + \sum_{\ell'} \exp\left(-\alpha_{\ell'} f_{d_{\ell'}} \lambda_0 t\right) \exp j\left(\theta_{\ell'}^{in} - 2\pi f_{d_{\ell'}}^{in} t\right), \quad \forall \ell' = \ell \end{aligned} \tag{5.20}$$

Note from (5.20) that IPWs have not phase effects related to the total travel distance, since HPWs and IPWs, for the same $\ell' = \ell$-th scatterer, were assumed orthogonal.

On the other hand, it is well known for HPWs that $\lambda_0 = c/f_c$, where c is the free-space speed of light. Hence, the total travel time for HPWs is given by

$$\tau_{\ell} = R_{\ell}/c, \tag{5.21}$$

and then, the model given in (5.20) can be expressed as

$$\begin{aligned} \tilde{h}(t) = & \sum_{\ell} \tilde{b}_{\ell} \exp j\left(\theta_{\ell} - 2\pi f_{d_{\ell}} t - 2\pi f_c \tau_{\ell}\right) \\ & + \sum_{\ell'} \exp\left(-\alpha_{\ell'} f_{d_{\ell'}} (c/f_c) t\right) \exp j\left(\theta_{\ell'}^{in} - 2\pi f_{d_{\ell'}}^{in} t\right), \quad \forall \ell' = \ell \end{aligned} \tag{5.22}$$

where f_{d_ℓ} and $f_{d_{\ell'}}^{in}$ are caused only by the single central frequency f_c.

Now, assuming a non-zero bandwidth B (see equations (3.13) and (3.14)), i.e., $f_c + f$, where $-B/2 \le f \le B/2$, and from the phase terms $(2\pi/\lambda_0)\hat{k}_\ell \bullet \vec{\gamma}_R = (2\pi f_c/c)\hat{k}_\ell \bullet \vec{\gamma}_R$, the new phase changes for the HPWs is as follows

$$\left(2\pi(f_c + f)/c\right)\hat{k}_\ell \bullet \vec{\gamma}_R = 2\pi f_{d_\ell} t + 2\pi f_{d_\ell}^B t \tag{5.23}$$

where the Doppler frequency components $f_{d_\ell}^B$, due to f, are given by

$$f_{d_\ell}^B = \frac{v}{\lambda_0^B}\cos\left(\phi_{R_\ell} + \varphi_R - \chi_R\right), \tag{5.24}$$

with $\lambda_0^B = c/f$. Besides, taking into account that for IPWs $\lambda_{eff_{\ell'}} = c_{eff_{\ell'}}/f_c$, where $c_{eff_{\ell'}}$ is the effective speed of the ℓ'-th IPW, the phase terms $\left(2\pi/\lambda_{eff_{\ell'}}\right)\hat{k}'_{\ell'} \bullet \vec{\gamma}_R$ follow

$$\left(2\pi(f_c + f)/c_{eff_{\ell'}}\right)\hat{k}'_{\ell'} \bullet \vec{\gamma}_R = 2\pi f_{d_{\ell'}}^{in} t + 2\pi f_{d_{\ell'}}^{in,B} t, \tag{5.25}$$

where the Doppler frequencies

$$f_{d_{\ell'}}^{in,B} = \frac{v}{\lambda_{eff_{\ell'}}^B}\sin\left(\phi_{R_{\ell'}} + \varphi_R - \chi_R\right), \tag{5.26}$$

with $\lambda_{eff_{\ell'}}^B = c_{eff_{\ell'}}/f$. According to (5.23) and (5.25), the non-zero bandwidth can be included in the FD-DG reference model as follows:

$$\begin{aligned}\tilde{H}(f,t) = &\sum_\ell \tilde{b}_\ell \exp j\left(\theta_\ell - 2\pi f_{d_\ell} t - 2\pi(f_c + f)\tau_\ell - 2\pi f_{d_\ell}^B t\right) \\ &+ \sum_{\ell'} \exp\left(-\alpha_{\ell'} f_{d_{\ell'}}\left(c/(f_c + f)\right)t\right)\exp j\left(\theta_{\ell'}^{in} - 2\pi f_{d_{\ell'}}^{in} t - 2\pi f_{d_{\ell'}}^{in,B} t\right),\end{aligned} \tag{5.27}$$

On the other hand, if a wideband signal and higher central frequency are considered, the amplitude and phase of the multipath plane waves are functions of frequency. This frequency dependence can be explained as an increase in the resolution on the scatterer interaction, which means that not only a single HPW and IPW exist for each $\ell'=\ell$-th scatterer and then new scatterers become visible; see Figure 5.4. If the bandwidth is large, many HPWs and IPWs with different wavelengths should be included for each $\ell'=\ell$-th scatterer due to the fine scattering mechanisms. If the carrier frequency is high, the resolution interaction increases and the number of possible scatterers increase. It should stand out that Figure 5.4

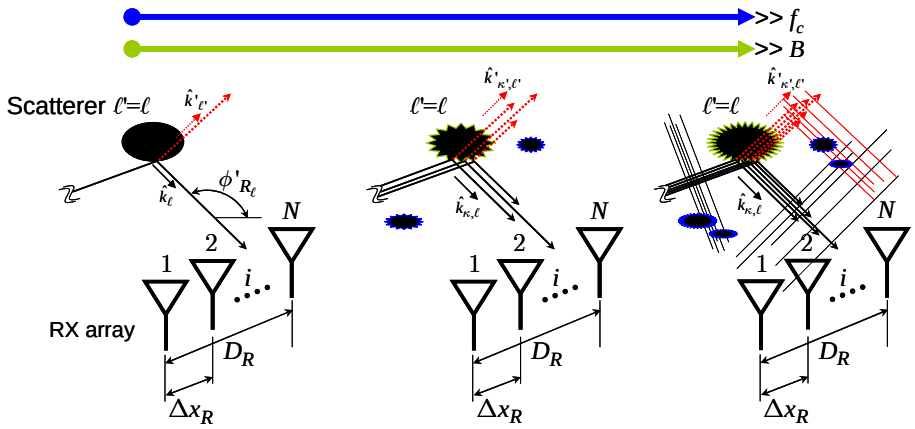

Figure 5.4. Geometry used at the receiver array for the FD-DG model when the bandwidth and carrier frequency increase.

(right) shows the direction of phase propagation of the HPWs and IPWs, and the plane wave fronts. These plane fronts extend along all area and they are orthogonal to $\hat{k}_\ell$ and $\hat{k}'_{\ell'}$ for HPWs and IPWs, respectively.

Other frequency-dependent effects are related to the TX and RX antenna patterns. Here, it is assumed that such effects are reflected directly on the radio channel information in (5.27) (see also (5.1)). This assumption permits a simplification of the modelling procedure and leave room for the application of antenna calibrations during the parameters estimation [8].

If it is considered that the amplitudes and phases change with frequency, because of the fine scattering resolution and possible changes in the material properties and antenna patterns, the model presented in (5.27) can be updated by

$$\begin{aligned}\tilde{H}(f,t)=&\sum_{\ell}\sum_{\kappa}\tilde{b}_{\kappa,\ell}\exp j\left(\theta_{\kappa,\ell}-2\pi f_{d_\ell}t-2\pi f_c\tau_\ell-2\pi f\tau_{\kappa,\ell}-2\pi f^B_{d_{\kappa,\ell}}t\right)\\&+\sum_{\ell'}\sum_{\kappa'}\Big[\exp\left(-\alpha_{\kappa',\ell'}\left(f_{d_{\ell'}}+f^B_{d_{\kappa',\ell'}}\right)\left(c/(f_c+f)\right)t\right)\\&\times\exp j\left(\theta^{in}_{\kappa',\ell'}-2\pi f^{in}_{d_{\ell'}}t-2\pi f^{in,B}_{d_{\kappa',\ell'}}t\right)\Big],\end{aligned}\tag{5.28}$$

$\forall\ell'=\ell$ and $\forall\kappa'=\kappa$, where the $\kappa'=\kappa$-th plane wave is a component wave for the $\ell'=\ell$-th scatterer. For the model given in (5.28), $\tau_{\kappa,\ell}$ are delays given by

$$\tau_{\kappa,\ell}=\tau_\ell\pm\tau''_{\kappa,\ell},\tag{5.29}$$

where $\tau''_{\kappa,\ell}$ are the delay spreading due to the fine resolution in the scatterer interaction (to be defined later). The phase terms $\theta_{\kappa,\ell}$ and $\theta^{in}_{\kappa',\ell'}$ can hold as random phases, following

$$\theta_{\kappa,\ell} = \theta_\ell \pm \theta''_{\ell,\kappa}, \tag{5.30}$$

$$\theta^{in}_{\kappa',\ell'} = \theta^{in}_{\ell'} \pm \theta''^{in}_{\ell',\kappa'}, \tag{5.31}$$

where $\theta''_{\ell,\kappa}$ and $\theta''^{in}_{\ell',\kappa'}$ are random phase changes as a result of frequency dependencies for realistic materials. Finally, consider that each $\kappa' = \kappa$-th HPW component have associate a Doppler frequency given by

$$f^B_{d_{\kappa,\ell}} = \frac{v}{\lambda^B_0}\cos\left(\phi^B_{R_{\kappa,\ell}} + \varphi_R - \chi_R\right), \tag{5.32}$$

and for each $\kappa' = \kappa$-th IPW component given by

$$f^{in,B}_{d_{\kappa',\ell'}} = \frac{v}{\lambda^B_{eff_{\kappa',\ell'}}}\sin\left(\phi^B_{R_{\kappa',\ell'}} + \varphi_R - \chi_R\right), \tag{5.33}$$

where for $\kappa' = \kappa$ and $\ell' = \ell$, the fine resolution in the AOAs, $\phi^B_{R_{\kappa,\ell}}$, are given by

$$\phi^B_{R_{\kappa,\ell}} = \phi'_{R_\ell} - \varphi_R \pm \phi''_{R_{\kappa,\ell}}, \tag{5.34}$$

being $\phi''_{R_{\kappa,\ell}}$ the AOA spreading, around ϕ_{R_ℓ}, due to the fine resolution in the scatterer interaction. Note that in (5.33) $\lambda^B_{eff_{\kappa',\ell'}} = c_{eff_{\kappa',\ell'}} / f$, and equation (5.34) indicates different possible angles of arrival for each $\kappa' = \kappa$-th sub-component around each $\ell' = \ell$-th component.

It is worth to indicate that if it is considered a wideband signal and high central frequencies simultaneously, the multipath propagation is as in (5.28). This multipath behaviour can be increased taking into account that $\lambda_0 = c/f_c$ and $\lambda_{eff_{\ell'}} = c_{eff_{\ell'}} / f_c$. If f_c increases λ_0 and $\lambda_{eff_{\ell'}}$ drop, and there exist new possible scatterers, which were invisible for the signals, having now some effects in the propagation. These effects can be included in (5.28) adding a number of scatterers, denoted by L, as a central frequency dependent function.

$$L \triangleq L(f_c)$$

In the same way, we can include in the model a specific number of frequency components due to the wideband signal, denoted by $I_\ell = I_{\ell'}$, for each $\ell' = \ell$-th path. Therefore, the new FD-DG reference channel model is given by

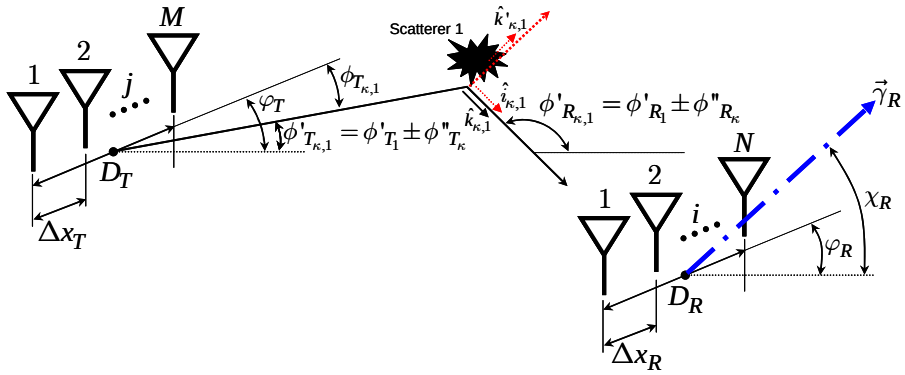

a)

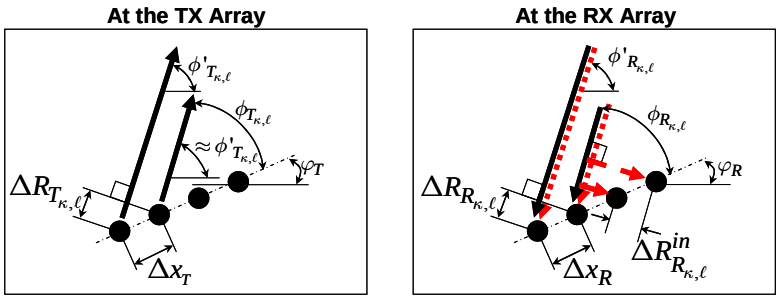

b)

Figure 5.5. TX and RX geometry used in the FD-DG-MIMO model for, a) waves grouping and, b) space array effects for phase analysis.

$$\tilde{H}(f,t) = \sum_{\ell=0}^{L-1}\sum_{\kappa=1}^{I_\ell} \tilde{b}_{\kappa,\ell} \exp j\left(\theta_{\kappa,\ell} - 2\pi f_{d_\ell} t - 2\pi f_c \tau_\ell - 2\pi f \tau_{\kappa,\ell} - 2\pi f^B_{d_{\kappa,\ell}} t\right)$$
$$+ \sum_{\ell'=0}^{L-1}\sum_{\kappa'=1}^{I_{\ell'}} \left[\exp\left(-\alpha_{\kappa',\ell'}\left(f_{d_{\ell'}} + f^B_{d_{\kappa',\ell'}}\right)\left(c/(f_c+f)\right)t\right)\right. \tag{5.35}$$
$$\left.\times \exp j\left(\theta^{in}_{\kappa',\ell'} - 2\pi f^{in}_{d_{\ell'}} t - 2\pi f^{in,B}_{d_{\kappa',\ell'}} t\right)\right].$$

The FD-DG model with HPWs and IPWs, including MIMO characteristics for wideband and UWB systems, is obtained introducing the space array effect at both ends of the link. In this way, from Figure 5.5, the path travel distance along the arrays introduces phase changes in both HPWs and IPWs according to the distance among antenna elements, denoted by Δx_T at the TX array, and denoted by Δx_R at the RX array. The phase changes at the TX, for HPWs, are given by

$$\begin{aligned}\left(2\pi/\lambda_0\right)\Delta R_{T_\ell} &= \left(2\pi/\lambda_0\right)\cos\left(\phi_{T_\ell}\right)\Delta x_T,\\ \left(2\pi/\lambda_0^B\right)\Delta R^B_{T_{\kappa,\ell}} &= \left(2\pi/\lambda_0^B\right)\cos\left(\phi^B_{T_{\kappa,\ell}}\right)\Delta x_T,\end{aligned} \tag{5.36}$$

where, the fine resolution of the AOD, $\phi^B_{T_{\kappa,\ell}}$, are defined by

$$\phi^B_{T_{\kappa,\ell}} = \phi'_{T_\ell} - \varphi_T \pm \phi''_{T_{\kappa,\ell}}, \tag{5.37}$$

and $\phi''_{T_{\kappa,\ell}}$ are the AOD spreading, around ϕ_{T_ℓ}, due to the fine resolution within the scatterer interaction. ΔR_{T_ℓ} and $\Delta R^B_{T_{\kappa,\ell}}$ are the HPWs distance displacements at the TX, for the principal and high resolution components, respectively. For the RX array, the phase changes in the HPWs are given by

$$\begin{aligned}\left(2\pi/\lambda_0\right)\Delta R_{R_\ell} &= \left(2\pi/\lambda_0\right)\cos\left(\phi_{R_\ell}\right)\Delta x_R,\\ \left(2\pi/\lambda_0^B\right)\Delta R^B_{R_{\kappa,\ell}} &= \left(2\pi/\lambda_0^B\right)\cos\left(\phi^B_{R_{\kappa,\ell}}\right)\Delta x_R,\end{aligned} \tag{5.38}$$

where ΔR_{R_ℓ} and $\Delta R^B_{R_{\kappa,\ell}}$ are the HPWs distance displacements at the RX, for principal and high resolution components, respectively. For IPWs, in the direction of phase propagation (only at the RX), the phase changes are given by

$$\begin{aligned}\left(2\pi/\lambda_{eff_{\ell'}}\right)\Delta R^{in}_{R_{\ell'}} &= \left(2\pi/\lambda_{eff_{\ell'}}\right)\sin\left(\phi_{R_{\ell'}}\right)\Delta x_R,\\ \left(2\pi/\lambda^B_{eff_{\kappa',\ell'}}\right)\Delta R^{in,B}_{R_{\kappa',\ell'}} &= \left(2\pi/\lambda^B_{eff_{\kappa',\ell'}}\right)\sin\left(\phi^B_{R_{\kappa',\ell'}}\right)\Delta x_R,\end{aligned} \tag{5.39}$$

where $\Delta R^{in}_{R_{\ell'}}$ and $\Delta R^{in,B}_{R_{\kappa',\ell'}}$ are the distance displacement for the IPW paths along the RX array.

The phase terms given in (5.36), (5.38) and (5.39), are obtained only for nearest antennas. If we consider every possible antenna element position at the TX and RX arrays as

$$x_T = \Delta x_T\left(j-1\right), \tag{5.40}$$

$$x_R = \Delta x_R\left(i-1\right), \tag{5.41}$$

where $j=\{1,2,\cdots,M\}$, $i=\{1,2,\cdots,N\}$, being M and N the number of antenna elements at the TX and RX, respectively, the model given in (5.35) can be updated as follows

$$
\begin{aligned}
&\tilde{H}(f,t,x_T,x_R)= \\
&=\sum_{\ell=0}^{L-1}\sum_{\kappa=1}^{I_\ell}\Big[\tilde{b}_{\kappa,\ell}\exp j\Big(\theta_{\kappa,\ell}-2\pi f_{d_\ell}t-2\pi f_c\tau_\ell-2\pi f\tau_{\kappa,\ell}-2\pi f^B_{d_{\kappa,\ell}}t\Big) \\
&\quad\times\exp-j\Big(2\pi\lambda_0^{-1}\cos\Big(\phi_{T_\ell}\Big)x_T\Big)\exp-j\Big(2\pi\lambda_0^{-1}\cos\Big(\phi_{R_\ell}\Big)x_R\Big) \\
&\quad\times\exp-j\Big(2\pi\Big(\lambda_0^B\Big)^{-1}\cos\Big(\phi^B_{T_{\kappa,\ell}}\Big)x_T\Big)\exp-j\Big(2\pi\Big(\lambda_0^B\Big)^{-1}\cos\Big(\phi^B_{R_{\kappa,\ell}}\Big)x_R\Big)\Big]+ \\
&\quad+\sum_{\ell'=0}^{L-1}\sum_{\kappa'=1}^{I_{\ell'}}\Big[\exp\Big(-\alpha_{\kappa',\ell'}\Big(f_{d_{\ell'}}+f^B_{d_{\kappa',\ell'}}\Big)\big(c/(f_c+f)\big)t\Big) \\
&\quad\times\exp j\Big(\theta^{in}_{\kappa',\ell'}-2\pi f^{in}_{d_{\ell'}}t-2\pi f^{in,B}_{d_{\kappa',\ell'}}t\Big) \\
&\quad\times\exp-j\Big(2\pi\lambda^{-1}_{eff_{\ell'}}\sin\Big(\phi_{R_{\ell'}}\Big)x_R\Big)\exp-j\Big(2\pi\Big(\lambda^B_{eff_{\kappa',\ell'}}\Big)^{-1}\sin\Big(\phi_{R_{\kappa',\ell'}}\Big)x_R\Big)\Big].
\end{aligned}
\tag{5.42}
$$

For simplicity, other variables to describe the AODs and AOAs will be used. These variables are the direction of departure (DOD) and direction of arrival (DOA). For HPWs, the DOD are denoted by Ω_{T_ℓ} and $\Omega"_{T_{\kappa,\ell}}$, and the DOA are denoted by Ω_{R_ℓ} and $\Omega"_{R_{\kappa,\ell}}$. For IPWs, the DOA are denoted by $\Omega^{in}_{R_{\ell'}}$ $\Omega"^{in}_{R_{\kappa',\ell'}}$. These variables are given by:

$$
\begin{aligned}
&\Omega_{T_\ell}\triangleq\cos\Big(\phi_{T_\ell}\Big), \\
&\Omega"_{T_{\kappa,\ell}}\triangleq\cos\Big(\phi^B_{T_{\kappa,\ell}}\Big),
\end{aligned}
\tag{5.43}
$$

$$
\begin{aligned}
&\Omega_{R_\ell}\triangleq\cos\Big(\phi_{R_\ell}\Big), \\
&\Omega"_{R_{\kappa,\ell}}\triangleq\cos\Big(\phi^B_{R_{\kappa,\ell}}\Big),
\end{aligned}
\tag{5.44}
$$

$$
\begin{aligned}
&\Omega^{in}_{R_{\ell'}}\triangleq\sin\Big(\phi_{R_{\ell'}}\Big), \\
&\Omega"^{in}_{R_{\kappa',\ell'}}\triangleq\sin\Big(\phi^B_{R_{\kappa',\ell'}}\Big).
\end{aligned}
\tag{5.45}
$$

Finally, replacing (5.43)-(5.45) in (5.42), the FD-DG-MIMO model can be given by:

$$
\begin{aligned}
&\tilde{H}\left(f,t,x_T,x_R\right)= \\
&=\sum_{\ell=0}^{L-1}\sum_{\kappa=1}^{I_\ell}\Bigg[\tilde{b}_{\kappa,\ell}\exp j\left(\theta_{\kappa,\ell}-2\pi f_{d_\ell}t-2\pi f_c\tau_\ell-2\pi f\tau_{\kappa,\ell}-2\pi f_{d_{\kappa,\ell}}^{B}t\right) \\
&\quad\times\exp-j\left(2\pi\lambda_0^{-1}\Omega_{T_\ell}x_T\right)\exp-j\left(2\pi\lambda_0^{-1}\Omega_{R_\ell}x_R\right) \\
&\quad\times\exp-j\left(2\pi\left(\lambda_0^{B}\right)^{-1}\Omega''_{T_{\kappa,\ell}}x_T\right)\exp-j\left(2\pi\left(\lambda_0^{B}\right)^{-1}\Omega''_{R_{\kappa,\ell}}x_R\right)\Bigg]+ \\
&\quad+\sum_{\ell'=0}^{L-1}\sum_{\kappa'=1}^{I_{\ell'}}\Bigg[\exp\left(-\alpha_{\kappa',\ell'}\left(f_{d_{\ell'}}+f_{d_{\kappa',\ell'}}^{B}\right)\left(c/\left(f_c+f\right)\right)t\right) \\
&\quad\times\exp j\left(\theta_{\kappa',\ell'}^{in}-2\pi f_{d_{\ell'}}^{in}t-2\pi f_{d_{\kappa',\ell'}}^{in,B}t\right) \\
&\quad\times\exp-j\left(2\pi\lambda_{eff_{\ell'}}^{-1}\Omega_{R_{\ell'}}^{in}x_R\right)\exp-j\left(2\pi\left(\lambda_{eff_{\kappa',\ell'}}^{B}\right)^{-1}\Omega''^{in}_{R_{\kappa',\ell'}}x_R\right)\Bigg].
\end{aligned}
\tag{5.46}
$$

Note that this reference model considers each $\ell'=\ell$-th path related to a single $\ell=\ell'$-th scatterer. Subsequently, the possible $n=n'$-th component due to the $\ell,n=\ell',n'$-th scatterer that produce the same path propagation delays must be included. This means that the same travel distance from the TX to the RX via a (ℓ,n)-th scatterer must be modelled. Hence, the FD-DG-MIMO channel model, with motion at the RX side, considering all possible propagation effects, bandwidth effects, high central frequency effects, and space effects is given by

$$
\begin{aligned}
&\tilde{H}\left(f,t,x_T,x_R\right)= \\
&=\sum_{\ell=0}^{L-1}\sum_{n=1}^{N_\ell}\sum_{\kappa=1}^{I_\ell}\Bigg[\tilde{b}_{\kappa,n,\ell}\exp j\left(\theta_{\kappa,n,\ell}-2\pi f_{d_{n,\ell}}t-2\pi f\tau_{\kappa,\ell}-2\pi f_{d_{\kappa,n,\ell}}^{B}t\right) \\
&\quad\times\exp-j\left(2\pi\lambda_0^{-1}\Omega_{T_{n,\ell}}x_T\right)\exp-j\left(2\pi\lambda_0^{-1}\Omega_{R_{n,\ell}}x_R\right) \\
&\quad\times\exp-j\left(2\pi\left(\lambda_0^{B}\right)^{-1}\Omega''_{T_{\kappa,n,\ell}}x_T\right)\exp-j\left(2\pi\left(\lambda_0^{B}\right)^{-1}\Omega''_{R_{\kappa,n,\ell}}x_R\right)\Bigg]+ \\
&\quad+\sum_{\ell'=0}^{L-1}\sum_{n'=1}^{N_{\ell'}}\sum_{\kappa'=1}^{I_{\ell'}}\Bigg[\tilde{b}_{\kappa',n',\ell'}^{in}\exp j\left(\theta_{\kappa',n',\ell'}^{in}-2\pi f_{d_{n',\ell'}}^{in}t-2\pi f_{d_{\kappa',n',\ell'}}^{in,B}t\right) \\
&\quad\times\exp-j\left(2\pi\lambda_{eff_{n',\ell'}}^{-1}\Omega_{R_{n',\ell'}}^{in}x_R\right)\exp-j\left(2\pi\left(\lambda_{eff_{\kappa',n',\ell'}}^{B}\right)^{-1}\Omega''^{in}_{R_{\kappa',n',\ell'}}x_R\right)\Bigg],
\end{aligned}
\tag{5.47}
$$

where $N_{\ell'}=N_\ell$ is the number of components included in the same path propagation delay, and

$$\tilde{b}^{in}_{\kappa',n',\ell'} = \exp\left(-\alpha_{\kappa',n',\ell'}\left(f_{d_{n',\ell'}} + f^{B}_{d_{\kappa',n',\ell'}}\right)\left(c/(f_c + f)\right)t\right), \tag{5.48}$$

$$\tau_{\kappa,\ell} = \tau_{\ell} \pm \tau''_{\kappa,\ell}, \tag{5.49}$$

$$\tau''_{\kappa,\ell} = \left\langle \sin\left(\phi''_{R_{\kappa,n,\ell}}\right) R_{R_{n,\ell}} / c \right\rangle_{n}, \tag{5.50}$$

$$f_{d_{n,\ell}} = \frac{v}{\lambda_0}\cos\left(\phi_{R_{n,\ell}} + \varphi_R - \chi_R\right), \tag{5.51}$$

$$f^{B}_{d_{\kappa,n,\ell}} = \frac{v}{\lambda^{B}_0}\cos\left(\phi^{B}_{R_{\kappa,n,\ell}} + \varphi_R - \chi_R\right), \tag{5.52}$$

$$f^{in}_{d_{n',\ell'}} = \frac{v}{\lambda_{eff_{n',\ell'}}}\sin\left(\phi_{R_{n',\ell'}} + \varphi_R - \chi_R\right), \tag{5.53}$$

$$f^{in,B}_{d_{\kappa',n',\ell'}} = \frac{v}{\lambda^{B}_{eff_{\kappa',n',\ell'}}}\sin\left(\phi^{B}_{R_{\kappa',n',\ell'}} + \varphi_R - \chi_R\right), \tag{5.54}$$

$$\phi_{T_{n,\ell}} = \phi'_{T_{n,\ell}} - \varphi_T, \tag{5.55}$$

$$\phi_{R_{n,\ell}} = \phi'_{R_{n,\ell}} - \varphi_R, \tag{5.56}$$

$$\phi^{B}_{T_{\kappa,n,\ell}} = \phi'_{T_{n,\ell}} - \varphi_T \pm \phi''_{T_{\kappa,n,\ell}}, \tag{5.57}$$

$$\phi^{B}_{R_{\kappa,n,\ell}} = \phi'_{R_{n,\ell}} - \varphi_R \pm \phi''_{R_{\kappa,n,\ell}}, \tag{5.58}$$

$$\begin{aligned} \Omega_{T_{n,\ell}} &= \cos\left(\phi_{T_{n,\ell}}\right), \\ \Omega''_{T_{\kappa,n,\ell}} &= \cos\left(\phi^{B}_{T_{\kappa,n,\ell}}\right), \end{aligned} \tag{5.59}$$

$$\begin{aligned} \Omega_{R_{n,\ell}} &= \cos\left(\phi_{R_{n,\ell}}\right), \\ \Omega''_{R_{\kappa,n,\ell}} &= \cos\left(\phi^{B}_{R_{\kappa,n,\ell}}\right), \end{aligned} \tag{5.60}$$

$$\begin{aligned} \Omega^{in}_{R_{n',\ell'}} &= \sin\left(\phi_{R_{n',\ell'}}\right), \\ \Omega''^{in}_{R_{\kappa',n',\ell'}} &= \sin\left(\phi^{B}_{R_{\kappa',n',\ell'}}\right), \end{aligned} \tag{5.61}$$

$$\theta_{\kappa,n,\ell} = \theta'_{n,\ell} \pm \theta''_{\kappa,n,\ell}, \tag{5.62}$$

$$\theta'_{n,\ell} = \theta_{n,\ell} - 2\pi f_c \tau_{n,\ell} \tag{5.63}$$

$$\theta^{in}_{\kappa',n',\ell'} = \theta^{in}_{n',\ell'} \pm \theta''^{in}_{\kappa',n',\ell'}. \tag{5.64}$$

Note that (5.48) is also time dependent, which fulfil the affirmation given in [3] about the space-time dependency for the complex wavevectors defined in (5.4). Besides, due to the wideband signal, $\tilde{b}^{in}_{\kappa',n',\ell'}$ is also frequency dependent. To reduce the complexity of the model, $\tilde{b}^{in}_{\kappa',n',\ell'}$ will be assumed constant through t. Hence, the IPWs path gains, $\left\{\tilde{b}^{in}_{\kappa',n',\ell'}\right\}$, can be spitted as follows

$$\tilde{b}^{in}_{\kappa',n',\ell'} \approx \tilde{a}^{in}_{\ell'} c^{in}_{n,\ell} g^{in}_{\kappa,n,\ell}, \tag{5.65}$$

where

$$\begin{aligned} \tilde{a}^{in}_{\ell'} &= \exp\left(-\alpha_{\ell'}\left|f_{d_{n',\ell'}}\right|\lambda_0\right), \forall n', \\ c^{in}_{n',\ell'} &= \exp\left(-\alpha_{n',\ell'}\left|f_{d_{n',\ell'}}\right|\lambda_0\right), \\ g^{in}_{\kappa',n',\ell'} &= \exp\left(-\alpha_{n',\ell'}\left|f^{B}_{d_{\kappa',n',\ell'}}\right|\lambda^{B}_0\right), \end{aligned} \tag{5.66}$$

and (see (5.6))

$$\begin{aligned} \alpha_{\ell'} &= \sqrt{k^2_{eff_{\ell'}} - k^2_0}, \\ \alpha_{n',\ell'} &= \sqrt{k^2_{eff_{n',\ell'}} - k^2_0}, \\ \alpha_{\kappa',n',\ell'} &= \sqrt{k^2_{eff_{\kappa',n',\ell'}} - k^2_0}. \end{aligned} \tag{5.67}$$

On the other hand, the HPWs path gains $\left\{\tilde{b}_{\kappa,n,\ell}\right\}$ include the *delay gain coefficients*, denoted by $\left\{\tilde{a}_\ell\right\}$, the *Doppler gain coefficients* due to f_c, denoted by $\left\{c_{n,\ell}\right\}$, and the *Doppler gain coefficients* due to $f_c + f$, denoted by $\left\{g_{\kappa,n,\ell}\right\}$, hence:

$$\tilde{b}_{\kappa,n,\ell} = \tilde{a}_\ell c_{n,\ell} g_{\kappa,n,\ell}. \tag{5.68}$$

5.2.1. DG processes for HPWs

Using equations (5.47) to (5.68), it is possible to define the complex DG processes for each plane wave set. For HPWs, note from (5.47) and (5.49) that a set of delays, $\left\{\tau''_{\kappa,\ell}\right\} \in \mathbb{R}$, is included to model the fine scattering mechanisms. Therefore, a set of frequency-spatio-temporal complex DG processes must be defined for HPWs based in (5.47), which is given by

$$\begin{aligned}&\tilde{\mu}_{\ell}\left(f,t,x_T,x_R\right)=\\&=\sum_{n=1}^{N_{\ell}}\Big[c_{n,\ell}\tilde{\mu}''_{n,\ell}\left(f,t,x_T,x_R\right)\exp j\left(\theta'_{n,\ell}-2\pi f_{d_{n,\ell}}t\right)\\&\quad\times\exp- j\left(2\pi\lambda_0^{-1}\Omega_{T_{n,\ell}}x_T\right)\exp- j\left(2\pi\lambda_0^{-1}\Omega_{R_{n,\ell}}x_R\right)\Big],\end{aligned}\tag{5.69}$$

where

$$\begin{aligned}&\tilde{\mu}''_{n,\ell}\left(f,t,x_T,x_R\right)=\\&=\sum_{\kappa=1}^{I_{\ell}}\Big[g_{\kappa,n,\ell}\exp j\left(\theta''_{\kappa,n,\ell}-2\pi f^{B}_{d_{\kappa,n,\ell}}t\right)\exp- j\left(2\pi\tau_{\kappa,\ell}f\right)\\&\quad\times\exp- j\left(2\pi\left(\lambda_0^{B}\right)^{-1}\Omega''_{T_{\kappa,n,\ell}}x_T\right)\exp- j\left(2\pi\left(\lambda_0^{B}\right)^{-1}\Omega''_{R_{\kappa,n,\ell}}x_R\right)\Big].\end{aligned}\tag{5.70}$$

To solve the cross products frequency-angle-space in (5.70), consider a frequency dependent wavelength $\lambda(f)$ (due to the wideband signal) as a discrete function defined as follows

$$\lambda[f_{\kappa}]=\frac{c}{f_c+f_{\kappa}},\tag{5.71}$$

where $f_{\kappa}=-B/2+(\kappa-1)\Delta f$, $\kappa=\{1,2,\cdots,I_{\ell}\}$ and Δf is the predefined resolution in the frequency domain useful to introduce the fine scattering components in (5.70). The equation (5.71) can be replaced by

$$\lambda[f'']=\left(\frac{1}{1+f''}\right)\lambda_0,\tag{5.72}$$

where

$$f''=f_{\kappa}/f_c.\tag{5.73}$$

Hence, equation (5.72) can be approximated using the geometric series

$$\lambda[f'']=\lambda_0\sum_{z=0}^{\infty}(-f'')^{z}.\quad|-f''|<1\tag{5.74}$$

The equation (5.74) is fulfilled if $|f_{\kappa}|<f_c\ \forall\kappa$, or $B<2f_c$. Reorganizing (5.74), it is then found

$$\lambda[f'']=\lambda_0+\lambda_0\sum_{z=1}^{\infty}(-f'')^{z}.\quad|-f''|<1\tag{5.75}$$

Using (5.75), it is possible to choose a set of constant values for the second term, according to the relative bandwidth given in (5.73), which is defined always inside of the interval (-1,1). Based on this consideration, it is shown in Figure 5.6 the variations of the relative wavelength without the carrier component, i.e., $\left|\left(\lambda[f\,'']/\lambda_0 - 1\right)\right|$, for the geometric series in (5.75) using a $3*10^3$ polynomial approximation. In Figure 5.6.a, $B = 7$ GHz and $f_c = \{4,6,12\}$ GHz. On the other hand, in Figure 5.6.b, $B = 7$ GHz and $f_c = \{6,7,12\}$ GHz, and in Figure 5.6.c $B = 1$ GHz and $f_c = \{6,7,12\}$ GHz. Note that B has been chosen wider than the bandwidth used during the experimental analysis, since this chapter is aimed to model general wideband MIMO channels. Moreover, note that the axes have different references as the span for visualization was different in each case.

Figure 5.6 shows that the possible higher phase variations (and non-linear trends) due to the cross products frequency-angle-space in the HPWs are presented at low central frequencies for $B < 2f_c$. If the central frequency, f_c, increases, and the bandwidth $B < f_c$, the wavelength variations due to the wideband signal, denoted by

$$\lambda_0^B = \lambda_0 \sum_{z=1}^{\infty} (-f\,'')^z, \quad |-f\,''| < 1 \tag{5.76}$$

can be modelled as second-order polynomial function, as follows:

$$\lambda_0^B \approx \lambda_0 \left(1.2712 f\,''^2 - 1.1835 f\,'' - 0.0073\right), \quad |f\,''| < 0.5 \tag{5.77}$$

This function has been reached by means of a linear regression considering the case $B = 7$ GHz, $f_c = 7$ GHz, and $I_\ell = 4000$, since such case includes other configurations as long as $B < f_c$, where most of mobile communications systems are included. Figure 5.7 shows the results for the geometric series, the second-order polynomial function and the error bounds. The error bounds indicate that an error of $0.05\lambda_0$ is introduced with the model approximation, which have not significant effects in the phases of the HPWs in (5.70).

For the subsequent analysis, and based on the results presented above, it will be then used the approximation

$$\lambda_0^B \approx \lambda_0 \varepsilon_\kappa, \tag{5.78}$$

where ε_κ is given as follows

$$\varepsilon_\kappa = 1.2712\left(\frac{f_\kappa}{f_c}\right)^2 - 1.1835\left(\frac{f_\kappa}{f_c}\right) - 0.0073, \quad \text{with } \varepsilon_\kappa \neq 0 \tag{5.79}$$

Besides, based on (5.78), the equation (5.52) can be approximated as follows

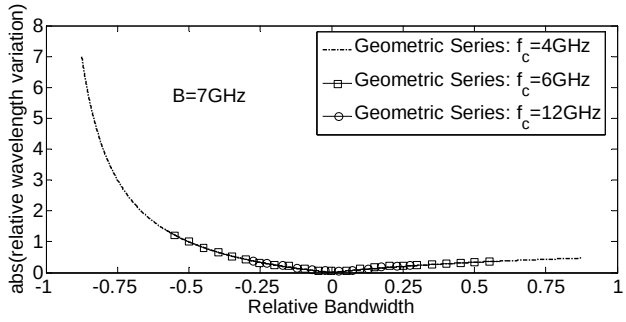

a)

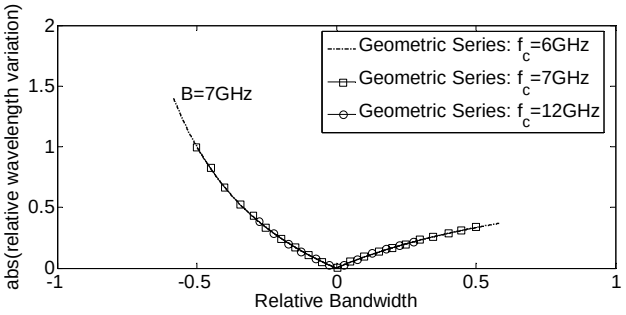

b)

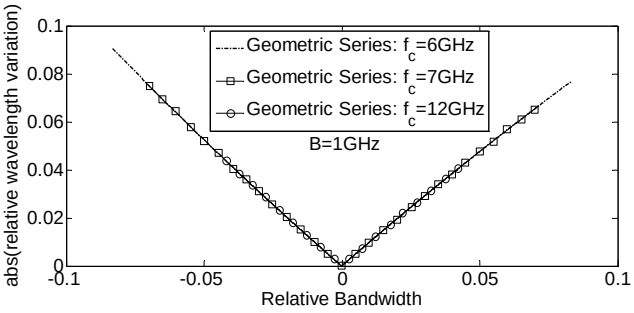

c)

Figure 5.6. Variation and trend of the relative wavelength vs. relative bandwidth: geometric series approximation, a) for $f_c = \{4,6,12\}$ GHz and $B = 7$ GHz, b) for $f_c = \{6,7,12\}$ GHz and $B = 7$ GHz and c) $f_c = \{4,6,12\}$ GHz and $B = 1$ GHz.

$$f^{B}_{d_{\kappa,n,\ell}} \approx f_{d_{n,\ell}} \cdot u_{\kappa,n,\ell}, \tag{5.80}$$

where

$$u_{\kappa,n,\ell} = \frac{\cos\left(\phi^{B}_{R_{\kappa,n,\ell}} + \varphi_R - \chi_R\right)}{\varepsilon_\kappa \cos\left(\phi_{R_{n,\ell}} + \varphi_R - \chi_R\right)}. \tag{5.81}$$

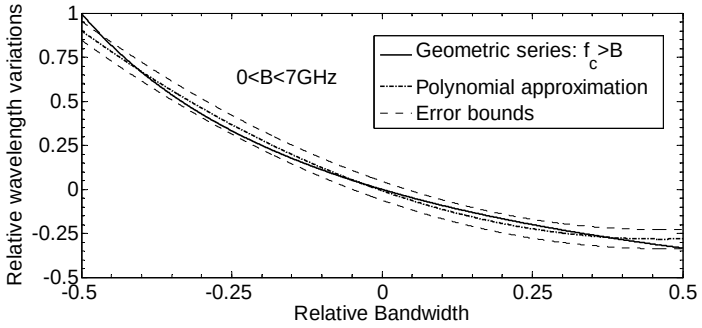

Figure 5.7. Relative wavelength variations: second-order polynomial approximation, geometric series, and error bounds for $f_c > 7$ GHz and $0 < B < 7$ GHz.

On the other hand, the DOD and DOA spreading included in (5.69), i.e., $\Omega"_{T_{\kappa,n,\ell}}$ and $\Omega"_{R_{\kappa,n,\ell}}$, respectively, can be expressed in terms of $\Omega_{T_{n,\ell}}$ and $\Omega_{R_{n,\ell}}$. In this way, it is assumed that the AOA spreading, $\phi"_{R_{\kappa,n,\ell}}$, follows a Laplace distribution with zero mean and standard deviation $\sigma_{\phi"}$ as is suggested in [9]:

$$p_{\phi"_{R_{\kappa,n,\ell}}}\left(\phi"_{R_{\kappa,n,\ell}}\right) = \frac{1}{\sigma_{\phi"}\sqrt{2}} \exp\left(-\left|\frac{\phi"_{R_{\kappa,n,\ell}}\sqrt{2}}{\sigma_{\phi"}}\right|\right), \tag{5.82}$$

and the AOD spreading, $\phi"_{T_{\kappa,n,\ell}}$, follows a distribution expressed as function of $p_{\phi"_{R_{\kappa,n,\ell}}}\left(\phi"_{R_{\kappa,n,\ell}}\right)$ [9]:

$$p_{\phi"_{T_{\kappa,n,\ell}}}\left(\phi"_{T_{\kappa,n,\ell}}\right) = \frac{\gamma^2 + 1 - 2\gamma\cos\left(\phi_{R_{n,\ell}} + \phi"_{R_{\kappa,n,\ell}}\right)}{\gamma^2 - 1} p_{\phi"_{R_{\kappa,n,\ell}}}\left(\phi"_{R_{\kappa,n,\ell}}\right), \tag{5.83}$$

where γ denotes the ratio of the propagation delay τ_ℓ of the scattered component to the propagation delay of the LOS component τ_0, i.e., $\gamma = \tau_\ell / \tau_0$.

In Figure 5.8 the theoretical distributions and the data obtained for a Laplacian random synthetic generator with $\sigma_{\phi"} = \{4º, 6º, 8º\}$ are plotted to model the AOA and AOD spreading, using $\phi_{R_{n,\ell}} = 30^o$ and $\gamma = 1.5$, which include values used in the literature [9],[13]. As it is appreciated, the AOA and AOD spreading are concentrated around 0º (relative to $\phi_{R_{n,\ell}}$ and $\phi_{T_{n,\ell}}$, respectively), with low probabilities for angles higher that 10º, even for higher values of $\sigma_{\phi"}$.

Following (5.82), it is then possible to obtain the theoretical and experimental PDF of the delay spreading, $\tau"_{\kappa,\ell}$, from (5.50). Here, only the experimental PDF is taken into account using the Laplacian random synthetic

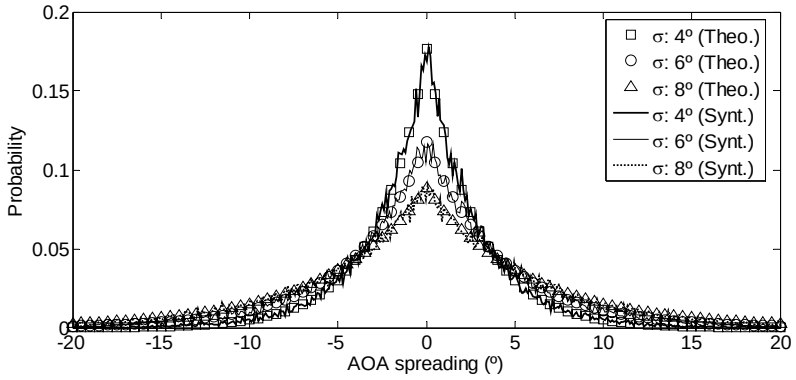

a)

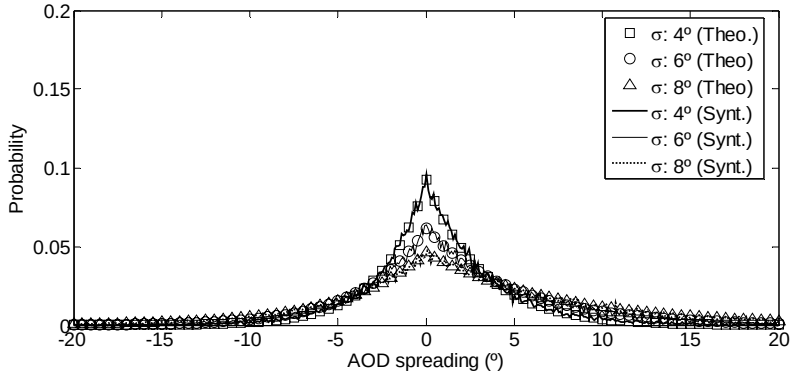

b)

Figure 5.8. PDFs of the theoretical and simulated distributions for, a) AOA spreading with $\sigma_{\phi''} = \{4^\circ, 6^\circ, 8^\circ\}$, and b) AOD spreading with $\sigma_{\phi''} = \{4^\circ, 6^\circ, 8^\circ\}$, $\phi_{R_{n,\ell}} = 30^\circ$ and $\gamma = 1.5$.

generator for the AOA spreading. Figure 5.9 depicts the PDF of $\tau''_{\kappa,\ell}$ around τ_ℓ for different $\sigma_{\phi''}$, with $R_{R_{n,\ell}} = 10$ m. Note that that the delay spreading caused by the fine scattering can reach up to 20 ns for wider AOA spreading but with low probabilities. In the case of $B = 200$ MHz, as the measurements performed for this Dissertation, the system resolution in the delay domain (i.e., 5 ns) can still solve some of these scattering components, but this effect is more appreciable (and probable) for UWB systems (resolution about 0.1 ns).

On the other hand, based on equations (5.55)-(5.61), $\Omega''_{T_{\kappa,n,\ell}}$ and $\Omega''_{R_{\kappa,n,\ell}}$ can be given by

$$\Omega''_{T_{\kappa,n,\ell}} = \Omega_{T_{n,\ell}} \alpha_{T_{\kappa,n,\ell}} - \sin\left(\phi'_{T_{n,\ell}} - \varphi_T\right) \alpha'_{T_{\kappa,n,\ell}}, \tag{5.84}$$

$$\Omega''_{R_{\kappa,n,\ell}} = \Omega_{R_{n,\ell}} \alpha_{R_{\kappa,n,\ell}} - \sin\left(\phi'_{R_{n,\ell}} - \varphi_R\right) \alpha'_{R_{\kappa,n,\ell}}, \tag{5.85}$$

where

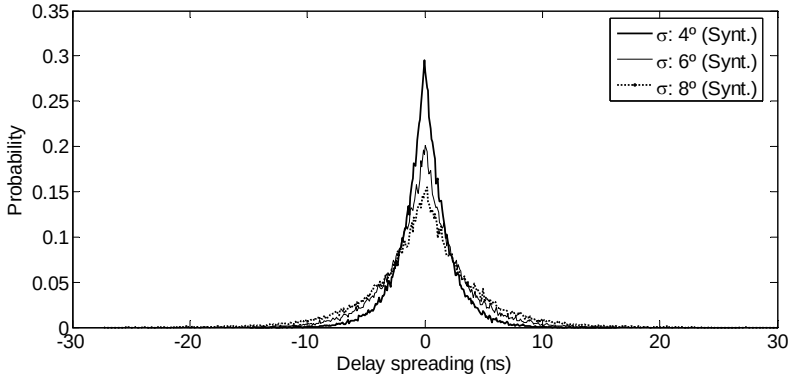

Figure 5.9. Experimental PDF of $\tau''_{\kappa,\ell}$ for AOA spreading, $\phi''_{R_{\kappa,n,\ell}}$, with $\sigma_{\phi''} = \{4^\circ, 6^\circ, 8^\circ\}$.

$$\alpha_{T_{\kappa,n,\ell}} = \cos\left(\phi''_{T_{\kappa,n,\ell}}\right), \quad \text{and} \quad \alpha'_{T_{\kappa,n,\ell}} = \sin\left(\phi''_{T_{\kappa,n,\ell}}\right), \tag{5.86}$$

$$\alpha_{R_{\kappa,n,\ell}} = \cos\left(\phi''_{R_{\kappa,n,\ell}}\right), \quad \text{and} \quad \alpha'_{R_{\kappa,n,\ell}} = \sin\left(\phi''_{R_{\kappa,n,\ell}}\right). \tag{5.87}$$

Since $\alpha'_{T_{\kappa,n,\ell}}$ and $\alpha'_{R_{\kappa,n,\ell}}$ have a minor contribution to $\Omega''_{T_{\kappa,n,\ell}}$ and $\Omega''_{R_{\kappa,n,\ell}}$, respectively, the second terms in (5.84) and (5.85) can be neglected. These approximations can be verified analyzing the PDF of $\Omega''_{R_{\kappa,n,\ell}}$ assuming a uniformly distributed random variable for $\phi'_{T_{n,\ell}}$ in the interval $[0, 2\pi)$, and a random variable for $\phi''_{R_{\kappa,n,\ell}}$ as outcomes of a random generator with Laplace distribution. For $\sigma_{\phi''} = 8^\circ$, in Figure 5.10 it is plotted the PFD of $\Omega''_{R_{\kappa,n,\ell}}$ as a result of (5.84), and also under the assumption that the second terms is neglected. As it is depicted in Figure 5.10, the approximations have a good fit with the original variables, hence:

$$\Omega''_{T_{\kappa,n,\ell}} \approx \Omega_{T_{n,\ell}} \alpha_{T_{\kappa,n,\ell}}, \tag{5.88}$$

$$\Omega''_{R_{\kappa,n,\ell}} \approx \Omega_{R_{n,\ell}} \alpha_{R_{\kappa,n,\ell}}. \tag{5.89}$$

In the same way, for further analysis, equation (5.81) could be expressed as follows

$$u_{\kappa,n,\ell} \approx \frac{\alpha_{R_{\kappa,n,\ell}}}{\varepsilon_\kappa}. \tag{5.90}$$

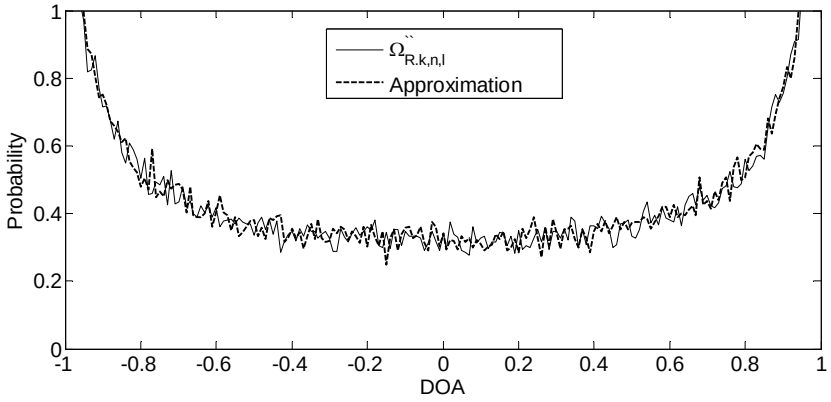

Figure 5.10. Experimental PDF of $\Omega"_{R_{\kappa,n,\ell}}$, with and without approximations.

In order to explore the phase modifications introduced by the coefficients $u_{\kappa,n,\ell}$, in Figure 5.11 are plotted the experimental distribution of $\measuredangle \exp\left(j\left(u_{\kappa,n,\ell}\right)\right)$ for different sequences of ε_κ (see (5.79)) with different bandwidths and central frequencies. It is assumed $\sigma_{\phi"} = 8^{\circ}$ for the random variables $\phi"_{R_{\kappa,n,\ell}}$. The results are compared using (5.81) and (5.90). It is proved here that the proposed approximations have a good fit for all distributions, and that the PDF follows a uniform distribution for small relative bandwidths.

Therefore, based on all approximations presented above, equation (5.70) can be expressed as follows:

$$\begin{aligned}
&\tilde{\mu}"_{n,\ell}(f,t,x_T,x_R) \approx \\
&\approx \sum_{\kappa=1}^{I_\ell}\Big[g_{\kappa,n,\ell}\exp j\left(\theta"_{\kappa,n,\ell} - 2\pi f_{d_{n,\ell}} u_{\kappa,n,\ell} t\right)\exp - j\left(2\pi\tau_{\kappa,\ell} f\right) \\
&\quad \times \exp - j\left[2\pi(\lambda_0)^{-1}\Omega_{T_{n,\ell}}\frac{\alpha_{T_{\kappa,n,\ell}}}{\varepsilon_\kappa}x_T\right] \\
&\quad \times \exp - j\left[2\pi(\lambda_0)^{-1}\Omega_{R_{n,\ell}}\frac{\alpha_{R_{\kappa,n,\ell}}}{\varepsilon_\kappa}x_R\right]\Big].
\end{aligned} \tag{5.91}$$

5.2.2. Random phases for HPWs

Following the formulation given in (5.91), note that $\tau_{\kappa,\ell}$ is not indexed with n, in the same way that τ_ℓ in (5.49). On the other hand, in (5.69) and (5.91), the set of phases $\left\{\theta'_{n,\ell}\right\}$ and $\left\{\theta"_{\kappa,n,\ell}\right\}$, respectively, will be considered as independent-uncorrelated outcomes of a random generator for each κ, n, and ℓ-

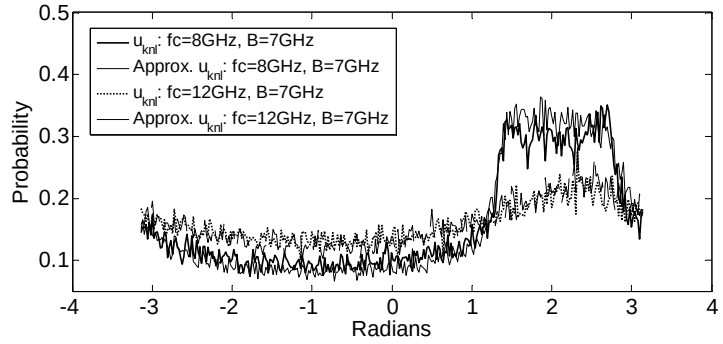

a)

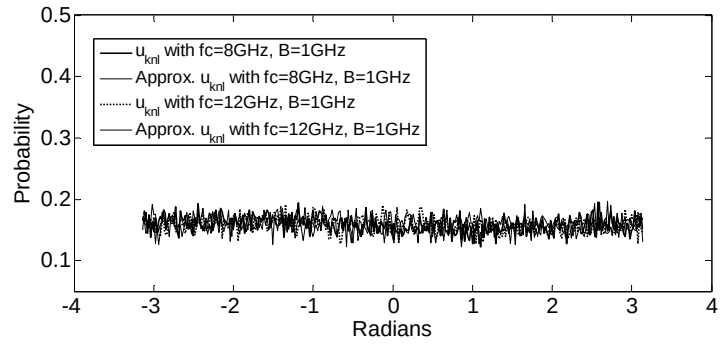

b)

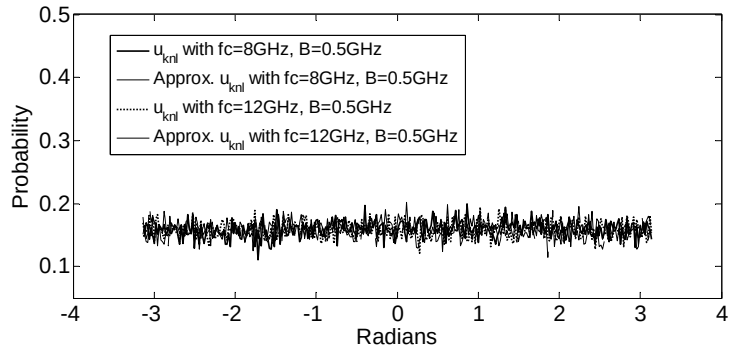

c)

Figure 5.11. Experimental PDF of $\angle\exp\left(j\left(u_{\kappa,n,\ell}\right)\right)$, with and without approximations under different bandwidths and central frequencies.

th HPW, having each one a uniform distribution $[0,2\pi)$. These independent-uncorrelated phases have the following statistic characteristics:

$$\mathrm{E}\left[e^{j\left(\theta'_{n,\ell}-\theta'_{m,s}\right)}\right]=0,\quad \forall\left(n,\ell\right)\neq\left(m,s\right) \tag{5.92}$$

$$\mathrm{E}\left[e^{j\left(\theta''_{\kappa,n,\ell}-\theta''_{r,m,s}\right)}\right]=0,\quad \forall(\kappa,n,\ell)\neq(r,m,s) \tag{5.93}$$

$$\mathrm{E}\left[\theta'_{n,\ell}\,\theta''_{\kappa,n,\ell}\right]-\mathrm{E}\left[\theta'_{n,\ell}\right]\mathrm{E}\left[\theta''_{\kappa,n,\ell}\right]=0.\quad \forall(\kappa,n,\ell) \tag{5.94}$$

The joint PDF of theses phases, denoted by $p_{\boldsymbol{\Psi}}\left(\hat{\boldsymbol{\theta}}\right)$, is as follows

$$p_{\boldsymbol{\Psi}}\left(\hat{\boldsymbol{\theta}}\right)=\frac{1}{(2\pi)^{\left(N_\ell L(1+I_\ell)\right)}},\quad 0\leq\hat{\boldsymbol{\theta}}<2\pi \tag{5.95}$$

where $\hat{\boldsymbol{\theta}}\in\mathbb{R}^{N_\ell L(1+I_\ell)\times 1}$ is a vector containing both set of random phases $\left\{\hat{\theta}_p\right\}=\left\{\theta'_{n,\ell}\right\}\cup\left\{\theta''_{\kappa,n,\ell}\right\}$, with entries $0\leq\hat{\theta}_p<2\pi$, and $p=\left\{1,\cdots,N_\ell L\left(1+I_\ell\right)\right\}$.

5.2.3. DG processes for IPWs

From (5.47), the spatio-temporal complex DG processes for the IPWs are defined by

$$\begin{aligned}\tilde{\mu}^{in}_{\ell'}(t,x_R)=&\sum_{n'=1}^{N_{\ell'}}\left[c^{in}_{n,\ell}\tilde{\mu}''^{in}_{n',\ell'}(t,x_R)\right]\exp j\left(\theta^{in}_{n',\ell'}-2\pi f^{in}_{d_{n',\ell'}}t\right)\\&\times\exp- j\left(2\pi\lambda^{-1}_{eff_{n',\ell'}}\Omega^{in}_{R_{n',\ell'}}x_R\right)\Bigg],\end{aligned} \tag{5.96}$$

$$\begin{aligned}\tilde{\mu}''^{in}_{n',\ell'}(t,x_R)=&\sum_{\kappa'=1}^{I_{\ell'}}\left[g^{in}_{\kappa',n',\ell'}\exp j\left(\theta''^{in}_{\kappa',n',\ell'}-2\pi f^{in,B}_{d_{\kappa',n',\ell'}}t\right)\right.\\&\left.\times\exp- j\left(2\pi\lambda^{-1}_{eff_{\kappa',n',\ell'}}\Omega''^{in}_{R_{\kappa',n',\ell'}}x_R\right)\right].\end{aligned} \tag{5.97}$$

Note that these processes are not defined in frequency domain, besides, from equation (5.5), note that $\lambda_{eff_{\ell'}}<\lambda_0$. Hence, as an approximation for modelling purposes, it is assumed that the sets of wavelengths $\left\{\lambda_{eff_{n',\ell'}}\right\}$ and $\left\{\lambda_{eff_{\kappa',n',\ell'}}\right\}$ are constants values for all waves components, i.e., $\lambda_{eff_{n',\ell'}}=\lambda_{eff},\forall n',\ell'$ and $\lambda_{eff_{\kappa',n',\ell'}}=\lambda^{B}_{eff},\forall\kappa',n',\ell'$, respectively, and that such values are a scaled value of λ_0 and λ^{B}_{0}, respectively:

$$\lambda_{eff}\approx\eta\lambda_0, \tag{5.98}$$

$$\lambda^{B}_{eff}\approx\eta\lambda^{B}_{0}, \tag{5.99}$$

where $0<\eta<1$. Based on these approximations, the Doppler frequencies $f_{d_{n',\ell'}}^{in}$ and $f_{d_{\kappa',n',\ell'}}^{in,B}$, from (5.53) and (5.54), respectively, can be expressed as follows

$$f_{d_{n',\ell'}}^{in} \approx f_{d_{n',\ell'}} u'_{n',\ell'}, \tag{5.100}$$

$$f_{d_{\kappa',n',\ell'}}^{in,B} \approx f_{d_{n',\ell'}} u_{\kappa',n',\ell'} u''_{\kappa',n',\ell'}, \tag{5.101}$$

where

$$u'_{n',\ell'} = \frac{\sin\left(\phi_{R_{n',\ell'}} + \varphi_R - \chi_R\right)}{\eta\cos\left(\phi_{R_{n',\ell'}} + \varphi_R - \chi_R\right)}, \tag{5.102}$$

$$u''_{\kappa',n',\ell'} = \frac{\sin\left(\phi^B_{R_{\kappa',n',\ell'}} + \varphi_R - \chi_R\right)}{\eta\cos\left(\phi^B_{R_{\kappa',n',\ell'}} + \varphi_R - \chi_R\right)}. \tag{5.103}$$

Replacing (5.81) in (5.101), it is then obtained

$$f_{d_{\kappa',n',\ell'}}^{in,B} \approx f_{d_{n',\ell'}} u_{\kappa',n',\ell'}^{in} \tag{5.104}$$

where

$$u_{\kappa',n',\ell'}^{in} = \frac{\sin\left(\phi^B_{R_{\kappa',n',\ell'}} + \varphi_R - \chi_R\right)}{\varepsilon_\kappa \eta\cos\left(\phi_{R_{n',\ell'}} + \varphi_R - \chi_R\right)} \tag{5.105}$$

Moreover, note that $\alpha_{\ell'}$, $\alpha_{n',\ell'}$ and $\alpha_{\kappa',n',\ell'}$, from (5.67), based on (5.78), (5.98), and (5.99), can then be defined as

$$\begin{aligned} \alpha_{\ell'} &\approx \sqrt{\left(2\pi/(\eta\lambda_0)\right)^2 - k_0^2}, \\ \alpha_{n',\ell'} &\approx \sqrt{\left(2\pi/(\eta\lambda_0)\right)^2 - k_0^2}, \\ \alpha_{k',n',\ell'} &\approx \sqrt{\left(2\pi/(\eta\lambda_0\varepsilon_\kappa)\right)^2 - k_0^2}, \end{aligned} \tag{5.106}$$

and (5.66) can be given by (see also (5.90)):

$$\begin{aligned}\tilde{a}_{\ell'}^{in} &\approx \exp\left(-\alpha_{\ell'}\left|f_{d_{n',\ell'}}\right|\lambda_0\right),\forall n',\\ c_{n',\ell'}^{in} &\approx \exp\left(-\alpha_{n',\ell'}\left|f_{d_{n',\ell'}}\right|\lambda_0\right),\\ g_{\kappa',n',\ell'}^{in} &\approx \exp\left(-\alpha_{\kappa',n',\ell'}\left|f_{d_{n',\ell'}}\right|\alpha_{R_{\kappa',n',\ell'}}\lambda_0\right).\end{aligned} \tag{5.107}$$

On the other hand, in order to explore the phase modifications introduced by means of the coefficients $u_{\kappa',n',\ell'}^{in}$, in Figure 5.12 are plotted the experimental distribution of $\measuredangle\exp\left(j\left(u_{\kappa',n',\ell'}^{in}\right)\right)$ for different sequences of ε_κ (with different bandwidths and central frequencies). It is assumed $\sigma_{\phi''}=8^{\circ}$ for the random variables $\phi''_{R_{\kappa,n,\ell}}$ and $\eta=\{0.5,0.9\}$. It is proved here that the PDF follows a uniform distribution for each relative bandwidth and η.

On the other hand, the DOA and DOA spreading for IPWs, $\Omega_{R_{n',\ell'}}^{in}$ and $\Omega''^{in}_{R_{\kappa',n',\ell'}}$, respectively, can be expressed in terms of $\Omega_{R_{n',\ell'}}$ and $\Omega''_{R_{\kappa',n',\ell'}}$, respectively. Based on (5.60) and (5.61) it is then obtained

$$\begin{aligned}\Omega_{R_{n',\ell'}}^{in} &= \sqrt{1-\Omega_{R_{n',\ell'}}^2},\\ \Omega''^{in}_{R_{\kappa',n',\ell'}} &\approx \sqrt{1-\left(\Omega_{R_{n',\ell'}}\alpha_{R_{\kappa',n',\ell'}}\right)^2},\end{aligned} \tag{5.108}$$

Based on the equalities and approximations presented above, equations (5.96) and (5.97) can be expressed as follows:

$$\begin{aligned}\tilde{\mu}_{\ell'}^{in}(t,x_R) \approx \sum_{n'=1}^{N_{\ell'}}\Big[&c_{n',\ell'}^{in}\tilde{\mu}''^{in}_{n',\ell'}(t,x_R)\exp j\left(\theta_{n',\ell'}^{in}-2\pi f_{d_{n',\ell'}}u'_{n',\ell'}t\right)\\ &\times\exp- j\left(2\pi\lambda_0^{-1}\sqrt{1-\Omega_{R_{n',\ell'}}^2}\,\frac{1}{\eta}x_R\right)\Big],\end{aligned} \tag{5.109}$$

$$\begin{aligned}\tilde{\mu}''^{in}_{n',\ell'}(t,x_R) \approx \sum_{\kappa'=1}^{I_{\ell'}}\Big[&g_{\kappa',n',\ell'}^{in}\exp j\left(\theta''^{in}_{\kappa',n',\ell'}-2\pi f_{d_{n',\ell'}}u_{\kappa',n',\ell'}^{in}t\right)\\ &\times\exp- j\left(2\pi\lambda_0^{-1}\sqrt{1-\left(\Omega_{R_{n',\ell'}}\alpha_{R_{\kappa',n',\ell'}}\right)^2}\,\frac{1}{\varepsilon_\kappa\eta}x_R\right)\Big].\end{aligned} \tag{5.110}$$

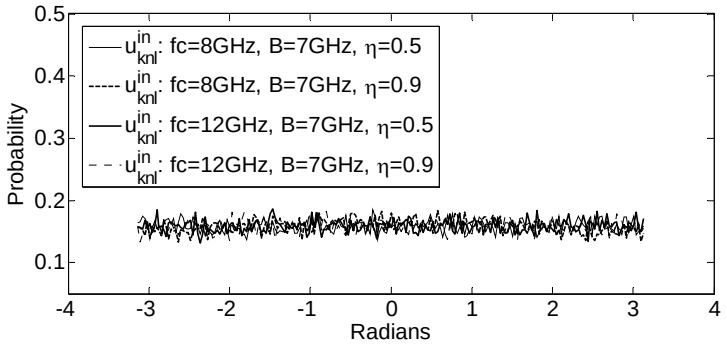

a)

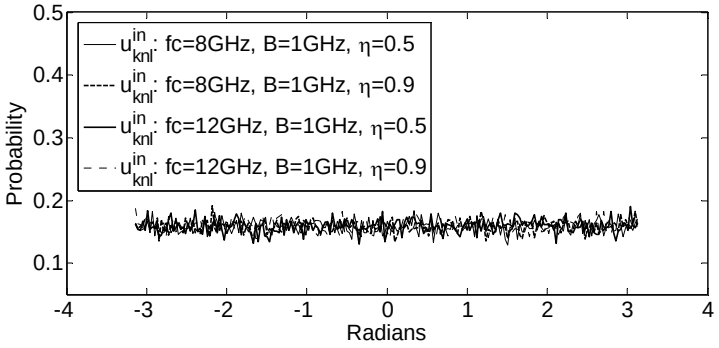

b)

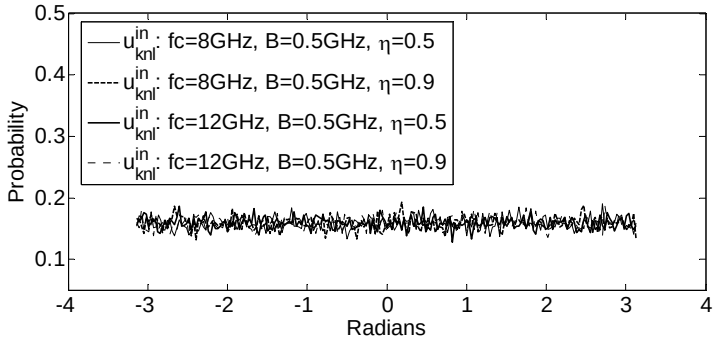

c)

Figure 5.12. Experimental PDF of $\angle\exp\left(j\left(u^{in}_{\kappa',n',\ell'}\right)\right)$, under different B and central f_c.

5.2.4. Random phases for IPWs

In the same way that HPWs, the set of IPW phases $\left\{\theta^{in}_{n',\ell'}\right\}$ and $\left\{\theta''^{in}_{\kappa',n',\ell'}\right\}$ are considered as independent-uncorrelated outcomes of a random generator having a uniform distribution $[0,2\pi)$, with the following statistic characteristics:

$$\mathrm{E}\left[e^{j\left(\theta^{in}_{n',\ell'}-\theta^{in}_{m',s'}\right)}\right]=0,\quad \forall\left(n',\ell'\right)\neq\left(m',s'\right) \tag{5.111}$$

$$\mathrm{E}\left[e^{j\left(\theta''^{in}_{\kappa',n',\ell'}-\theta''^{in}_{r',m',s'}\right)}\right]=0,\quad \forall\left(\kappa',n',\ell'\right)\neq\left(r',m',s'\right) \tag{5.112}$$

$$\mathrm{E}\left[\theta^{in}_{n',\ell'}\theta''^{in}_{\kappa',n',\ell'}\right]-\mathrm{E}\left[\theta^{in}_{n',\ell'}\right]\mathrm{E}\left[\theta''^{in}_{\kappa',n',\ell'}\right]=0,\quad \forall\left(\kappa',n',\ell'\right) \tag{5.113}$$

$$p_{\boldsymbol{\Psi}^{\mathrm{in}}}\left(\hat{\boldsymbol{\theta}}^{\mathrm{in}}\right)=\frac{1}{\left(2\pi\right)^{\left(N_{\ell'}L\left(1+I_{\ell'}\right)\right)}},\quad 0\leq\hat{\boldsymbol{\theta}}^{\mathrm{in}}<2\pi \tag{5.114}$$

where $\hat{\boldsymbol{\theta}}^{\mathrm{in}}\in\mathbb{R}^{N_{\ell'}L\left(1+I_{\ell'}\right)\times 1}$ is a vector containing both set of random phases $\left\{\hat{\theta}^{in}_{p'}\right\}=\left\{\theta^{in}_{n',\ell'}\right\}\cup\left\{\theta''^{in}_{\kappa',n',\ell'}\right\}$, with entries $0\leq\hat{\theta}^{in}_{p'}<2\pi$, and $p'=\left\{1,\cdots,N_{\ell'}L\left(1+I_{\ell'}\right)\right\}$.

So far independent-uncorrelated characteristics for the phases in each group of plane waves are fulfilled. Other useful characteristic for the proposed model is the independent-uncorrelated phases between HPWs and IPWs, i.e.,

$$\mathrm{E}\left[\left(\hat{\boldsymbol{\theta}}-\mathrm{E}\left[\hat{\boldsymbol{\theta}}\right]\right)\left(\hat{\boldsymbol{\theta}}^{\mathrm{in}}-\mathrm{E}\left[\hat{\boldsymbol{\theta}}^{\mathrm{in}}\right]\right)^{T}\right]=\mathbf{0}_{N_\ell L\left(1+I_\ell\right)}, \tag{5.115}$$

$$p_{\boldsymbol{\Psi}^{\mathrm{tot}}}\left(\hat{\boldsymbol{\theta}}^{\mathrm{tot}}\right)=\frac{1}{\left(2\pi\right)^{2\left(N_\ell L\left(1+I_\ell\right)\right)}},\quad 0\leq\hat{\boldsymbol{\theta}}^{\mathrm{tot}}<2\pi \tag{5.116}$$

where $\mathbf{0}_{N_\ell L\left(1+I_\ell\right)}$ indicates a $N_\ell L\left(1+I_\ell\right)\times N_\ell L\left(1+I_\ell\right)$ cero matrix and $\hat{\boldsymbol{\theta}}^{\mathrm{tot}}\in\mathbb{R}^{2N_\ell L\left(1+I_\ell\right)\times 1}$ is a vector containing the elements of $\hat{\boldsymbol{\theta}}$ and $\hat{\boldsymbol{\theta}}^{\mathrm{in}}$. Note that it is assumed $N_\ell=N_{\ell'}$ and $I_\ell=I_{\ell'}$, $\forall\ell$, with $\ell=\ell'$.

5.2.5. Uncorrelated-Scattering for HPWs and IPWs

The useful uncorrelated-scattering (US) condition, to derive the FD-DGUS-MIMO model, is obtained imposing US components for different τ_ℓ and $\tau''_{\kappa,\ell}$, and US condition between HPWs and IPWs (necessary for the formulation of the PSD functions). This means that the DG processes must be all uncorrelated:

$$\mathrm{E}\left[\tilde{\mu}_\ell\tilde{\mu}_s\right]-\mathrm{E}\left[\tilde{\mu}_\ell\right]\mathrm{E}\left[\tilde{\mu}_s\right]=0,\quad \forall\ell\neq s \tag{5.117}$$

$$\mathrm{E}\left[\tilde{\mu}''_{n,\ell}\,\tilde{\mu}''_{m,s}\right]-\mathrm{E}\left[\tilde{\mu}''_{n,\ell}\right]\mathrm{E}\left[\tilde{\mu}''_{m,s}\right]=0,\quad \forall\left(n,\ell\right)\neq\left(m,s\right) \tag{5.118}$$

$$\mathrm{E}\left[\tilde{\mu}_\ell\tilde{\mu}''_{n,\ell}\right]-\mathrm{E}\left[\tilde{\mu}_\ell\right]\mathrm{E}\left[\tilde{\mu}''_{n,\ell}\right]=0,\quad \forall\left(n,\ell\right) \tag{5.119}$$

$$\mathrm{E}\left[\tilde{\mu}_{\ell'}^{in}\tilde{\mu}_{s'}^{in}\right]-\mathrm{E}\left[\tilde{\mu}_{\ell'}^{in}\right]\mathrm{E}\left[\tilde{\mu}_{s'}^{in}\right]=0,\quad \forall \ell'\neq s' \tag{5.120}$$

$$\mathrm{E}\left[\tilde{\mu}''^{in}_{n',\ell'}\,\tilde{\mu}''^{in}_{m',s'}\right]-\mathrm{E}\left[\tilde{\mu}''^{in}_{n',\ell'}\right]\mathrm{E}\left[\tilde{\mu}''^{in}_{m',s'}\right]=0,\quad \forall\left(n',\ell'\right)\neq\left(m',s'\right) \tag{5.121}$$

$$\mathrm{E}\left[\tilde{\mu}_{\ell'}^{in}\tilde{\mu}''^{in}_{n',\ell'}\right]-\mathrm{E}\left[\tilde{\mu}_{\ell'}^{in}\right]\mathrm{E}\left[\tilde{\mu}''^{in}_{n',\ell'}\right]=0,\quad \forall\left(n',\ell'\right) \tag{5.122}$$

$$\mathrm{E}\left[\tilde{\mu}_{\ell}\tilde{\mu}_{\ell'}^{in}\right]-\mathrm{E}\left[\tilde{\mu}_{\ell}\right]\mathrm{E}\left[\tilde{\mu}_{\ell'}^{in}\right]=0,\quad \forall \ell', \text{with } \ell'=\ell \tag{5.123}$$

$$\mathrm{E}\left[\tilde{\mu}''_{n,\ell}\,\tilde{\mu}''^{in}_{n',\ell'}\right]-\mathrm{E}\left[\tilde{\mu}''_{n,\ell}\right]\mathrm{E}\left[\tilde{\mu}''^{in}_{n',\ell'}\right]=0,\quad \forall\left(n',\ell'\right), \text{with } n'=n,\ \ell'=\ell, \tag{5.124}$$

$$\mathrm{E}\left[\tilde{\mu}_{\ell}\tilde{\mu}''^{in}_{n',\ell'}\right]-\mathrm{E}\left[\tilde{\mu}_{\ell}\right]\mathrm{E}\left[\tilde{\mu}''^{in}_{n',\ell'}\right]=0,\quad \forall\left(n',\ell'\right), \text{with } \ell'=\ell \tag{5.125}$$

$$\mathrm{E}\left[\tilde{\mu}''_{n,\ell}\,\tilde{\mu}_{\ell'}^{in}\right]-\mathrm{E}\left[\tilde{\mu}''_{n,\ell}\right]\mathrm{E}\left[\tilde{\mu}_{\ell'}^{in}\right]=0,\quad \forall\left(n,\ell\right), \text{with } \ell=\ell', \tag{5.126}$$

The conditions presented between (5.117) and (5.126) are satisfied if, and only if, the discrete Doppler frequencies $f_{d_{n,\ell}}$, $f^{B}_{d_{\kappa,n,\ell}}$, $f^{in}_{d_{n',\ell'}}$ and $f^{in,B}_{d_{\kappa',n',\ell'}}$ are chosen in such a way that the sets $\left\{f_{d_{n,\ell}}\right\}$, $\left\{f^{B}_{d_{\kappa,n,\ell}}\right\}$, $\left\{f^{in}_{d_{n',\ell'}}\right\}$ and $\left\{f^{in,B}_{d_{\kappa',n',\ell'}}\right\}$ are mutually disjoint for different delays:

$$\begin{aligned}
&\left\{f_{d_{n,\ell}}\right\}\cap\left\{f_{d_{n,s}}\right\}\cap\left\{f^{B}_{d_{\kappa,n,\ell}}\right\}\cap\left\{f^{B}_{d_{r,n,s}}\right\}=\{0\},\forall n,\ \text{if } (\kappa,\ell)\neq(r,s),\\
&\left\{f^{in}_{d_{n',\ell'}}\right\}\cap\left\{f^{in}_{d_{n',s'}}\right\}\cap\left\{f^{in,B}_{d_{\kappa',n',\ell'}}\right\}\cap\left\{f^{in,B}_{d_{r',n',s'}}\right\}=\{0\},\forall n',\ \text{if } (\kappa',\ell')\neq(r',s'),\\
&\left\{\left\{f_{d_{n,\ell}}\right\}\cup\left\{f^{B}_{d_{\kappa,n,\ell}}\right\}\right\}\cap\left\{\left\{f^{in}_{d_{n',\ell'}}\right\}\cup\left\{f^{in,B}_{d_{\kappa',n',\ell'}}\right\}\right\}=\{0\},\forall(\kappa=\kappa',n=n',\ell=\ell'),
\end{aligned} \tag{5.127}$$

It is worth to indicate that the parameters of the FD-DGUS-MIMO model given in (5.47) can be determined from measurements using the DG processes (5.69), (5.91), (5.109) and (5.110). In the following analysis, these parameters are assumed known and constant quantities.

5.3. 2D-space-time-frequency correlation functions

So far the principal characteristics of the FD-DGUS-MIMO model described in (5.47) are as follow:

- The model includes inhomogeneous plane waves as result of the close scatterers at the RX side.
- The model is applicable to mobile radio channels where the RX is in motion, considering all possible phase changes due to Doppler effects.

- The model is an UWB-MIMO model and considers all possible amplitude and phase changes due to each frequency component of the signal bandwidth.
- The model includes the possible high central frequency dependence, which is also related to the resolution variations in the scatterer interaction.
- The model use uncorrelated DG processes with useful characteristics for both analysis and simulation implementations.

In order to determine the most general model characteristics, in this section some functions are obtained, i.e., the 2D-space-time-frequency correlation function (2D-STFCF) and the 2D-direction-Doppler-delay power spectral density function (2D-D^3-PSD).

The 2D-STFCF, denoted by $r_{\tilde{H}\tilde{H}}$, of the 2D-space-time transfer function (5.47), $\tilde{H}(f,t,x_T,x_R)$, is defined as follows (an extension of the formulations given in [9])

$$\begin{aligned} &r_{\tilde{H}\tilde{H}}(f',f'+\nu;t,t+\tau';x_T,x_T+\varsigma_T;x_R,x_R+\varsigma_R)\triangleq \\ &\lim_{\substack{B,T\to\infty \\ D_T,D_R\to\infty}} \frac{1}{8BTD_TD_R}\int_{-B}^{B}\int_{-T}^{T}\int_{-D_T}^{D_T}\int_{-D_R}^{D_R}\Big[\tilde{H}^*(f,t,x_T,x_R) \\ &\times\tilde{H}(f+\nu,t+\tau',x_T+\varsigma_T,x_R+\varsigma_R)\Big]dx_Rdx_Tdtdf, \end{aligned} \tag{5.128}$$

where ν, τ', ς_T and ς_R are the frequency, time, TX-space and RX-space displacements, respectively. This autocorrelation function is obtained based on the correlation properties of the DGUS processes (5.69), (5.91), (5.109) and (5.110).

For HPWs, using (5.69) and (5.91), and from the theoretical definition of correlation

$$\begin{aligned} &r_{\tilde{\mu}_\ell\tilde{\mu}_s}(\nu,\tau',\varsigma_T,\varsigma_R)\triangleq \\ &\lim_{\substack{B,T\to\infty \\ D_T,D_R\to\infty}} \frac{1}{8BTD_TD_R}\int_{-B}^{B}\int_{-T}^{T}\int_{-D_T}^{D_T}\int_{-D_R}^{D_R}\Big[\tilde{\mu}_\ell^*(f,t,x_T,x_R) \\ &\times\tilde{\mu}_s(f'+\nu,t+\tau',x_T+\varsigma_T,x_R+\varsigma_R)\Big]dx_Rdx_Tdtdf, \end{aligned} \tag{5.129}$$

the correlation function $r_{\tilde{\mu}_\ell\tilde{\mu}_s}(\nu,\tau',\varsigma_T,\varsigma_R)$, in a closed form, has been obtained for $\ell=s$ as follows (all the intermediate steps have been omitted for simplicity)

$$
\begin{aligned}
&r_{\tilde{\mu}_\ell\tilde{\mu}_s}(\nu,\tau',\varsigma_T,\varsigma_R)= \\
&=\sum_{n=1}^{N_\ell}\sum_{\kappa=1}^{I_\ell}\Big[c_{n,\ell}^2 g_{\kappa,n,\ell}^2 \exp\Big(-j2\pi f_{d_{n,\ell}}\tau'\big(1+u_{\kappa,n,\ell}\big)\Big) \\
&\times\exp\Big(-j2\pi\lambda_0^{-1}\Omega_{T_{n,\ell}}\varsigma_T\Big(1+\alpha_{T_{\kappa,n,\ell}}/\varepsilon_\kappa\Big)\Big) \\
&\times\exp\Big(-j2\pi\lambda_0^{-1}\Omega_{R_{n,\ell}}\varsigma_R\Big(1+\alpha_{R_{\kappa,n,\ell}}/\varepsilon_\kappa\Big)\Big)\exp\big(-j2\pi\tau_{\kappa,\ell}\nu\big)\Big],
\end{aligned}
\tag{5.130}
$$

and $r_{\tilde{\mu}_\ell\tilde{\mu}_s}(\nu,\tau',\varsigma_T,\varsigma_R)=0$ for $\ell\neq s$, where $\ell,s=\{0,1,\cdots,L-1\}$.

For IPWs, using (5.109) and (5.110), the correlation function

$$
\begin{aligned}
&r_{\tilde{\mu}^{in}_{\ell'}\tilde{\mu}^{in}_{s'}}(\tau',\varsigma_R)\triangleq \\
&\lim_{\substack{T\to\infty\\ D_R\to\infty}}\frac{1}{4TD_R}\int_{-T}^{T}\int_{-D_R}^{D_R}\Big(\tilde{\mu}^{in*}_{\ell'}(t,x_R)\tilde{\mu}^{in}_{s'}\big(t+\tau',x_R+\varsigma_R\big)\Big)dx_R dt
\end{aligned}
\tag{5.131}
$$

has been obtained for $\ell'=s'$ in the close form as follows (intermediate steps omitted)

$$
\begin{aligned}
&r_{\tilde{\mu}^{in}_{\ell'}\tilde{\mu}^{in}_{s'}}(\tau',\varsigma_R)= \\
&=\sum_{n'=1}^{N_{\ell'}}\sum_{\kappa'=1}^{I_{\ell'}}\Bigg[\Big(c^{in}_{n',\ell'}g^{in}_{\kappa',n',\ell'}\Big)^2\exp\Big(-j2\pi f_{d_{n',\ell'}}\big(u'_{n',\ell'}+u^{in}_{\kappa',n',\ell'}\big)\tau'\Big) \\
&\times\exp\Bigg(-j\frac{2\pi}{\lambda_0}\Bigg(\sqrt{1-\Omega^2_{R_{n',\ell'}}}\Big/\eta+\sqrt{1-\Big(\Omega_{R_{n',\ell'}}\alpha_{R_{\kappa',n',\ell'}}\Big)^2}\Big/\big(\varepsilon_\kappa\eta\big)\Bigg)\varsigma_R\Bigg)\Bigg],
\end{aligned}
\tag{5.132}
$$

and $r_{\tilde{\mu}^{in}_{\ell'}\tilde{\mu}^{in}_{s'}}(\tau',\varsigma_R)=0$ for $\ell'\neq s'$, where $\ell',s'=\{0,1,\cdots,L-1\}$.

Finally, the model (5.47) is used to get the closed form of (5.128), expressed in terms of (5.130) and (5.132). First, (5.47) is expressed in terms of (5.69) and (5.109):

$$
\tilde{H}(f,t,x_T,x_R)=\sum_{\ell=0}^{L-1}\tilde{a}_\ell\tilde{\mu}_\ell(f,t,x_T,x_R)+\sum_{\ell'=0}^{L-1}\tilde{a}^{in}_{\ell'}\tilde{\mu}^{in}_{\ell'}(t,x_R).
\tag{5.133}
$$

Hence, the 2D-STFCF is given by (intermediate steps omitted)

$$
r_{\tilde{H}\tilde{H}}(\nu,\tau',\varsigma_T,\varsigma_R)=\sum_{\ell=0}^{L-1}\tilde{a}^2_\ell r_{\tilde{\mu}_\ell\tilde{\mu}_\ell}(\nu,\tau',\varsigma_T,\varsigma_R)+\sum_{\ell'=0}^{L-1}\Big(\tilde{a}^{in}_{\ell'}\Big)^2 r_{\tilde{\mu}^{in}_{\ell'}\tilde{\mu}^{in}_{\ell'}}(\tau',\varsigma_R).
\tag{5.134}
$$

In (5.134) $r_{\tilde{\mu}_\ell\tilde{\mu}_\ell}(\nu,\tau',\varsigma_T,\varsigma_R)$ and $r_{\tilde{\mu}^{in}_{\ell'}\tilde{\mu}^{in}_{\ell'}}(\tau',\varsigma_R)$ are the autocorrelation functions of the HPWs and IPWs, which were modelled as DGUS processes. These functions are obtained from (5.130) and (5.132) for $\ell = s$ and $\ell' = s'$, respectively. Besides, note that $r_{\tilde{H}\tilde{H}}(\nu,\tau',\varsigma_T,\varsigma_R)$ is only function of the separation variables of each domain. Therefore, $\tilde{H}(f,t,x_T,x_R)$ presented as in (5.133) is a wide-sense stationary process (WSS), also US (then WSSUS), which give us useful characteristics for spectral analysis.

5.4. Scattering function

A general closed form for the scattering function (SF) of a DGUS model offers many advantages for modelling. The SF of a DGUS model is completely determined by the model parameters, which permits to model perfectly all types of measured channels in stationary conditions [6].

The SF of the FD-DGUS-MIMO model, called 2D-D^3-PSD, denoted by $\tilde{S}(\tau, f_d,\Omega_T,\Omega_R)$, is reached by means of the four-dimensional Fourier transform of $r_{\tilde{H}\tilde{H}}(\nu,\tau',\varsigma_T,\varsigma_R)$:

$$\tilde{S}(\tau, f_d,\Omega_T,\Omega_R) = \int_{-\infty}^{\infty}\int_{-\infty}^{\infty}\int_{-\infty}^{\infty}\int_{-\infty}^{\infty} r_{\tilde{H}\tilde{H}}(\nu,\tau',\varsigma_T,\varsigma_R)e^{j2\pi\nu\tau}e^{-j2\pi\tau' f_d}e^{-j\frac{2\pi}{\lambda_0}\varsigma_T\Omega_T}e^{-j\frac{2\pi}{\lambda_0}\varsigma_R\Omega_R}d\nu d\tau' d\varsigma_T d\varsigma_R. \quad (5.135)$$

Substituting (5.134) in (5.135), it is then obtained

$$\tilde{S}(\tau, f_d,\Omega_T,\Omega_R) = \tilde{S}_{HPWs}(\tau, f_d,\Omega_T,\Omega_R) + \tilde{S}_{IPWs}(\tau, f_d,\Omega_T,\Omega_R), \quad (5.136)$$

where

$$\tilde{S}_{HPWs}(\tau, f_d,\Omega_T,\Omega_R) = \int_{-\infty}^{\infty}\int_{-\infty}^{\infty}\int_{-\infty}^{\infty}\int_{-\infty}^{\infty}\left(\sum_{\ell=0}^{L-1}\tilde{a}_\ell^2 r_{\tilde{\mu}_\ell\tilde{\mu}_\ell}(\nu,\tau',\varsigma_T,\varsigma_R)\right)e^{j2\pi\left(\nu\tau-\tau' f_d-\frac{\varsigma_T\Omega_T}{\lambda_0}-\frac{\varsigma_R\Omega_R}{\lambda_0}\right)}d\nu d\tau' d\varsigma_T d\varsigma_R, \quad (5.137)$$

and

$$\tilde{S}_{IPWs}(\tau, f_d,\Omega_T,\Omega_R) = \int_{-\infty}^{\infty}\int_{-\infty}^{\infty}\int_{-\infty}^{\infty}\int_{-\infty}^{\infty}\left(\sum_{\ell'=0}^{L-1}\tilde{a}^{in}_{\ell'} r_{\tilde{\mu}^{in}_{\ell'}\tilde{\mu}^{in}_{\ell'}}(\tau',\varsigma_R)\right)e^{j2\pi\left(\nu\tau-\tau' f_d-\frac{\varsigma_T\Omega_T}{\lambda_0}-\frac{\varsigma_R\Omega_R}{\lambda_0}\right)}d\nu d\tau' d\varsigma_T d\varsigma_R. \quad (5.138)$$

Solving (5.137) and (5.138), the closed forms of the SF for the HPWs and the IPWs are then given by (intermediate steps omitted for simplicity):

$$\begin{aligned}
&\tilde{S}_{HPWs}(\tau, f_d, \Omega_T, \Omega_R) = \\
&= \sum_{\ell=0}^{L-1} \tilde{a}_\ell^2 \sum_{n=1}^{N_\ell} \sum_{\kappa=1}^{I_\ell} \Big[\left(c_{n,\ell} g_{\kappa,n,\ell}\right)^2 \delta\Big(f_d - f_{d_{n,\ell}}\left(1+u_{\kappa,n,\ell}\right)\Big) \delta\left(\tau - \tau_{\kappa,\ell}\right) \\
&\quad \times \delta\Big(\Omega_T - \Omega_{T_{n,\ell}}\left(1+\alpha_{T_{\kappa,n,\ell}}/\varepsilon_\kappa\right)\Big) \delta\Big(\Omega_R - \Omega_{R_{n,\ell}}\left(1+\alpha_{R_{\kappa,n,\ell}}/\varepsilon_\kappa\right)\Big)\Big],
\end{aligned} \tag{5.139}$$

$$\begin{aligned}
&\tilde{S}_{IPWs}(\tau, f_d, \Omega_T, \Omega_R) = \delta(\tau)\delta(\Omega_T) \times \\
&\times \sum_{\ell'=0}^{L-1} \left(\tilde{a}_{\ell'}^{in}\right)^2 \sum_{n'=1}^{N_{\ell'}} \sum_{\kappa'=1}^{I_{\ell'}} \Big[\left(c_{n',\ell'}^{in} g_{\kappa',n',\ell'}^{in}\right)^2 \delta\Big(f_d - f_{d_{n',\ell'}}\left(u'_{n',\ell'} + u_{\kappa',n',\ell'}^{in}\right)\Big) \\
&\times \delta\left(\Omega_R - \left(\sqrt{1-\Omega_{R_{n',\ell'}}^2}/\eta + \sqrt{1-\left(\Omega_{R_{n',\ell'}}\alpha_{R_{\kappa',n',\ell'}}\right)^2}/\left(\varepsilon_\kappa \eta\right)\right)\right)\Big].
\end{aligned} \tag{5.140}$$

Note in (5.140) that two delta functions appear for the SF of the IPWs, i.e., $\delta(\tau)$ and $\delta(\Omega_T)$. These delta functions are a result of the undefined delay and DOD domains for the IPWs. For the subsequent formulations this characteristic must be taken into account to avoid possible wrong analysis. Finally, as it is usually assumed that the SF is normalised in such a way that the area under $\tilde{S}(\tau, f_d, \Omega_T, \Omega_R)$ is equal to one [6], the coefficients $\tilde{a}_\ell$, $c_{n,\ell}$, $g_{\kappa,n,\ell}$, $\tilde{a}_{\ell'}^{in}$, $c_{n',\ell'}^{in}$, and $g_{\kappa',n',\ell'}^{in}$ have to satisfy the following condition:

$$\begin{aligned}
&\sum_{\ell=0}^{L-1} \tilde{a}_\ell^2 = \sum_{n=1}^{N_\ell} c_{n,\ell}^2 = \sum_{\kappa=1}^{I_\ell} g_{\kappa,n,\ell}^2 = 1, \\
&\sum_{\ell'=0}^{L-1} \left(\tilde{a}_{\ell'}^{in}\right)^2 = \sum_{n'=1}^{N_\ell} \left(c_{n',\ell'}^{in}\right)^2 = \sum_{\kappa'=1}^{I_\ell} \left(g_{\kappa',n',\ell'}^{in}\right)^2 = 1,
\end{aligned} \tag{5.141}$$

for $\ell = \{0,1,\ldots,L-1\}$, $n = \{1,2\ldots,N_\ell - 1\}$, $\kappa = \{1,2\ldots,I_\ell - 1\}$, $\ell = \ell'$, $n = n'$, $\kappa = \kappa'$, $N_\ell = N_{\ell'}$ and $I_\ell = I_{\ell'}$.

5.5. Characteristic functions and quantities

Based on the definition of $\tilde{S}(\tau, f_d, \Omega_T, \Omega_R)$ given in (5.139) and (5.140), some important functions and quantities of the FD-DGUS-MIMO model can be obtained. Here the closed forms of the delay-Doppler PSD, the delay-DOA PSD, delay-DOD PSD, DOD-DOA PSD, Doppler-DOA PSD, and delay PSD are obtained. Besides, the first moment (average), and the square root of the second central moment (deviation) of the delay, Doppler, DOD and DOA PSDs are derived as well.

5.5.1. Characteristic functions

5.5.1.1. Delay-Doppler PSD

The delay-Doppler PSD, $\tilde{S}_{\tau f_d}(\tau, f_d)$, is defined as follows

$$\tilde{S}_{\tau f_d}(\tau, f_d) \triangleq \int_{-\infty}^{\infty}\int_{-\infty}^{\infty} \tilde{S}(\tau, f_d, \Omega_T, \Omega_R) d\Omega_T d\Omega_R. \tag{5.142}$$

The closed form of $\tilde{S}_{\tau f_d}(\tau, f_d)$ is then given by

$$\begin{aligned}
&\tilde{S}_{\tau f_d}(\tau, f_d) = \\
&= \sum_{\ell=0}^{L-1}\sum_{n=1}^{N_\ell}\sum_{\kappa=1}^{I_\ell} \left(\tilde{a}_\ell c_{n,\ell} g_{\kappa,n,\ell}\right)^2 \delta\Big(f_d - f_{d_{n,\ell}}\left(1+u_{\kappa,n,\ell}\right)\Big)\delta\left(\tau-\tau_{\kappa,\ell}\right) + \\
&+\delta(\tau)\sum_{\ell'=0}^{L-1}\sum_{n'=1}^{N_{\ell'}}\sum_{\kappa'=1}^{I_{\ell'}} \left(\tilde{a}^{in}_{\ell'} c^{in}_{n',\ell'} g^{in}_{\kappa',n',\ell'}\right)^2 \delta\Big(f_d - f_{d_{n',\ell'}}\left(u'_{n',\ell'} + u^{in}_{\kappa',n',\ell'}\right)\Big).
\end{aligned} \tag{5.143}$$

Note that the delay-Doppler PSD for the FD-DGUS-MIMO model is fully determined by the model parameters $\tilde{a}_\ell$, $c_{n,\ell}$, $g_{\kappa,n,\ell}$, $\tilde{a}^{in}_{\ell'}$, $c^{in}_{n',\ell'}$, $g^{in}_{\kappa',n',\ell'}$, $f_{d_{n,\ell}}$, $u_{\kappa,n,\ell}$, $\tau_{\kappa,\ell}$, $u'_{n',\ell'}$, $u^{in}_{\kappa',n',\ell'}$, L, $N_\ell = N_{\ell'}$, $I_\ell = I_{\ell'}$, which have been defined through Section 5.2.

5.5.1.2. Delay-DOA PSD

The delay-DOA PSD, $\tilde{S}_{\tau\Omega_R}(\tau,\Omega_R)$, is defined as follows

$$\tilde{S}_{\tau\Omega_R}(\tau,\Omega_R) \triangleq \int_{-\infty}^{\infty}\int_{-\infty}^{\infty} \tilde{S}(\tau, f_d, \Omega_T, \Omega_R) df_d d\Omega_T. \tag{5.144}$$

The closed form of $\tilde{S}_{\tau\Omega_R}(\tau,\Omega_R)$ is then given by

$$\begin{aligned}
&\tilde{S}_{\tau\Omega_R}(\tau,\Omega_R) = \\
&= \sum_{\ell=0}^{L-1}\sum_{n=1}^{N_\ell}\sum_{\kappa=1}^{I_\ell} \left(\tilde{a}_\ell c_{n,\ell} g_{\kappa,n,\ell}\right)^2 \delta\left(\tau-\tau_{\kappa,\ell}\right)\delta\Big(\Omega_R - \Omega_{R_{n,\ell}}\left(1+\alpha_{R_{\kappa,n,\ell}}/\varepsilon_\kappa\right)\Big) + \\
&+\delta(\tau)\sum_{\ell'=0}^{L-1}\sum_{n'=1}^{N_{\ell'}}\sum_{\kappa'=1}^{I_{\ell'}}\Bigg[\left(\tilde{a}^{in}_{\ell'} c^{in}_{n',\ell'} g^{in}_{\kappa',n',\ell'}\right)^2 \\
&\quad\times\delta\left(\Omega_R - \left(\sqrt{1-\Omega^2_{R_{n',\ell'}}}\Big/\eta + \sqrt{1-\left(\Omega_{R_{n',\ell'}}\alpha_{R_{\kappa',n',\ell'}}\right)^2}\Big/\left(\varepsilon_\kappa\eta\right)\right)\right)\Bigg].
\end{aligned} \tag{5.145}$$

Note that the delay-DOA PSD for the FD-DGUS-MIMO model is fully determined by the model parameters $\tilde{a}_\ell$, $c_{n,\ell}$, $g_{\kappa,n,\ell}$, $\tilde{a}^{in}_{\ell'}$, $c^{in}_{n',\ell'}$, $g^{in}_{\kappa',n',\ell'}$, $\tau_{\kappa,\ell}$, $\Omega_{R_{n,\ell}}$, $\alpha_{R_{\kappa,n,\ell}}$, ε_κ, η, L, $N_\ell = N_{\ell'}$, $I_\ell = I_{\ell'}$, which have been defined through the Section 5.2.

5.5.1.3. Delay-DOD PSD

The delay-DOD PSD, $\tilde{S}_{\tau\Omega_T}(\tau,\Omega_T)$, is defined as follows

$$\tilde{S}_{\tau\Omega_T}(\tau,\Omega_T) \triangleq \int_{-\infty}^{\infty}\int_{-\infty}^{\infty} \tilde{S}(\tau, f_d, \Omega_T, \Omega_R) df_d\, d\Omega_R. \tag{5.146}$$

The closed form of $\tilde{S}_{\tau\Omega_T}(\tau,\Omega_T)$ is then given by

$$\begin{aligned}
&\tilde{S}_{\tau\Omega_T}(\tau,\Omega_T) = \\
&= \sum_{\ell=0}^{L-1}\sum_{n=1}^{N_\ell}\sum_{\kappa=1}^{I_\ell}\left(\left(\tilde{a}_\ell c_{n,\ell} g_{\kappa,n,\ell}\right)^2 \delta(\tau-\tau_{\kappa,\ell})\delta\left(\Omega_T - \Omega_{T_{n,\ell}}\left(1+\alpha_{T_{\kappa,n,\ell}}/\varepsilon_\kappa\right)\right)\right) + \\
&+\delta(\tau)\delta(\Omega_T)\sum_{\ell'=0}^{L-1}\sum_{n'=1}^{N_{\ell'}}\sum_{\kappa'=1}^{I_{\ell'}}\left(\tilde{a}^{in}_{\ell'} c^{in}_{n',\ell'} g^{in}_{\kappa',n',\ell'}\right)^2.
\end{aligned} \tag{5.147}$$

According to (5.141), $\tilde{S}_{\tau\Omega_T}(\tau,\Omega_T)$ can be given as:

$$\begin{aligned}
&\tilde{S}_{\tau\Omega_T}(\tau,\Omega_T) = \\
&= \sum_{\ell=0}^{L-1}\sum_{n=1}^{N_\ell}\sum_{\kappa=1}^{I_\ell}\left(\left(\tilde{a}_\ell c_{n,\ell} g_{\kappa,n,\ell}\right)^2 \delta(\tau-\tau_{\kappa,\ell})\delta\left(\Omega_T - \Omega_{T_{n,\ell}}\left(1+\alpha_{T_{\kappa,n,\ell}}/\varepsilon_\kappa\right)\right)\right) + \\
&+\delta(\tau)\delta(\Omega_T).
\end{aligned} \tag{5.148}$$

Note that the delay-DOD PSD for the FD-DGUS-MIMO model is fully determined by the model parameters $\tilde{a}_\ell$, $c_{n,\ell}$, $g_{\kappa,n,\ell}$, $\tau_{\kappa,\ell}$, $\Omega_{T_{n,\ell}}$, $\alpha_{T_{\kappa,n,\ell}}$, ε_κ, L, $N_\ell = N_{\ell'}$, $I_\ell = I_{\ell'}$, which have been defined through the Section 5.2.

5.5.1.4. DOD-DOA PSD

The DOD-DOA PSD, $\tilde{S}_{\Omega_T\Omega_R}(\Omega_T,\Omega_R)$, is defined as follows

$$\tilde{S}_{\Omega_T\Omega_R}(\Omega_T,\Omega_R) \triangleq \int_{-\infty}^{\infty}\int_{-\infty}^{\infty} \tilde{S}(\tau, f_d, \Omega_T, \Omega_R) d\tau df_d. \tag{5.149}$$

The closed form of $\tilde{S}_{\Omega_T\Omega_R}(\Omega_T,\Omega_R)$ is then given by

$$\begin{aligned}
&\tilde{S}_{\Omega_T\Omega_R}(\Omega_T,\Omega_R)= \\
&=\sum_{\ell=0}^{L-1}\sum_{n=1}^{N_\ell}\sum_{\kappa=1}^{I_\ell}\Big[\left(\tilde{a}_\ell c_{n,\ell} g_{\kappa,n,\ell}\right)^2 \delta\Big(\Omega_T-\Omega_{T_{n,\ell}}\left(1+\alpha_{T_{\kappa,n,\ell}}/\varepsilon_\kappa\right)\Big) \\
&\quad\times\delta\Big(\Omega_R-\Omega_{R_{n,\ell}}\left(1+\alpha_{R_{\kappa,n,\ell}}/\varepsilon_\kappa\right)\Big)\Big]+ \\
&+\delta(\Omega_T)\sum_{\ell'=0}^{L-1}\sum_{n'=1}^{N_{\ell'}}\sum_{\kappa'=1}^{I_{\ell'}}\Big[\left(\tilde{a}_{\ell'}^{in} c_{n',\ell'}^{in} g_{\kappa',n',\ell'}^{in}\right)^2 \\
&\quad\times\delta\left(\Omega_R-\left(\sqrt{1-\Omega_{R_{n',\ell'}}^2}\Big/\eta+\sqrt{1-\left(\Omega_{R_{n',\ell'}}\alpha_{R_{\kappa',n',\ell'}}\right)^2}\Big/\left(\varepsilon_\kappa\eta\right)\right)\right)\Big].
\end{aligned} \tag{5.150}$$

Note that the DOD-DOA PSD for the FD-DGUS-MIMO model is fully determined by the model parameters: $\tilde{a}_\ell$, $c_{n,\ell}$, $g_{\kappa,n,\ell}$, $\tilde{a}_{\ell'}^{in}$, $c_{n',\ell'}^{in}$, $g_{\kappa',n',\ell'}^{in}$, $\Omega_{T_{n,\ell}}$, $\Omega_{R_{n,\ell}}$, $\alpha_{T_{\kappa,n,\ell}}$, $\alpha_{R_{\kappa,n,\ell}}$, ε_κ, η, L, $N_\ell = N_{\ell'}$, $I_\ell = I_{\ell'}$, which have been defined through the Section 5.2.

5.5.1.5. Doppler-DOA PSD

The Doppler-DOA PSD, $\tilde{S}_{f_d\Omega_R}(f_d,\Omega_R)$, is defined as follows

$$\tilde{S}_{f_d\Omega_R}(f_d,\Omega_R)\triangleq\int_{-\infty}^{\infty}\int_{-\infty}^{\infty}\tilde{S}(\tau,f_d,\Omega_T,\Omega_R)d\tau d\Omega_T. \tag{5.151}$$

The closed form of $\tilde{S}_{f_d\Omega_R}(f_d,\Omega_R)$ is then given by

$$\begin{aligned}
&\tilde{S}_{f_d\Omega_R}(f_d,\Omega_R)= \\
&=\sum_{\ell=0}^{L-1}\sum_{n=1}^{N_\ell}\sum_{\kappa=1}^{I_\ell}\Big[\left(\tilde{a}_\ell c_{n,\ell} g_{\kappa,n,\ell}\right)^2 \delta\Big(f_d-f_{d_{n,\ell}}\left(1+u_{\kappa,n,\ell}\right)\Big) \\
&\quad\times\delta\Big(\Omega_R-\Omega_{R_{n,\ell}}\left(1+\alpha_{R_{\kappa,n,\ell}}/\varepsilon_\kappa\right)\Big)\Big]+ \\
&+\sum_{\ell'=0}^{L-1}\sum_{n'=1}^{N_{\ell'}}\sum_{\kappa'=1}^{I_{\ell'}}\Big[\left(\tilde{a}_{\ell'}^{in} c_{n',\ell'}^{in} g_{\kappa',n',\ell'}^{in}\right)^2 \delta\Big(f_d-f_{d_{n',\ell'}}\left(u'_{n',\ell'}+u_{\kappa',n',\ell'}^{in}\right)\Big) \\
&\quad\times\delta\left(\Omega_R-\left(\sqrt{1-\Omega_{R_{n',\ell'}}^2}\Big/\eta+\sqrt{1-\left(\Omega_{R_{n',\ell'}}\alpha_{R_{\kappa',n',\ell'}}\right)^2}\Big/\left(\varepsilon_\kappa\eta\right)\right)\right)\Big].
\end{aligned} \tag{5.152}$$

Note that the Doppler-DOA PSD for the FD-DGUS-MIMO model is fully determined by the model parameters $\tilde{a}_\ell$, $c_{n,\ell}$, $g_{\kappa,n,\ell}$, $\tilde{a}_{\ell'}^{in}$, $c_{n',\ell'}^{in}$, $g_{\kappa',n',\ell'}^{in}$, $f_{d_{n,\ell}}$,

$\Omega_{R_{n,\ell}}$, $\alpha_{R_{\kappa,n,\ell}}$, ε_κ, η, $u_{\kappa,n,\ell}$, $u'_{n',\ell'}$, $u^{in}_{\kappa',n',\ell'}$, L, $N_\ell = N_{\ell'}$, $I_\ell = I_{\ell'}$, which have been defined through the Section 5.2.

5.5.1.6. Delay PSD

The delay PSD, $\tilde{S}_{\tau\tau}(\tau)$, is defined as follows

$$\begin{aligned}\tilde{S}_{\tau\tau}(\tau) &\triangleq \int_{-\infty}^{\infty} \tilde{S}_{\tau f_d}(\tau, f_d) df_d = \\ &= \int_{-\infty}^{\infty} \tilde{S}_{\tau\Omega_R}(\tau,\Omega_R) d\Omega_R = \int_{-\infty}^{\infty} \tilde{S}_{\tau\Omega_T}(\tau,\Omega_T) d\Omega_T.\end{aligned} \tag{5.153}$$

The closed form of $\tilde{S}_{\tau\tau}(\tau)$ is then given by (see also (5.141))

$$\tilde{S}_{\tau\tau}(\tau) = \sum_{\ell=0}^{L-1} \sum_{n=1}^{N_\ell} \sum_{\kappa=1}^{I_\ell} \left(\left(\tilde{a}_\ell c_{n,\ell} g_{\kappa,n,\ell} \right)^2 \delta\left(\tau - \tau_{\kappa,\ell}\right) \right) + \delta(\tau) \tag{5.154}$$

Note that the delay PSD for the FD-DGUS-MIMO model is fully determined by the model parameters $\tilde{a}_\ell$, $c_{n,\ell}$, $g_{\kappa,n,\ell}$, $\tau_{\kappa,\ell}$, L, $N_\ell = N_{\ell'}$, $I_\ell = I_{\ell'}$, which have been defined through the Section 5.2.

5.5.2. Characteristic Quantities

Here the first moment (average), and the square root of the second central moment (deviation) of the delay, Doppler, DOD and DOA PDSs are derived from $\tilde{S}(\tau, f_d, \Omega_T, \Omega_R)$.

5.5.2.1. Delay average and Delay spread

The delay average, $\tilde{D}^{(1)}_{\tau\tau}$ (the first moment of $\tilde{S}_{\tau\tau}(\tau)$), is defined as follows [6]

$$\tilde{D}^{(1)}_{\tau\tau} \triangleq \int_{-\infty}^{\infty} \tau \tilde{S}_{\tau\tau}(\tau) d\tau \Bigg/ \int_{-\infty}^{\infty} \tilde{S}_{\tau\tau}(\tau) d\tau. \tag{5.155}$$

The closed form of $\tilde{D}^{(1)}_{\tau\tau}$ is then given by (see also (5.141))

$$\tilde{D}^{(1)}_{\tau\tau} = \frac{1}{2} \sum_{\ell=0}^{L-1} \sum_{n=1}^{N_\ell} \sum_{\kappa=1}^{I_\ell} \left(\tilde{a}_\ell c_{n,\ell} g_{\kappa,n,\ell} \right)^2 \tau_{\kappa,\ell}. \tag{5.156}$$

On the other hand, the delay spread $\tilde{D}_{\tau\tau}^{(2)}$, (the square root of the second central moment of $\tilde{S}_{\tau\tau}(\tau)$), is defined as follows [6]

$$\tilde{D}_{\tau\tau}^{(2)} \triangleq \sqrt{\int_{-\infty}^{\infty}\left(\tau-\tilde{D}_{\tau\tau}^{(1)}\right)^2 \tilde{S}_{\tau\tau}(\tau)d\tau \Big/ \int_{-\infty}^{\infty}\tilde{S}_{\tau\tau}(\tau)d\tau}. \tag{5.157}$$

The closed form of $\tilde{D}_{\tau\tau}^{(2)}$ is then given by

$$\tilde{D}_{\tau\tau}^{(2)} = \sqrt{\frac{1}{2}\sum_{\ell=0}^{L-1}\sum_{n=1}^{N_\ell}\sum_{\kappa=1}^{I_\ell}\left(\tilde{a}_\ell c_{n,\ell} g_{\kappa,n,\ell}\right)^2\left(\tau_{\kappa,\ell}\right)^2 - \left(\tilde{D}_{\tau\tau}^{(1)}\right)^2}. \tag{5.158}$$

5.5.2.2. Doppler average and Doppler spread

The Doppler average, $\tilde{D}_{f_d f_d}^{(1)}$ (the first moment of the Doppler PSD $\tilde{S}_{f_d f_d}(f_d)$), is defined as follows

$$\tilde{D}_{f_d f_d}^{(1)} \triangleq \int_{-\infty}^{\infty} f_d \tilde{S}_{f_d f_d}(f_d)df_d \Big/ \int_{-\infty}^{\infty}\tilde{S}_{f_d f_d}(f_d)df_d, \tag{5.159}$$

where $\tilde{S}_{f_d f_d}(f_d)$ is obtained by

$$\tilde{S}_{f_d f_d}(f_d) = \int_{-\infty}^{\infty}\tilde{S}_{\tau f_d}(\tau, f_d)d\tau, \tag{5.160}$$

being the closed form given by

$$\begin{aligned}\tilde{S}_{f_d f_d}(f_d) = &\sum_{\ell=0}^{L-1}\sum_{n=1}^{N_\ell}\sum_{\kappa=1}^{I_\ell}\left(\tilde{a}_\ell c_{n,\ell} g_{\kappa,n,\ell}\right)^2 \delta\left(f_d - f_{d_{n,\ell}}\left(1+u_{\kappa,n,\ell}\right)\right) + \\ &+ \sum_{\ell'=0}^{L-1}\sum_{n'=1}^{N_{\ell'}}\sum_{\kappa'=1}^{I_{\ell'}}\left(\tilde{a}_{\ell'}^{in} c_{n',\ell'}^{in} g_{\kappa',n',\ell'}^{in}\right)^2 \delta\left(f_d - f_{d_{n',\ell'}}\left(u'_{n',\ell'} + u_{\kappa',n',\ell'}^{in}\right)\right).\end{aligned} \tag{5.161}$$

Therefore, the closed form of $\tilde{D}_{f_d f_d}^{(1)}$ is then given by (see also (5.141))

$$\tilde{D}_{\tau\tau}^{(1)} = \frac{1}{2}\sum_{\ell=0}^{L-1}\sum_{n=1}^{N_\ell}\sum_{\kappa=1}^{I_\ell}\left(\tilde{a}_\ell c_{n,\ell} g_{\kappa,n,\ell}\right)^2 f_{d_{n,\ell}}\left(1+u_{\kappa,n,\ell}\right). \tag{5.162}$$

On the other hand, the Doppler spread $\tilde{D}^{(2)}_{f_d f_d}$, (the square root of the second central moment of $\tilde{S}_{f_d f_d}(f_d)$), is defined as follows [6]

$$\tilde{D}^{(2)}_{f_d f_d} \triangleq \sqrt{\int_{-\infty}^{\infty}\left(f_d - \tilde{D}^{(1)}_{f_d f_d}\right)^2 \tilde{S}_{f_d f_d}(f_d)df_d \Big/ \int_{-\infty}^{\infty}\tilde{S}_{f_d f_d}(f_d)df_d}. \tag{5.163}$$

The closed form of $\tilde{D}^{(2)}_{f_d f_d}$ is then given by

$$\tilde{D}^{(2)}_{f_d f_d} = \sqrt{\frac{1}{2}\sum_{\ell=0}^{L-1}\sum_{n=1}^{N_\ell}\sum_{\kappa=1}^{I_\ell}\left(\tilde{a}_\ell c_{n,\ell} g_{\kappa,n,\ell}\right)^2\left(f_{d_{n,\ell}}\left(1+u_{\kappa,n,\ell}\right)\right)^2 - \left(\tilde{D}^{(1)}_{f_d f_d}\right)^2}. \tag{5.164}$$

5.5.2.3. DOD average and DOD spread

The DOD average, $\tilde{D}^{(1)}_{\Omega_T\Omega_T}$ (the first moment of the Doppler PSD $\tilde{S}_{\Omega_T\Omega_T}(\Omega_T)$), is defined as follows

$$\tilde{D}^{(1)}_{\Omega_T\Omega_T} \triangleq \int_{-\infty}^{\infty}\Omega_T\tilde{S}_{\Omega_T\Omega_T}(\Omega_T)d\Omega_T \Big/ \int_{-\infty}^{\infty}\tilde{S}_{\Omega_T\Omega_T}(\Omega_T)d\Omega_T, \tag{5.165}$$

where $\tilde{S}_{\Omega_T\Omega_T}(\Omega_T)$ is obtained by

$$\tilde{S}_{\Omega_T\Omega_T}(\Omega_T) = \int_{-\infty}^{\infty}\tilde{S}_{\tau\Omega_T}(\tau,\Omega_T)d\tau, \tag{5.166}$$

being the closed form given by

$$\begin{aligned}\tilde{S}_{\Omega_T\Omega_T}(\Omega_T) = &\sum_{\ell=0}^{L-1}\sum_{n=1}^{N_\ell}\sum_{\kappa=1}^{I_\ell}\left(\tilde{a}_\ell c_{n,\ell} g_{\kappa,n,\ell}\right)^2\delta\left(\Omega_T - \Omega_{T_{n,\ell}}\left(1+\frac{\alpha_{T_{\kappa,n,\ell}}}{\varepsilon_\kappa}\right)\right)+\\ &+\delta(\Omega_T)\sum_{\ell'=0}^{L-1}\sum_{n'=1}^{N_{\ell'}}\sum_{\kappa'=1}^{I_{\ell'}}\left(\tilde{a}^{in}_{\ell'} c^{in}_{n',\ell'} g^{in}_{\kappa',n',\ell'}\right)^2.\end{aligned} \tag{5.167}$$

Therefore, the closed form of $\tilde{D}^{(1)}_{\Omega_T\Omega_T}$ is then given by (see also (5.141))

$$\tilde{D}^{(1)}_{\Omega_T\Omega_T} = \frac{1}{2}\sum_{\ell=0}^{L-1}\sum_{n=1}^{N_\ell}\sum_{\kappa=1}^{I_\ell}\left(\tilde{a}_\ell c_{n,\ell} g_{\kappa,n,\ell}\right)^2\Omega_{T_{n,\ell}}\left(1+\frac{\alpha_{T_{\kappa,n,\ell}}}{\varepsilon_\kappa}\right). \tag{5.168}$$

On the other hand, the Doppler spread $\tilde{D}^{(2)}_{\Omega_T\Omega_T}$, (the square root of the second central moment of $\tilde{S}_{\Omega_T\Omega_T}(\Omega_T)$), is defined as follows [6]

$$\tilde{D}^{(2)}_{\Omega_T\Omega_T} \triangleq \sqrt{\int_{-\infty}^{\infty}\left(\Omega_T - \tilde{D}^{(1)}_{\Omega_T\Omega_T}\right)^2 \tilde{S}_{\Omega_T\Omega_T}(\Omega_T)d\Omega_T \Big/ \int_{-\infty}^{\infty}\tilde{S}_{\Omega_T\Omega_T}(\Omega_T)d\Omega_T}. \quad (5.169)$$

The closed form of $\tilde{D}^{(2)}_{\Omega_T\Omega_T}$ is then given by

$$\tilde{D}^{(2)}_{\Omega_T\Omega_T} = \sqrt{\frac{1}{2}\sum_{\ell=0}^{L-1}\sum_{n=1}^{N_\ell}\sum_{\kappa=1}^{I_\ell}\left(\tilde{a}_\ell c_{n,\ell} g_{\kappa,n,\ell}\right)^2 \left(\Omega_{T_{n,\ell}}\left(1+\frac{\alpha_{T_{\kappa,n,\ell}}}{\varepsilon_\kappa}\right)\right)^2 - \left(\tilde{D}^{(1)}_{\Omega_T\Omega_T}\right)^2}. \quad (5.170)$$

5.5.2.4. DOA average and DOA spread

The DOA average, $\tilde{D}^{(1)}_{\Omega_R\Omega_R}$ (the first moment of the Doppler PSD $\tilde{S}_{\Omega_R\Omega_R}(\Omega_R)$), is defined as follows

$$\tilde{D}^{(1)}_{\Omega_R\Omega_R} \triangleq \int_{-\infty}^{\infty}\Omega_R\tilde{S}_{\Omega_R\Omega_R}(\Omega_R)d\Omega_R \Big/ \int_{-\infty}^{\infty}\tilde{S}_{\Omega_R\Omega_R}(\Omega_R)d\Omega_R, \quad (5.171)$$

where $\tilde{S}_{\Omega_R\Omega_R}(\Omega_R)$ is obtained by

$$\tilde{S}_{\Omega_R\Omega_R}(\Omega_R) = \int_{-\infty}^{\infty}\tilde{S}_{\tau\Omega_R}(\tau,\Omega_R)d\tau, \quad (5.172)$$

being the closed form given by

$$\begin{aligned}
&\tilde{S}_{\Omega_R\Omega_R}(\Omega_R) = \\
&= \sum_{\ell=0}^{L-1}\sum_{n=1}^{N_\ell}\sum_{\kappa=1}^{I_\ell}\left(\tilde{a}_\ell c_{n,\ell} g_{\kappa,n,\ell}\right)^2 \delta\left(\Omega_R - \Omega_{R_{n,\ell}}\left(1+\alpha_{R_{\kappa,n,\ell}}/\varepsilon_\kappa\right)\right) + \\
&+ \sum_{\ell'=0}^{L-1}\sum_{n'=1}^{N_{\ell'}}\sum_{\kappa'=1}^{I_{\ell'}}\left[\left(\tilde{a}^{in}_{\ell'} c^{in}_{n',\ell'} g^{in}_{\kappa',n',\ell'}\right)^2\right. \\
&\left.\times\delta\left(\Omega_R - \left(\sqrt{1-\Omega^2_{R_{n',\ell'}}}\Big/\eta + \sqrt{1-\left(\Omega_{R_{n',\ell'}}\alpha_{R_{\kappa',n',\ell'}}\right)^2}\Big/\varepsilon_\kappa\eta\right)\right)\right].
\end{aligned} \quad (5.173)$$

Therefore, the closed form of $\tilde{D}^{(1)}_{\Omega_R\Omega_R}$ is then given by (see also (5.141))

$$\begin{aligned}\tilde{D}^{(1)}_{\Omega_R\Omega_R} &= \frac{1}{2}\sum_{\ell=0}^{L-1}\sum_{n=1}^{N_\ell}\sum_{\kappa=1}^{I_\ell}\left(\tilde{a}_\ell c_{n,\ell} g_{\kappa,n,\ell}\right)^2\left(\Omega_R - \Omega_{R_{n,\ell}}\left(1+\alpha_{R_{\kappa,n,\ell}}/\varepsilon_\kappa\right)\right)+\\ &+\frac{1}{2}\sum_{\ell'=0}^{L-1}\sum_{n'=1}^{N_{\ell'}}\sum_{\kappa'=1}^{I_{\ell'}}\left[\left(\tilde{a}^{in}_{\ell'} c^{in}_{n',\ell'} g^{in}_{\kappa',n',\ell'}\right)^2\right.\\ &\left.\times\left(\Omega_R - \left(\sqrt{1-\Omega^2_{R_{n',\ell'}}}\Big/\eta + \sqrt{1-\left(\Omega_{R_{n',\ell'}}\alpha_{R_{\kappa',n',\ell'}}\right)^2}\Big/\left(\varepsilon_\kappa\eta\right)\right)\right)\right].\end{aligned} \tag{5.174}$$

On the other hand, the Doppler spread $\tilde{D}^{(2)}_{\Omega_R\Omega_R}$, (the square root of the second central moment of $\tilde{S}_{\Omega_R\Omega_R}(\Omega_R)$), is defined as follows [6]

$$\tilde{D}^{(2)}_{\Omega_R\Omega_R} \triangleq \sqrt{\int_{-\infty}^{\infty}\left(\Omega_R - \tilde{D}^{(1)}_{\Omega_R\Omega_R}\right)^2 \tilde{S}_{\Omega_R\Omega_R}(\Omega_R)d\Omega_R \Big/ \int_{-\infty}^{\infty}\tilde{S}_{\Omega_R\Omega_R}(\Omega_R)d\Omega_R}. \tag{5.175}$$

The closed form of $\tilde{D}^{(2)}_{\Omega_R\Omega_R}$ is then given by

$$\begin{aligned}&\tilde{D}^{(2)}_{\Omega_R\Omega_R} =\\ &=\left[\frac{1}{2}\sum_{\ell=0}^{L-1}\sum_{n=1}^{N_\ell}\sum_{\kappa=1}^{I_\ell}\left(\tilde{a}_\ell c_{n,\ell} g_{\kappa,n,\ell}\right)^2\left(\Omega_R - \Omega_{R_{n,\ell}}\left(1+\frac{\alpha_{R_{\kappa,n,\ell}}}{\varepsilon_\kappa}\right)\right)^2 - \left(\tilde{D}^{(2)}_{\Omega_R\Omega_R}\right)^2 +\right.\\ &\left.+\frac{1}{2}\sum_{\ell'=0}^{L-1}\sum_{n'=1}^{N_{\ell'}}\sum_{\kappa'=1}^{I_{\ell'}}\left(\left(\tilde{a}^{in}_{\ell'} c^{in}_{n',\ell'} g^{in}_{\kappa',n',\ell'}\right)^2\left(\Omega_R - \left(\frac{\sqrt{1-\Omega^2_{R_{n',\ell'}}}}{\eta} + \frac{\sqrt{1-\left(\Omega_{R_{n',\ell'}}\alpha_{R_{\kappa',n',\ell'}}\right)^2}}{\varepsilon_\kappa\eta}\right)\right)^2\right)\right]^{1/2}.\end{aligned} \tag{5.176}$$

5.6. Perfect wideband MIMO channel modelling

Once the post-processing of channel measurements is performed, the channel characteristics can be presented in the form of PSDs, e.g., Delay-Doppler PSD (in the case of channel sounders), Delay-DOD/DOA PSDs, etc. In this way, the aim of the perfect channel modelling is to find an analytical channel model and/or a simulation model that its PSD characteristics (see the PSDs obtained in Section 5.5.1) approximate as close as possible to the corresponding measured PSD system functions [6],[7] (see Figure 5.13).

This section shows the exact and general solution to this problem for a wideband MIMO channel, taking into account the consistency of the measured PSD system functions. A perfect 2D-space-time-frequency channel simulator, derived from a perfect 2D-space-time-frequency channel model (as the FD-DGUS-MIMO model proposed in Section 5.2), enable the emulation of measured direction-dispersive wideband mobile MIMO radio channels without producing any model error or making approximations. The only approximations considered here are the functions obtained for some model parameters due to the cross-products of the wideband signals (see Section 5.2.1 and 5.2.3), but the low influence of these approximations has been already verified. It is worth to indicate that this perfect wideband channel modelling strategy take into account the existence of IPWs [3], and it was not so far formulated in literature for MIMO.

5.6.1. Measurement vs. model PSDs: perfect and non-perfect

The channel model $\tilde{H}(f,t,x_T,x_R)$ given in (5.133) is perfect if and only if

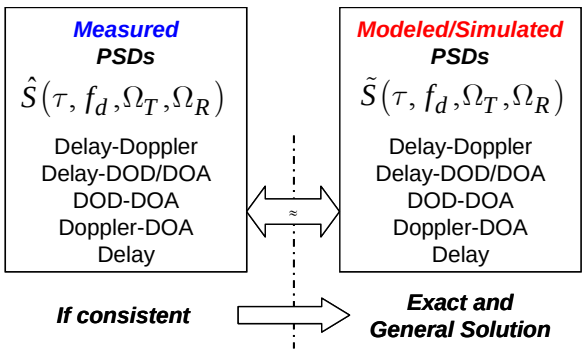

Figure 5.13. Perfect MIMO channel modelling based on perfect fitting of the PSD characteristics

$$\tilde{S}(\tau, f_d, \Omega_T, \Omega_R) = \hat{S}(\tau, f_d, \Omega_T, \Omega_R) \rightarrow \tilde{S}_{\tau f_d}(\tau, f_d) = \hat{S}_{\tau f_d}(\tau, f_d),$$
$$\tilde{S}_{\tau\Omega_R}(\tau, \Omega_R) = \hat{S}_{\tau\Omega_R}(\tau, \Omega_R),$$
$$\tilde{S}_{\tau\Omega_T}(\tau, \Omega_T) = \hat{S}_{\tau\Omega_T}(\tau, \Omega_T),$$
$$\tilde{S}_{\Omega_T\Omega_R}(\Omega_T, \Omega_R) = \hat{S}_{\Omega_T\Omega_R}(\Omega_T, \Omega_R),$$
$$\tilde{S}_{f_d\Omega_R}(f_d, \Omega_R) = \hat{S}_{f_d\Omega_R}(f_d, \Omega_R),$$
$$\tilde{S}_{\tau\tau}(\tau) = \hat{S}_{\tau\tau}(\tau).$$

On the other hand, the channel model (5.133) is non-perfect if

$$\tilde{S}_{\tau f_d}(\tau, f_d) = \hat{S}_{\tau f_d}(\tau, f_d), \quad \tilde{S}_{\tau\Omega_R}(\tau, \Omega_R) \approx \hat{S}_{\tau\Omega_R}(\tau, \Omega_R), \cdots$$
$$\tilde{S}_{\tau f_d}(\tau, f_d) \approx \hat{S}_{\tau f_d}(\tau, f_d), \quad \tilde{S}_{\tau\Omega_R}(\tau, \Omega_R) = \hat{S}_{\tau\Omega_R}(\tau, \Omega_R), \cdots$$

and so on.

It is worth to indicate that the measured PSDs $\hat{S}_{\tau f_d}(\tau, f_d)$, $\hat{S}_{\tau\Omega_R}(\tau, \Omega_R)$, $\hat{S}_{\tau\Omega_T}(\tau, \Omega_T)$, $\hat{S}_{\Omega_T\Omega_R}(\Omega_T, \Omega_R)$, $\hat{S}_{f_d\Omega_R}(f_d, \Omega_R)$, and $\hat{S}_{\tau\tau}(\tau)$ are assumed consistent and discrete with respect to the variables τ, f_d, Ω_R and Ω_T.

5.6.2. Model parameters calculation from PSD measurements

Given $\hat{S}_{\tau f_d}(\tau, f_d)$, $\hat{S}_{\tau\Omega_R}(\tau, \Omega_R)$, $\hat{S}_{\tau\Omega_T}(\tau, \Omega_T)$, $\hat{S}_{\Omega_T\Omega_R}(\Omega_T, \Omega_R)$, and $\hat{S}_{f_d\Omega_R}(f_d, \Omega_R)$ obtained from wideband MIMO measurements, and taking into account their discrete representation with respect to the variables τ, f_d, Ω_R and Ω_T, it is possible to obtain the PSD system function matrices $\hat{\mathbf{S}}_{\tau f_d}$, $\hat{\mathbf{S}}_{\tau\Omega_R}$, $\hat{\mathbf{S}}_{\tau\Omega_T}$, $\hat{\mathbf{S}}_{\Omega_T\Omega_R}$, $\hat{\mathbf{S}}_{f_d\Omega_R}$, and then calculate the FD-DGUS-MIMO channel model parameters.

The measured delay-Doppler PSD matrix, $\hat{\mathbf{S}}_{\tau f_d}$, is given by (see also Figure 5.14)

$$\hat{\mathbf{S}}_{\tau f_d} = \begin{pmatrix} \hat{s}_{1,0} & \cdots & \hat{s}_{1,L_m-1} \\ \vdots & \hat{s}_{n,\ell_m} & \vdots \\ \hat{s}_{N_m,0} & \cdots & \hat{s}_{N_m,L_m-1} \end{pmatrix} \tag{5.177}$$

where $\hat{\mathbf{S}}_{\tau f_d} \in \mathbb{R}^{N_m \times L_m}$, $N_m = 2 f_{d_{\max}} / \Delta f_d + 1$, $L_m = \tau_{\max} / \Delta\tau + 1$, being Δf_d and $\Delta\tau$ the resolution of the channel sounder in the Doppler and delay domains.

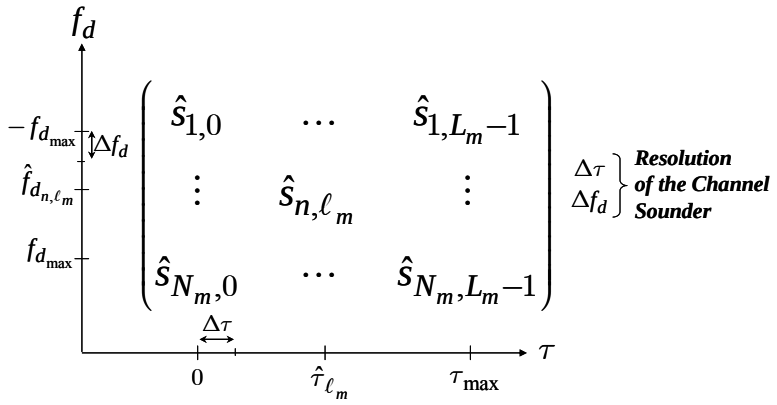

Figure 5.14. Delay-Doppler PSD experimental matrix.

This representation assumes the norm $\left\|\hat{\mathbf{S}}_{\tau f_d}\right\|_F = 1$, i.e., the Frobenius norm of $\hat{\mathbf{S}}_{\tau f_d}$ equal to one. In (5.177) the measured Doppler frequency $\hat{f}_{d_{n,\ell_m}}$ and the measured propagation delay $\hat{\tau}_{\ell_m}$ are given as follows

$$\hat{f}_{d_{n,\ell_m}} = -f_{d_{\max}} + \Delta f_d\,(n-1) \tag{5.178}$$

$$\hat{\tau}_{\ell_m} = \Delta\tau(\ell_m) \tag{5.179}$$

where $\ell_m = \ell = \{0,1,\cdots,L_m-1\}$ and $n = \{1,2,\cdots,N_m\}$.

Now, if the MIMO channel model is perfect, i.e., $\tilde{S}_{\tau f_d}(\tau, f_d) = \hat{S}_{\tau f_d}(\tau, f_d)$, then $N_\ell = N_m$ and $L = L_m$, and from (5.143), with $\ell = \ell'$, $n = n'$ and $\kappa = \kappa'$, the HPWs and IPWs Doppler components must fulfil

$$f_{d_{n,\ell}}\left(\left(1+u_{\kappa,n,\ell}\right)+\left(u'_{n,\ell}+u^{in}_{\kappa,n,\ell}\right)\right) = \hat{f}_{d_{n,\ell}}, \tag{5.180}$$

and the HPW delay components (see also (5.49)) must fulfil

$$\tau_\ell + \tau''_{\kappa,\ell} = \hat{\tau}_\ell, \tag{5.181}$$

where $\tau''_{\kappa,\ell}$ was defined in (5.50), and from Figure 5.9, $\max\left(\left|\tau''_{\kappa,\ell}\right|\right) \approx 20$ ns, and for a given system bandwidth B, then

$$I_\ell = \left\lfloor 2\left(20\times10^{-9}\right)B \right\rfloor, \tag{5.182}$$

and $\kappa = \{1,2,\cdots,I_\ell\}$. In (5.182) B is given in Hz. Note that $\lfloor\cdot\rfloor$ indicates selection of the lower nearest integer.

Therefore, the delay-Doppler PSD of the FD-DGUS-MIMO model, $\tilde{S}_{\tau f_d}(\tau, f_d)$, for the perfect case, can be represented by the delay-Doppler PSD matrix $\tilde{\mathbf{S}}_{\tau f_d}$ as follows:

$$\tilde{\mathbf{S}}_{\tau f_d} = \begin{pmatrix} \tilde{s}_{1,0} & \cdots & \tilde{s}_{1,L-1} \\ \vdots & \tilde{s}_{n,\ell} & \vdots \\ \tilde{s}_{N_\ell,0} & \cdots & \tilde{s}_{N_\ell,L-1} \end{pmatrix}, \tag{5.183}$$

where the entries $\tilde{s}_{n,\ell}$ are given by

$$\tilde{s}_{n,\ell} = \left(\tilde{a}_\ell c_{n,\ell}\right)^2 \sum_{\kappa=1}^{I_\ell} \left(g_{\kappa,n,\ell}\right)^2 + \left(\tilde{a}_\ell^{in} c_{n,\ell}^{in}\right)^2 \sum_{\kappa=1}^{I_\ell} \left(g_{\kappa,n,\ell}^{in}\right)^2 = \hat{s}_{n,\ell}. \tag{5.184}$$

If the marginal conditions given in (5.141) are taken into account, the coefficients $\tilde{a}_\ell$, $c_{n,\ell}$, $g_{\kappa,n,\ell}$ can be obtained as follows

$$\tilde{a}_\ell = \sqrt{\sum_{n=1}^{N_m} \hat{s}_{n,\ell} - \left(\tilde{a}_\ell^{in}\right)^2}, \tag{5.185}$$

$$c_{n,\ell} = \frac{1}{\tilde{a}_\ell} \sqrt{\hat{s}_{n,\ell} - \left(\tilde{a}_\ell^{in} c_{n,\ell}^{in}\right)^2} \tag{5.186}$$

$$g_{\kappa,n,\ell} = \frac{1}{\left(\tilde{a}_\ell c_{n,\ell}\right)} \sqrt{\hat{s}_{n,\ell} - \left(\tilde{a}_\ell^{in} c_{n,\ell}^{in} g_{\kappa,n,\ell}^{in}\right)^2} \tag{5.187}$$

The closed forms for the channel model parameters showed above (see also (5.107)) follow the desired relationship for the perfect channel modelling strategy, i.e., $\tilde{\mathbf{S}}_{\tau f_d} = \hat{\mathbf{S}}_{\tau f_d}$, but in case of limited resolution in the Doppler frequency domain is difficult to assure the US condition given in (5.127). To obtain a US model, it is recommendable to replace $f_{d_{n,\ell}}\left(\left(1+u_{\kappa,n,\ell}\right)+\left(u'_{n,\ell}+u_{\kappa,n,\ell}^{in}\right)\right)$ in (5.180) by

$$f_{d_{\kappa,n,\ell}}^{US} = f_{d_{n,\ell}}\left(\left(1+u_{\kappa,n,\ell}\right)+\left(u'_{n,\ell}+u_{\kappa,n,\ell}^{in}\right)\right)+\left(\beta_{\kappa,n,\ell}-1/2\right)\Delta f_d, \tag{5.188}$$

where $\beta_{\kappa,n,\ell}$ is a i.i.d variable which is uniformly distributed within [0,1).

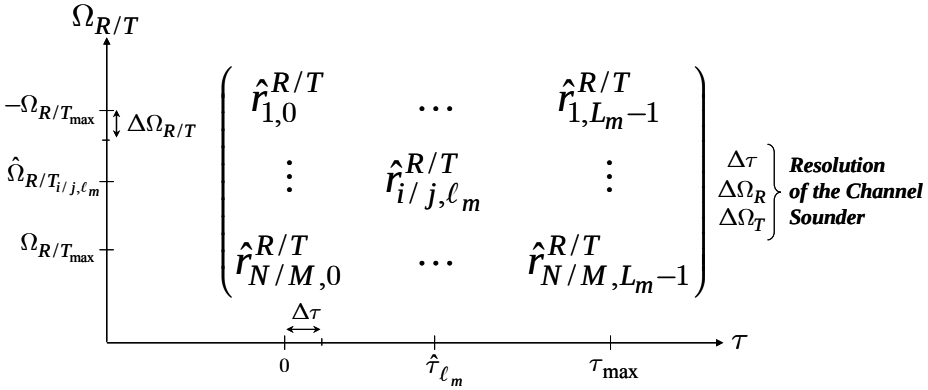

Figure 5.15. Delay-DOA/DOD PSD experimental matrix.

On the other hand, in the same way that the PSD matrix $\hat{\mathbf{S}}_{\tau f_d}$ presented in (5.177), the measured delay-DOA and delay-DOD PSD matrices, i.e., $\hat{\mathbf{S}}_{\tau\Omega_R}$ and $\hat{\mathbf{S}}_{\tau\Omega_T}$, respectively, can be given by (see also Figure 5.15):

$$\hat{\mathbf{S}}_{\tau\Omega_R} = \begin{pmatrix} \hat{r}^{R}_{1,0} & \cdots & \hat{r}^{R}_{1,L_m-1} \\ \vdots & \hat{r}^{R}_{i,\ell_m} & \vdots \\ \hat{r}^{R}_{N,0} & \cdots & \hat{r}^{R}_{N,L_m-1} \end{pmatrix} \tag{5.189}$$

$$\hat{\mathbf{S}}_{\tau\Omega_T} = \begin{pmatrix} \hat{r}^{T}_{1,0} & \cdots & \hat{r}^{T}_{1,L_m-1} \\ \vdots & \hat{r}^{T}_{j,\ell_m} & \vdots \\ \hat{r}^{T}_{M,0} & \cdots & \hat{r}^{T}_{M,L_m-1} \end{pmatrix} \tag{5.190}$$

where $\hat{\mathbf{S}}_{\tau\Omega_R} \in \mathbb{R}^{N\times L_m}$ and $\hat{\mathbf{S}}_{\tau\Omega_T} \in \mathbb{R}^{M\times L_m}$. From Figure 5.15, $\hat{\Omega}_{R_{i,\ell_m}} = -\Omega_{R_{\max}} + \Delta\Omega_R(i-1), \hat{\Omega}_{T_{j,\ell_m}} = -\Omega_{T_{\max}} + \Delta\Omega_T(j-1)$, $j=\{1,2,\cdots,M\}$, $i=\{1,2,\cdots,N\}$, $\ell_m = \ell$, being $\Delta\Omega_R$ and $\Delta\Omega_T$ the resolution of the channel sounder in the Ω_R and Ω_T directions, respectively. The matrices defined in (5.189) and (5.190) assume the norms $\left\|\hat{\mathbf{S}}_{\tau\Omega_R}\right\|_F = 1$ and $\left\|\hat{\mathbf{S}}_{\tau\Omega_T}\right\|_F = 1$.

Therefore, assuming that $\hat{S}_{\tau f_d}(\tau, f_d)$, $\hat{S}_{\tau\Omega_R}(\tau,\Omega_R)$, and $\hat{S}_{\tau\Omega_T}(\tau,\Omega_T)$ are consistent, their matrix representation $\hat{\mathbf{S}}_{\tau f_d}$, $\hat{\mathbf{S}}_{\tau\Omega_R}$ and $\hat{\mathbf{S}}_{\tau\Omega_T}$ have some interesting properties useful to obtain the remaining channel model parameters.

First, the path gains $\tilde{a}_\ell$ are identically obtained either from (5.177) or from (5.189) and (5.190) using the model PSDs matrices $\tilde{\mathbf{S}}_{\tau\Omega_R}$ and $\tilde{\mathbf{S}}_{\tau\Omega_T}$ (see also (5.145) and (5.147)):

$$\tilde{r}_{i,\ell}^{R} = \left(\tilde{a}_\ell c_{n,\ell}\right)^2 \sum_{\kappa=1}^{I_\ell}\left(g_{\kappa,n,\ell}\right)^2 + \left(\tilde{a}_\ell^{in} c_{n,\ell}^{in}\right)^2 \sum_{\kappa=1}^{I_\ell}\left(g_{\kappa,n,\ell}^{in}\right)^2 = \hat{r}_{i,\ell}^{R}, \tag{5.191}$$

$$\tilde{r}_{j,\ell}^{T} = \left(\tilde{a}_\ell c_{n,\ell}\right)^2 \sum_{\kappa=1}^{I_\ell}\left(g_{\kappa,n,\ell}\right)^2 + \left(\tilde{a}_\ell^{in} c_{n,\ell}^{in}\right)^2 \sum_{\kappa=1}^{I_\ell}\left(g_{\kappa,n,\ell}^{in}\right)^2 = \hat{r}_{j,\ell}^{T}. \tag{5.192}$$

Therefore

$$\tilde{a}_\ell = \sqrt{\sum_{n=1}^{N_m} \hat{s}_{n,\ell} - \left(\tilde{a}_\ell^{in}\right)^2} = \sqrt{\sum_{i=1}^{N} \hat{r}_{i,\ell}^{R} - \left(\tilde{a}_\ell^{in}\right)^2} = \sqrt{\sum_{j=1}^{M} \hat{r}_{j,\ell}^{T} - \left(\tilde{a}_\ell^{in}\right)^2}. \tag{5.193}$$

Thus, being $\tilde{a}_\ell$ and $c_{n,\ell}$ known, i.e., from (5.193) and (5.186), respectively, then equations (5.187), (5.191) and (5.192) can be used to obtain $g_{\kappa,n,\ell}$. Note that $\tilde{a}_\ell^{in}$, $c_{n,\ell}^{in}$ and $g_{\kappa,n,\ell}^{in}$ are known from (5.107).

On the other hand, the entries of the ℓ-th column of $\hat{\mathbf{S}}_{\tau f_d}$ may differ from the entries of ℓ-th column of $\hat{\mathbf{S}}_{\tau\Omega_R}$ and $\hat{\mathbf{S}}_{\tau\Omega_T}$ only by permutation [7]. If this condition is fulfilled, then, for any value of $n = \{1,2,\cdots,N_m\}$, integers $j \in \{1,2,\cdots,M\}$, $i \in \{1,2,\cdots,N\}$ can be found so that $\hat{r}_{i,\ell}^{R} = \hat{r}_{j,\ell}^{T} = \hat{s}_{n,\ell}$ holds. Hence, with the indexes i and j it can be then determined $\hat{\Omega}_{R_{i,\ell}} = -\Omega_{R_{\max}} + \Delta\Omega_R (i-1)$, and $\hat{\Omega}_{T_{j,\ell}} = -\Omega_{T_{\max}} + \Delta\Omega_T (j-1)$.

Therefore, the desired discrete DOA and DOD (see (5.145) and (5.147))

$$\Omega_{R_{n,\ell}}\left(1+\frac{\alpha_{R_{\kappa,n,\ell}}}{\varepsilon_\kappa}\right) + \left(\frac{\sqrt{1-\Omega_{R_{n',\ell'}}^2}}{\eta} + \frac{\sqrt{1-\left(\Omega_{R_{n',\ell'}}\alpha_{R_{\kappa',n',\ell'}}\right)^2}}{\varepsilon_\kappa \eta}\right),$$

and

$$\Omega_{T_{n,\ell}}\left(1+\frac{\alpha_{T_{\kappa,n,\ell}}}{\varepsilon_\kappa}\right),$$

of the FD-DGUS-MIMO channel model can be obtained respectively by:

$$\Omega_{R_{n,\ell}}\left(1+\frac{\alpha_{R_{\kappa,n,\ell}}}{\varepsilon_\kappa}\right)+\left(\frac{\sqrt{1-\Omega^2_{R_{n',\ell'}}}}{\eta}+\frac{\sqrt{1-\left(\Omega_{R_{n',\ell'}}\alpha_{R_{\kappa',n',\ell'}}\right)^2}}{\varepsilon_\kappa\eta}\right)=\hat{\Omega}_{R_{i,\ell}} \tag{5.194}$$

$$\Omega_{T_{n,\ell}}\left(1+\frac{\alpha_{T_{\kappa,n,\ell}}}{\varepsilon_\kappa}\right)=\hat{\Omega}_{T_{j,\ell}} \tag{5.195}$$

The model parameter $\Omega_{R_{n,\ell}}$ in (5.194) must be solved by numerical methods. Besides, note from (5.181), (5.188), (5.194), and (5.195), that the remaining model parameters $\tau''_{\kappa,\ell}$, $u_{\kappa,n,\ell}$, $u'_{n,\ell}$, $u^{in}_{\kappa,n,\ell}$, $\alpha_{R_{\kappa',n',\ell'}}$, $\alpha_{T_{\kappa,n,\ell}}$, ε_κ, and η were defined in Section 5.2. For readability they are redefined below:

$$u_{\kappa,n,\ell}\approx\frac{\alpha_{R_{\kappa,n,\ell}}}{\varepsilon_\kappa},$$

$$\alpha_{R_{\kappa,n,\ell}}=\cos\left(\phi''_{R_{\kappa,n,\ell}}\right),$$

$$\alpha_{T_{\kappa,n,\ell}}=\cos\left(\phi''_{T_{\kappa,n,\ell}}\right),$$

$$p_{\phi''_{R_{\kappa,n,\ell}}}\left(\phi''_{R_{\kappa,n,\ell}}\right)=\frac{1}{\sigma_{\phi''}\sqrt{2}}\exp\left(-\left|\frac{\phi''_{R_{\kappa,n,\ell}}\sqrt{2}}{\sigma_{\phi''}}\right|\right),$$

$$p_{\phi''_{T_{\kappa,n,\ell}}}\left(\phi''_{T_{\kappa,n,\ell}}\right)=\frac{\gamma^2+1-2\gamma\cos\left(\phi_{R_{n,\ell}}+\phi''_{R_{\kappa,n,\ell}}\right)}{\gamma^2-1}p_{\phi''_{R_{\kappa,n,\ell}}}\left(\phi''_{R_{\kappa,n,\ell}}\right),$$

$$\gamma=\tau_\ell/\tau_0,$$

$$\tau_{\kappa,\ell}=\tau_\ell+\tau''_{\kappa,\ell},$$

$$\tau_\ell=R_\ell/c,$$

$$R_{n,\ell}=R_{T_{n,\ell}}+R_{R_{n,\ell}},$$

$$\tau''_{\kappa,\ell}=\tau''_{\kappa,\ell}=\left\langle\sin\left(\phi''_{R_{\kappa,n,\ell}}\right)R_{R_{n,\ell}}/c\right\rangle_n,$$

$$u^{in}_{\kappa,n,\ell}=\frac{\sin\left(\phi^B_{R_{\kappa,n,\ell}}+\varphi_R-\chi_R\right)}{\varepsilon_\kappa\eta\cos\left(\phi_{R_{n,\ell}}+\varphi_R-\chi_R\right)},$$

$$u'_{n,\ell}=\frac{\sin\left(\phi_{R_{n,\ell}}+\varphi_R-\chi_R\right)}{\eta\cos\left(\phi_{R_{n,\ell}}+\varphi_R-\chi_R\right)},$$

$$\phi^{B}_{R_{\kappa,n,\ell}} = \phi'_{R_{n,\ell}} - \varphi_R + \phi''_{R_{\kappa,n,\ell}}, \quad \phi_{R_\ell} = \phi'_{R_\ell} - \varphi_R, \quad \phi_{R_{n,\ell}} = \cos^{-1}\left(\Omega_{R_{n,\ell}}\right),$$

$$\varepsilon_\kappa = 1.2712\left(\frac{f_\kappa}{f_c}\right)^2 - 1.1835\left(\frac{f_\kappa}{f_c}\right) - 0.0073, \quad \text{with } \varepsilon_\kappa \neq 0,$$

$$f_\kappa = -B/2 + (\kappa - 1)\Delta f, \quad \text{with } \kappa = \{1,2,\cdots,I_\ell\},$$

$$I_\ell = \left\lfloor 2\left(20\times 10^{-9}\right)B \right\rfloor,$$

$$\eta = \in \mathbb{R}\{0,\cdots,1\}.$$

According to these parameters definition, which are a result of the cross-products and the IPWs propagation, the angular DOA estimations, i.e., $\Omega_{R_{n,\ell}}$, have to be performed before than the Doppler components $f_{d_{n,\ell}}$ due to the angular dependence in $u^{in}_{\kappa,n,\ell}$ and $u'_{n,\ell}$. Besides, note that φ_R and χ_R are the array angle orientation and the angle of displacement at the RX, respectively (see Figure 5.5).

To conclude, note that consistent measured matrices $\hat{\mathbf{S}}_{\Omega_T\Omega_R}$ and $\hat{\mathbf{S}}_{f_d\Omega_R}$ can be used as well to find the channel model parameters by means of $\tilde{\mathbf{S}}_{\Omega_T\Omega_R}$ and $\tilde{\mathbf{S}}_{f_d\Omega_R}$ obtained from (5.150) from (5.152), respectively. Besides, note that $\tilde{\mathbf{S}}_{f_d\Omega_R}$ has the quality of the DOD-Doppler dependence which can be used to check the calculations described above, or used directly for the calculation of $f_{d_{n,\ell}}$ and $\Omega_{R_{n,\ell}}$.

5.6.3. Model parameters from non-consistent measurements

Since measurement errors are possible, $\hat{S}_{\tau\Omega_R}(\tau,\Omega_R)$ and $\hat{S}_{\tau\Omega_T}(\tau,\Omega_T)$ could be not consistent with $\hat{S}_{\tau f_d}(\tau, f_d)$. Besides, note that $\hat{S}_{f_d\Omega_R}(f_d,\Omega_R)$ could be not consistent with $\hat{S}_{\tau f_d}(\tau, f_d)$ in the f_d domain. In such cases, for instance equation (5.193) is not fulfilled and the permutation of the columns between $\hat{S}_{\tau\Omega_R}(\tau,\Omega_R)$, $\hat{S}_{\tau\Omega_T}(\tau,\Omega_T)$ and $\hat{S}_{\tau f_d}(\tau, f_d)$ is not feasible. In theses cases, only semi-perfect models can be derived.

A possible solution follows the no-perfect case given in Section 5.6.1. Hence, for any measured value $\hat{s}_{n,\ell}$, we have to find the entry $\hat{r}^R_{i,s}$ or $\hat{r}^T_{j,s}$ which is closest to $\hat{s}_{n,\ell}$. Here, the index s refers to the s-th propagation path and ranges from $\ell - \ell_0$ to $\ell + \ell_0$, where ℓ_0 denotes a sufficiently large integer. The procedure can be described by

$$\begin{aligned}&\text{find}\left[\hat{r}^R_{i,s} \cong \hat{s}_{n,\ell}, \left\{\hat{r}^R_{i,\ell-\ell_0},\cdots,\hat{r}^R_{i,s},\cdots,\hat{r}^R_{i,\ell+\ell_0}\right\}\right],\\&\text{find}\left[\hat{r}^T_{j,s} \cong \hat{s}_{n,\ell}, \left\{\hat{r}^T_{j,\ell-\ell_0},\cdots,\hat{r}^T_{j,s},\cdots,\hat{r}^T_{j,\ell+\ell_0}\right\}\right].\end{aligned} \tag{5.196}$$

Once $\hat{r}^R_{i,s}$ and $\hat{r}^T_{j,s}$ have been found, the next step is to construct the auxiliary Delay-DOA/DOD matrices $\widehat{\mathbf{S}}_{\tau\Omega_R}$ and $\widehat{\mathbf{S}}_{\tau\Omega_T}$ containing $\hat{s}_{n,\ell}$ (from $\hat{\mathbf{S}}_{\tau f_d}$) in the i-th and j-th rows, respectively, and in the ℓ-th columns, being $\hat{s}_{n,\ell}$ the best approximation to the entries $\hat{r}^R_{i,s}$ or $\hat{r}^T_{j,s}$ of the measured $\hat{\mathbf{S}}_{\tau\Omega_R}$ and $\hat{\mathbf{S}}_{\tau\Omega_T}$. The resulting auxiliary Delay-DOA/DOD matrices $\widehat{\mathbf{S}}_{\tau\Omega_R}$ and $\widehat{\mathbf{S}}_{\tau\Omega_T}$ are then consistent with $\hat{\mathbf{S}}_{\tau f_d}$ and can now be used as starting point for the perfect fitting procedure addressed in the previous section. The same procedure can be applied to make consistent $\hat{\mathbf{S}}_{f_d\Omega_R}$ with $\hat{\mathbf{S}}_{\tau f_d}$ in the f_d domain.

5.6.4. Parameters estimation based on the 2D-STFCF

Other method to determine channel model parameters for measurement-based simulation models can take advantage of the channel correlation functions [9], if both measurements and model fulfil WSSUS conditions [10],[11]. This is the case of the FD-DGUS-MIMO model in (5.133) and the measurements performed for this PhD Dissertation (as the multivariate normality of data has been verified in Section 3.5.3).

The procedure is based on the fitting between the model and measurements using the temporal correlation function (TCF), $r_{\tau'\tau'}(\tau')$, the frequency correlation function (FCF), $r_{\nu\nu}(\nu)$, and, as a new characteristic, the space correlation functions (SCF) of the channel, i.e., $r_{\varsigma_T\varsigma_T}(\varsigma_T)$ and $r_{\varsigma_R\varsigma_R}(\varsigma_R)$. First, the TCF, FCF, and SCFs can be estimated directly from frequency time-variant MIMO measurements (from real-time channel sounding point of view) and their closed forms obtained from (5.134) as follows:

$$\begin{aligned}\tilde{r}_{\nu\nu}(\nu) &\triangleq r_{\tilde{H}\tilde{H}}(\nu,0,0,0),\\ \tilde{r}_{\tau'\tau'}(\tau') &\triangleq r_{\tilde{H}\tilde{H}}(0,\tau',0,0),\\ \tilde{r}_{\varsigma_T\varsigma_T}(\varsigma_T) &\triangleq r_{\tilde{H}\tilde{H}}(0,0,\varsigma_T,0),\\ \tilde{r}_{\varsigma_R\varsigma_R}(\varsigma_R) &\triangleq r_{\tilde{H}\tilde{H}}(0,0,0,\varsigma_R).\end{aligned} \tag{5.197}$$

Note that the theoretical $\tilde{r}_{\nu\nu}(\nu)$, $\tilde{r}_{\tau'\tau'}(\tau')$, $\tilde{r}_{\varsigma_T\varsigma_T}(\varsigma_T)$, and $\tilde{r}_{\varsigma_R\varsigma_R}(\varsigma_R)$ are obtained setting to cero the undesired displacement variables in the 2D-STFCF $r_{\tilde{H}\tilde{H}}(\nu,\tau',\varsigma_T,\varsigma_R)$, from (5.134).

On the other hand, the method based on the correlation functions (CF) introduces some enhancements using the samples in the frequency, time, and space domains, improving the estimation of TCF, FCF, and SCFs from measurements. The main idea is to take into account the MIMO time-variant channel frequency response (CFR), and use the samples from different measured domains for the averaging of the CF estimations, in the same way used in (3.19) for the estimation of the spatial covariance matrix. The validation of this procedure has been done already comparing both the TCF and FCF with the SAGE algorithm [12], but the space domain has not been included so far, i.e., $\tilde{r}_{\varsigma_T\varsigma_T}(\varsigma_T)$ vs. $\hat{r}_{\varsigma_T\varsigma_T}(\varsigma_T)$, and $\tilde{r}_{\varsigma_R\varsigma_R}(\varsigma_R)$ vs. $\hat{r}_{\varsigma_R\varsigma_R}(\varsigma_R)$. As the aim of this PhD Dissertation does not include the parameter estimation procedures, this is an open issue for future investigations.

Moreover, as it was already mentioned, sophisticated super-resolution parameter estimation techniques have been used to estimate the parameter of a channel model (e.g., SAGE). However, a serious drawback of the aforementioned representation of the radio channel is associated with a large number of specular components, often required to accurately simulate the physical channel. In this case, the number of the model parameters to be estimated is also large, which can cause a serious degradation in performance of the chosen parameter estimation method. To circumvent this problem, the stochastic maximum likehood (ML) method has been proposed [14].

Here, for future channel model parameters estimations based on the closed forms $\tilde{r}_{\nu\nu}(\nu)$, $\tilde{r}_{\tau'\tau'}(\tau')$, $\tilde{r}_{\varsigma_T\varsigma_T}(\varsigma_T)$, and $\tilde{r}_{\varsigma_R\varsigma_R}(\varsigma_R)$, and the estimated versions from measurements $\hat{r}_{\nu\nu}(\nu)$, $\hat{r}_{\tau'\tau'}(\tau')$, $\hat{r}_{\varsigma_T\varsigma_T}(\varsigma_T)$, and $\hat{r}_{\varsigma_R\varsigma_R}(\varsigma_R)$, it is proposed to follow an iterative nonlinear least squares approximation (INLSA) algorithm as in [12], since the proposed FD-DGUS-MIMO model and the measurements fulfil the desired WSSUS condition.

To conclude, it is worth to indicate that the estimation procedure indicated in this section, and the previous perfect channel modelling strategy, are the first methods proposed in the literature addressing the effects of the fine scattering in the propagation and including HPWs and IPWs in formulations.

5.7. FD-DGUS-MIMO channel simulations

Based on the parameters defined in Section 5.2, the simulation of the 2D-STFCF (5.134) is presented here, aimed to verify the effects of IPWs on the correlation characteristics. For this goal a geometrical model as in [15], with $N_\ell = 25$ Laplacian scatterers, with $\sigma_{\phi''} = 4^\circ$, lying in L ellipses (with eccentricity of 0.8), will be used as reference for the generation of the distances $R_{T_{n,\ell}}$ and

$R_{R_{n,\ell}}$, and the channel model parameters τ_ℓ, $f_{d_{n,\ell}}$, $\Omega_{T_{n,\ell}}$, and $\Omega_{R_{n,\ell}}$. Note that these model parameters are the same as some obtained from measurements.

On the other hand, it has been set a time window $T = 400\,\text{ms}$, bandwidth $B = \{200, 700\}\,\text{MHz}$, and $f_c = 2\,\text{GHz}$. Note that the used relative bandwidth permits us to include the cross-products modelled in this chapter.

On the other hand, the ULA lengths at the TX and RX were defined by $D_T = D_R = 0.3\,\text{m}$, and 10 m of separation between TX and RX. Besides, the RX displacement was set to generate a maximum Doppler, $f_{d_{\max}}$, of 10 Hz. The arrays angle orientation were $\varphi_R = \varphi_T = 45^\text{o}$, and the angle of displacement at the RX $\chi_R = 30^\text{o}$. The system resolution in the frequency and time domains followed $\Delta f = 2\,\text{MHz}$ and $\Delta t = 10^{-3}\,s$, respectively. The IPWs parameter η has been set to 0.5, as an example case (see also (5.106) and (5.107)) to depict channel simulation results with and without IPWs.

Figure 5.16.a shows the frequency-time correlation function with and without consider IPWs for $f_c = 2\,\text{GHz}$ and $B = 200\,\text{MHz}$. On the other hand, Figure 5.16.b shows the frequency-time correlation function with and without consider IPWs for $f_c = 2\,\text{GHz}$ and $B = 700\,\text{MHz}$. From Figure 5.16 it is observed that IPWs have affects on the correlation characteristics of the simulated FD-DGUS-MIMO channel if the bandwidth increases; only slightly differences are perceived for $B = 200\,\text{MHz}$.

This correlation characteristic can affect the performance of a MIMO system, especially for higher relative bandwidths. Besides, from Figure 5.16.a it is observed that the relative bandwidth used during the measurement campaigns performed for this PhD Dissertation does not shows any harmful effect on the correlation characteristics in time and frequency. In the same way, the correlation characteristics in the space domain at the RX do not show strong dependence on the existence of IPW for $f_c = 2\,\text{GHz}$ and $B = 200\,\text{MHz}$ (see Figure 5.17). Note that only the RX spatial domain is plotted since the IPWs were modelled only at the RX side (see (5.4)).

It is worth to indicate that simulations at $f_c = 12\,\text{GHz}$ were performed, but at such frequencies if the same relative bandwidth is desired for comparison analysis, i.e., $B / f_c = 0.35$, the bandwidth must be set to $B = 4200\,\text{MHz}$. Due to computational restrictions for the multidimensional 2D-STFCF, and using the resolution parameters described above, this simulations never reached the final solution and are not plotted here.

To conclude, based on the results presented in Figure 5.16.a and Figure 5.17, and for the measurement setup used during this PhD. Dissertation, the FD-DGUS-MIMO model in (5.133) can be applied taking into account only HPWs.

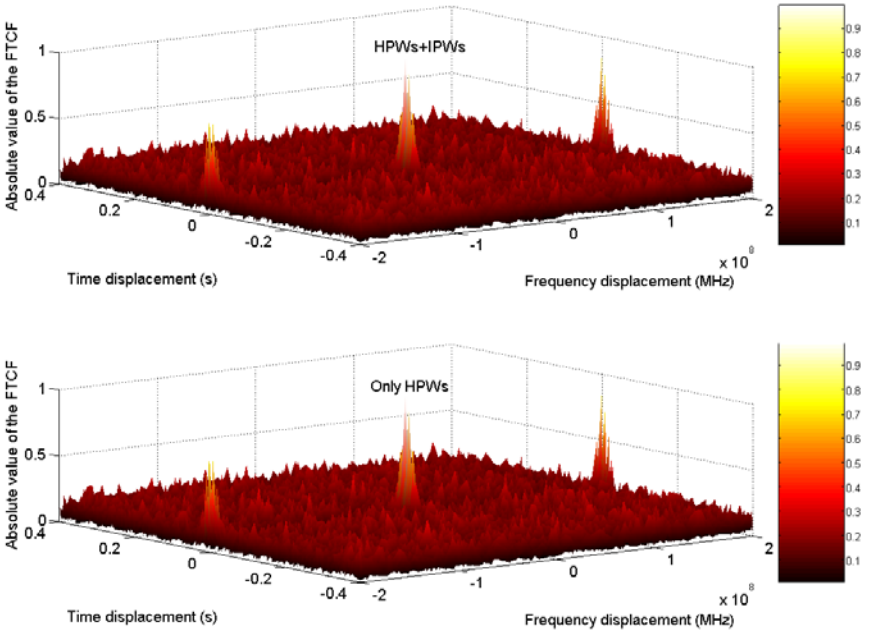

a)

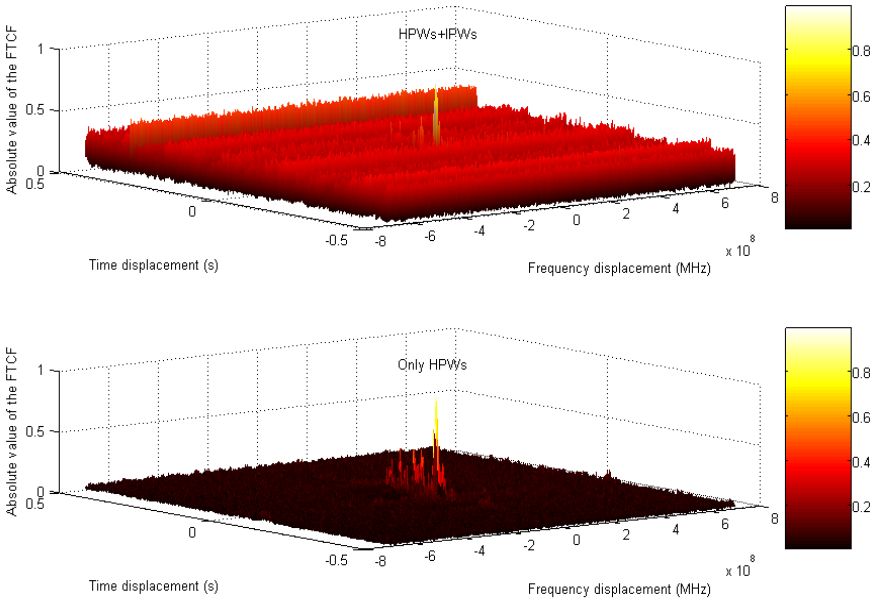

b)

Figure 5.16. Simulation results of the correlation functions of the FD-DGUS-MIMO model, a) frequency-time correlation function with/without IPWs at 2 GHz and 200 MHz bandwidth, and, b) frequency-time correlation function with/without IPWs at 2 GHz and 700 MHz bandwidth.

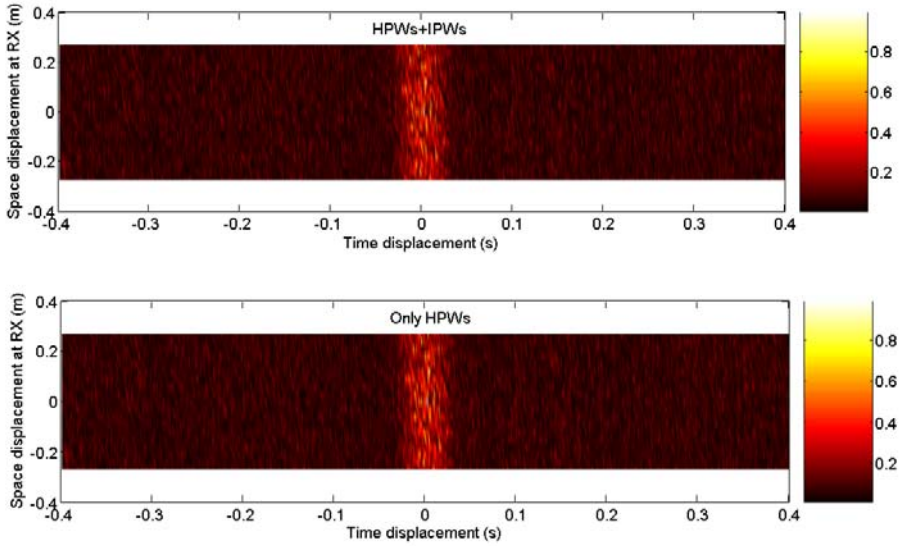

Figure 5.17. Simulation results of the correlation function of the FD-DGUS-MIMO model: RX-space-time correlation function with/without IPWs at 2 GHz and 200 MHz bandwidth.

5.8. Conclusions

In this chapter a new FD-DGUS-MIMO channel model which includes parameters for modelling space-time channels with different relative wideband signals, high central frequencies and the inclusion of the effects of close scatterers using HPWs and IPWs has been proposed. Despite the existence of IPWs has been reported in physics studies since 1959, the proposed model is the first channel model including both types of plane waves, which permit us to model frequency-dependent effects including possible effects related with wave propagation and the interaction between waves, scatterers and the antennas.

On the other hand, it has been imposed desired WSSUS conditions for the proposed FD-DGUS-MIMO channel model, which offer suitable characteristics for the application of perfect modelling techniques and then obtaining the channel model parameters from channel sounder or VNA measurements. The imposed DGUS characteristics allowed the calculation of closed forms for the 2D-STFCF and 2D-D^3-PSD functions, which permit us the application of perfect and non-perfect modelling techniques based on PSDs estimations from real world measurements. Besides, based on both the estimation of the CFs from measurements and the closed forms of the CFs obtained from the 2D-STFCF, the application of INLSA algorithms is feasible. These two techniques for channel model parameters estimations allow the formulation of dedicated simulations

models for realistic performance analysis of wideband, high frequency and even UWB-MIMO systems.

Since high order statistics have been used for the perfect modelling proposal following the formulated and estimated PSDs, the model does not consider any approximation, except the approximations used for the parameters resulting from cross-products due to the wideband signals and then from the fine scattering. It is worth to indicate that these approximations have shown low effects in the model performance.

To conclude, despite the proposed FD-DGUS-MIMO channel model has been formulated based on a 2D spatial approximation (azimuthally) and it has been proposed for ULAs, as the MIMO measurements performed for this Dissertation, the model can be extended to 3D and including other arrays geometries.

References

[1] G. D. Durgin, *Space-Time Wireless Channels*, Pearson Education, Inc., NJ, US, 2003, p. 72-173.

[2] M. Born and E. Wolf, *Principles of Optics: Electromagnetic Theory of Propagation, Interference, and Diffraction of Light*, Pergamon Press, New York, 6th edition, 1980. p. 560-564.

[3] P. Cornille, "On the propagation of inhomogeneous waves," *J. Phys. D: Appl. Phys.*, Vol. 23, pp.129-135, 1990.

[4] J. B. Schneider and R. J. Kruhlak, "Dispersion of homogeneous and inhomogeneous waves in the yee finite-difference time-domain grid," *IEEE Trans. on Microwave Theory and Techniques*, Vol. 49, No. 2, pp. 280-287, Feb. 2001.

[5] B. Allen, et all, *Ultra-wideband antennas and propagation for communications, radar and imaging*, Jhon Wiley and Sons Inc., West Sussex, UK, 2007.

[6] M. Pätzold, "Perfect channel modeling and simulation of measured wide-band mobile radio channels," 3G Mobile Communication Technologies, Conference Publication No. 471, IEE, 2000.

[7] M. Pätzold and Q. Yao, "Perfect modelling and simulation of measured spatio-temporal wireless channels," Proc. 5th Int. Symp. on Wireless Personal Multimedia Communications, WPMC '02, Honolulu, Hawaii, 27. - 30. Oct. 2002.

[8] E. Boyer, et al, "Final Report on estimation methods for channel parameters and metrics," 507325 NEWCOM, DR2.13, pp. 10-11, March 2007.

[9] M. Pätzold and N. Youssef, "Modelling and simulation of direction-selective and frequency-selective mobile radio channels," *Int. J. Electr. and Commun.*, Vol. AEÜ-55, No. 6, pp. 433-442, Nov. 2001.

[10] D. Umansky, "Design of measurement-based wideband mobile radio channel simulators", IEEE 4th International Symposium on Wireless Communication System - ISWCS, Trondheim, Norway, 17-19 October 2007.

[11] D. Umansky and M. Pätzold, "Estimation of path gains and Doppler frequencies from the temporal autocorrelation function of mobile fading channels," 13th European Wireless Conf., 2007.

[12] D. Umansky and M. Pätzold, "Design of wideband mobile radio channel simulators based on real-world measurement data", IEEE Vehicular Technology Conference - VTC Spring, 2008.

[13] Pagani, P. and Pajusco, P., "Modeling the space-and time-variant ultra-wideband propagation channel," IEEE International Conference on Ultra-Wideband, Sept. 2006.

[14] C. B. Ribeiro, E. Ollila, and V. Stucki, "Stochastic maximum likelihood method for propagation parameter stimation", Proc. 15th Int. Symp. on Personal, Indoor and Mobile Radio Communications - PIMRC, 2004.

[15] M. Pätzold and B. O. Hogstad, "A wideband MIMO channel model derived from the geometric elliptical scattering model", *Wireless Communications and Mobile Computing*, Vol. 8, No. 5, pp. 597-605, 2007.

CHAPTER 6

CONCLUSIONS AND FUTURE RESEARCH

6.1. Introduction

The frequency dependent wideband MIMO channel has been investigated for this Dissertation addressing different fields. Homogeneous and in-homogeneous plane wave propagation, deterministic Gaussian perfect MIMO channel modelling, measurement data processing, multivariate statistic data analysis, linear algebra applied for solving non-positiveness of particular experimental covariance matrices, and MIMO channel synthetic generation were the main research topics included.

Central frequency and bandwidth effects have been considered from experimental and theoretical viewpoints. Realistic wideband multi-spectral MIMO channel measurements, their multivariate normality and linearity analysis, and the MIMO system performance analysis have been carried out from an experimental point of view. From a theoretical point of view, reliable synthetic multi-spectral MIMO data generation, alternating projections of non-positive experimental covariance matrices to allow Cholesky factorisations, and new strategies for wideband MIMO channel modelling fulfilling WSSUS conditions were carried out.

6.2. Conclusions

6.2.1. General conclusions of the Dissertation

The theoretical formulations and experimental procedures proposed in this Dissertation allow to the research community the characterisation of realistic frequency dependent MIMO channels at different frequency bands from 2 to 12 GHz in wideband conditions. These results can be applied to different mobile communication standards and easily extended to UWB-MIMO and higher central frequencies, being also applicable to cognitive radio systems where frequency dependency is inherent. Indoor MIMO channel characteristics at different central frequencies between 2 and 12 GHz, with the same electrical separation between

antennas elements, have shown remarkable differences. These results allow us to choice particular space-time processing, i.e., beamforming, SM, or ST coding, according to the frequency band within the analysed scenarios and the possible target system.

On the other hand, this PhD. Dissertation has verified that multivariate normality and WSSUS condition are key issues for experimental analysis and modelling of space-time-frequency channels. The multivariate normality condition is usually assumed during measurement campaigns and the WSSUS condition is imposed within channel models since allow us to include useful channel characteristics for correlation and spectral analysis. Despite these conditions are usually fulfilled for SISO and narrowband channels, for wideband-MIMO and UWB-MIMO channels they are not always fulfilled. In this PhD. Dissertation it has been demonstrated from experimental wideband MIMO data that the multivariate normality condition is not always satisfied in the frequency and space domains. This characteristic can introduce wrong analysis during the synthetic channel generation based on the estimation of covariance matrices. From an experimental analysis point of view, the application of multivariate normality and linearity tests has demonstrated to be a useful tools for reliable MIMO channel analysis.

From a theoretical point of view, the wideband/UWB-MIMO channel does not follow in fact the WSSUS condition. As it was addressed in this Dissertation, one possible way for close formulation of correlation and PSD functions of these channels is to impose this characteristic by means of reliable approximations. Once the WSSUS condition is imposed, as in the proposed FD-DGUS-MIMO channel model, perfect MIMO channel modelling techniques and other strategies for channel parameter estimations can be applied. However, if we desire a full formulation of these frequency-dependent MIMO channels, homogeneous and in-homogeneous plane waves have to be taken into account. This PhD. Dissertation has demonstrated that in-homogeneous plane waves introduce other frequency dependent effects that can modify the correlation characteristics of the wideband MIMO channel. To allow the perfect MIMO channel modelling taking into account both type of plane waves, the WSSUS condition must be fulfilled in both groups. This condition has been reached following close formulations and approximations for both the relative bandwidth dependence and the cross-products within the model.

6.2.2. Particular conclusions of the Dissertation

The specific conclusions of this Dissertation are included below following the list of contributions indicated in Section 1.5. These conclusions permit the reader find the main important outputs of the research addressed within this work.

6.2.2.1. Measurement setup and experimental procedure

A measurement campaign in two indoor scenarios following static conditions, high SNR regimen, and isolation of the path-loss effect for the acquisition of reliable MIMO data between 2 and 12 GHz has been designed and

performed. The measurement setup was proposed, the robotic linear positioning system and the acquisition software were implemented, the UWB antennas were characterized, the minimum conditions for measurements were defined, and the performance of the VNA was verified. Subsequently, a post-processing of data to obtain the normalized non-frequency selective MIMO channel matrix was proposed, which allowed a reliable estimation of FSC MIMO matrices of the system.

6.2.2.2. Channel synthetic generation

A reliable multi-spectral synthetic generator of MIMO channels based on real MIMO data obtained from VNA measurements has been proposed. For the synthetic generation, the well known coloring matrix method was used. This method was carried out performing the Cholesky factorisation of the estimated FSC MIMO matrix, obtaining then the coloring matrix of the MIMO system, which was finally used for the generation of thousands realisations of the MIMO channel.

6.2.2.3. Alternating projection (AP) method for CCM

Based on experimental results, it has been proved that a complex FSC MIMO matrix estimated from real measurement data can be indefinite, being the Cholesky factorisation unsuitable. Moreover, it has been demonstrated that this effect is more probable for large-scale MIMO arrays, appearing higher negative eigenvalues.

In order to make the estimated FSC MIMO matrix positive definite and useful to apply Cholesky, a simple and iterative CP based on the AP method has been proposed. Using specific parameters and number of iterations according to the MIMO matrix dimensions, this procedure finds the Hermitian positive definite FSC MIMO matrix with unit diagonal which is the closest in the Frobenius norm to the original FSC MIMO matrix. In this sense, the proposed procedure can reduce the overall time to carry out a measurement campaign and the channel analysis due to the reduced number of samples that it is possible to use to calculate the experimental FSC MIMO matrices.

The performance of the CP has been investigated for different array configurations. It has been checked the eigenvalue distribution of all estimated FSC MIMO matrices, following an adjustment of all matrices detected as non-positive definite. Results suggest a careful selection of the CP parameters in order to guarantee a 100% success rate and a minimum impact on the CDF of the eigenvalues of the FSC MIMO matrix. Lower values of tol and more iterations are required for large-scale arrays. Besides, optimum values for $\varepsilon_{\min}$ were found for different array dimensions, which can increase the performance of the CP.

Once ensured the positiveness of all FSC MIMO matrices, the Cholesky factorisation has been used to generate as many multi-spectral MIMO channel samples as necessary to assess the ergodic and outage (at 1% and 10%) capacities. Results have proved that the MIMO capacity is not significantly sensitive to the

parameter ε once the positiveness is assured. These results guarantee the reliability of the MIMO channel characterisation presented in this PhD Dissertation.

6.2.2.4. MIMO channel parameter evaluation

The impact of frequency on the MIMO channel characteristics for two different indoor scenarios has been investigated based on experimental multi-spectral measurements between 2 and 12 GHz. A synthetic channel generation has been applied and validated, doing fair comparisons in four different central frequencies under a high SNR regime. The results presented in this Dissertation have shown useful remarks for designs and deployment of wireless systems using MIMO techniques as beamforming, SM, and ST coding, operating at 2, 2.4, 6 and 12 GHz.

The experimental results have shown that the CDFs of the MIMO capacity, eigenvalues, multipath richness, spatial correlation (TX and RX), and the AOA and AOD for two indoor environments have a strong frequency dependence. Besides, these results have indicated that Zone B, which represented a high multipath richness environment, depicts better characteristics for the applicability of SM and ST coding up to 12 GHz. On the other hand, beamforming techniques can be applied up to 12 GHz regardless the indoor scenario due to the high directivity of radio channels at elevated frequencies.

The MIMO system performance analysis have shown remarkable differences between 2 and 12 GHz. Compared with the i.i.d channel for $M = N = \{2, 3, 4\}$ cases, the 1%, 10% and 50% outage capacities were reduced while the frequency was increased. The maximum relative capacity reduction was for $M = N = 4$ at 12 GHz. These results were found in LOS and NLOS conditions. These changes versus frequency were related to the increment of the RX/TX spatial correlation and a reduction of the angular spread, which caused a reduction in the MIMO system eigenvalues while the frequency grows. Reductions in the eigenvalues power were stronger for the smallest eigenvalues, showing modifications with frequency in the distribution of the largest eigenvalue. The differences in capacity, eigenvalues, spatial correlation, and angular characteristics, were lower between 2 and 2.4 GHz, and for NLOS cases.

Experimental results confirm that at higher central frequencies the multipath richness of the channel is reduced, even in NLOS conditions. The performed analysis indicate up to 50% less multipath richness at 12 GHz in NLOS compared with 2 GHz, and much lower in LOS. From a system performance point of view, the reduction in the multipath richness is a drawback for SM and diversity techniques, and in the worst case (Zone A) the performance could be reduced in more than 50% for both propagation conditions at 12 GHz, and in more than 10% at 6 GHz.

Based on correlation and angular results, it was verified that beamforming techniques can offer better performance in LOS cases and higher central frequencies (particularly in Zone A) due to the higher correlation among antenna elements. On the other hand, these increments in the spatial correlation are a

drawback for SM and ST coding, since lower power is carried by the rest of orthogonal modes of the MIMO channel. In these cases, water-filling techniques must be mandatory for SM, but perfect knowledge of the channel is required at the TX. For ST coding, the unknown channel become in a loss of performance at higher frequencies, and according to the correlation results at 12 GHz for Zone A, this MIMO technique for LOS conditions in this kind of scenarios (with low multipath richness) can be prohibitive.

The AOA and AOD analysis based on the phase of the complex spatial correlation coefficients shown different angular characteristics at different central frequencies, mainly in LOS in Zone B, which have proved a strong frequency dependence on the indoor multipath propagation. According to the phase distributions, the multi-spectral MIMO measurements addressed useful characteristics for angular channel parameter estimations. The MIMO channel measurements between 2 and 12 GHz captured angular information with different spatial resolution and fine scattering propagation at higher frequencies. These characteristics can be exploited by super-resolution channel parameter estimations based on parametric methods. In this way, the formulation of new models including multi-spectral resolution and wideband characteristics is a promising research area.

6.2.2.5. Multivariate and linearity analysis of MIMO data

The intrinsic relationship between the non-positiveness of the FSC MIMO matrices with the non multivariate normality of the MIMO data for large-scale channel matrices has been also addressed. The non multivariate normality is increased with the array sizes, even when the normality of the MIMO channel entries is guaranteed (SISO case). It was exposed the theory about MCND and MVCND, being as well tested the UCND and MCND of the MIMO data for different array sizes and frequency window widths, being found the most suitable configuration for experimental analysis. The MVCND was not tested due to the current PDF function consider a Kronecker assumption for the covariance matrix, which is not entirely correct for realistic MIMO channels.

As a possible source of inaccuracy for the covariance estimator applied in this Dissertation, it has been also tested the linearity of the MIMO data entries. This characteristic was checked for different array sizes and segmentations. Matrix size and frequency window width dependency was observed in the linearity of the MIMO data. If higher window widths and arrays sizes are used, higher non-linearity is found.

For reliable experimental MIMO channel analysis there exist a trade-off between normality, linearity and number of samples. It was observed that the assumption of multivariate normality and linearity is key point for MIMO data analysis, but not so much works have been focused in this issue. The understanding of the effects of the non-normality and non-linearity, and its relationship with non-positiveness of experimental FSC MIMO matrices, deal the way for new researches in MIMO analysis based on experimental data.

6.2.2.6. FD-DGUS-MIMO model

A new FD-DGUS-MIMO channel model which includes parameters for modelling space-time channels with different relative wideband signals, high central frequencies and the inclusion of the effects of close scatterers using HPWs and IPWs has been proposed. Despite the existence of IPWs has been reported in physics studies since 1959, the proposed model is the first channel model including both types of plane waves, which permit us to model frequency-dependent effects including possible effects related with wave propagation and the interaction between waves, scatterers and the antennas.

On the other hand, it has been imposed WSSUS conditions for the proposed FD-DGUS-MIMO channel model, which offer suitable characteristics for the application of perfect modelling techniques and then obtaining the channel model parameters from channel sounder or VNA measurements. The imposed DGUS characteristics allowed the calculation of closed forms for the 2D-STFCF and 2D-D^3-PSD functions, which permit us the application of perfect and non-perfect modelling techniques based on PSDs estimations from real world measurements. Besides, based on both the estimation of CFs from measurements and closed forms of the CFs obtained from the 2D-STFCF, the application of INLSA algorithms is feasible. These two techniques for channel model parameters estimations allow the formulation of dedicated simulations models for realistic performance analysis of wideband, high frequency and even UWB-MIMO systems.

Since high order statistics have been used for the perfect modelling proposal following the formulated and estimated PSDs, the model does not consider any approximation, except the approximations used for the parameters resulting from cross-products due to the wideband signals and then from the fine scattering. It is worth to indicate that these approximations have shown low effects in the model performance.

Despite the proposed FD-DGUS-MIMO channel model has been formulated based on a 2D spatial approximation (azimuthally) and it has been proposed for ULAs, as the MIMO measurements performed for this Dissertation, the model can be extended to 3D and including other arrays geometries.

6.3. Future research

The future research topics included in this section follow the classification of contributions indicated in Section 1.5, in the same way as in the conclusions listed above.

6.3.1.1. Measurement setup and experimental procedure

The inclusion of complex antenna characteristics (in azimuth and elevation) within the experimental procedure is a key issue for future multi-spectral MIMO channel analysis. In this way, the development of new algorithms and models are

required to integrate the 3D information of the antenna pattern within the synthetic channel generation. Once this information is included for experimental analysis, possible correlation effects at higher central frequencies related to narrow beams in vertical planes for typical omnidirectional antennas (see Figure 2.9) can be avoided.

6.3.1.2. Channel synthetic generation

In this Dissertation was addressed a synthetic channel generator based on FSC MIMO matrices. For future research, the inclusion of full space-time-frequency correlation matrices seems to be promising (see equation (3.19)). The main drawbacks of this option are the size of the obtained correlation/covariance matrices, the number of samples required for the estimator, the multivariate normality in all domains, increments of the probability of being non-positive definite, computational restrictions, and time consuming for Cholesky factorisations and synthetic generation. As possible solutions are the reduction of the number of samples for the covariance estimators and then the application of the CP procedure based on the AP method, or a hybrid procedure based on the AP method and the SCE method as it was described in Section 3.6.

6.3.1.3. Alternating projection (AP) method for CCM

As it was described in Section 3.4.1, the inclusion of the new parameter $\varepsilon_{\min}$ permits to improve the performance of the CP procedure based on the AP method. For future research, the synthetic channel generation following this procedure can increase the accuracy of the MIMO outage analysis, since a range of small enough possible positive eigenvalues can be used for projections. Hence, the characteristics of the eigenvalue decomposition of the FSC MIMO matrix will be completely fulfilled, i.e., a set of positive ordered eigenvalues with their corresponding eigenvectors. Note that this proposal differs from the AP method used in this Dissertation, which included only one option for ε, which replaced all the negative/cero eigenvalues of the non-positive definite experimental FSC MIMO matrices.

6.3.1.4. MIMO channel parameter evaluation

To improve the understanding of the frequency dependency of the MIMO channel, spatial filtering can be used to study the multi-spectral directional characteristics of the channel between 2 and 12 GHz. As it was indicated in Section 4.4.2, spectral or parametric methods can be applied for angular estimations using ULAs. For future research, the formulations included in Section 4.4.2 can be used for this aim based on the MIMO data obtained for this Dissertation and using the same array configurations. Possible extensions could include different array geometries.

6.3.1.5. Multivariate and linearity analysis of MIMO data

A deeper study about the MIMO matrix variate complex distributions is necessary for the complete understanding of MIMO channels. The multivariate complex normal distribution of the sampled complex MIMO channel transfer matrix and the Wishart distribution of the sampled complex covariance MIMO matrix are the two principal topics for future research. Besides, the link between the measurement procedures and post-processing techniques is another key point in the statistical analysis and simulation of the MIMO channel. In this way, multivariate normality tests can be used for verification of process stationary intervals in all domains (assuring WSS within the MIMO data).

On the other hand, future multivariate analysis of MIMO data can take advantage of the non-singular MIMO matrix variate complex normal distribution addressed in equation (3.30). This distribution belongs to the class of matrix variate elliptically contoured distributions (see Appendix A.1). In particular for $\mathbf{M}_x = 0$, the distribution belongs to:

a) Right spherical (isotropic) distributions if $\mathbf{\Sigma}_{x_T}^{[\nu,\tau']} = \mathbf{I}_M$.

b) Left spherical distributions if $\mathbf{\Sigma}_{x_R}^{[\nu,\tau']} = \mathbf{I}_N$.

c) Spherical distributions if $\mathbf{\Sigma}_{x_R}^{[\nu,\tau]} = \mathbf{I}_N$ and $\mathbf{\Sigma}_{x_T}^{[\nu,\tau]} = \mathbf{I}_M$.

These possible options are linked to the channel propagation conditions. They are only reached under both normalized channels and uncorrelated conditions. Space uncorrelated conditions, either at the TX or at the RX, can reach cases a) and b), respectively. If the un-correlation happens at both ends of the link, the case c) is reached. Otherwise, the MIMO channel belongs to the matrix variate elliptically contoured distribution (see Appendix A.1). As it was performed in Figure 3.8, we can take advantage of these characteristics for future simple visual inspection of the MIMO channel characteristics and its stationary intervals.

This statistical and geometrical analysis will contribute in future works to the understanding of the multi-spectral MIMO channel behaviour in real propagation conditions, since the eigenvectors and eigenvalues of $\mathbf{\Sigma}_x^{[\nu,\tau']} = \mathbf{\Sigma}_{x_R}^{[\nu,\tau']} \otimes \mathbf{\Sigma}_{x_T}^{[\nu,\tau']}$ have a strong relationship with multipath direction of arrival and departure, which are related to the spatial correlation at both ends of the link, and also define the MIMO channel capacity.

On the other hand, the covariance matrix characteristics, i.e., the Wishart distribution (see Appendix A.2), may be exploited to prove the normality of MIMO data and process stationary. The drawback of this option is that the theoretical Wishart distribution is itself confident in the multivariate normality of the MIMO data, which indicates they can be only used to reject cases of not multivariate normality.

Moreover, the independence of the time snapshot samples of $\widehat{\mathbf{h}}_{\omega,v}^{[t_\kappa]}$, and the total number of time samples, K, plays a crucial role for covariance analysis, since the number of samples have to be higher than the MIMO matrix dimensions, i.e., $K > NM$, to follow a Wishart distribution. The last necessary condition is not fulfilled for the performed measurement campaigns in Zones A and B when $N = M > 7$ due to $K = 50$. For future researcher activities in this field, and as a simple solution, it is possible to consider the frequency domain bin samples as a new sampled independent population, i.e., $\widehat{\mathbf{h}}_{\omega,v}^{[f_0,t_\kappa]}, \widehat{\mathbf{h}}_{\omega,v}^{[f_1,t_\kappa]}, \ldots \widehat{\mathbf{h}}_{\omega,v}^{[f_{I-1},t_\kappa]}$, being independent variables with $N_{NM}\left(\boldsymbol{\mu}_x, \boldsymbol{\Sigma}_x^{[\nu]}\right)$ distribution. This assumption increases the total number of samples to estimated the complex covariance matrix $\widehat{\boldsymbol{\Sigma}}_x^{[\nu,\tau']}$ (see (3.28)), being $KI > NM$, which agrees with the Wishart distribution assumption. Hence, for future works, the following statements must be verified in the MIMO data:

- $\hat{\boldsymbol{\mu}}_x$ and $KI\widehat{\boldsymbol{\Sigma}}_x^{[\nu,\tau']}$ are independently distributed.
- $\hat{\boldsymbol{\mu}}_x \sim N_{NM}\left(\boldsymbol{\mu}_x, \frac{1}{KI}\boldsymbol{\Sigma}_x^{[\nu,\tau']}\right)$.
- and $KI\widehat{\boldsymbol{\Sigma}}_x^{[\nu,\tau]} \sim W_{NM}\left(KI-1, \boldsymbol{\Sigma}_x^{[\nu,\tau']}\right)$.

where $W_{NM}\left(KI-1, \boldsymbol{\Sigma}_x^{[\nu,\tau']}\right)$ denotes Wishart distribution, with $KI-1$ degrees of freedom. More details about the Wishart distribution can be found in the Appendix A.2.

6.3.1.6. FD-DGUS-MIMO model

Future research related to the FD-DGUS-MIMO is aimed to improve the modelling of the IPWs, including 3D propagation and deeper analysis of the space-time-frequency dependency of these waves. So far the model has been designed for ULA in 2D propagation conditions, but most realistic conditions including IPWs in the local area (mainly in confined environments) require 3D considerations. Besides, it is possible to model the parameter $\alpha_{\ell'}$ (see equations (5.6) and (5.106)) as a local area size dependent function

$$\alpha_{\ell'}\left(\lambda_0, \tau_\ell, \Omega_{R_\ell}\right), \quad \forall\ \ell' \neq \ell$$

where $\{\tau_\ell\}$ are the set of delays ($\tau_\ell \in \mathbb{R}_+, \forall \ell$) for HPW, and $\left\{\Omega_{R_\ell}\right\}$ the set of direction of arrivals ($\Omega_{R_\ell} \in \mathbb{R}_+, \forall \ell$) for HPW as well. Based on this hypothesis, the reduction of the MIMO channel simulator complexity (and the time consuming for simulations) is feasible, since this amplitude decay constant defines the amplitude of the IPWs components (see (5.107)). This means that some scatterers

can be avoided as potential contributors of IPWs due to their contributions would be weaker.

Perhaps one of the most interesting future research topics in plane wave propagation modelling is the consideration of millimetre-waves (MMW) as target frequency band for communication systems. As it was indicated in this Dissertation, the effective wavelength, $\lambda_{eff_{\ell'}}$, of the IPWs is always shorter than the free-space wavelength, i.e., $\lambda_{eff_{\ell'}} < \lambda_0$. This characteristic at MMW can affect extremely the space-time-frequency correlation features of the channel if confined areas are considered as target scenarios. An inspection of the model parameters included in (5.134) verifies this affirmation.

On the other hand, for this PhD. Dissertation has been proposed the perfect MIMO channel modelling procedure based on the theoretical and experimental PSDs. In this way, the future work includes the estimation of the PSDs based on the multi-spectral MIMO data, and then the application of the procedure proposed in Section 5.6.2 for model parameters estimations. Moreover, the correlation functions, i.e., the theoretical definition in (5.134) of the 2D-STFCF and its experimental counterpart, are other useful alternative for future model parameters estimation (see Section 5.6.4) based on the INLSA algorithm.

Finally, it is worth to indicate that the proposed FD-DGUS-MIMO model is expected to be extended to UWB-MIMO and higher central frequencies.

APPENDIX A

MULTIVARIATE STATISTICS FOR MIMO

A.1. Matrix variate complex normal distribution

The MIMO complex random matrix $\widehat{\mathbf{H}}_{\omega,v}^{[f_{l'},t_{\kappa'}]} \in \mathbb{C}^{N\times M}$ is said to have a the matrix variate complex normal distribution (MVCND),

$$\widehat{\mathbf{H}}_{\omega,v}^{[f_{l'},t_{\kappa'}]} \sim N_{N,M}\left(\mathbf{M}_x, \boldsymbol{\Sigma}_{x_R}^{[\nu,\tau']} \otimes \boldsymbol{\Sigma}_{x_T}^{[\nu,\tau']}\right) \tag{A.1}$$

with complex mean matrix $\mathbf{M}_x \in \mathbb{C}^{N\times M}$ and complex covariance matrix $\boldsymbol{\Sigma}_{x_R}^{[\nu,\tau']} \otimes \boldsymbol{\Sigma}_{x_T}^{[\nu,\tau']}$, where $\boldsymbol{\Sigma}_{x_R}^{[\nu,\tau']} > 0$ and $\boldsymbol{\Sigma}_{x_T}^{[\nu,\tau']} > 0$, if

$$vec\left(\widehat{\mathbf{H}}_{\omega,v}^{[f_{l'},t_{\kappa'}]}\right) \sim N_{NM}\left(vec\left(\mathbf{M}_x\right), \boldsymbol{\Sigma}_{x_R}^{[\nu,\tau']} \otimes \boldsymbol{\Sigma}_{x_T}^{[\nu,\tau']}\right) \tag{A.2}$$

being $\boldsymbol{\Sigma}_{x_R}^{[\nu,\tau']} \in \mathbb{C}^{N\times N}$ and $\boldsymbol{\Sigma}_{x_T}^{[\nu,\tau']} \in \mathbb{C}^{M\times M}$ the complex covariance matrices at the RX and TX sides, respectively. Under the Kronecker separability assumption, the PDF of $\widehat{\mathbf{H}}_{\omega,v}^{[f_{l'},t_{\kappa'}]}$ is given by:

$$\begin{aligned} &p\left(\widehat{\mathbf{H}}_{\omega,v}^{[f_{l'},t_{\kappa'}]}\right) = (2\pi)^{-\frac{NM}{2}} \det\left(\boldsymbol{\Sigma}_{x_R}^{[\nu,\tau']}\right)^{-\frac{M}{2}} \det\left(\boldsymbol{\Sigma}_{x_T}^{[\nu,\tau']}\right)^{-\frac{N}{2}} \cdot \\ &\cdot \exp\left\{Tr\left[-\frac{1}{2}\left(\boldsymbol{\Sigma}_{x_R}^{[\nu,\tau']}\right)^{-1}\left(\widehat{\mathbf{H}}_{\omega,v}^{[f_{l'},t_{\kappa'}]} - \mathbf{M}_x\right)\left(\boldsymbol{\Sigma}_{x_T}^{[\nu,\tau']}\right)^{-1}\left(\widehat{\mathbf{H}}_{\omega,v}^{[f_{l'},t_{\kappa'}]} - \mathbf{M}_x\right)^H\right]\right\}. \end{aligned} \tag{A.3}$$

The PDF in (A.3) is obtained from the multivariate complex normal distribution (MCND) of the space sampled variables of $\widehat{\mathbf{H}}_{\omega,v}$. Thus, consider a space dimension vector of the space-frequency-time sampled observation matrix, $\widehat{\mathbf{H}}_{\omega,v}$, as

$$\widehat{\mathbf{h}}_{\omega,v}^{[f_{l'},t_{\kappa'}]} = vec\left(\widehat{\mathbf{H}}_{\omega,v}^{[f_{l'},t_{\kappa'}]}\right) \in \mathbb{C}^{NM\times 1}. \tag{A.4}$$

Under the assumption of non-frequency-selectivity and total stationary process, it then said that the vector $\widehat{\mathbf{h}}_{\omega,v}^{[f_l',t_\kappa']}$ is a NM -dimensional MCND if and only if all linear combinations (in a space of $I \times K$ size) of that vector are univariate complex normal:

$$\widehat{\mathbf{h}}_{\omega,v}^{[f_l',t_\kappa']} \sim N_{NM}\left(\boldsymbol{\mu}_x, \boldsymbol{\Sigma}_x^{[\nu,\tau']}\right) \Leftrightarrow \mathbf{b}^T\widehat{\mathbf{h}}_{\omega,v}^{[f_l',t_\kappa']} \sim N\left(\mathbf{b}^T\boldsymbol{\mu}_x, \mathbf{b}^T\boldsymbol{\Sigma}_x^{[\nu,\tau']}\mathbf{b}\right), \quad \forall \mathbf{b} \in \mathbb{R}^{NM\times 1}, \tag{A.5}$$

where $N_{NM}\left(\boldsymbol{\mu}_x, \boldsymbol{\Sigma}_x^{[\nu,\tau']}\right)$ denote MCND with mean vector $\boldsymbol{\mu}_x \in \mathbb{C}^{NM\times 1}$ and covariance matrix $\boldsymbol{\Sigma}_x^{[\nu,\tau']} \in \mathbb{C}^{NM\times NM}$. The PDF in such case, $p_{\widehat{\mathbf{h}}_{\omega,v}^{[f_l',t_\kappa']}}\left(\widehat{H}_{11}^{\omega,v},\cdots,\widehat{H}_{NM}^{\omega,v}\right)$, is given by

$$\begin{aligned}
&p_{\widehat{\mathbf{h}}_{\omega,v}^{[f_l',t_\kappa']}}\left(\widehat{H}_{11}^{\omega,v},\widehat{H}_{21}^{\omega,v},\ldots,\widehat{H}_{N1}^{\omega,v},\widehat{H}_{12}^{\omega,v},\widehat{H}_{22}^{\omega,v}\ldots,\widehat{H}_{N2}^{\omega,v},\ldots,\widehat{H}_{1M}^{\omega,v},\widehat{H}_{2M}^{\omega,v},\ldots,\widehat{H}_{NM}^{\omega,v}\right) = \\
&= (2\pi)^{-\frac{NM}{2}}\det\left(\boldsymbol{\Sigma}_x^{[\nu,\tau']}\right)^{-\frac{1}{2}}\exp\left\{Tr\left[-\frac{1}{2}\left(\boldsymbol{\Sigma}_x^{[\nu,\tau']}\right)^{-1}\left(\widehat{\mathbf{h}}_{\omega,v}^{[f_l',t_\kappa']}-\boldsymbol{\mu}_x\right)\left(\widehat{\mathbf{h}}_{\omega,v}^{[f_l',t_\kappa']}-\boldsymbol{\mu}_x\right)^H\right]\right\} = \\
&= (2\pi)^{-\frac{NM}{2}}\det\left(\boldsymbol{\Sigma}_x^{[\nu,\tau']}\right)^{-\frac{1}{2}}\exp\left\{-\frac{1}{2}\left(\widehat{\mathbf{h}}_{\omega,v}^{[f_l',t_\kappa']}-\boldsymbol{\mu}_x\right)^H\left(\boldsymbol{\Sigma}_x^{[\nu,\tau']}\right)^{-1}\left(\widehat{\mathbf{h}}_{\omega,v}^{[f_l',t_\kappa']}-\boldsymbol{\mu}_x\right)\right\}, \\
&\widehat{\mathbf{h}}_{\omega,v}^{[f_l',t_\kappa']} \in \mathbb{C}^{NM\times 1}, \boldsymbol{\mu}_x \in \mathbb{C}^{NM\times 1}, \boldsymbol{\Sigma}_x^{[\nu,\tau']} > 0, \boldsymbol{\Sigma}_x^{[\nu,\tau']} \in \mathbb{C}^{NM\times NM},
\end{aligned} \tag{A.6}$$

Therefore, (A.3) is obtained from (A.6) taking into account that:

$$\boldsymbol{\mu}_x = vec\left(\mathbf{M}_x\right), \tag{A.7}$$

$$\boldsymbol{\Sigma}_x^{[\nu,\tau']} = \boldsymbol{\Sigma}_{x_R}^{[\nu,\tau']} \otimes \boldsymbol{\Sigma}_{x_T}^{[\nu,\tau']}, \tag{A.8}$$

$$\det\left(\boldsymbol{\Sigma}_{x_R}^{[\nu,\tau']} \otimes \boldsymbol{\Sigma}_{x_T}^{[\nu,\tau']}\right)^{-\frac{1}{2}} = \det\left(\boldsymbol{\Sigma}_{x_R}^{[\nu,\tau']}\right)^{-\frac{M}{2}}\det\left(\boldsymbol{\Sigma}_{x_T}^{[\nu,\tau']}\right)^{-\frac{N}{2}}, \tag{A.9}$$

$$\left(\boldsymbol{\Sigma}_{x_R}^{[\nu,\tau']} \otimes \boldsymbol{\Sigma}_{x_T}^{[\nu,\tau']}\right)^{-1} = \left(\boldsymbol{\Sigma}_{x_R}^{[\nu,\tau']}\right)^{-1} \otimes \left(\boldsymbol{\Sigma}_{x_T}^{[\nu,\tau']}\right)^{-1}. \tag{A.10}$$

On the other hand, for $\widehat{\mathbf{h}}_{\omega,v}^{[f_l',t_\kappa']} \sim N_{NM}\left(\boldsymbol{\mu}_x, \boldsymbol{\Sigma}_x^{[\nu,\tau']}\right)$, the equidensity contours of a non-singular MCND, as in (A.6), are ellipsoids centred at the mean. The directions of the principal axes of such ellipsoids are given by the eigenvectors of $\boldsymbol{\Sigma}_x^{[\nu,\tau']}$, and their squared relative lengths are given by the corresponding eigenvalues. Applying the eigendecomposition (with displacement variables neglected)

$$\mathbf{\Sigma}_x = \mathbf{U}\mathbf{V}\mathbf{U}^H = \mathbf{U}\mathbf{V}^{½}\left(\mathbf{U}\mathbf{V}^{½}\right)^H, \tag{A.11}$$

the unit eigenvectors, $\mathbf{u}_q \in \mathbb{C}^{NM\times 1}$, are the columns of $\mathbf{U} \in \mathbb{C}^{NM\times NM}$, and the corresponding eigenvalues, $\{\vartheta_q\}$, are on the diagonal matrix $\mathbf{V} \in \mathbb{R}^{NM\times NM}$, where $q = \{1,2,\cdots,NM\}$ and $\vartheta_1 > \vartheta_2 \cdots > \vartheta_{NM}$. Then, the MCND must fulfil

$$\begin{aligned} &\widehat{\mathbf{h}}_{\omega,v}^{[f_{l'},t_{\kappa'}]} \sim N_{NM}\left(\boldsymbol{\mu}_x,\mathbf{\Sigma}_x\right) \Leftrightarrow \widehat{\mathbf{h}}_{\omega,v}^{[f_{l'},t_{\kappa'}]} \sim \boldsymbol{\mu}_x + \mathbf{U}\mathbf{V}^{½}N_{NM}\left(0,\mathbf{I}_{NM}\right), \\ &\widehat{\mathbf{h}}_{\omega,v}^{[f_{l'},t_{\kappa'}]} \sim N_{NM}\left(\boldsymbol{\mu}_x,\mathbf{\Sigma}_x\right) \Leftrightarrow \widehat{\mathbf{h}}_{\omega,v}^{[f_{l'},t_{\kappa'}]} \sim \boldsymbol{\mu}_x + \mathbf{V}N_{NM}\left(0,\mathbf{V}\right), \end{aligned} \tag{A.12}$$

where $\mathbf{I}_{NM}$ is a NM by NM identity matrix. Therefore, the distribution $N_{NM}\left(\boldsymbol{\mu}_x,\mathbf{\Sigma}_x\right)$ is a distribution of the form $N_{NM}\left(0,\mathbf{I}_{NM}\right)$ scaled by $\mathbf{V}^{½}$, rotated by $\mathbf{U}$ and translate by $\boldsymbol{\mu}_x$. Here, for any $\boldsymbol{\mu}_x$, full rank matrix $\mathbf{U}$ and positive eigenvalues $\{\vartheta_q\}$, the distribution is non-singular MCND, but if any ϑ_q is zero then $\mathbf{\Sigma}_x = \mathbf{U}\mathbf{V}\mathbf{U}^H$ is singular and the contour ellipsoids become infinitely thins and with zero volume because at least one of the principal axes has length of zero.

A.2. Matrix variate complex Wishart distribution

Consider a vector $\widehat{\mathbf{h}}_{\omega,v}^{[t_{\kappa'}]} = vec\left(\widehat{\mathbf{H}}_{\omega,v}^{[t_{\kappa'}]}\right) \in \mathbb{C}^{NM\times 1}$ where the frequency domain has been avoided. Besides, consider the time snapshots samples, $\widehat{\mathbf{h}}_{\omega,v}^{[t_0]}, \widehat{\mathbf{h}}_{\omega,v}^{[t_1]}, \ldots \widehat{\mathbf{h}}_{\omega,v}^{[t_{K-1}]}$, as independent $N_{NM}\left(\boldsymbol{\mu}_x,\mathbf{\Sigma}_x^{[\tau']}\right)$ variables, and the complex covariance matrix $\mathbf{\Sigma}_x^{[\tau']} > 0$ and $K > NM$.

If the sampled complex vector mean $\hat{\boldsymbol{\mu}}_x$ and the sampled complex covariance matrix $\widehat{\mathbf{\Sigma}}_x^{[\tau']}$ are given respectively by:

$$\hat{\boldsymbol{\mu}}_x = \frac{1}{K}\sum_{\kappa=0}^{K-1}\widehat{\mathbf{h}}_{\omega,v}^{[t_{\kappa'}]}, \tag{A.13}$$

$$\widehat{\mathbf{\Sigma}}_x^{[\tau]} = \frac{1}{K}\sum_{\kappa=0}^{K-1}\left(\widehat{\mathbf{h}}_{\omega,v}^{[t_{\kappa'}]} - \hat{\boldsymbol{\mu}}_x\right)\left(\widehat{\mathbf{h}}_{\omega,v}^{[t_{\kappa'}+\tau']} - \hat{\boldsymbol{\mu}}_x\right)^H, \tag{A.14}$$

then:

- $\hat{\boldsymbol{\mu}}_x$ and $K\widehat{\mathbf{\Sigma}}_x^{[\tau']}$ are independently distributed,

- $\hat{\boldsymbol{\mu}}_x \sim N_{NM}\left(\boldsymbol{\mu}_x, \frac{1}{K}\boldsymbol{\Sigma}_x^{[\tau']}\right)$,
- and $K\widehat{\boldsymbol{\Sigma}}_x^{[\tau']} \sim W_{NM}\left(K-1, \boldsymbol{\Sigma}_x^{[\tau']}\right)$,

where $W_{NM}\left(K-1, \boldsymbol{\Sigma}_x^{[\tau']}\right)$ denote matrix variate complex Wishart distribution (MVCWD), with $K-1$ degrees of freedom, if its PDF is given by

$$p\left(K\widehat{\boldsymbol{\Sigma}}_x^{[\tau]}\right) = \left(2^{\frac{NM(K-1)}{2}}\Gamma_{NM}\left(\frac{1}{2}(K-1)\right)\det\left(\boldsymbol{\Sigma}_x^{[\tau']}\right)^{\frac{(K-1)}{2}}\right)^{-1} \times \det\left(K\widehat{\boldsymbol{\Sigma}}_x^{[\tau]}\right)^{\frac{1}{2}((K-1)-NM-1)} \exp\left\{Tr\left[-\frac{1}{2}\left(\boldsymbol{\Sigma}_x^{[\tau']}\right)^{-1} K\widehat{\boldsymbol{\Sigma}}_x^{[\tau']}\right]\right\}, \quad \text{(A.15)}$$

with $K\widehat{\boldsymbol{\Sigma}}_x^{[\tau]} > 0, (K-1) \geq NM,$

where $\Gamma_{NM}(\cdot)$ denote multivariate gamma function

$$\Gamma_{NM}\left(\frac{1}{2}(K-1)\right) = \pi^{\frac{1}{4}NM(NM-1)}\prod_{q=1}^{NM}\Gamma\left(\frac{1}{2}(K-1)-\frac{1}{2}(q-1)\right). \quad \text{(A.16)}$$

The main assumption of this definition is that the sampled complex covariance matrix $K\widehat{\boldsymbol{\Sigma}}_x^{[\tau']}$ is Wishart distributed if the samples come from a multivariate complex normal population. In such case, $\widehat{\boldsymbol{\Sigma}}_x^{[\tau']}$ is the maximum likelihood estimator (MLE) of $\boldsymbol{\Sigma}_x^{[\tau']}$ under the assumption that $\boldsymbol{\Sigma}_x^{[\tau]}$ is positive definite. Noted that $\left(\hat{\boldsymbol{\mu}}_x, \widehat{\boldsymbol{\Sigma}}_x^{[\tau']}\right)$ formed a complete sufficient set of statistics for $\left(\boldsymbol{\mu}_x, \boldsymbol{\Sigma}_x^{[\tau']}\right)$. Hence, the MVCWD can give us information about the MCND of a MIMO data set.

A.3. Surfaces of constant variance

The MCND given in (A.6) can be represented experimentally as surfaces of constant variance (SCV), σ^2, which correspond to surfaces of equal probability for MCND vectors satisfying

$$\left(\widehat{\mathbf{h}}_{\omega,v}^{[f_l',t_k']} - \hat{\boldsymbol{\mu}}_x\right)^H \left(\widehat{\boldsymbol{\Sigma}}_x^{[\nu,\tau']}\right)^{-1} \left(\widehat{\mathbf{h}}_{\omega,v}^{[f_l',t_k']} - \hat{\boldsymbol{\mu}}_x\right) = \sigma^2. \quad \text{(A.17)}$$

These SCV are NM-dimensional ellipsoids centred at $\hat{\boldsymbol{\mu}}_x$, with exes of symmetry given by the eigenvectors of $\widehat{\boldsymbol{\Sigma}}_x^{[\nu,\tau']}$, denoted by $\hat{\mathbf{u}}_q \in \mathbb{C}^{NM\times 1}$, and major and minor axes (of square relative length) given by its eigenvalues, denoted by $\left\{\hat{\vartheta}_q\right\}$, where $q=\{1,2,\cdots,NM\}$ and $\hat{\vartheta}_1 > \hat{\vartheta}_2 \cdots > \hat{\vartheta}_{NM}$ (see also equations (A.11) and (A.12)).

For the MCND visual test using MIMO data, the NM-dimensional ellipsoids are obtained using $\hat{\mathbf{u}}_q \in \mathbb{C}^{NM\times 1}$ and $\left\{\hat{\vartheta}_q\right\}$ from the eigendecomposition

$$\widehat{\boldsymbol{\Sigma}}_x^{[\nu,\tau']} = \widehat{\mathbf{U}}\widehat{\mathbf{V}}\widehat{\mathbf{U}}^H = \left(\hat{\mathbf{u}}_1 \cdots \hat{\mathbf{u}}_{NM}\right)\begin{pmatrix} \hat{\vartheta}_1 & 0 & 0 \\ 0 & \ddots & 0 \\ 0 & 0 & \hat{\vartheta}_{NM} \end{pmatrix}\left(\hat{\mathbf{u}}_1 \cdots \hat{\mathbf{u}}_{NM}\right)^H, \tag{A.18}$$

where

$$\widehat{\boldsymbol{\Sigma}}_x^{[\nu,\tau']} = \frac{1}{KI}\sum_{l'=0}^{I-1}\sum_{\kappa'=0}^{K-1}\left(\widehat{\mathbf{h}}_{\omega,v}^{[fl',t_\kappa']} - \hat{\boldsymbol{\mu}}_x\right)\left(\widehat{\mathbf{h}}_{\omega,v}^{[fl'+\nu,t_{\kappa'}+\tau']} - \hat{\boldsymbol{\mu}}_x\right)^H. \tag{A.19}$$

These ellipsoids are centred at

$$\hat{\boldsymbol{\mu}}_x = \frac{1}{KI}\sum_{\kappa'=0}^{K-1}\sum_{l'=0}^{I-1}\widehat{\mathbf{h}}_{\omega,v}^{[fl',t_\kappa']}, \tag{A.20}$$

and the range of σ^2 for the current multivariate vector data $\widehat{\mathbf{h}}_{\omega,v}^{[f_{l'},t_{\kappa'}]}$ is obtained computing (A.17) for all temporal and frequency samples K and I. Each sample of σ^2 defines, for each ellipsoid, the different size of the minor and mayor axes, y_q, together with the eigenvalues of $\widehat{\boldsymbol{\Sigma}}_x^{[\nu,\tau']}$ as follows:

$$y_q = \sigma\hat{\vartheta}_q^{-1/2}. \tag{A.21}$$

Therefore, the orientation and magnitude of these axes are totally described by

$$y_q = \sigma\hat{\vartheta}_q^{-1/2} = \hat{\mathbf{u}}_q^H\widehat{\mathbf{h}}_{\omega,v}. \tag{A.22}$$

Thus, for instance, for the channel configuration $(N=2,\ M=1)$ the minor, y_1, and mayor, y_2, axes are given by

$$y_1 = \sigma\hat{\vartheta}_1^{-1/2} = \begin{pmatrix} \hat{u}_{11} \\ \hat{u}_{21} \end{pmatrix}^H \begin{pmatrix} \widehat{h}_{11} \\ \widehat{h}_{21} \end{pmatrix}, \tag{A.23}$$

$$y_2 = \sigma\hat{\vartheta}_2^{-1/2} = \begin{pmatrix} \hat{u}_{12} \\ \hat{u}_{22} \end{pmatrix}^H \begin{pmatrix} \widehat{h}_{11} \\ \widehat{h}_{21} \end{pmatrix}, \tag{A.24}$$

where $\hat{u}_{11}$ and $\hat{u}_{21}$ are the entries of $\hat{\mathbf{u}}_1$, and $\hat{u}_{12}$ and $\hat{u}_{22}$ are the entries of $\hat{\mathbf{u}}_2$. Note that $\widehat{\mathbf{U}} \in \mathbb{C}^{2\times 2}$ and $\widehat{\mathbf{V}} \in \mathbb{R}^{2\times 2}$. Besides, note that equations (A.23) and (A.24) depicts the projection of the MIMO data in the new axes defined by $\hat{\mathbf{u}}_1$ and $\hat{\mathbf{u}}_2$.

In order to clarify these issues, Figure A.1 shows an example for the SIMO configuration described above using real measurement data. Figure A.1.a shows the ellipses depicting the SCV (real part of $\widehat{\mathbf{h}}$), and Figure A.1.b the PDFs from the

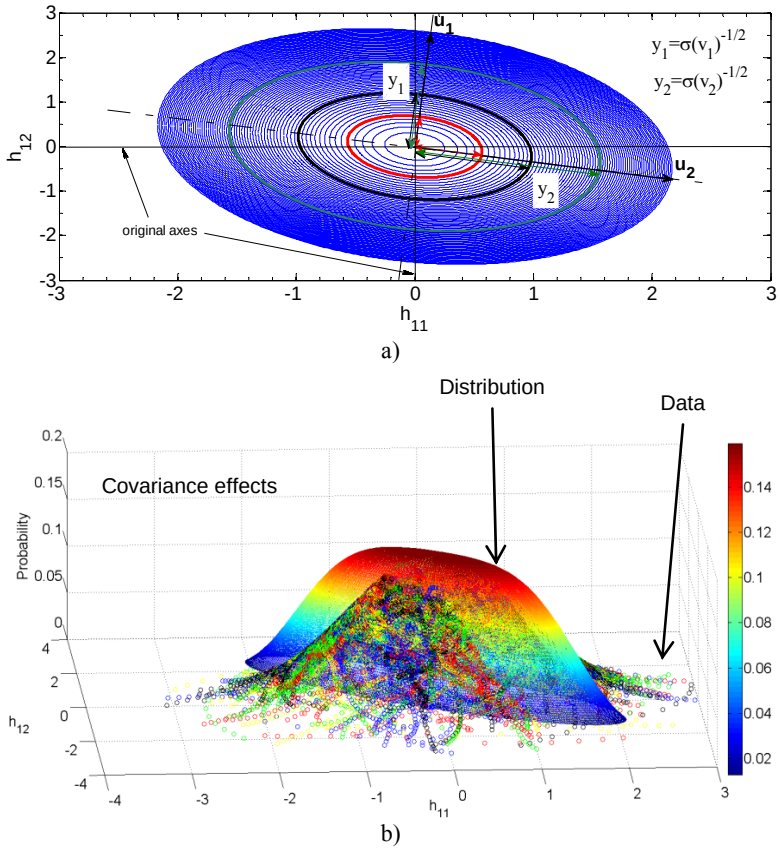

Figure A.1. Multivariate normal distribution (MND) analysis with $\hat{\boldsymbol{\mu}}_x = \mathbf{0}$: a) surfaces of constant variance for $(N = 2,\ M = 1)$, and b) theoretical and experimental PDFs.

theoretical and experimental data (real part of $\widehat{\mathbf{h}}$).